

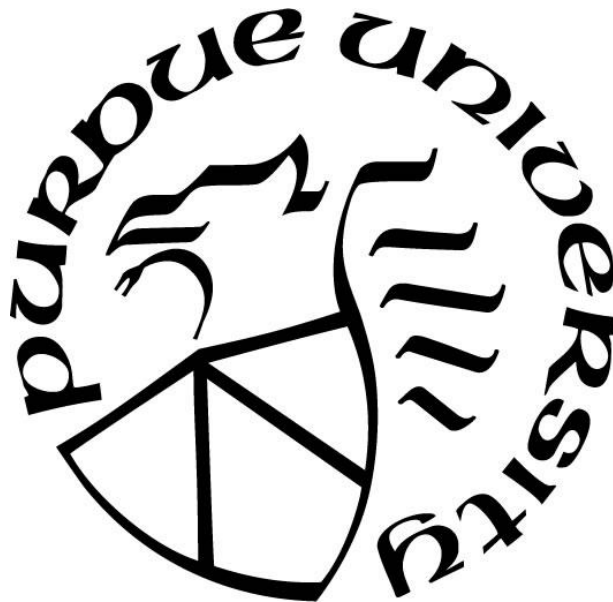
**INVESTIGATION OF CHEMICAL LOOPING FOR HIGH EFFICIENCY
HEAT PUMPING**

by
Nelson James

A Dissertation

*Submitted to the Faculty of Purdue University
In Partial Fulfillment of the Requirements for the degree of*

Doctor of Philosophy



School of Mechanical Engineering
West Lafayette, Indiana
May 2019

**THE PURDUE UNIVERSITY GRADUATE SCHOOL
STATEMENT OF COMMITTEE APPROVAL**

Dr. James Braun, Co-Chair

School of Mechanical Engineering

Dr. Eckhard Groll, Co-Chair

School of Mechanical Engineering

Dr. W. Travis Horton

Lyles School of Civil Engineering

Dr. Timothée Pourpoint

School of Aeronautics and Astronautics

Approved by:

Dr. Jay Gore

Head of the Graduate Program

For my family, friends, and all who've supported my journey

ACKNOWLEDGMENTS

My time here at Purdue has provided me with the opportunity to grow in many aspects of my life. I am grateful to the many people I have met and the resources that I have been able to utilize to help me towards the completion of this degree. While it is difficult to name everyone, I wish to express my gratitude to all who encouraged my success.

The support of my co-advisors Jim Braun and Eckhard Groll has been instrumental to my success while at Purdue. They have pushed me to take advantage of many opportunities to develop as a researcher and scholar. From teaching courses, to traveling to present research and learn new skills, they have helped me to be a more rounded professional. Most importantly, they have always pushed me towards exploring my interest. I appreciate them allowing me to work with them on multiple grants and their support in letting me pitch and secure funding for exploring the chemical looping concept. I would like to thank them for their trust in me to allow me to explore such a novel concept. Their unwavering guidance and support was truly appreciated. I would also like to thank my committee members Prof. Travis Horton and Prof. Timothée Pourpoint for their advice and support throughout my studies.

My family, friends, and loved ones were instrumental in helping me persevere through this program. The check-ins of my parents and siblings helped me to never feel far removed from home. I would like to offer special thanks to Brittini Echols for her love and support in helping me cross the finish line. Additionally, the colleagues that I have had the privilege of working alongside at Herrick Laboratories have truly enriched my experiences during my graduate studies. I would like to thank Dominique Lumpkin and Sheldon Anderson for their friendship and the many adventures we took together over the years. I would also like to thank Davide Ziavani, Orkan Kurtulus, Abhinav Krishna, Brandon Woodland, Ian Bell, Howard Cheung, Christian Back, Stephen Caskey, Harshad Inamdar, and Supriya Dhakar for their guidance and friendship throughout my graduate studies. Your insights on technical and professional matters were always appreciated and your friendship was truly invaluable.

The staff at Herrick has been a constant source of support throughout my time at Purdue. The experimental aspects of this work would not have been possible without the aid and assistance of Frank Lee and Bob Brown. Your technical skills and willingness to help have been invaluable in helping me to surmount numerous challenges during construction and operation of my equipment. The office staff including Donna Cackley, Cindy Cory, and Kim Stockment helped make the Herrick community an open and welcoming environment. Their assistance in organizing events, streamlining deliveries, and showing interest in the well-being of the students was a constant reminder of the lab's support. I would also like to thank Prof. Rhoades, Allison Murray and Trevor Fleck for allowing me to use the resources of their research group.

I would like to thank all those who helped provide financial support to me during my studies. The Center for High Performance Buildings at Purdue provided financial and technical support to the pursuit of my dissertation topic. The Lambert fellowship allowed for me to gain valuable teaching experience. Purdue's Alliance for Graduate Education and the Professoriate, ASHRAE's Grant-in-Aid, the Winkelman Fellowship, and The GEM Consortium, all provided financial support that was truly appreciated.

TABLE OF CONTENTS

LIST OF TABLES	11
LIST OF FIGURES	12
NOMENCLATURE	18
ABSTRACT.....	20
CHAPTER 1. INTRODUCTION	22
1.1 Motivation.....	22
1.1.1 Growing Populations	23
1.1.2 Increasing Standards of Living	23
1.1.3 Warming Temperatures	24
1.1.4 Paths Forward	25
1.2 Heat Pumping Cycles.....	26
1.2.1 Vapor Compression Cycles	26
1.2.2 Gas Cycles	27
1.2.3 Sorption Cycles.....	28
1.2.4 Chemical Heat Pumps.....	28
1.2.5 Caloric Cycles.....	29
1.2.6 Thermoacoustic Cycles.....	29
1.2.7 Thermoelectric Devices	30
1.2.8 Thermionic Devices.....	30
1.3 Chemical Looping Heat Pump.....	31
1.4 Research Objectives and Approach	33
1.5 References.....	33
CHAPTER 2. LITERATURE REVIEW	39
2.1 Chemical Heat Pumps.....	39
2.1.1 Thermally Driven Chemical Heat Pumps	40
2.1.2 Mechanically Driven Chemical Heat Pumps	44
2.1.3 Electrochemically Driven Chemical Heat Pumps	45
2.2 Contributions.....	48
2.3 References.....	48

CHAPTER 3. WORKING FLUID SELECTIONS.....	55
3.1 Liquid Fuel Cells.....	56
3.2 Organic Thermally Regenerative Fuel Cells.....	58
3.3 Electro-Organic Synthesis	59
3.4 Proton Exchange Membrane CLHP.....	61
3.5 References.....	63
CHAPTER 4. THERMODYNAMIC SYSTEM MODEL.....	70
4.1 CLHP Model Development	70
4.1.1 System Conditions.....	70
4.1.2 Reaction Stoichiometry and Flow Rates.....	71
4.1.3 Pump Modeling	72
4.1.4 Electrochemical Cell Work.....	72
4.1.5 Expansion and Evaporation	74
4.1.6 System Performance Metric	75
4.2 CLHP Model Results	75
4.2.1 CLHP Working Fluids Comparisons.....	75
4.2.2 CLHP Parametric Study	77
4.3 Comparisons to other Heat Pumps.....	80
4.3.1 Electrochemical Systems	81
4.3.2 Conventional Systems	82
4.4 References.....	83
CHAPTER 5. ELECTROCHEMICAL CELL EXPERIMENTAL SETUP	85
5.1 Test Stand Overview.....	85
5.1.1 Working Fluid Selection.....	87
5.1.2 Component Sizing	87
5.2 Components	88
5.2.1 Electrochemical Cell.....	88
5.2.2 Storage Vessels.....	90
5.2.3 Pump.....	91
5.2.4 Metering Valve	92
5.2.5 Evaporator.....	92

5.2.6	Condenser	93
5.2.7	Vortex Tube	94
5.2.8	Power Supply.....	94
5.3	Instrumentation	95
5.3.1	Thermocouples	95
5.3.2	Pressure Transducers	95
5.3.3	Flow Meters	96
5.3.4	Current Transducer	96
5.3.5	Concentration Sensor.....	97
5.3.6	Data Acquisition	97
5.3.7	Sensor Accuracy	98
5.4	Sensor Calibration.....	98
5.4.1	Pressure Transducer Calibration.....	99
5.4.2	Thermocouple Calibration.....	99
5.4.3	Flow Meter Calibration.....	100
5.4.4	Current Transducer Calibration.....	101
5.4.5	Photometric Sensor Calibration.....	101
5.5	Flammability Concerns	102
5.6	Operating Procedures.....	103
5.7	Data Reduction.....	104
CHAPTER 6.	1 st GENERATION CELL EXPERIMENTATION	105
6.1	Initial Testing.....	105
6.2	Test Stand Modifications	107
6.3	Additional Testing	111
6.4	References.....	115
CHAPTER 7.	CUSTOM CELL FABRICATION	116
7.1	New Cell Hardware.....	116
7.2	MEA Fabrication	119
7.3	References.....	123
CHAPTER 8.	IONOMER AND MEMBRANE SELECTION	124
8.1	Ionomer Content	124

8.2	Membrane Selection	125
8.3	Composite Membranes	127
8.4	Nafion Doping	128
8.5	Alternative Membrane Materials	129
8.6	Membrane Selection	131
8.7	References.....	132
CHAPTER 9. CATALYST SELECTION		135
9.1	Catalyst Mixtures	136
9.2	Catalyst Testing	137
9.3	Catalyst Performance Prediction Methods.....	139
9.3.1	Machine Learning Approach	139
9.3.2	Density-Functional Theory Approach	142
9.4	References.....	149
CHAPTER 10. ELECTROCHEMICAL CELL MODELING		153
10.1	One-Dimensional Model	154
10.1.1	Anode Coolant Channel	155
10.1.2	Anode Flow Plate	155
10.1.3	Anode Reactant Flow Channel.....	156
10.1.4	Anode Diffusion Layer.....	158
10.1.5	Anode Catalyst Layer	159
10.1.6	Proton Conducting Membrane	161
10.1.7	Cathode Catalyst Layer	162
10.1.8	Cathode Diffusion Layer	163
10.1.9	Cathode Flow Channel	164
10.1.10	Cathode Flow Plate	164
10.1.11	Cathode Cooling Channel	165
10.1.12	Cell Overpotentials	165
10.1.13	Solution Procedure.....	166
10.2	Parameter Identification	168
10.3	Predicting Exchange Current Density	171
10.4	2D Model.....	171

10.5	Validation Studies	174
10.6	Cell Sensitivity Analysis	180
10.7	References	186
CHAPTER 11. DETAILED SYSTEM MODELING		190
11.1	Isopropanol-Acetone Mixture Modeling	190
11.2	Calculation Procedures	192
11.3	System Sensitivity Analysis	195
11.4	Cell Modifications	197
11.5	System Modifications	200
11.6	Energy Savings and System Scale	202
11.7	References	205
CHAPTER 12. CONCLUSIONS AND RECOMMENDATIONS		206
APPENDIX A. DFT CALCULATIONS		210
APPENDIX B. CELL OPTIMIZATIONS		213
VITA		216

LIST OF TABLES

Table 3.1: List of potential working fluids for CLHP.	62
Table 5.1: List of major components supplier and model numbers.....	87
Table 5.2: Sensor specifications.	98
Table 5.3: Flammability Precautions.	103
Table 6.1: Membrane electrode assemblies used for first phase of testing.	105
Table 6.2: Membrane electrode assemblies used for testing after equipment modifications.....	111
Table 9.1: Properties of catalyst powders.	136
Table 9.2: Proposed catalyst combinations to investigate for CLHP usage.	137
Table 9.3: Example physiochemical properties used in artificial neural network catalyst prediction.....	142
Table 9.4: Tailored Catalyst combinations to investigate validity of binding energy approach.....	147
Table 10.1: Constant parameters referenced from literature (Vetter et al. 2018).	168
Table 10.2: Results of parameter fitting to determine membrane and electrode properties.....	170
Table 10.3: Baseline Parameters for Sensitivity Study.....	180
Table 11.1: Properties of electrochemical cell for comprehensive model.....	195
Table A.1: DFT energies of clean surfaces	212
Table A.2: DFT energies of free gasses	212
Table A.3: DFT energies of CO adsorbed system	213
Table A.4: DFT energies of OH adsorbed system	213
Table A.5: DFT energies of O adsorbed system	214
Table B.1: Optimization of voltages for 3 segment cell	215
Table B.2: Optimization of voltages for 5 segment cell	216
Table B.3: Optimization of voltages for 8 segment cell	217

LIST OF FIGURES

Figure 1.1: Breakdown of U.S. electricity consumption and end-use in buildings.	22
Figure 1.2: Trends in global average GDP (OECD, 2014).	24
Figure 1.3: Global urbanization trends. Percent of population in each region	25
Figure 1.4: Diagram of vapor compression heat pumping cycle.	26
Figure 1.5: Schematic of chemical looping heat pump concept.	32
Figure 2.1: Results of Google Scholar and ScienceDirect searches for “chemical heat pump” publications.	40
Figure 2.2: Diagram of indirect electrochemical heat pump proposed by Gerlach (2004).	47
Figure 3.1: Electrolyte and ion transport for various fuel cell types. (a) proton exchange membrane fuel cell (b) alkaline fuel cell (c) molten carbonate fuel cell (d) solid oxide fuel cell.	56
Figure 3.2: Diagram of CLHP using PEM electrochemical cell and a single circuit.	61
Figure 3.3: Diagram of CLHP using PEM electrochemical cells and a dual circuit arrangement.	63
Figure 4.1: Inputs and outputs of CLHP thermodynamic model.	70
Figure 4.2: Cooling Coefficient of Performance for dual circuit CLHPs operating between 20 ^o C and 35 ^o C.	76
Figure 4.3: Voltage requirements of dual circuit CLHP operating between 20 ^o C and 35 ^o C.	76
Figure 4.4: Parametric analysis of heat exchanger approach temperature.	78
Figure 4.5: Parametric analysis of sink temperature variation.	78
Figure 4.6: Parametric analysis of pump efficiency.	79
Figure 4.7: Parametric analysis of electrochemical cell efficiency.	80
Figure 4.8: Performance of various electrochemical systems in response to electrochemical cell efficiency.	81
Figure 4.9: COP _C of vapor compression and CLHP systems vs source temperature for sink temperature of 35 ^o C.	83
Figure 5.1: Electrochemical cell experimental setup.	86

Figure 5.2: Instrumentation and piping diagram of electrochemical cell test stand.	86
Figure 5.3: CAD model used during construction phase of electrochemical cell test stand.....	88
Figure 5.4: FC-100 100 cm ² electrochemical cell hardware.....	89
Figure 5.5: Exploded view of electrochemical cell components.	89
Figure 5.6: Supply cylinder for isopropanol with liquid level line installed.	91
Figure 5.7: BT100-2J peristaltic pump.	92
Figure 5.8: Acetone metering valve.....	92
Figure 5.9: Lytron 4105G1SB heat exchanger with mounted UF12A12 fan.	93
Figure 5.10: Copper tubing and insulation used to facilitate condensation of leftover vapor.	93
Figure 5.11: Exair 3225 vortex tube used to drive condensation.	94
Figure 5.12: Connections and control for TDK-Lambda ZUP6-33/U power supply.	95
Figure 5.13: Calorimetric sensing of Sensirion SLI-0430 flow meters.....	96
Figure 5.14: CR Magnetics CR5210-12 Current transducer.	96
Figure 5.15: Photometric sensor used for acetone concentration detection (http://www.kemtrak.com/products_DCP007.html).	97
Figure 5.16: Agilent 34970A data acquisition system.....	98
Figure 5.17: Setra 205-2 calibration results.....	99
Figure 5.18: Omega PX176 calibration results.....	99
Figure 5.19: Thermocouple calibration results.	100
Figure 5.20: Thermocouple calibration results over selected temperature range.	100
Figure 5.21: Calibration setup for liquid flow meters.....	100
Figure 5.22: Calibration results for isopropanol flow meter.....	101
Figure 5.23: Calibration results for acetone flow meter.	101
Figure 5.24: Current transducer calibration results.....	101
Figure 5.25: Calibration results for concentration sensor at low concentration.	102
Figure 5.26: Calibration results for concentration sensor at high concentrations.....	102
Figure 6.1: Voltage current relationship from standard MEA testing.	106
Figure 6.2: Blockage of flow channels by carbon electrodes.	106
Figure 6.3: Swollen membrane after operating cell using alcohol.	107

Figure 6.4: ElectroChem Inc. flow field with 1/8" channels.	108
Figure 6.5: ElectroChem Inc. flow field with 1/32" channels.	108
Figure 6.6: CAD file of custom fuel cell flow field.	109
Figure 6.7: CNC machining of custom flow fields.	109
Figure 6.8: Custom flow field with 1/32" vertical channels.	109
Figure 6.9: Custom flow field with 1/32" serpentine channel.	109
Figure 6.10: SPEEK membrane after operation in alcohol electrochemical cell.	110
Figure 6.11: Voltage current relationship of EC-MEA-Custom-A.	112
Figure 6.12: Reaction rate vs. voltage efficiency for EC-MEA-Custom-A.	112
Figure 6.13: Voltage current relationship of EC-MEA-Custom-B.	113
Figure 6.14: Reaction rate vs. voltage efficiency for EC-MEA-Custom-B.	113
Figure 6.15: Voltage current relationship of EC-MEA-Custom-C.	114
Figure 6.16: Reaction rate vs. voltage efficiency for EC-MEA-Custom-C.	114
Figure 7.1: Flow fields with 20 cm ² active area.	117
Figure 7.2: Laser cut EPDM gasket.	117
Figure 7.3: Gasket fitted to expose 20 cm ² active area.	117
Figure 7.4: Cell leakage using 20 cm ² flow fields.	118
Figure 7.5: Schematic of 20 cm ² electrochemical cell.	118
Figure 7.6: Machined graphite flow plates.	119
Figure 7.7: Boiling membrane in 1M sulfuric acid.	120
Figure 7.8: Catalyst ink before sonication.	121
Figure 7.9: Catalyst ink after sonication.	121
Figure 7.10: Catalyst spray application on membrane in area outlined by metal stencil.	121
Figure 7.11: Laser cutting mounting pattern into membrane electrode assembly.	122
Figure 7.12: In-house manufactured membrane electrode assembly after hot-pressing.	122
Figure 8.1: Interface of catalyst layer and membrane.	124
Figure 8.2: Comparison of different ionomer contents in catalyst layer.	125
Figure 8.3: Effect of isopropanol concentration on Nafion conductivity (Affoune et al. 2005).	126

Figure 8.4: Setup for impregnating Teflon sheet with Nafion solution with gravity filling.	128
Figure 8.5: Comparison of Inorganic filling content in Nafion for composite membranes.....	130
Figure 8.6: Composite PBI membrane with catalyst layers.....	131
Figure 8.7: Results of membrane comparison testing.....	132
Figure 9.1: Reaction progress diagram with and without catalyst.....	135
Figure 9.2: Binary catalyst comparisons for cell operated at 30 °C.....	138
Figure 9.3: Binary catalyst comparisons for cell operated at 40 °C.....	138
Figure 9.4: Binary catalyst comparisons for cell operated at 50 °C.....	139
Figure 9.5: PtRu Tertiary Catalyst at 30 °C.....	140
Figure 9.6: PtSn Tertiary Catalyst at 30 °C.....	140
Figure 9.7: PtRu Tertiary Catalyst at 40 °C.....	140
Figure 9.8: PtSn Tertiary Catalyst at 40 °C.....	140
Figure 9.9: PtRu Tertiary Catalyst at 50 °C.....	140
Figure 9.10: PtSn Tertiary Catalyst at 50 °C.....	140
Figure 9.11: Artificial neural network system architecture.	141
Figure 9.12: Example simulation of molecular dissociation on a metallic surface.	143
Figure 9.13: Example of alcohol binding to 3x2x2 atom metallic slab.	144
Figure 9.14: Scatter and contour plot for the Isopropanol-Acetone cell conductivity based on DFT calculated binding energies.	146
Figure 9.15: Plot showing the binding energies of O and OH the pure metallic surfaces and combinations of these elements in varying ratios to PtRu.	147
Figure 9.16: Scatterplot of cell conductivity for different catalyst combinations.	148
Figure 9.17: Contour plot of cell conductivity for different catalyst combinations.	148
Figure 10.1: Schematic of domains for 1-D cell model.....	154
Figure 10.2: Top-view of the electrochemical cell showing flow field grooves.	157
Figure 10.3: Calculation diagram for 1D cell model solution.	167
Figure 10.4: Activity plots based on DFT calculate binding energies and catalyst area specific exchange current densities determined through parameter fitting.....	172

Figure 10.5: Flow through 2D cell model showing a discretization region.....	172
Figure 10.6: Parity plot showing the relationship between the calculated cell currents from the 2D model and the measured currents from the experimental setup.	174
Figure 10.7: Accuracy of 2D cell model in simulating PEM electrolyzer.....	175
Figure 10.8: Voltage trends between modeled CLHP cell (a) and PEM electrolyzer values (b) from Laoun et al. (2008).	176
Figure 10.9: Membrane thickness trends between modeled CLHP cell (a) and PEM electrolyzer values (b) from Laoun et al. (2008).	177
Figure 10.10: Catalyst loading influence on PEM electrolyzer (Nguyen, 2018) (a) and methanol fuel cell (Zhu et al. 2002) (b).	178
Figure 10.11: Results from CLHP model on the influence of the catalyst layer.	178
Figure 10.12: Results from CLHP model prediction of influence of carbon fraction (a) and influence of carbon fraction on methanol fuel cell (b) (Zhu et al. 2002).	179
Figure 10.13: Influence of reactant mass flow rate on voltage efficiency for CLHP cell model and isopropanol fuel cell (Qi et al. 2002).	179
Figure 10.14: Sensitivity study on cell area.	181
Figure 10.15: Sensitivity study on coolant temperature.	181
Figure 10.16: Sensitivity analysis for cathode pressure.	182
Figure 10.17: Sensitivity analysis for anode flow rate.	182
Figure 10.18: Sensitivity analysis for coolant massflow.	183
Figure 10.19: Sensitivity analysis for catalyst loading.	183
Figure 10.20: Sensitivity analysis for particle diameter.	183
Figure 10.21: Sensitivity analysis for exchange current density.	183
Figure 10.22: Sensitivity analysis for catalyst carbon fraction.	183
Figure 10.23: Sensitivity analysis for cooling channel thickness.	184
Figure 10.24: Impact of cooling channel thickness on coolant pressure drop.	184
Figure 10.25: Sensitivity analysis for flow plate thickness.	185
Figure 10.26: Sensitivity analysis for diffusion layer thickness.	185
Figure 10.27: Sensitivity analysis for anode channel.	185

Figure 10.28: Sensitivity analysis for cathode channel.	185
Figure 10.29: Pressure drops in anode and cathode channels.....	185
Figure 11.1: System schematic for CLHP cycle modeling.....	190
Figure 11.2: T-x diagram of CLHP cycle.	191
Figure 11.3: T-P-x diagram of CLHP cycle.....	191
Figure 11.4: Flow chart of calculation process for system model incorporating working fluid composition and comprehensive cell model.	194
Figure 11.5: Sensitivity analysis for system concentration changes.....	196
Figure 11.6: Sensitivity analysis for source temperature.....	197
Figure 11.7: Sensitivity analysis for sink temperature.....	197
Figure 11.8: Sensitivity analysis of anode reactant flow rate.	197
Figure 11.9: Sensitivity analysis of coolant mass flow.....	197
Figure 11.10: Cell divided into multiple voltage regions.	199
Figure 11.11: Effects of dividing the cell into multiple voltage regions.	199
Figure 11.12: Concentration impact on performance for 8-segment cell with multiple applied voltages.	200
Figure 11.13: Schematic for CLHP system incorporating a regenerator.....	201
Figure 11.14: Concentration effects on CLHP performance with segmented cell and regeneration.	201
Figure 11.15: Effect of reactant mass flow on system COP for different CLHP architectures using a 200 cm ² cell.....	202
Figure 11.16: Effect of reactant mass flow on system capacity for different CLHP architectures using a 200 cm ² cell.	202
Figure 11.17: Comparison of CLHP efficiency to IEA performance targets.	204
Figure 11.18: Variation in volumetric cooling density as a function of COP.	204

NOMENCLATURE

Symbol	Description	Units
A	Area	(m ²)
c _p	specific heat capacity	(J/mol-K)
F	Faraday's constant	(Col/mol)
g	Gibbs free energy	(J/mol)
h	enthalpy	(J/mol)
h _f ^o	enthalpy of formation	(J/mol)
I	current	(A)
i ₀	exchange current density	(A/m ²)
j	flux	(1/m ² -s)
k	thermal conductivity	(W/m ²)
k _B	Boltzman's Constant	(eV)
L	length	(m)
ṁ	mass flow rate	(kg/s)
M	molar mass	(g/mol)
n	number of moles	(-)
ṅ	molar flow rate	(mol/s)
η	efficiency	(-)
P	pressure	(Pa)
P ^o	reference pressure	(Pa)
Φ	potential	(V)
Q̇	heat flow rate	(W)
R	universal gas constant	(J/mol-K)
ρ	density	(kg/m ³)
s	entropy	(J/mol-K)
s _f ^o	entropy of formation	(J/mol-K)
σ	conductivity	(S-m)
T	temperature	(K)

T^0	reference temperature	(K)
v	specific volume	(m ³ /kg)
V	voltage	(V)
V^0	reversible voltage	(V)
w^0	molar work	(J/mol)
\dot{W}	power	(W)
y	gas mole fraction	(-)
x	liquid mole fraction	(-)

Subscripts

ACTN	acetone
Act	activation
cell	electrochemical cell
cool	cooling load
cond	condenser
diff	diffusive
e	electrons
H ₂	hydrogen
evap	evaporator
IPA	isopropanol
Liq	liquid
p	protons
Sat	saturation
vap	vaporization

ABSTRACT

Author: James, Nelson, A. PhD

Institution: Purdue University

Degree Received: May 2019

Title: Investigation of Chemical Looping for High Efficiency Heat Pumping

Committee Chair: James Braun and Eckhard Groll

The demand for heat pumping technologies is expected to see tremendous growth over the next century. Traditional vapor compression cycles are approaching practical limits of efficiency and running out of possibilities for environmentally friendly and safe refrigerants. As a result, there is an increasing interest in pursuing non-vapor compression technologies that can achieve higher efficiencies with alternative working fluids. The chemical looping heat pump (CLHP) investigated here utilizes a chemical reaction to alternate a working fluid between more and less volatiles states. This allows the main compression to take place in the liquid phase and enables the utilization of a range of different working fluids that would not be appropriate for vapor compression technology.

Thermodynamic models were developed to assess the potential performance of a chemical looping heat pump driven by electrochemical cells. A number of potential working fluids were identified and used to model the system. The thermodynamic models indicated that the chemical looping heat pump has the potential to provide 20% higher COPs than conventional vapor compression systems.

An experimental test stand was developed to investigate the efficiency with which the electrochemical reactions could be performed. The working fluids selected were isopropanol and acetone for reasons of performance and availability. The test stand was designed to measure not only the power consumed to perform the conversion reaction but also the concentration of products formed after the reaction. The experimental tests showed that it was possible to perform the reactions at the voltages required for an efficient chemical looping heat pump. However, the tests also showed that the reactions

proceed much slower than expected. To increase the rates of the reactions, an optimization effort on the membrane and catalyst selections was performed.

Traditional catalyst materials used by solid polymer electrochemical cells, like those used in the testing, perform best in hydrated environments. The fluids isopropanol and acetone tend to displace water in the membranes, reducing the system conductivity. Multiple membrane types were explored for anhydrous operation. Reinforced SPEEK membranes were found to be the most suitable choice for compatibility with the CLHP working fluids. Multiple catalyst mixtures were also tested in the experimental setup. Density functional theory was used to develop a computational framework to develop activity maps which could predict the performance of catalyst materials based on calculated parameters.

A detailed model of the CLHP electrochemical cell was developed. Built on open-source tools, the model was designed to determine the charge, mass, and heat transfers within the cell. The conversion of reactants along the channel of the cell as well as overall power consumption are predicted by the model. The model was validated against measurements and used to determine parameters for a CLHP cell that would have improved conversion performance and energy efficiency compared with the tested cell.

The cell model was integrated into an overall system model which incorporates the effect of concentration changes throughout the entire cycle. Compared to the early-stage thermodynamic modeling, consideration of incomplete reactions provided more accurate predictions of the potential performance of CLHP systems. Different cell and system architectures were investigated to boost system performance. The model predictions demonstrated that the CLHP has the potential to provide high heat pumping efficiencies, but more work is still needed to improve the energy density of the system.

CHAPTER 1. INTRODUCTION

The motivation for the present study is described below. The trends in the global demand for heating and cooling are presented along with the challenges of meeting this demand with current technologies. An overview of a variety of alternative heating and cooling technologies are described. The working principles of the chemical looping heat pump are presented along with an overview of the research objectives of this work.

1.1 Motivation

The applications of heat pumping technologies have provided a number of benefits to the modern world. From thermal regulation in buildings and data centers to the preservation of food and medical supplies, climate control technologies can be found in many places. Cooling technologies are a major end use of energy in the United States. The residential and commercial building sectors within the U.S. consume around 2.7 million GWh of electricity (EIA, 2017) with about 25% dedicated to space cooling and refrigeration (DOE, 2012).

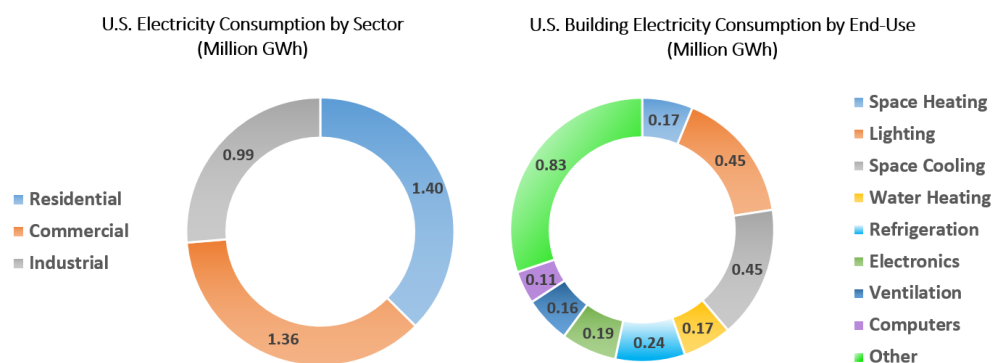


Figure 1.1: Breakdown of U.S. electricity consumption and end-use in buildings.

The global demands for heat pumping systems will see tremendous growth in the coming decades. Some estimates predict a 6-fold global increase in the energy demand for air conditioning systems by the year 2100 (IPCC, 2014). Although cooling technologies provide a plethora of benefits they also contribute to a fair amount of pollution. Most heat pumping

systems run on electricity. With most electricity being generated through the burning of fossil fuels, the increase in cooling demand will lead to the increased burning of carbon-based fuels and in turn the increased release of CO₂. As a greenhouse gas, excessive CO₂ release will promote undesirable climate change. Many conventional heat pump systems also leak refrigerants that are highly potent greenhouse gases. Air conditioning equipment accounts for about 700 million metric tons of direct and indirect CO₂ equivalent emissions globally with ~74% being attributed to electricity consumption and ~26% to refrigerant leakage (Goetzler et al. 2016). These emissions will produce many challenges if society hopes to meet an increasing cooling demand while minimizing adverse effects on the environment. A variety of factors will contribute to this increased demand. Most notably, these are population growth, standard of living improvements, and warming temperatures.

1.1.1 Growing Populations

Global population levels are expected to see continuous growth over the next century. Predictions place the totals around 8.5 billion by 2030, 9.7 billion by 2050 and 11.2 billion by 2100 (United Nations, 2015). As the number of people increases, a greater demand will be placed on the energy sector. This includes the demand for space heating and cooling technologies. In addition to the increased use of air conditioning, other factors that accompany a growing population will also increase the demand for cooling. More food will need to be produced to adequately feed a larger population. Currently up to 20% of produced food is lost due to inadequate refrigeration and estimates state that global food production will need to increase by 70% by 2050 to feed the population (Coulomb et al. 2015). This means more refrigeration will be required to stave off preventable losses and preserve future food supplies.

1.1.2 Increasing Standards of Living

An estimated 15% of the global population has access to air conditioning (Goetzler et al. 2016). The economic statuses of many nations are expected to increase in the coming decades. In 2016 the average global GDP per capita was ~\$14,971. By 2060 the average is expected to be \$42,304 (OECD, 2014). As the economic standings of developing nations increase, the ability of their populaces to gain access to the benefits of climate control will simultaneously increase. Since many regions which require significant heating are already economically developed, heating

demand is not expected to greatly increase. However, the drive for more electrification may increase the demand for heat pump based heating devices in lieu of direct fuel burning. The greatest increase in climate control technologies will be for air conditioning. In fact, global cooling demand is expected to surpass heating demand by 2060 (Birmingham Energy Institute, 2015). The improvements in the standard of living of much of the world's population will be a major driver behind rising energy demand. In addition to many people getting access to air conditioning for the first time, the per capita energy demand for air conditioning is also expected to rise due to decreasing average household size and the increasing floor area of dwellings (IPCC 2014).

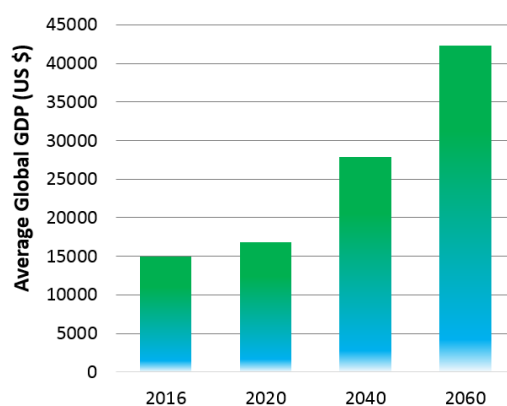


Figure 1.2: Trends in global average GDP (OECD, 2014).

1.1.3 Warming Temperatures

The warming of the planet and the demand for air conditioning are intimately connected. As temperatures rise, the demand for residential and commercial air conditioning will increase. This commercial air conditioning will increase. This will lead to more energy being expended to meet this cooling demand. As the demand for energy increases, more greenhouse gases will be released via the production of electricity by conventional means. This will amplify the increasing temperatures which in turn further increases the need for cooling.

Much of the world lives in urban environments. By 2050, 66% of the global population is expected to reside within cities (United Nations, 2014). Urban areas tend to have higher

temperatures than surrounding rural regions. This is due to surface modifications that include replacing vegetation with pavement and buildings. These man-made structures absorb more heat than vegetation and in turn warm the surrounding air. This creates what is called the heat island effect. The artificially increased temperatures in turn increase the demand for cooling technologies (Akabari et al. 2001).

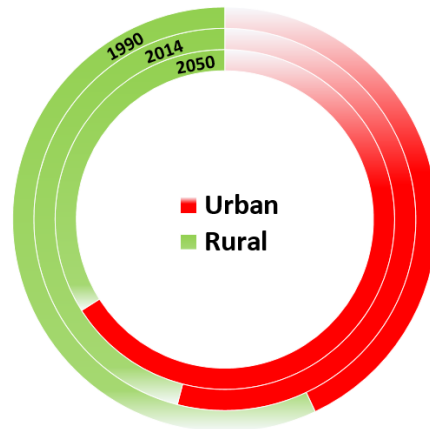


Figure 1.3: Global urbanization trends. Percent of population in each region (United Nations, 2014).

1.1.4 Paths Forward

With so many factors driving its growth, it is a near certainty that the demand for heat pumping systems will drastically increase. To slow the rate of growth in energy consumption and environmental impacts, a multitude of approaches will be needed. Modification of present behavior as well as improved processes can lead to a reduction in the rate of growth of cooling demand. Renewable energy sources can be more widely utilized to generate ‘cleaner’ electricity to power cooling systems. Additionally, the improvement of the efficiency of heat pumping equipment can serve to help reduce the energy requirements needed to provide a given amount of cooling. This work will focus on a new approach to develop high efficiency heat pumps.

1.2 Heat Pumping Cycles

Since the dawn of refrigeration, an astonishing amount of effort has been devoted to the development and improvement of heat pumping cycles. A variety of systems employing different technologies and methods have been implemented in order to produce a heat pumping effect. Some of these technologies are highlighted below.

1.2.1 Vapor Compression Cycles

The most popular and developed heat pumping technology is the vapor compression (VC) cycle. Proposed by Oliver Evans in 1805 and reduced to practice by Jacob Perkins in 1834, the basic principles of the VC system have been around for over a century (Calm 2008). As depicted in Fig 1.4, these systems function as reverse Rankine cycles. They evaporate a volatile fluid at low pressure to absorb heat. The evaporated vapor is then compressed to high pressure and condensed to release heat. The condensed liquid is throttled to low pressure and the evaporation process repeats again. A number of methods have been investigated to improve on the efficiency of simple vapor compression systems. These methods include sub-cooling cycles, expansion loss recovery devices, and multistage cycles employing vapor and liquid injection (Park et al, 2015).

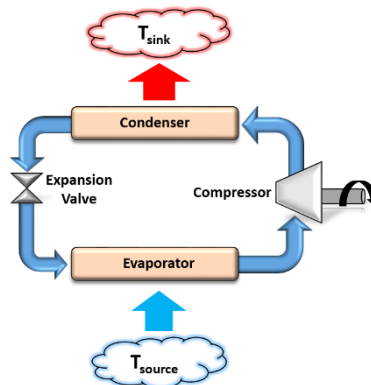


Figure 1.4: Diagram of vapor compression heat pumping cycle.

As dominant as VC cycles have become, a number of alternative systems are actively being investigated with hopes of replacing VC systems. One present drawback of VC heat pumps is their use of environmentally harmful working fluids. Over the past few decades, efforts have been made to utilize refrigerants with low ozone depletion (ODP) and global warming (GWP) potentials (Calm, 1997). The ozone layer helps shield the surface of the earth from UV radiation.

Should the efficacy of the ozone layer to block this radiation decrease, a wide variety of health concerns could arise (Gruijl et al. 2003). The discovery of the depletion of stratospheric ozone by compounds containing bromine and chlorine led to the halt of refrigerants containing these compounds. Even with the switch to low ODP refrigerants, the issue of global warming still remains. Many conventional refrigerant compounds have fairly high GWPs. This means that for every amount of the substance that is released into the atmosphere a disproportionately large global warming effect is produced in comparison to an equivalent amount of CO₂. This is being addressed by the use of natural refrigerants and the development of lower GWP refrigerants.

Systems using these alternative refrigerants are sometimes less efficient or require more charge in comparison to traditional high GWP refrigerant systems (Goetzler et al. 2014). This creates the need to look at the total environmental warming impact of a refrigerant choice. A system with a lower efficiency or requiring a larger mass charge of refrigerant may ultimately lead to increased global warming despite the fact that a lower GWP refrigerant was used (Pham et al. 2010). Much work is being done on identifying the next generation of refrigerants for use in vapor compression systems.

1.2.2 Gas Cycles

A number of heat pumping cycles have been developed which fully utilize a working fluid that remains in the gaseous phase. The most common are the reverse Brayton, Stirling, and Ericsson cycles. The reverse Brayton cycle with regeneration has 4 stages of operation: 1) isentropic compression; 2) constant pressure regeneration cooling; 3) isentropic expansion; 4) constant pressure regeneration heating. The heating and cooling of the gas during the compression and expansion stages leads to heat transfer irreversibilities that prevent the ideal reverse Brayton cycle from reaching Carnot efficiencies. The reversed Stirling cycle also operates in 4 stages: isothermal compression, constant volume regeneration cooling, isothermal expansion, and constant volume regeneration heating. In the ideal case this cycle can approach Carnot efficiencies. The reverse Ericsson cycle is similar to the Stirling cycle with the constant volume regeneration replaced with constant pressure regeneration. While devices that approach isentropic compression and expansion processes are possible, isothermal devices are more challenging to realize. A number of methods have been developed to simulate isothermal

processes including liquid-flooding (Hugenroth, 2006). Gas cycles typically cannot outperform VC systems in most air conditioning and refrigeration applications due to a requirement for very high compressor and expander efficiencies that are not practical to achieve. Gas cycles are more common for very lower temperature applications, such as for cooling of infrared sensors used in night vision systems.

1.2.3 Sorption Cycles

Absorption and adsorption cycles have also seen a fair amount of use as heat pumping systems. These are typically thermally or compressor driven systems that employ the reversible desorption and resorption of a gas from a liquid or solid substrate. There are two modes of sorption reactions, physisorption and chemisorption. In physisorption, the bonding of the gas is a result of van der waal attractions typically at gas-solid interfaces. These are usually weaker bonds that don't produce any significant change to the electronic orbital structure of the species involved. In contrast, chemisorption results in stronger bonds and usually entails the alteration of the orbital structure of the chemical species.

The classification of sorption heat pump cycles is generally determined by the phase in which the sorption reaction takes place. Cycles where sorption interactions occur between a gas and a solid are called adsorption cycles while sorption cycles where a gas interacts with a liquid are called absorption cycles. In thermally driven systems, heat is used to drive a desorption reaction at high pressure while cooling allows for resorption to take place at lower pressure. Compressor driven systems use the pressure differential generated by a compressor to drive desorption at low pressure and resorption at high pressure. A wide variety of working fluid combinations have been investigated for use with sorption heat pumps (Srihirin et al. 2001, Critoph et al. 2005). Though typically larger than vapor compression systems, their ability to operate with a variety of energy inputs including thermal energy make sorption cycles attractive for certain applications.

1.2.4 Chemical Heat Pumps

Chemical reactions have also been investigated for use in heat pumping systems. These cycles utilize reversible reactions in order to drive a heat pumping process. This process can be direct, where the absorption of heat is due to the endothermic nature of a reaction or indirect where a

secondary effect promoted by the chemical reaction absorbs heat (Gerlach, 2004). A myriad of reactive pairs have been identified for use in chemical heat pumps for a variety of operating conditions. The majority of systems explored using chemical reactions have been direct systems.

Metal hydride heat pumps are generally considered chemical or adsorption heat pumps. They employ materials that have a high affinity for hydrogen. Using the reversible chemisorption of hydrogen these systems operate in a similar fashion to sorption systems. Chemical heat pumps have a wide range of applications and are actively being pursued as environmentally friendly alternatives to vapor compression systems (Wongsuwan et al. 2001).

1.2.5 Caloric Cycles

Certain materials change temperature when exposed to external stimuli. This can be leveraged to generate a heat pumping effect. The stimulation can come from an electric field (electrocaloric), a magnetic field (magnetocaloric), induced stress (elastocaloric), or compression (barocaloric). The general principle of a caloric cycle is as follows. First, increasing stimulation is applied to a substance, during which the temperature of the substance increases. The substance is then cooled by exchanging heat with the ambient. After the substance has cooled, the stimulation is then removed. When this happens the material's temperature drops below that of the ambient. Heat exchange with the material can then be used for cooling. Afterwards, the process is repeated (Andrej et al. 2015). A challenge various caloric cycles face is material selection for stability, cost, and performance. In addition, many materials don't undergo large temperature changes when exposed to external stimuli. This means that some caloric effects will need to be cascaded in order to achieve appreciable temperature lifts (Ozbolt et al. 2014, Qian et al. 2016).

1.2.6 Thermoacoustic Cycles

Thermoacoustic devices operate on the conversion of acoustic energy into thermal energy. An acoustic wave expands and contracts a gas in a housing causing it to cool and heat respectively. An external heat transfer fluid is used to interact with the gas to achieve external heating and cooling. These devices can utilize either a standing or traveling acoustic wave and consist of an acoustic driver, resonator, and heat exchangers. Although many researchers have investigated

thermoacoustic cycles they are generally uncompetitive with vapor compression cycles (Brown et al. 2014). Some niche applications may exist for their application such as thermally driven devices in automotive systems (Zink et al. 2010).

1.2.7 Thermoelectric Devices

In 1834, Jean Peltier discovered what is known today as the Peltier effect. It is the heating or cooling of a junction of two dissimilar conductors as an electric current flows through them. Goldsmid et al. (1954) proposed the use of semiconductors as thermoelectric materials and to this day the pursuit of thermoelectric heat pumping systems receives much attention. Since electrons serve as the working fluid, thermoelectric devices are noiseless, and do not utilize environmentally harmful working fluids or materials (Riffat et al. 2003). However, thermoelectric devices typically exhibit COPs much lower than that of vapor compression systems. For this reason, they generally only find commercial uses in niche applications where compactness is required (Brown et al.2014).

Thermoelectrics have also been proposed as integrated components to create hybrids with vapor compression cycles to boost performance. Yazawa et al. (2016) and Dai et al. (2017) studied thermoelectric devices used as subcoolers for transcritical CO₂ heat pump cycles. They found that the system performance could be improved by integration of the thermoelectrics particularly at high ambient temperatures.

1.2.8 Thermionic Devices

Thermionic heat pumps are based on the principle of thermionic emission which was observed in the days of Thomas Edison. The first heat pump based on this concept was proposed by Mahan (1994). When a voltage is applied across electrodes that are separated by a distance shorter than the mean free path, high energy electrons will leave one surface while lower energy electrons will return to that surface. This leads to the cooling of the surface from which the high energy electrons emit and the heating of the surface where the high energy electrons gather. Investigations into the use of thermionic refrigeration appear to be limited to the cooling of

microelectronics and academic interest. They have little potential to displace vapor compression systems for space cooling (Fernandez et al. 2010 and Brown et al. 2014).

1.3 Chemical Looping Heat Pump

To date, most alternative heat pumping systems have not proven to be cost competitive with vapor compression systems for most applications with the current standards for energy efficiencies and environmental impacts. However, this situation could change in the future as requirements for energy performance and environmental restrictions on working fluids change. Thus, it is important to develop viable alternatives to vapor compression heat pump systems to meet future requirements.

Chemical looping is a process where a reaction is decomposed into sub-reactions using intermediates. These intermediates are then regenerated over the course of the reaction (Fan, 2010). In this manner, the reaction can be controlled in order to obtain a more desirable outcome. Chemical looping has seen uses in a number of applications. Chemical looping combustion is a process wherein the typical combustion process is split into multiple steps, typically an oxidation and reduction reaction. This can allow for the easy separation and then sequestration of CO₂ (McGlashan 2008). Air separation is another area where chemical looping has been utilized. Oxygen from air is absorbed in an oxidation reactor and that oxygen is released to a separate reduction reactor (Song et al. 2014, Moghtaderi 2010, Wang et al. 2014, and Shah et al. 2012). Chemical looping has also been applied to the processing of spent organic solvents (Chiu et al. 2014).

Borrowing from the concept of chemical looping, a heat pumping process is considered in this thesis where the working fluid is chemically transformed into an intermediate state to facilitate compression in the liquid phase. The proposed system utilizes the property changes of a fluid that occur after a chemical reaction in order to pump heat. In this way, it operates as an indirect chemical heat pump. Typical vapor compression systems make use of a compressor in order to pressurize a gaseous working fluid for condensation. The chemical looping heat pump concept seeks to replace the gas phase compression of typical vapor compression systems with liquid phase pumping. This is accomplished by leveraging the change in saturation pressure that can occur after a fluid undergoes a chemical reaction.

The operating principles of the CLHP are demonstrated in Figures 1.5. Starting at state ①, a substance in the liquid state denoted as ‘A’ is pumped to high pressure. A chemical reaction is then utilized to convert fluid ‘A’ into fluid ‘B’ at state ②. The reaction is chosen so that fluid B is a more volatile compound than fluid A. An energy input such as heat or work is required to drive the reaction. Fluid B is then throttled to low pressure, state ③, and then evaporated, state ④. The process from ② - ④ is similar to that of vapor compression cycles. A reverse reaction is then used to convert fluid B back into fluid A. Due to the selection of fluid B being more volatile than fluid A, the output of this reaction can be in the liquid state depending on the temperature and pressure of the reaction.

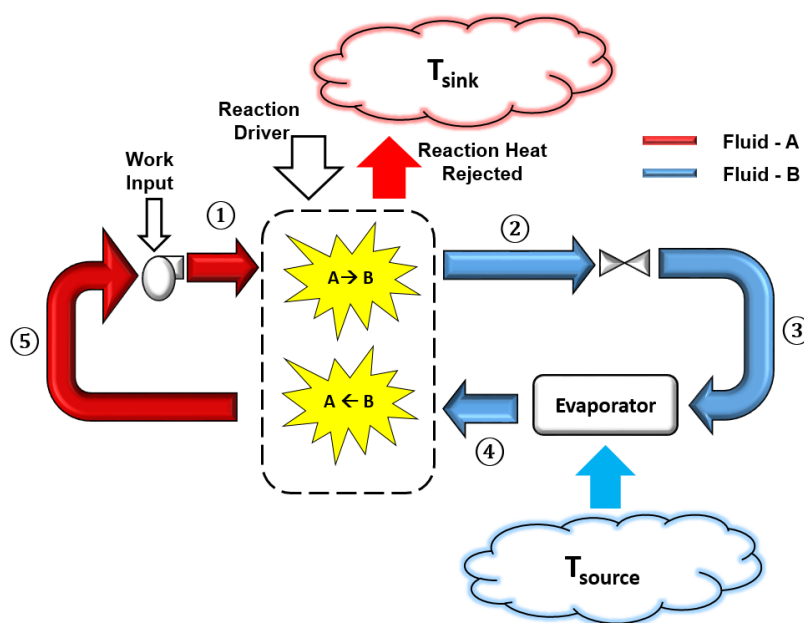


Figure 1.5: Schematic of chemical looping heat pump concept.

Significantly less work is required to pump a liquid than to compress a gas. By deviating from gas phase compression, the efficiency of the heat pump cycle is now primarily determined by the efficiency with which the chemical reaction can be performed as opposed to the efficiency of the mechanical compressor. For an appropriately selected reaction mechanism, this system could potentially outperform conventional vapor compression heat pumps.

1.4 Research Objectives and Approach

The goal of this project is the evaluation of the chemical looping heat pump concept for possible commercial applications. This will involve an evaluation of the system's thermodynamic potential, as well as technical and economic feasibility.

To this end, a review of previous chemically based heat pumping technologies is presented to assess the state of the art in the field (Chapter 2). Being a novel system, a thermodynamic model of the CLHP is created to develop some insight into the cycle's performance capabilities and operating characteristics (Chapter 4). To aid in developing the model, an extensive review of potential reactive working fluids is performed and multiple system architectures are presented (Chapter 3). Following the system modeling, the details of an experimental setup designed to evaluate the performance of an electrochemical cell are described (Chapter 5). The results of the initial experimental testing are then presented (Chapter 6). After initial testing, it became apparent that some optimization would be needed in the development of the cells. The manufacturing procedure of new cell hardware and components is described in Chapter 7. Optimization efforts for the cell membrane and catalyst layers are presented in Chapter 8 and Chapter 9, respectively. A detailed model of the electrochemical cell used in the CLHP is developed in Chapter 10. Using that model, a comprehensive assessment of the CLHP system performance is presented in (Chapter 11).

1.5 References

Akabari, H., Pomerantz, M., Taha, H., Cool Surfaces and Shade Trees to Reduce Energy use and Improve Air Quality in Urban Areas. *Solar Energy*, Vol.70 pp 2295 - 310, 2001

Andrej Kitanovski, Uroš Plaznik, Urban Tomc, Alojz Poredoš, Present and future caloric refrigeration and heat-pump technologies, *International Journal of Refrigeration*, Volume 57, September 2015, Pages 288-298, ISSN 0140-7007, <http://dx.doi.org/10.1016/j.ijrefrig.2015.06.008>.

- Birmingham Energy Institute, 2015. Doing Cold Smarter. University of Birmingham, Edgbaston, Birmingham
- Brown, J., Domanski, P., 2014. Review of Alternative Cooling Technologies. Applied Thermal Engineering, vol. 64, p.252 - 262
- Calm, J., The next generation of refrigerants - Historical review, considerations, and outlook, International Journal of Refrigeration, vol 31, p. 1123-1133, 2008
- Calm, J., Didion, D., Trade-Offs in Refrigerant Selections: Past, Present, and Future, Refrigerants for the 21st Century ASHRAE/NIST Refrigerants Conference, National Institute of Standards and Technology, 1997
- Chiu, P., Ku, Y., Wu, H., Kuo, Y., Tseng, Y., 2014. Spent Isopropanol Solution as Possible Liquid Fuel for Moving Bed Reactor in Chemical Looping Combustion. Energy & Fuels, vol.28, p.657 - 665.
- Coulomb, D., Dupont, J., Pichard, A., 2015. The Role of Refrigeration in the Global Economy, International Institute of Refrigeration, 29th Informatory Note on Refrigeration Technologies
- Critoph, R., Zhong, Y., 2005. Review of Trends in Solid Sorption Refrigeration and Heat Pumping Technologies. Proceedings of the Institution of Mechanical Engineers, Part E: Journal of Process Mechanical Engineering, vol. 219, p.285 - 300
- Dai, B., Liu, S., Zhu, K., Sun, Z., Ma, Y., 2017. Thermodynamic Performance Evaluation of Transcritical Carbon Dioxide Refrigeration Cycle Integrated with Thermoelectric Subcooler and Expander. Energy, vol.122, p.787-800.
- DOE, 2012. 2011 Buildings Energy Data Book. Buildings Technologies Program, Energy Efficiency and Renewable Energy, U.S. Department of Energy

- EIA, 2017. Monthly Energy Review: 7.6 Electricity End Use. U.S. Energy Information Administration, U.S. Department of Energy
- Fan, L., Chemical Looping Systems for Fossil Energy Conversions, American Institute of Chemical Engineers and John Wiley & Sons, Inc., 2010
- Fernandez, N., Stout, T.B., 2010. The Prospects of Alternatives to Vapor Compression Technology for Space cooling and Refrigeration Appliances. Report: Pacific Northwest National Laboratory.
- Gerlach, D., 2004. An Investigation of Electrochemical Processes for Refrigeration. Ph.D. Thesis, University of Illinois at Urbana-Champaign.
- Goetzler, W., Sutherland, T., Rassi, M., Burgos, J., 2014. Research and Development Roadmap for Next-Generation Low Global Warming Potential Refrigerants, U.S. Department of Energy, Building Technologies Office, Report
- Goetzler, W., Guernsey, M., Young, J., Fuhrman, J., Abdelaziz, O., 2016. The Future of Air Conditioning for Buildings. U.S. Department of Energy, Building Technologies Office, Report
- Goldsmid, H., Douglas, R., 1954. The use of Semiconductors in Thermoelectric Refrigeration. British Journal of Applied Physics, vol.5, p. 386 - 390
- Gruijl, F., Longstreth, J., Norval, M., Cullen, A., Slaper, H., Kripke, M., Takizawa, Y., Van der Leun, J., Health effects from stratospheric ozone depletion and interactions with climate change, Photochemical & Photobiological Sciences, vol 2, p. 16-28, 2003
- Hugenroth, J., Liquid Flooded Ericsson Cycle Cooler, Ph.D. Thesis, Purdue University, West Lafayette, IN. 2006

- IPCC, 2014: Climate Change 2014: Impacts, Adaptations, and Vulnerability. Part A: Global Sectoral Aspects. Contributions of Working Group II to the Fifth Assessment Report of the Intergovernmental Panel on Climate Change
- Mahan, G. 1994. Thermionic Refrigeration. *Journal of Applied Physics*, vol .76, p.4362 - 4366.
- McGlashan, N., 2008. Chemical-Looping Combustion - A Thermodynamic Study. *Proceedings of the Institution of Mechanical Engineers, Part C: Journal of Mechanical Engineering Science*, vol. 222, p. 1005 - 1019
- Moghtaderi, B., 2010. Application of Chemical Looping Concept for Air Separation at High Temperatures. *Energy & Fuels*, vol.24, p.190 - 198
- OECD, 2014, Long-term baseline projections, No. 95 (Edition 2014), *OECD Economic Outlook: Statistics and Projections (database)*. DOI: <http://dx.doi.org/10.1787/data-00690-en>
- M. Ožbolt, A. Kitanovski, J. Tušek, A. Poredoš, Electrocaloric refrigeration: Thermodynamics, state of the art and future perspectives, *International Journal of Refrigeration*, Volume 40, April 2014, Pages 174-188, ISSN 0140-7007, <http://dx.doi.org/10.1016/j.ijrefrig.2013.11.007>.
- Park, C., Lee, H., Hwang, Y., Radermacher, R., Recent advances in vapor compression cycle technologies, *International Journal of Refrigeration*, vol 60, p.118-134, 2015
- Pham, H., Sach, H., Next Generation Refrigerants: Standards and Climate Policy Implications of Engineering Constraints, *ACEEE Summer Study on Energy Efficiency in Buildings*, 2010

- Riffat, S., Ma, X., 2003. Thermoelectrics: A Review of Present and Potential Applications. Applied Thermal Engineering, vol.23, p -913 – 935
- Shah, K., Moghtaderi, B., Wall, T., 2012. Selection of Suitable Oxygen Carriers for Chemical Looping Air Separation: A Thermodynamic Approach Energy & Fuels, vol.26, p. 2038 - 2045
- Song, H., Shah, K., Doroodchi, E., Wall, T., Moghtaderi, B., 2014. Analysis on Chemical Reaction Kinetics of CuO/SiO₂ Oxygen Carriers for Chemical Looping Air Separation. Energy & Fuels, vol.28, p.173 - 182
- Srikhirin, P., Aphornratanta, S., Chungpaibulpatana, S., 2001. A Review of Absorption Refrigeration Technologies. Renewable and Sustainable Energy Reviews, vol.5, p.343 – 372
- Suxin Qian, Yunlong Geng, Yi Wang, Jiazhen Ling, Yunho Hwang, Reinhard Radermacher, Ichiro Takeuchi, Jun Cui, A review of elastocaloric cooling: Materials, cycles and system integrations, International Journal of Refrigeration, Volume 64, April 2016, Pages 1-19, ISSN 0140-7007, <http://dx.doi.org/10.1016/j.ijrefrig.2015.12.001>.
- United Nations, Department of Economic and Social Affairs, Population Division (2014). World Urbanization Prospects: The 2014 Revision, Highlights (ST/ESA/SER.A/352)
- United Nations, Department of Economic and Social Affairs, Population Division (2015). World Population Prospects: The 2015 Revision, Key Findings and Advance Tables. Working Paper No. ESA/P/WP.241
- Wang, K., Yu, Q., Qin, Q., Duan, W., 2014. Feasibility of a Co Oxygen Carrier for Chemical Looping Air Separation: Thermodynamics and Kinetics. Chemical Engineering & Technology, vol.37, p.1500 - 1506

Wongsuwan, W., Kumar, S., Neveu, P., Meunier, F., 2001. A Review of Chemical Heat Pump technology and applications, Applied Thermal Engineering, vol.21, p.1489- 1519

Yazawa, K., Liu, Y., Kurtulus, O., Groll, E., 2016. Cost Optimization of Thermoelectric Sub-Cooling in Air-cooled CO₂ Air Conditioners. International Refrigeration and Air Conditioning Conference, Purdue University

Zink, F., Vipperman, J., Schaefer, L., 2010. Environmental Motivation to Switch to Thermoacoustic Refrigeration. Applied Thermal Engineering, vol 30, p.119 - 126

CHAPTER 2. LITERATURE REVIEW

A review of the pertinent literature was performed not only to assess the novelty of the chemical looping heat pump concept but also to gain deeper insight into how similar chemically reactive systems operate.

2.1 Chemical Heat Pumps

A great deal of work has been done in relation to the use of chemical reactions in heat pumping systems. Broadly known as chemical heat pumps, these systems utilize a chemical reaction in some manner in order to facilitate a heat pumping effect. Chemical heat pumps have been studied for a wide range of heat pumping applications with hopes of being more environmentally friendly and achieving higher performance than traditional vapor compression systems. They can be driven by either thermal energy or work input and can be classified as direct or indirect systems (Gerlach, 2004). Direct chemical heat pumps utilize the endothermic nature of a reaction to absorb heat and the exothermic behavior of a separate reaction to reject heat. Indirect systems utilize chemical reactions to promote a secondary effect. This secondary effect is then used to drive a heat pumping cycle.

Chemical heat pumps have seen growing interest as an alternative technology for realizing more efficient heat pumping. Searches for “chemical heat pump” in Google Scholar and ScienceDirect, a subscription based database of scientific journals, show increasing publications on the topic of chemical heat pumps in relation to the start of the millennium.

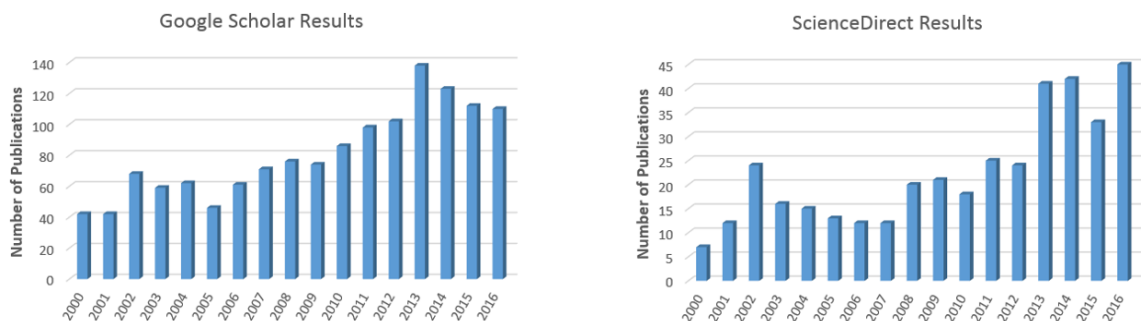


Figure 2.1: Results of Google Scholar and ScienceDirect searches for “chemical heat pump” publications.

2.1.1 Thermally Driven Chemical Heat Pumps

The majority of literature on chemical heat pumps pertains to thermally driven systems. Such systems typically find applications in waste heat recovery as well as solar thermal processes. A common characteristic among thermally driven systems is that relatively low temperature heat is used to drive a chemical reaction. Generally, this takes the form of a decomposition or desorption reaction. The products of the reaction are separated and then recombined under different conditions. This recombination generally occurs at higher temperature and is typically an adsorption or synthesis reaction (Wongsuwan et al. 2001). There are myriads of working fluids that have been proposed for use in thermally driven chemical heat pumps. Depending on the reactants used, the system can operate between solid and gaseous phases or liquid and gaseous phases. Additionally, these heat pumps can operate in batch or continuous modes.

Organic liquid-vapor chemical heat pumps have been investigated by a number of researchers. One of the most widely investigated systems uses isopropanol, acetone, and hydrogen (IAH) as working fluids. Kim et al. (1992) experimentally investigated the dehydrogenation and hydrogenation stages of an IAH chemical heat pump. They determined rate equations for the dehydrogenation and optimal molar flow ratios for the reactors. Gastauer et al. (1993) studied the dehydrogenation of isopropanol to acetone in the vapor phase. They found that nickel catalysts were highly active and selective for this application. Chung et al. (1997) studied the design of a chemical heat pump using IAH. They focused on the optimal reflux ratio and number of trays in the distillation column to maximize performance. Meng et al. (1997) also studied the IAH

chemical heat pump. They examined the nature of the catalytic dehydrogenation reaction and found that using Ru-Pt catalyst and a liquid film can greatly improve the reaction performance and in turn the system performance. KlinSoda et al. (2007) reported on the construction of a demonstration unit for an IAH chemical heat pump. They were able to achieve a temperature lift from 80 °C to 136 °C with a thermodynamic efficiency of 27%. Guo et al. (2012) studied an IAH chemical heat pump. They performed multi-parameter optimization on the system and found much room existed to improve the performance of the heat pump. Xin et al. (2013) also studied an IAH chemical heat pump for upgrading waste heat. The cycle is based on the catalytic dehydrogenation of liquid phase isopropanol to acetone and hydrogen. They found that a reactive distillation column could perform the dehydrogenation step more efficiently and with less energy input. Guo et al. (2012) applied entransy theory to the evaluation of an IAH chemical heat pump. The concept of entransy considers the heat transfer capacity of a system and the loss of such capacity during a heat transfer process. Guo et al. (2012) claimed the entransy parameter is more succinct than exergy expressions and is suitable for performance optimization calculations.

Guosheng et al. (2004) examined the dehydration of tert-butyl alcohol to isobutene and water using a reactive distillation column and cation exchange resin catalyst. They determined that a chemical heat pump could be developed for upgrading heat from temperatures below 100°C. Tanisho et al. (1985) examined the reaction between alcohols and aldehydes for a chemical heat pump. They showed that methyl alcohol and acetaldehyde could potentially be used for a heat transport and upgrading system. Cai et al. (2011) reviewed work on a number of organic chemical heat pumps including, isopropanol, tert-butanol, cyclohexane, paraldehyde, and hemiacetal systems. They identified catalyst selection, heat transfer optimization, system control, and the study of multiphase reaction mechanisms as pivotal areas of research for future organic chemical heat pumps.

The techno-economic feasibility of high temperature lift chemical heat pumps was examined by Spoelstra et al. (2002). They assessed isopropanol and salt/ammonia heat pumps for industrial waste heat recovery. Their economic analysis concluded that the ammonia salt heat pump would provide a greater rate of return than the isopropanol system. Karaca et al. (2002) performed an economic analysis of four thermally driven organic chemical heat pumps. Systems using

methanol – formaldehyde – hydrogen, ethanol – acetaldehyde – hydrogen, i-propanol – acetone – hydrogen, and n-butanol – butyraldehyde – hydrogen were compared for the recovery of industrial waste heat. Thermodynamic models were developed to evaluate the performance of each system. The cost of each system was compared to that of operating a steam boiler. It was found that the chemical heat pumps had similar levelized total annual cost. However methanol – formaldehyde – hydrogen, ethanol – acetaldehyde – hydrogen systems were considered more suitable for low heat duty applications while i-propanol – acetone – hydrogen and n-butanol – butyraldehyde – hydrogen systems are better for higher heat duties.

Inorganic working fluids have also received attention for thermally driven chemical heat pumps. Wentworth et al. (1980) proposed an absorption system using calcium chloride and ammonia as the working pair. The calcium chloride is suspended in an inert solvent and allowed to react with ammonia. By suspending the calcium chloride in a solvent, many heat and mass transfer problems associated with typical gas-solid reactions are avoided. Wentworth et al. concluded that using calcium chloride suspended in n-heptanol would be suitable for solar thermally driven heating cooling and thermal storage. Fadhel et al. (2009) theoretically and experimentally investigated the use of a calcium chloride-ammonia heat pump for use as a solar assisted dryer. Lee et al. (2005), experimentally investigated the use of non-uniform reaction blocks to improve the performance of chemical heat pumps using metal chlorides and ammonia as working fluids.

Another chemical heat pumping concept using ammoniated salts was investigated by Mbaye et al. (1998). This system uses MnCl and ammonia as working fluids. A numerical model of the system was developed. The model assumed heat transfer to be the rate determining step during ammoniated salt decomposition and showed good agreement with experimental results. Aidoun et al. (2004) looked at the development of transient heat transfer coefficients for a CoCl-NH_3 based chemical heat pump. They found that the transient coefficients were more representative of the cyclical heat pumping process. Goetz et al. (1993) analyzed the performance of Ca, Mn, Mg, Fe, and Ni chloride chemical heat pumps and proposed various methods to improve performance, including internal heat recovery and reactive gas circulating pumps.

Ogura et al. (2001) and Fujimoto et al. (2002) compared the performance of a $\text{CaO}/\text{H}_2\text{O}/\text{Ca}(\text{OH})_2$ chemical heat pump to other heat pumps. The system operates on the endothermic dissociation of $\text{Ca}(\text{OH})_2$ and the exothermic recombination of CaO and H_2O . Evaporation and condensation of the released water could be used for further heating and cooling. Ogura et al. (2001) generated thermodynamic models of the system and experimentally investigated the reactions. They concluded that the $\text{CaO}/\text{H}_2\text{O}/\text{Ca}(\text{OH})_2$ chemical heat pump could be more efficient than absorption and adsorption systems by simultaneously using wider operating temperatures. Fujimoto et al. (2002) developed dynamic models to aid in the control of $\text{CaO}/\text{H}_2\text{O}/\text{Ca}(\text{OH})_2$ chemical heat pumps. Ogura, et al. (2007) experimentally investigated the characteristic of heat storage and release under repetitive operation for the $\text{CaO}/\text{H}_2\text{O}/\text{Ca}(\text{OH})_2$ chemical heat pump.

A chemical heat pump using magnesium oxide/water as a working pair was investigated by Kato et al. (2005) for applications in enhancing cogeneration from engines and fuel cells. The system operates using the endothermic dehydration and the exothermic hydration of the magnesium oxide. Kato et al. (2005) experimentally studied the forward and reverse reactions of the hydration and dehydration. Through thermal storage for load leveling and enhancing useful heat recovery, the magnesium oxide chemical heat pump was shown to have great potential benefits for cogeneration systems. Kato et al. (1999) looked at the use of $\text{CaO}/\text{PbO}/\text{CO}_2$ chemical heat pumps for high temperature heat recovery. They studied the kinetics of the CaO/CO_2 and Pb/CO_2 reactions and determined that the system would have practical value if operated in a plant at scale.

Chemical reactions can be used to store heat over long periods of time and distances. Many systems have been proposed using chemical heat pumps as novel thermal storage and transit methods. Ogura (2012) proposed a method of using a $\text{CaSO}_4\text{-H}_2\text{O}$ chemical heat pump integrated into a shipping container to capture and transport waste heat from an industrial site as well as provide cooling at the endpoint. This was found to be more effective than using latent heat transport methods. Sakamoto et al. (2014) studied the reaction between CaCl_2 and NH_3 for thermal energy storage. A review of a variety of thermochemical storage methods, including chemical heat pumps was presented by Ding et al. (2012) and Yan et al. (2015). Thermochemical

storage methods have a number of advantages over sensible storage methods including, higher energy density and longer-term storage.

2.1.2 Mechanically Driven Chemical Heat Pumps

Relatively little literature has been published on chemical heat pumps driven by a mechanical input, such as a compressor. A system utilizing the reversible polymerization/de-polymerization of acetaldehyde and paraldehyde was proposed by Kawasaki et al. (1999). The system closely resembles a traditional vapor compression cycle with the evaporator and condenser being replaced with an endothermic and exothermic reactor. In the proposal, the reactors would be filled with an acid catalyst. Low pressure acetaldehyde would be compressed by a compressor. The high pressure gas would then enter the exothermic reactor where a polymerization of the acetaldehyde to paraldehyde would take place while rejecting heat. The output of this reactor would be liquid paraldehyde. The liquid would then be throttled to low pressure and enter the endothermic reactor. Here the paraldehyde would undergo a polymerization reaction to become acetaldehyde while absorbing heat. The gaseous output of this reaction is then returned to the compressor. The thermodynamic analysis performed on this compressor driven chemical heat pump showed similar performance to vapor compression systems.

Flueckiger et al. (2012) further studied the acetaldehyde - paraldehyde chemical heat pump for applications to compact thermal management systems. In this study, a pervaporation membrane was included in the cycle to separate the reaction products from the reactants. Thermodynamically this provides more favorable reaction constants and allows the reactions to go further to completion. They modeled the system and determined that a reactor volume of 93 cm³ would be sufficient to pump 5W of heat for compact thermal management.

Cacciola et al. (1987) proposed a compressor driven high temperature chemical heat pump for the industrial sector. The system utilizes a high temperature exothermic reactor and a comparatively low temperature endothermic reactor. A compressor is used to bring the gas to high pressure and an expander is used to recover energy as the pressure was reduced. They presented a modeling framework to evaluate compressor driven chemical heat pump systems and evaluated the performance of a cyclohexane/benzene cycle. Their results showed poor system

performance but they believed there was room for improvements with appropriate optimizations. Aristov et al. (1993) and Cacciola et al. (1993) investigated alternative configurations of the high temperature cyclohexane-benzene chemical heat pump. They found that the use of hydrogen permeable membranes could lead to system performance improvements.

2.1.3 Electrochemically Driven Chemical Heat Pumps

Another way of promoting a chemical reaction is through the application of an electrical current. Termed electrochemistry, these processes typically entail the use of electrodes separated by an ion conducting electrolyte. Oxidation and reduction reactions take place separately at each electrode. Ions travel through the electrolyte and electrons travel through an external circuit bridging the electrodes. Different methods of integrating electrochemical cells into heat pumping cycles have been investigated.

Many electrochemical heat pumps are direct type chemical heat pumps. Kreysa et al. (1990) proposed a concept and developed a theoretical framework to analyze a heat pump based on the heat of reaction of reversible electrochemical reactions. One reaction takes place at low temperature absorbing heat while the reverse reaction takes place at an elevated temperature to release heat. A number of candidate reactions were proposed for the system based on fast electrochemical reactions. Dittmar et al. (1995) studied similar electrochemical heat pumps for high temperature waste heat reclamation. They experimentally investigated NiCd, $\text{AgNO}_3/\text{Fe}(\text{NO}_3)_2$, $\text{CuSO}_4/\text{Fe}(\text{SO}_4)_3$, and $\text{CuSO}_4/\text{Na}_4\text{Fe}(\text{CN})_6$ systems. Ishihara et al. (1999) proposed a high temperature heat pump using an electrolytic reaction at low temperature to absorb heat. The products of the reaction are then thermochemically recombined at higher temperatures to release heat. Newell (2000) presented a concept for an electrochemical heat pump based on water electrolysis and a hydrogen oxygen fuel cell. Under ideal operation, an electrolyzer will absorb heat when splitting water and a fuel cell will release heat when recombining hydrogen and oxygen into water. Coupling an electrolyzer at low temperature and a fuel cell at high temperature can produce a heat pumping effect. Gerlach (2004) experimentally investigated the cooling associated with batch charging and discharging of a NiCd battery as well as the cooling phenomenon that occurs during the electrolysis of chloride solutions. Gerlach et al. (2007) modeled the performance of direct electrochemical heat pumps taking into account

various properties and losses such as flow channel size and pumping and electrical resistances. They determined that because the electrical energy cycled through the system is larger than the heat absorbed by the system that direct electrochemical heat pumps are highly sensitive to small inefficiencies in the cell performance.

Indirect chemical heat pumps using electrochemical cells have also been investigated. For some systems, the electrochemical device serves the function of a compressor. In this manner, the gaseous working fluid dissociates into ions and electrons at one electrode. The ions travel through the electrolyte to recombine with the electrons at the other electrode. If the pressures between the electrodes are different, then part of the electrical work is used to overcome the pressure differential. Jalan et al. (1987) analyzed a bromine based electrochemical heat pump. The system mirrors that of a vapor compression heat pump except an electrochemical device using a bromine ion conducting anion membrane is used to compress the bromine from low to high pressure. A high temperature electrochemically driven heat pump was proposed by Jeter (1987). The system is also analogous to a vapor compression cycle and utilizes sodium as the working fluid. Sufficiently high temperature heat input is used to evaporate liquid sodium which is then electrochemically compressed using a beta-alumina solid electrolyte. Tao et al. (2016) proposed an ammonia based heat pump using an electrochemical cell. The cell uses the electro-osmotic drag generated by hydrogen transport to pull ammonia refrigerant from a region of low pressure to one of high pressure for subsequent condensation and evaporation.

Tao et al. (2015) investigated the use of an electrochemical hydrogen compressor in conjunction with metal hydride beds to generate a batch mode heat pumping cycle. James et al. (2016) also investigated the use of an electrochemical hydrogen compressor though paired with a slurry containing metal hydride materials for continuous instead of batch mode operation.

Lawless (1997) investigated the use of ceramic oxygen ion conducting electrolyte electrochemical cells for oxygen compression for Joule-Thompson Cryocoolers. Muller et al. (2009) looked at the use of proton conducting electrochemical compressors for pulse tube refrigeration cryocoolers. Through modeling, they determined that the system should operate at lower frequencies than traditional pulse tube cryocoolers.

Various patents have been filed on the use of electrochemical compressors in heat pumping systems. Tsenter (2000) proposed the use of an electrochemical hydrogen compressor to compress a secondary liquid. Rather than using metal hydrides to generate a cooling effect, the hydrogen pressurizes a diaphragm to compress a conventional refrigerant. Bloomfield (1985) proposed an electrochemical compressor based on electro-osmotic drag. A co-fluid is circulated with an electroactive fluid such as hydrogen. As the hydrogen travels through the cell, it will drag species of the co-fluid along. This leads to the pressurization of both fluids. Bahar (2010) proposed an enclosed system where the pressurization of hydrogen could potentially be used to pressurize other working fluids through mixing. The use of electrochemical hydrogen compression in Joule-Thompson refrigeration cycles has also been patented (Gross 1987, Trusch 1991).

An indirect electrochemical heat pump was proposed by Gerlach (2004). This system utilizes the evolution of a high pressure condensable gas to generate a heat pumping effect. A hydrochloric acid solution is pumped to high pressure and then an electrolyzer is used to generate gaseous chlorine and hydrogen. The chlorine is condensed, throttled, then evaporated while the hydrogen is throttled or expanded to produce work and more cooling. Afterwards, the low pressure gases are combined in a galvanic cell to reconstitute HCl and reabsorbed into the hydrochloric acid solution. A schematic of the cycle is shown in Figure 2.2.

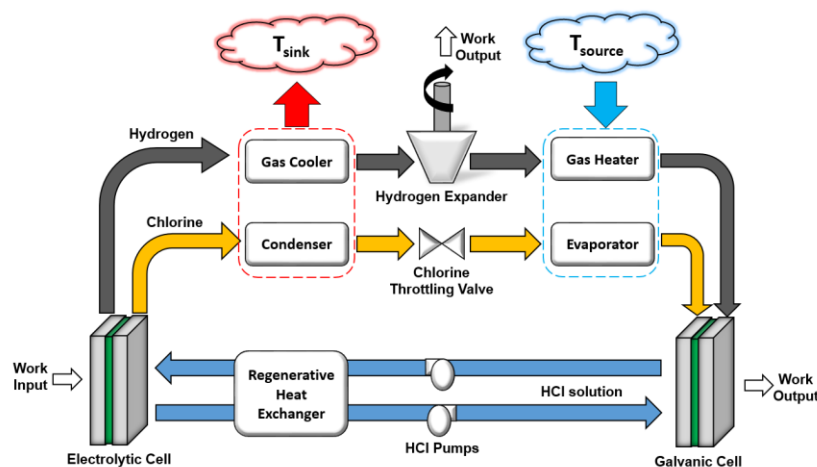


Figure 2.2: Diagram of indirect electrochemical heat pump proposed by Gerlach (2004).

2.2 Contributions

The review of the literature shows that little work has been done in regard to heat pumping systems utilizing a chemical reaction with the goal of allowing for compression to take place in the liquid phase. With the exception of a hydrochloric acid system proposed by Gerlach (2004), this concept has not been explored. This project seeks to deepen the understanding of such systems through the following:

- development of thermodynamic models to evaluate the performance of the chemical looping heat pump;
- identification and comparison of working fluids for use in the system;
- experimental evaluation of fundamental concepts;
- leveraging of experimental results to optimize reactor systems used in CLHP concept;
- development of detailed system and component models to refine design of the heat pump concept and to understand the system size requirements.

2.3 References

- Aidoun, Z., Ternan, M, 2004. The unsteady state overall heat transfer coefficient in a chemical heat pump reactor: the $\text{NH}_3\text{-CoCl}_2$ system. *Chemical Engineering Science*, vol.59, p.4023 - 4031.
- Aristov, I., Parmon, V., Cacciola, G. 1993. High-Temperature Chemical Heat Pump Based on Reversible Catalytic Reactions of Cyclohexane Dehydrogenation/ Benzene Hydrogenation: Comparison of Potentialities of Different Flow Diagrams. *International Journal of Energy Research*, vol. 17, p.293 - 303.
- Bahar, B., 2010. Self-Contained Electrochemical Heat Transfer System. U.S. Patent # US8627671
- Bloomfield, D., 1985. Electrochemically Driven Heat Pump. U.S. Patent# US4593534

- Cacciola, G., Anikeev, V., Recupero, V., Kirillov, V., Parmon, V., 1987. Chemical Heat Pump Using Heat of Reversible Catalytic Reactions. *International Journal of Energy Research*, vol. 11, p.519-529.
- Cacciola, G., Aristov, Yu. I., Restuccia, G. and Parmon, V. N. 1993. Influence of hydrogen-permeable membranes upon the efficiency of the high-temperature chemical heat pumps based on cyclohexane dehydrogenation-benzene hydrogenation reactions. *International Journal of Hydrogen Energy*, vol. 18, p.673 - 690.
- Cai, J., Li, X., Tao, Y., Huai, X., Guo, Z., 2011. Advances in Organic Liquid-Gas Chemical Heat Pumps. *Chemical Engineering and Technology*, vol.34, p.1603 - 1613
- Chung, Y., Kim, B., Yeo, Y., Song, H., 1997. Optimal Design of a Chemical Heat Pump using the 2-Propanol/Acetone/Hydrogen System. *Energy*, vol.22, p.525 - 536
- Ding, Y., Riffat, S., 2012. Thermochemical Energy Storage Technologies for Building Applications: A State-of-the-Art Review. *International Journal of Low-Carbon Technologies*, vol.8, p.106-116.
- Dittmar, L., Jüttner, K., Kreysa, G. 1995. A New Concept of an Electrochemical Heat Pump System: Theoretical Consideration and Experimental Results. *Electrochemical Engineering and Energy: Proceedings of the Third European Symposium on Electrical Engineering*
- Fadhel, M.I., Sopian, K., Duad, W.R.W., 2010. Performance analysis of Solar-Assisted Chemical Heat Pump Dryer. *Solar Energy*, vol. 84, p.1920-1928.
- Flueckiger, S., Volle, F., Garimella, S., Mongia, R., 2012. Thermodynamic and Kinetic Investigation of a Chemical Reaction-Based Miniature Heat Pump. *Energy Conversion and Management*. Vol.64, p.222-231.

- Fujimoto, S., Bilgen, E., Ogura, H., 2002. CaO/Ca(OH)₂ Chemical Heat Pump System., Energy Conversion and Management, Vol. 43, p.947-960.
- Gastauer, P., Prevost, M., 1993. Dehydrogenation of Isopropanol at Low Temperatures in the Vapor Phase as a Reaction for a Chemical Heat Pump. Journal of Chemical Engineering of Japan, vol.26, p. 580 - 583
- Gerlach, D., 2004. An Investigation of Electrochemical Processes for Refrigeration. Ph.D. Thesis, University of Illinois at Urbana-Champaign.
- Gerlach, D., Newell, T., 2007. Basic Modelling of Direct Electrochemical Cooling. International Journal of Energy Research, vol.31, p.439 - 454
- Goetz, V., Elie, F., Spinner, B., 1993. The Structure and Performance of Single Effect Solid-Gas Chemical Heat Pumps. Heat Recovery Systems & CHP, vol.13, p.79-96
- Guo, J., Huai, X., 2012. The Application of Entransy Theory in Optimization Design of Isopropanol-Acetone-Hydrogen Chemical Heat Pump. Energy, vol.43, p.355 - 360
- Guo, J., Huai, X., Li, X., Xu, M., 2012. Performance Analysis of Isopropanol-Acetone Hydrogen Chemical Heat Pump. Applied Energy, vol.93, p.261 - 267.
- Gross, S., 1986. Closed Cryogenic Cooling System Without Moving Parts. U.S. Patent Number: US4671080
- Guosheng, Z., Bolun, Y., 2004. Dehydration of Tert-Butyl Alcohol in Reactive Distillation Adapted to Chemical Heat Pump. Journal of Chemical Industry and Engineering (China). vol.3

- Ishihara, A., Motohira, N., Ota, K., Kamiya, N., 1999. High Temperature Electrochemical Heat Pump using Water Gas Shift Reaction. Part I: Theoretical Considerations. *Journal of Applied Electrochemistry*, vol.29, p.1079 - 1084
- Jalan, V., Poirier, J., Lilly, R., 1987. Electrochemically Driven Heat Pump. Report: National Science Foundation, NSF Grant ISI-8660631, Washington D.C.
- James, N., Braun, J., Groll, E., Horton, W., 2016. Compressor Driven Metal Hydride Heat Pumps using an Adsorptive Slurry and Isothermal Compression. *Science and Technology for the Built Environment*, vol.22, p.565 - 575.
- Jeter, S., A concept for an innovative high-temperature heat pump, *Energy*, 1987, v.12, issue 2, p.163-170
- Karaca, F., Kincay, O., Bolat, E., 2002. Economic Analysis and Comparison of Chemical Heat Pump Systems. *Applied Thermal Engineering*, vol.22, p.1789 - 1799
- Kato, Y., Harada, N., Yoshizawa, Y., 1999. Kinetic Feasibility of a Chemical Heat Pump for Heat Utilization of High-Temperature Processes. *Applied Thermal Engineering*, vol.19, p.239 - 254
- Kato, Y., Sasaki, Y., Yoshizawa, Y., 2005. Magnesium Oxide/Water Chemical Heat Pump to Enhance Energy Utilization of a Cogeneration System. *Energy*, vol. 30, p.2144-2155.
- Kawasaki, H., Watanabe, T., Kanzawa, A. (1999). Proposal of a chemical heat pump with paraldehyde depolymerization for cooling. *Applied Thermal Engineering*, 19, 133 - 143
- Kim, T., Yeo, Y., Song, H., 1992. Chemical Heat Pump Based on Dehydrogenation and Hydrogenation of i-Propanol and Acetone. *International Journal of Energy Research*, vol.16, p.897 - 916

- KlinSoda, I., Piumsomboon, P., 2007. Isopropanol-Acetone-Hydrogen Chemical Heat Pump: A Demonstration Unit. *Energy Conversion and Management*, vol.48, p.1200 - 1207
- Kreysa, G., Darbyshire, G., 1990. Theoretical Consideration of Electrochemical Heat Pump Systems. *Electrochimica Acta*, vol.35, p.1283 - 1289
- Lawless, W., 1997. Solid State Oxygen Compressors for Joule-Thompson Cryocoolers. NASA Technical Report AD-A323328 DSWA-TR-96-45
- Lee, C., Park, S., Choi, S., Kim, Y., Kim, S., 2005. Characteristics of Non-Uniform Reaction Blocks for Chemical Heat Pump. *Chemical Engineering Science*, vol.60, p.1401 - 1409
- Mbaye, M., Aidoun, Z., Valkov, V., Legault, A., 1998. Analysis of Chemical Heat Pumps(CHPS): Basic Concepts and Numerical Model Description. *Applied Thermal Engineering*, vol.18, p. 131-146.
- Meng, N., Shinoda, S., Saito, Y., 1997. Improvements on Thermal Efficiency of Chemical Heat Pump Involving the Reaction Couple of 2-Propanol Dehydrogenation and Acetone Hydrogenation. *International Journal of Hydrogen Energy*, vol.22, p.361 - 367
- Muller, J., Johnson, L., Kirkconnell, C., Hon, R., 2009. Proton Conductive Membrane Compressor-Driven Pulse Tube Cryocooler. *International Cryocooler Conference*, Boulder, Co.
- Newell, T., 2000. Thermodynamic Analysis of an Electrochemical Refrigeration Cycle. *International Journal of Energy Research*, vol.24, p.443 - 453
- Ogura, H., Yamaoto, T., Kage, H., 2003. Efficiencies of CaO/H₂O/Ca(OH)₂ Chemical Heat Pump for Heat Storing and Heating/Cooling. *Energy*, vol. 28, p.1479-1493.

- Ogura, H., Yasuda, S., Otsubo, Y., Mujumdar, A., 2007. Continuous Operation of a Chemical Heat Pump. *Asia Pacific Journal of Chemical Engineering.*, vol.2, p.118-123
- Ogura, H., 2012. Energy Recycling System Using Chemical Heat Pump Container. *Energy Procedia*, vol. 14, p.2048-2053
- Sakamoto, Y. and Yamamoto, H., 2014. Performance of Thermal Energy Storage Unit Using Solid Ammoniated Salt (CaCl₂-NH₃ System). *Natural Resources*, vol.5, p.337-342
- Spoelstra, S., Haije, W., Dijkstra, J., 2002. Techno-Economic Feasibility of High Temperature High-Lift Chemical Heat Pumps for Upgrading Industrial Waste Heat. *Applied Thermal Engineering*, vol.22, p.1619 - 1630
- Tao, Y., Lee, H., Hwang, Y., Radermacher, R., Wang, C., 2015. Electrochemical Compressor Driven Metal Hydride Heat Pump. *International Journal of Refrigeration*, vol.60, p.278 – 288
- Tao, Y., Hwang, Y., Radermacher, R., Wang, C., 2016. Performance Investigation on Electrochemical Compressor with Ammonia. 23rd International Compressor Engineering Conference, Purdue University, West Lafayette, IN.
- Tanisho, S., Fahim, M., Wakao, N., 1985. Heat Transport Cycle with Methyl Alcohol Acetaldehyde Chemical Reaction. *Energy Research*, vol.9, p.449 - 453
- Trusch, R., 1991. Joule-Thomson Refrigeration Cycle Employing a Reversible Electrochemical Compressor. U.S. Patent #: US5024060
- Tsenter, B., 2000. Electrochemical Heat Pump System., U.S. Patent# US6553771

- Wongsuwan, W., Kumar, S., Neveu, P., Meunier, F. A Review of Chemical Heat Pump technology and applications. Applied Thermal Engineering, 2001
- Wentworth, W.E., Johnston, D.W., Raldow, W.M., (1980). Chemical Heat Pumps Using a Dispersion of a Metal Salt Ammoniate in an Inert Solvent. Solar Energy, vol.26, p.141-146
- Xin, F., Xu, M., Huai, X., Li, X., 2013. Study on Isopropanol-Acetone-Hydrogen Chemical Heat Pump: Liquid Phase Dehydrogenation of Isopropanol Using Reactive Distillation Column. Applied Thermal Engineering, vol.58, p.369 - 373
- Yan, T., Wang, R., Li, T., Wang, L., Fred, I., 2015. A Review of Promising Candidate Reactions for Chemical Heat Storage. Renewable and Sustainable Energy Reviews, vol.43, p.13 - 31

CHAPTER 3. WORKING FLUID SELECTIONS

To gain an understanding of the performance of the CLHP and the effect of working fluid, a thermodynamic model of the processes and system were developed. The first step in generating a model for the CLHP was to determine what kind of working fluids and reactor could be used in the cycle. Chemical reactions can take place between a near inexhaustible combination of reactants and in a wide variety of reactor systems. Two criteria were used in narrowing the search for potential solutions. First, to utilize evaporation and condensation in the cycle it is desirable that the working fluid operate in the two-phase region at typical conditions of interest to air conditioning and refrigeration. To further reduce the possible candidate fluids, a focus was given to electrically driven reaction methods. This was done so that the resulting system could serve as a drop in replacement for current electrically driven vapor compression system applications. Being that few references could be found for mechanically driven chemically reactive systems, the focus was further narrowed to electrochemical methods.

Through searching the literature, a number of electrochemical systems were identified that could potentially be used for the CLHP. These systems utilize electrochemical cells similar to those used in the fuel cell industry and potentially condensable electro-active organic working fluids. Electrochemical cells work through interactions between an anode, cathode, and electrolyte. At the anode, a chemical undergoes oxidation generating electrons. The electrons are transferred through an external circuit while ions generated either at the anode or cathode travel through the electrolyte. At the cathode, the electrons combine with ions and other potential species in a reduction reaction.

Fuel cells are common electrochemical devices. There are a variety of electrolytes that are used in fuel cell systems. Examples of various fuel cell types are shown in Figure 3.1. Proton exchange membrane (PEM) cells use a solid membrane to conduct protons between the anode and cathode. Alkaline fuel cells transmit negatively charged hydroxide ions to move charge. They can utilize solid or liquid phase electrolytes. Many alkaline electrolyte solutions are susceptible to poisoning and deactivation from atmospheric CO₂. Molten carbonate fuel cells have electrolytes that conduct carbonate ions and solid oxide fuel cells can transmit oxygen ions

between the electrodes. Applications combining such cells and potentially condensable organic fluids include electro-organic synthesis, liquid fuel cells, and thermally regenerative fuel cells.

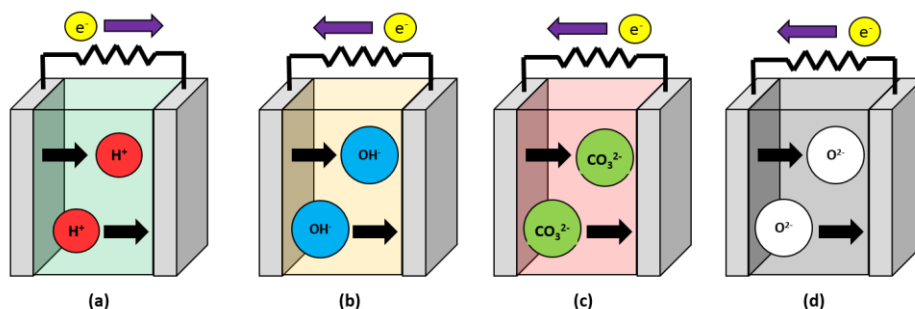


Figure 3.1: Electrolyte and ion transport for various fuel cell types. (a) proton exchange membrane fuel cell (b) alkaline fuel cell (c) molten carbonate fuel cell (d) solid oxide fuel cell.

3.1 Liquid Fuel Cells

Fuel cells are reactive engines that have received a great deal of attention for their ability to perform high efficiency conversions of fuel into electricity. Rather than combusting a fuel and using that heat to drive a heat engine, fuel cells electrochemically combine a fuel and an oxidizer and directly induce the flow of electrons. One of the most popular fuels for use with fuel cells is hydrogen. Hydrogen is an attractive fuel because after reaction with oxygen, the only product is environmentally benign water. Scenarios have been proposed where hydrogen serves as a ubiquitous energy carrier being shipped from a production site to end-use consumption (Barreto et al. 2003). One of the challenges of using hydrogen is that it has fairly low energy density. At atmospheric conditions hydrogen is a gas. To boost the energy density of hydrogen for storage and transport purposes, many different hydrogen carriers have been investigated including liquified hydrogen, physisorbed/chemisorbed hydrogen, and liquid organic hydrides (Carrier 2011). Such fluids may be of interest for use in the CLHP.

Liquid organic hydrogen carriers (LOHCs) are organic compounds that contain hydrogen molecules that can be released under appropriate conditions. Various studies have been done on LOHCs that release hydrogen once heated (He et al. 2015, Teichmann et al. 2011 and 2012). Other LOHCs have been studied that can be directly consumed in electrochemical cells. Araujo et al. (2012) theoretically looked at over 28 LOHCs that could work as fuels in PEM fuel cells.

They assessed the open circuit potential and energy density of carbocyclic and heterocyclic saturated hydrocarbons and found a number of promising candidates. Kariya et al. (2006) experimentally investigated cyclohexane, methylcyclohexane, cyclohexene, 2-propanol, and cyclohexanol applied to a PEM fuel cell. Soloveichik (2014) reviewed 18 different LOHCs for use in liquid fuel cells. The review concluded that research efforts for liquid fuel cells need to be focused on inexpensive electrocatalyst and membrane development. Nagao et al. (2015) investigated the use of quinones as LOHCs for fuel cells with promising results. Taneda et al. (2006a) and (2006b) looked at using acetaldehyde and ethanol as a fuel for PEM fuel cells.

Demirci (2007) reviewed 14 potential LOHCs for fuel cells, comparing the thermodynamic-energetic properties and the toxicological-ecological hazards of the various chemicals. It was concluded that borohydride, ethanol, and 2-propanol would be the most ideal candidates due to adequate performance of their systems and minor toxicity of their by-products. Demirci (2009) expanded this study and looked at the impacts of candidate LOHCs for fuel cells through the lens of green chemistry. A green fluid would be one that simultaneously achieves various environmental, health, safety, and economic targets. While no fluid was found to be intrinsically “green”, if adequate safety measures and technologies are utilized then many fluids may be considered relatively green.

Alcohols have been of great interest as fuels for liquid fuel cells. Arun Kumar et al. (2008) studied ethanol, 1-propanol, 2-propanol, butanol, and methanol for low power applications. They determined that 2-propanol was best suited for low current density applications while methanol was superior for high current density uses. Cao et al. (2003) and Qi et al. (2002) investigated PEM fuel cells using aqueous 2-propanol as a fuel. Qi et al. (2003) experimentally investigated a PEM fuel cell using neat isopropanol as a fuel. A sulfonated polyetheretherketone membrane (sPEEK) was used as the proton conductor. Relatively high performance was obtained when compared to other liquid feed fuel cells. Kobayashi et al. (2003) looked at the use of base metals as anode catalysts for alcohol fuel cells. They tested Pt, Ni, Cu, Co, and Mn metal with 2-propanol and methanol. Ni proved to show moderate performance in comparison to Pt for 2-propanol cells while Pt was vastly superior for methanol cells. An et al. (2010) and Santasalo-Aarino et al. (2010) investigated alcohol fuel cells utilizing alkaline electrolytes. An et al. (2010)

studied ethylene glycol cells while Santasalo-Aarino et al. (2010) looked at methanol, ethanol, and isopropanol.

3.2 Organic Thermally Regenerative Fuel Cells

Thermally regenerative fuel cells are devices that utilize dissociation and synthesis reactions to generate electrical power from a heat source. Typically, high temperature heat is absorbed to break apart chemical bonds. The products of that dissociation are then sent to a lower temperature electrochemical cell where they are recombined to generate electricity. Ando et al. (1997) studied such devices for solar-thermal dehydrogenation and electrochemical hydrogenation of various alcohols. They calculated the open circuit potential of various working fluids including methanol, ethanol, isopropanol, cyclohexane, methylcyclohexane, ethylcyclohexane, and cyclohexanol. They also performed experiments on isopropanol-acetone systems. Ando et al. (2001) and (2004) further expanded this study to investigate means of improving acetone hydrogenation at the cell cathode. They found that lower cell temperatures, sulfuric acid addition, and higher acetone concentrations improved the power output of the system.

Chaurasia et al. (2003) investigated the isopropanol-acetone regenerative fuel cell. They focused on studying the effect of different catalysts to maximize the performance of the system. Setzler et al. (2012) also experimentally studied isopropanol-acetone thermally regenerative fuel cells. They performed experiments on the high temperature dissociation reaction using a copper sponge as a catalyst. They also performed low temperature tests using a PEM fuel cell and acetone/hydrogen working fluids. They found the process to be feasible but challenging to implement at large scales due to low cell potentials.

Ludwig et al. (1991) investigated a thermally regenerative fuel cell based on hydrochloric acid and the ionic liquid 1-methyl,3-ethylimidazolium chloride. The system showed promise for regeneration temperatures of about 200°C. Carrier et al. (2012) studied the application of thermally regenerative fuel cells as bottoming cycles for truck engines. They identified 1-Phenyl-1-propanol as a suitable working fluid for the system due to its stability and selectivity at the desired operating range.

3.3 Electro-Organic Synthesis

Electrochemical reactions have received a great deal of interest for their ability to help synthesize various products of commercial value. The synthesis of chemicals is an important process finding applications in many sectors such as pharmaceuticals and manufacturing. Electrochemical synthesis reactions are generally less polluting and are easier to control than synthesis via traditional chemical pathways (Singh et al. 1999). The field of electro-organic synthesis involves the use of electrochemical devices to aid in the synthesis of organic compounds.

One such reaction is the hydrogenation of fatty acids in edible oils. This is done to improve the oil's oxidative stability. Pintauro et al. (2005) studied the hydrogenation of soybean oils with the use of a proton exchange membrane electrochemical cell. They found that it was possible to partially hydrogenate the acids using a cell with a palladium cathode and a platinum anode.

Little work has been published on the coupling of conventional refrigerants and electrochemical cells. Inaba et al. (1995) studied the dechlorination of HCFC-124 to HFC-134 on a solid polymer composite electrode. They found that the process could be accelerated by irradiation by a xenon arc lamp.

Many other synthesis reactions have been studied including the hydrogenation of allyl alcohol to 1-propanol using a PEM reactor (Yuan et al. 2003), the hydrogenation of *o*-xylene in a PEM reactor (Fonocho et al. 2012), the hydrogenation of ethylene in a PEM reactor (Sedighi et al. 2010), the hydrogenation of decene and acetone in a PEM reactor (Benziger et al. 2010), the oxidation of toluene and benzyl alcohol (Girt 1997), the hydrogenation of cyclo-octene, α -methyl styrene, and diethyl maleate (Ogumi et al. 1981), Wacker and π -allyl type oxidations, the hydroxylation of benzene (Otsuka et al. 1998), the oxidation of glycerol (Okada 2013), and the reduction of carbon dioxide to methane and ethylene (DeWulf et al. 1998). Jörissen (1996) and (2003) studied the potential of using solid polymer electrolyte technology for electro-organic synthesis. This included the examination of different electrolyte types, electrode materials, and reactor configurations. Hoormann et al. (2001) investigated the methoxylation of *p*-

methoxytoluene in a PEM reactor and studied ways to minimize power consumption. These methods included use of co-solvents and other means of membrane preparation.

Various methods have been investigated to lower the power consumption required to perform electro-organic synthesis. One such method is the use of bilateral reactions. This consists of running two complementary reactions on each side of an electrochemical cell. The reactants are chosen such that one compound acts as an ion donor or receiver for the other. This reduces the voltage requirement in relation to that which would be needed to drive each reaction separately. Itoh et al. (2000) studied the coupling of benzene hydrogenation and water electrolysis in a PEM cell and found that the voltage requirement was reduced in comparison to standard water electrolysis. Huang et al. (2016) studied the bilateral hydrogenation of phenol and the dehydrogenation of 2-propanol in a PEM fuel cell. Similarly, reduced voltages were observed in comparison to standard processes. Green et al. (2012) and Kariya et al. (2006) investigated the concurrent hydrogenation of acetone to isopropanol and water electrolysis in a PEM reactor for simulating the reduction of biomasses and for modeling energy storage.

Cogeneration generally refers to systems where multiple useful outputs are produced from a single process. PEM fuel cells have been proposed as reactors for the cogeneration of electricity and useful chemical byproducts. Yuan et al. (2005) experimentally investigated several organic alcohols and acids as precursors for cogeneration systems. Yuan et al. (2001) studied the cogeneration of cyclohexylamine and electrical power. Alcaide et al. (2006) reviewed 34 cogeneration reactions that have been proposed for alkaline, PEM, phosphoric acid, molten carbonate, and solid oxide fuel cells. Wiyaratn (2010) also reviewed alkaline, PEM, and solid oxide fuel cells for use in chemical and electricity cogeneration systems. Datta et al. (1996) looked at the use of ethanol for power generation and the concurrent production of acetaldehyde. Zhang et al. (2012) studied the use of glycerol and anion exchange membranes fuel cells for the cogeneration of electricity and valuable chemicals. Langer et al. (1979) looked at various cogeneration systems and discussed various design decisions for industrially viable systems.

3.4 Proton Exchange Membrane CLHP

When using electrochemical cells, the choice of the electrolyte influences the type of reactants that can be used within the cell. For this investigation, proton exchange membrane (PEM) cells were chosen as the reaction mechanism. PEM cells have been widely studied for a variety of applications. They are one of the most popular choices for low temperature reactions in the range of interest for commercial and residential heat pumping. Using electrochemical cells such as these, an embodiment of the CLHP is shown in Figure 3.2. Here the cell is performing bilateral reactions with the forward and reverse chemical transformations simultaneously occurring within the anode and cathode of the cell. The work input of an electrical current is used as the reaction driver.

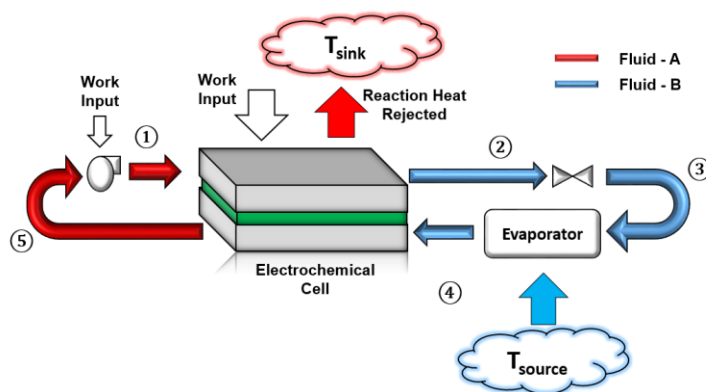


Figure 3.2: Diagram of CLHP using PEM electrochemical cell and a single circuit.

The CLHP utilizes the change in saturation temperature of a fluid in order to re-pressurize the fluid in the liquid phase after the evaporation stage. As such, one of the most important criteria for a potential CLHP working fluid is that there be a significant change in the saturation temperature of the fluid after it undergoes a transformation in a PEM cell. Imposing another criteria that the difference in normal boiling points of the chemicals before and after the reaction be greater than 15 °C, possible working fluid pairs for the CLHP were selected and are shown in Table 3.1. For each pair, the chemical transformation can be achieved via hydrogenation and dehydrogenation reactions in a PEM cell. These fluids were selected from the aforementioned work done investigating organic fluids in liquid fuel cells and in electro-organic synthesis. The

substances in Table 3.1 should not be considered an exhaustive list of all the possible working fluids that can be used in a CLHP using PEM cells.

Table 3.1: List of potential working fluids for CLHP.

Pair Abbreviation	Compound	Reaction Formula	$\Delta T_{\text{boiling}} [^{\circ}\text{C}]$
MTH	Methanol	$\text{CH}_3\text{OH} \leftrightarrow \text{CH}_2\text{O} + \text{H}_2$	83.59
	Formaldehyde		
ETH	Ethanol	$\text{C}_2\text{H}_6\text{O} \leftrightarrow \text{C}_2\text{H}_4\text{O} + \text{H}_2$	57.28
	Acetaldehyde		
IPA	Isopropanol	$\text{C}_3\text{H}_8\text{O} \leftrightarrow \text{C}_3\text{H}_6\text{O} + \text{H}_2$	26.38
	Acetone		
BUT	Butanol	$\text{C}_4\text{H}_{10}\text{O} \leftrightarrow \text{C}_4\text{H}_8\text{O} + \text{H}_2$	20.06
	Butanone		
PENT	2-Pentanol	$\text{C}_5\text{H}_{12}\text{O} \leftrightarrow \text{C}_5\text{H}_{10}\text{O} + \text{H}_2$	16.79
	2-Pentanone		
PGLY	Propylene Glycol	$\text{C}_3\text{H}_8\text{O}_2 \leftrightarrow \text{C}_3\text{H}_6\text{O}_2 + \text{H}_2$	31.3
	Hydroxyacetone		
OXYL	o-xylene	$\text{C}_8\text{H}_{10} + 3\text{H}_2 \leftrightarrow \text{C}_8\text{H}_{16}$	118
	1,2-dimethylcyclohexane		
TETRA	tetrahydrofuran	$\text{C}_4\text{H}_8\text{O} \leftrightarrow \text{C}_4\text{H}_4\text{O} + 2\text{H}_2$	34.25
	furan		
ANIL	aniline	$\text{C}_6\text{H}_7\text{N} + 3\text{H}_2 \leftrightarrow \text{C}_6\text{H}_{13}\text{N}$	49.9
	cyclohexylamine		

Since polymer membranes ideally only transmit protons, it may be possible to concurrently utilize different reacting pairs in the CLHP. In this manner, one chemical transformation could be occurring on one side of the cell and a reaction involving a dissimilar chemical pair could occur on the other side of the cell. As will be shown later, the work requirement to drive the reactions is mainly determined by the chemical species involved in reaction. Thus, the coupling of different working pairs may prove advantageous to the overall process. An embodiment of the CLHP using two reacting pairs in two different circuits is shown in Figure 3.3. Fluids 1A and 1B make up one circuit and fluids 2A and 2B make up a second circuit.

PEM cells have been chosen as the reactor to utilize for further investigation into the CLHP system. In addition, nine different working fluid pairs were identified for potential use in the cycle. With these choices, a thermodynamic model was constructed to estimate the performance of a potential CLHP system that is described in the next chapter.

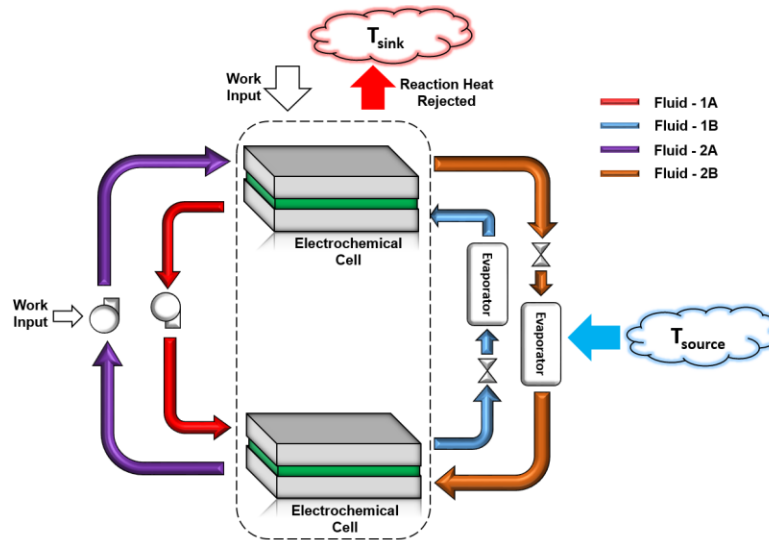


Figure 3.3: Diagram of CLHP using PEM electrochemical cells and a dual circuit arrangement.

3.5 References

Alcaide, F., Cabot, P., Brillas, E., 2006. Fuel Cells for Chemicals and Energy Cogeneration.

Journal of Power Sources, vol. 153, p.47 - 60

An, L., Zhao, T., Shen, S., Wu, Q., Chen, R., 2010. Performance of a Direct Ethylene Glycol Fuel Cell with an Anion-Exchange Membrane. International Journal of Hydrogen Energy, vol.35, p.4329-4335

Ando, Y., Doi, T., Takashima, T., Tanaka, T., 1997. Proposal and Fundamental Analysis of Thermally Regenerative Fuel Cell Utilizing Solar Heat. 32nd Intersociety Energy Conversion Engineering Conference.

Ando, Y., Tanaka, T., Doi, T., Takashima, T., 2001, A Study on a Thermally Regenerative Fuel Cell Utilizing Low-Temperature Thermal Energy. Energy Conversion and Management, vol. 42, p.1807 - 1816.

- Ando Y., Aoyama, Y., Sasaki, T., Saito, Y., Hatori, H., Tanaka, T., 2004. Effect of Catalytic and Electrochemical Acetone Hydrogenation on the I-V Characteristics of an Acetone/Hydrogen-Based Thermally Regenerative Fuel Cell. *Bulletin of the Chemical Society of Japan*, vol.77, p.1855 - 1859
- Araujo, C., Simone, D., Konezny, S., Shin, A., Crabtree, R., Soloveichik, G., Batista, V., 2012. Fuel Selection for a Regenerative Organic Fuel Cell/Flow Battery: Thermodynamic Considerations. *Energy & Environmental Science*, vol.5, p.9534 - 9542
- Arun Kumar, J., Kalyani, P., Saravanan, R., 2008. Studies on PEM Fuel Cells Using Alcohols for Low Power Applications. *International Journal of Electrochemical Science*, vol.3, p.961-969
- Barreto, L., Makihira, A., Riahi, K., 2003, The Hydrogen Economy in the 21st Century: A Sustainable Development Scenario. *International Journal of Hydrogen Energy*, vol. 28, p.267-284.
- Benziger J., Nehlsen, J., 2010. A Polymer Electrolyte Hydrogen Pump Hydrogenation Reactor. *Industrial and Engineering Chemistry Research*, vol. 49, p.11052 – 11060.
- Cao, D., Bergens, S., 2003. A Direct 2-Propanol Polymer Electrolyte Fuel Cell. *Journal of Power Sources*, vol.124, p.12-17.
- Carrier, A., 2011. The Transportation and Transformation of Energy Through Reversible Hydrogenation. Ph.D. Thesis, Queen's University, Ontario, Canada.
- Carrier, A., Dean, D., Little, V., Vandersleen, J., Davis, B., Jessop, P., 2012. Towards an Organic Thermally Regenerative Fuel Cell for Truck Engines. *Energy and Environmental Sciences*, vol.5 p.7111 - 7123

- Chaurasia, P., Ando, Y., Tanaka, T., 2003, Regenerative Fuel Cell with Chemical Reactions. Energy Conversion and Management, vol.44, p.611-628
- Datta, R., Malhotra, S., 1996. Development of Ethanol-Based Fuel Cells for Cogeneration and Transportation Applications: Final Report. Report, Iowa Energy Center. Ames, Iowa
- Demirci, U., 2007. Direct Liquid-Feed Fuel Cells: Thermodynamic and Environmental Concerns. Journal of Power Sources, vol.169, p.239-246
- Demirci, U., 2009. How Green are the Chemicals used as Liquid Fuels in Direct Liquid Feed Fuel Cells?. Environmental International, vol.35, p.626-631.
- DeWulf, D., Bard, A., 1988. The Electrochemical Reduction of CO₂ to CH₄ and C₂H₄ at Cu/Nafion Electrodes (Solid Polymer Electrolyte Structures). Catalysis Letter 1, p.73 - 80
- Fonocho R., Gardner, C., Ternan, M., 2012. A Study of the Electrochemical Hydrogenation of O-Xylene in a PEM Hydrogenation Reactor. Electrochimica Acta, vol. 75, p.171-178.
- Green, S., Tompsett, G., Kim, H., Kim, W., Huber, G., 2012. Electrocatalytic Reduction of Acetone in a Proton-Exchange-Membrane Reactor: A Model Reaction for the Electrocatalytic Reduction of Biomass. ChemSusChem, vol. 5, p. 2410 - 2420
- Girt, R., 1997. Scale-Up of the Solid Polymer Electrolyte Reactor for Electro-Organic Synthesis. Ph.D. Thesis, University of Newcastle upon Tyne.
- He, T., Pei, Q., Chen, P., 2015. Liquid Organic Hydrogen Carriers. Journal of Energy Chemistry, vol. 24. P.587 - 594
- Hoormann, D., Kubon, C., Jörissen, J., Kröner, L., Pütter, H., 2001. Analysis and Minimization of Cell Voltage in Electro-Organic Syntheses using the Solid Polymer Electrolyte Technology. Journal of Electroanalytical Chemistry, vol. 507, p.215 - 225

- Huang, S., Wu, X., Chen, W., Wang, T., Wu, Y., He, G., 2016. A Bilateral Electrochemical Hydrogen Pump Reactor for 2-Propanol Dehydrogenation and Phenol Hydrogenation. *Green Chemistry*, vol. 18, p.2353 - 2363
- Inaba, M., Sawai, K., Ogumi, Z., Takehara, Z., 1995. Electroreduction of Chlorofluoroethane on a Solid Polymer Electrolyte Composite Electrode. *Chemistry Letters*, p.471 - 472
- Itoh, N., Xu, W., Hara, S., Sakaki, K., 2000. Electrochemical Coupling of Benzene Hydrogenation and Water Electrolysis. *Catalysis Today*, vol.56, p.307 - 314
- Jörissen, J., 2003. Electro-organic Synthesis Without Supporting Electrolyte: Possibilities of Solid Polymer Electrolyte Technology. *Journal of Applied Electrochemistry*, vol.33, p.969 - 977
- Kariya, N., Fukuoka, A., Ichikawa, M., 2006. Direct PEM Fuel Cell Using “Organic Chemical Hydrides” with Zero-CO₂ Emission and Low Crossover. *Physical Chemistry Chemical Physics*, vol.8, p.1724-1730
- Kobayashi, T., Otomo, J., Wen, C., Takashi, H., 2003. Direct Alcohol Fuel Cell - Relation Between the Cell Performance and the Absorption of Intermediate Originating in the Catalyst -Fuel Combinations. *Journal of Power Sources*, vol. 124, p.34-39.
- Langer, S., Pietsch, S., Sakellaropoulos, P., 1979. Electrogenative Chemical Reactions. *Energy*, vol. 4, p.225 - 233.
- Ludwig, F., McHardy, J., Kindler, A., Basiulis, D., 1991. Thermally Regenerative Fuel Cells. Report. Department of the Navy, Office of Naval Research.
- Nagao, M., Kobayashi, K., Yamamoto, Y., Hibino, T., 2015. Rechargeable PEM Fuel Cell Batteries Using Quinones as Hydrogen Carriers. *Journal of the Electrochemical Society*, vol.162, p.F410 - F418

- Ogumi, Z., Nishio, K., Yoshizawa, S., 1981. Application of the SPE Method to Organic Electrochemistry - II. Electrochemical Hydrogenation of Olefinic Double Bonds. *Electrochimica Acta*, vol. 26, p.1779 - 1782
- O'Hayre, R., Cha, S., Colella, W., Prinz, F., 2016, *Fuel Cell Fundamentals*, John Wiley and Sons
- Okada, K., 2013. Electrochemical Oxidation of Glycerol in a Proton-Exchange Membrane Reactor. Ph.D. Thesis, University of Michigan, Ann Arbor Michigan.
- Otsuka, K., Yamanaka, I., 1998. Electrochemical Cells as Reactors for Selective Oxygenation of Hydrocarbons at Low Temperature. *Catalysis Today*, vol. 41, p.311 - 325.
- Pintauro, P., Gil, M., Warner, K., List, G., Neff, W., 2005. Electrochemical Hydrogenation of Soybean Oil in Hydrogen Gas. *Industrial and Engineering Chemistry Research*, vol. 44, p.6188 - 6195
- Qi, Z., Kaufman, A., 2002. Performance of 2-Propanol in Direct -Oxidation Fuel Cells. *Journal of Power Sources*, vol.112, p.121-129
- Qi, Z., Kaufman, A., 2003. Liquid-Feed Direct Oxidation Fuel Cells Using Neat 2 Propanol as Fuel. *Journal of Power Sources*, vol.118, p.54-60
- Santasalo-Aarino, A., Kallio, T., Kontturi, K., 2010. Methanol, Ethanol, and Iso-propanol Performance in Alkaline Direct Alcohol Fuel Cell (ADAFC). 218th Electrochemical Society Meeting, Las Vegas, Nevada
- Sedighi, S., Gardner, C., 2010. A Kinetic Study of the Electrochemical Hydrogenation of Ethylene. *Electrochimica Acta*, vol.55, p.1701 - 1708

- Setzler, B., Al-Ansary, H., 2012, Further Development of the Isopropanol-Acetone Chemical Heat Engine. World Renewable Energy Forum, 41st American Solar Energy Society Annual Conference, Denver, CO.
- Singh K., Shukla, K., 1999, Electroorganic Synthesis: An Edge Over Conventional Chemical Methods. Journal of Scientific and Industrial Research. Vol. 58, p. 327 -331
- Soloveichik, G., 2014. Liquid Fuel Cells. Beilstein Journal of Nanotechnology, vol.5, p.1399-1418
- Taneda, K., Yamazaki, Y., 2006a. I-V Characteristics of a Direct Type Fuel Cell Using Acetaldehyde as a Fuel. Journal of Power Sources, vol.157, p.177-180
- Taneda, K., Yamazaki, Y., 2006b. Study of Direct Type Ethanol Fuel Cells Analysis of Anode Products and Effect of Acetaldehyde. Electrochimica Acta, vol.52, p.1627 - 1631
- Teichmann, D., Arlt, W., Wasserscheid, P., Freymann, R., 2011. A Future Energy Supply Based on Liquid Organic Hydrogen Carriers (LOHC). Energy and Environmental Sciences, vol.4, p. 2767 - 2773
- Teichmann, D., Arlt, W., Wasserscheid, P., 2012. Liquid Organic Hydrogen Carriers as an Efficient Vector for the Transport and Storage of Renewable Energy., International Journal of Hydrogen Energy, vol.37, p. 18118 - 18132
- Wiyaratn, W., 2010. Review on Fuel Cell Technology for Valuable Chemicals and Energy Co Generation. Engineering Journal, vol.14, p.1 - 14
- Yuan, X., Ma, Z., Jiang, Q., Wu, W., 2001. Cogeneration of Cyclohexylamine and Electrical Power using PEM Fuel Cell Reactor. Electrochemistry Communications, vol.3, p.599 - 602

Yuan X., Ma, Z., He, Q., Hagen, J., Drillet, J., Schmidt, V., 2003, Electro-generative Hydrogenation of Allyl Alcohol Applying PEM Fuel Cell Reactor. *Electrochemistry Communications*. Vol. 5, p.189 - 193

Yuan, X., Ma, Z., Bueb, H., Drillet, J., Hagan, J., Schmidt, V., 2005. Cogeneration of Electricity and Organic Chemicals Using a Polymer Electrolyte Fuel Cell. *Electrochimica Acta*, vol.50, p. 5172 - 5180

Zhang, Z., Xin, L., Li, W., 2012. Electrocatalytic Oxidation of Glycerol on Pt/C in Anion Exchange Membrane Fuel Cell: Cogeneration of Electricity and Valuable Chemicals. *Applied Catalysis B: Environmental*, vol.119, p.40 - 48

CHAPTER 4. THERMODYNAMIC SYSTEM MODEL

4.1 CLHP Model Development

A thermodynamic model was developed in order to assess the performance of the CLHP using PEM cells. The inputs and outputs to the model are shown in Figure 4.1. There are many similarities between the modeling of the single circuit CLHP shown in Figure 3.2 and the dual circuit embodiment shown in Figure 3.3. For both systems, the fluids going through a circuit undergo the same steps of pumping, hydrogenation/ dehydrogenation, throttling, and evaporation. The modeling approach for the single circuit CLHP will be described and can be easily extended to a dual circuit CLHP by adjusting the inputs and outputs of the electrochemical cells. The following assumptions were made to simplify the modeling:

- Chemical Reactions go to completion
- No crossover of chemicals through the cell membrane
- Negligible pressure drops in lines

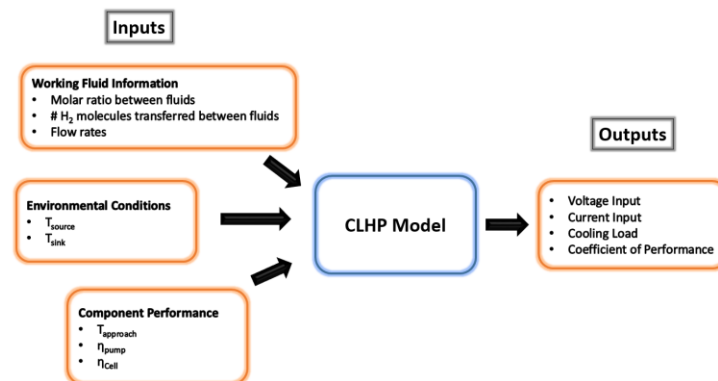


Figure 4.1: Inputs and outputs of CLHP thermodynamic model.

4.1.1 System Conditions

In the CLHP, the electrochemical cells are cooled by rejecting heat to the ambient. Using an approach temperature, the temperatures of the evaporator and of the electrochemical cell are determined from Equations 4.1 and 4.2.

$$T_{evap} = T_{source} - T_{approach} \quad (4.1)$$

$$T_{cell} = T_{sink} + T_{approach} \quad (4.2)$$

Once the working pair for a circuit had been identified, the low and high side pressures are calculated using the saturation pressures of the fluids. From the state points in Figure 3.2, states ① and ② are at high pressure and states ③ - ⑤ are at low pressure. The low and high side pressures are given by Equations 4.3 and 4.4.

$$P_{low} = P_{sat}(fluidB, T_{evap}) \quad (4.3)$$

$$P_{high} = P_{sat}(fluidB, T_{cell}) \quad (4.4)$$

To ensure that the fluid at state ⑤ would be in the liquid phase after the chemical reaction, the required saturation temperature of the fluid is evaluated at P_{low} . If T_{cell} is greater than the saturation temperature at ⑤, then the temperature lift is outside of the range of the particular working fluid pair. A different pair would have to be used or the temperature lift reduced.

4.1.2 Reaction Stoichiometry and Flow Rates

The reactions taking place in the electrochemical cells were assumed to be steady state Faradaic processes such that the rates of the reactions were governed by Faraday's Law of Electrolysis, Equation 4.5. This means that the rate at which the reactions take place is assumed to be directly proportional to the current passed through the cell (Wendt et al. 1999).

$$n = \frac{Q}{v_e F} = \frac{I \cdot t}{v_e F} \quad (4.5)$$

Once the molar flow rate of a chemical species entering a cell is specified, the stoichiometric equation of the reaction in conjunction with Faraday's Law of electrolysis is used to determine the necessary current that needs to be passed through the cell for the reaction to go to completion. This is additionally used to determine the necessary molar flow rate of an alternative

reacting pair on the opposite side of the cell, as is the case in the dual circuit CLHP. For each system, the flow rate of one fluid needs to be specified. From here, the molar ratios from the stoichiometric reaction equations are used to determine the molar flow rates of the other fluid in the pair as well as the hydrogen transferred during the reaction. Using Equation 4.6 as an example illustrating the use of aniline and cyclohexylamine, specification of the aniline molar flow rate dictates that the flow of cyclohexylamine be equal to that of aniline and the molar flow rate of hydrogen is 3 times higher than that of aniline.



4.1.3 Pump Modeling

The fluid going through the pump was assumed to be an incompressible liquid. Once the molar flow rates of the fluids is known, the molar masses are used to determine the mass flow rates. A constant value was assumed for the liquid densities. Knowing the mass flow rate, liquid density, and pressure differential the pump work is calculated using Equation 4.7. An isentropic efficiency parameter was used to account for irreversibilities during the pumping process.

$$\dot{W}_{pump} = \frac{\dot{m}_{fluid,①} v_{fluid,①} (P_{high} - P_{low})}{\eta_{pump}} \quad (4.7)$$

4.1.4 Electrochemical Cell Work

The ideal work required to drive the chemical reactions is equal to the change in Gibbs free energy between the product and reactant streams as shown in Equation 4.8 (Revankar et al. 2014). For the single circuit CLHP, the reactants were taken as the input streams to the cell at states ① and ④ and the products are the output streams at states ② and ⑤. For the CLHP using dual circuits, the reactant and product streams need to be adjusted accordingly. Using this formulation, if the work came out as positive then the electrochemical process produced work, whereas if the work was negative then the process consumed work.

$$w_{cell}^o = -\Delta\bar{g} = -(\sum \bar{g}_{products} - \sum \bar{g}_{reactants}) \quad (4.8)$$

The Gibbs free energy is calculated according to Equation 4.9. Using the enthalpy and entropy of formation, the enthalpy and entropy of each stream is calculated as functions of temperature and pressure according to Equations 4.10 – 4.13. The formation properties should be selected so as to represent the phase of the fluid at the specified state. The state entering the cell from the evaporator is gaseous while all other inputs and outputs were assumed to be in the liquid phase.

$$g = h - Ts \quad (4.9)$$

$$h = h_f^o + h(T) \quad (4.10)$$

$$h(T) = \int_{T^o}^T c_p dT \quad (4.11)$$

$$s = s_f^o + s(T) \quad (4.12)$$

$$s(T) = \int_{T^o}^T \frac{c_p}{T} dT - R \ln \left(\left(\frac{P}{P^o} \right)^n \right) \quad (4.13)$$

Using the change in Gibbs free energy, the reversible voltage required to drive the reaction could be found from Equation 4.14. Here F is Faraday's Constant and n_e is the number of electrons transferred during the reaction. This is related to the amount of H_2 transferred during the stoichiometric reaction via Equation 4.15.

$$V_{cell}^o = \frac{-\Delta g}{n_e F} \quad (4.14)$$

$$n_e = 2 \cdot n_{H_2} \quad (4.15)$$

Equation 4.14 represents the ideal voltage required to drive the electrochemical reaction. In reality, irreversibilities will necessitate greater voltage input to drive the reaction. For a work producing reaction, the actual voltage will be given by Equation 4.16 and for a work consuming reaction, the required voltage is given by Equation 4.17.

$$V_{cell} = V_{cell}^o \cdot \eta_{cell} \quad (4.16)$$

$$V_{cell} = \frac{V_{cell}^o}{\eta_{cell}} \quad (4.17)$$

The electrical current that needed to pass through the cell is calculated from the molar flow rates of the fluids and the number of electrons transferred via each reaction (n_e) as shown in Equation 4.18.

$$I = \dot{n}_{fluid} \cdot n_e \cdot F \quad (4.18)$$

Using the actual cell voltage and the calculated current, the power consumed or produced during the chemical transformations is given by Equation 4.19.

$$\dot{W}_{cell} = V_{cell} \cdot I \quad (4.19)$$

4.1.5 Expansion and Evaporation

After leaving the electrochemical cell at ②, the fluid is throttled to low pressure in an isenthalpic expansion process and Equation 4.20 applies.

$$h_{③} = h_{②} \quad (4.20)$$

After the expansion process the fluid is evaporated to a saturated vapor. The properties of many of the fluids investigated were not found in traditional thermophysical property tables or databases. Therefore, saturation temperatures and pressures were used in conjunction with the Clausius–Clapeyron equation to determine the enthalpy of vaporization of the fluid, Equation 4.21. In order to account for the quality of the fluid after the expansion stage, the difference in the enthalpies of the liquid state evaluated before and after the expansion stage is used to adjust the total enthalpy of vaporization according to Equation 4.22. The total rate of cooling is determined from Equation 4.23.

$$h_{vap} = \frac{\ln\left(\frac{P_2}{P_1}\right) \cdot R}{\frac{1}{T_2} - \frac{1}{T_1}} \quad (4.21)$$

$$h_{evap} = h_{vap} - (h_{Liq,②} - h_{Liq,③}) \quad (4.22)$$

$$\dot{Q}_{cool} = \dot{n}_{fluidB} h_{evap} \quad (4.23)$$

4.1.6 System Performance Metric

For this thermodynamic modeling, the cooling coefficient of performance (COP_C) was used as the primary metric to evaluate the performance of the system. The coefficient of performance of the entire system is calculated as the ratio of the cooling capacity to the sum of the work inputs as shown in Equation 4.24. As it was defined, the total electrochemical work input will be negative. Because of this, the absolute value of the electrochemical work was taken. For the dual circuit arrangement, the COP_C was determined using the sum of the cooling capacity of both evaporators and the sum of the work consumed by both electrochemical cells and pumps as shown in Equation 4.25.

$$COP_C = \frac{\dot{Q}_{cool}}{\dot{W}_{pump} + abs(\dot{W}_{cell})} \quad (4.24)$$

$$COP_C = \frac{\dot{Q}_{cool,1} + \dot{Q}_{cool,2}}{\dot{W}_{pump,1} + \dot{W}_{pump,2} + abs(\dot{W}_{cell,1} + \dot{W}_{cell,2})} \quad (4.25)$$

4.2 CLHP Model Results

The chemical looping heat pump is a novel system that hasn't previously been evaluated. The thermodynamic model was developed for the purpose of gaining a better understanding of the CLHP's performance and to determine whether it has the potential to be a viable alternative to conventional heat pumping systems. The influence of the working fluid selections, system parameters, and comparisons to other systems are shown below.

4.2.1 CLHP Working Fluids Comparisons

Using the aforementioned CLHP models, the relative performance of various working fluid pairs were evaluated. The following inputs were provided to the model:

- $T_{source} = 20 \text{ }^\circ\text{C}$
- $T_{sink} = 35 \text{ }^\circ\text{C}$
- $T_{approach} = 5 \text{ }^\circ\text{C}$
- $\eta_{pump} = 0.8$
- $\eta_{cell} = 0.6$

The efficiency of electrochemical cells depends on a number of factors, including the current density at which they are operated. The value of 60% represents a typical level of efficiency that can be achieved by various fuel cells. Following the nomenclature from Table 3.1, the calculated COP_C of the various fluid combinations using the dual circuit embodiment are shown in Figure 4.2. The circuit combinations are represented by the rows and the columns of the chart. For the instances where the same fluid pairs are in both circuits, the single circuit CLHP arrangement could be used to produce the same result. Overall the performance of the CLHP degraded when different fluid pairs were used in combination with each other. This was due to an increase in the required voltage to drive the reactions. For the dual circuit CLHP, the total voltage was taken as the sum of the voltages of the two cells. As shown by Figure 4.3, the overall voltage requirement increased when multiple fluid pairs were used consecutively. This was due in part to the differences in the oxidation and reduction potentials of the chemical species. Combinations where relatively higher voltages were required generally produce lower COP_C 's.

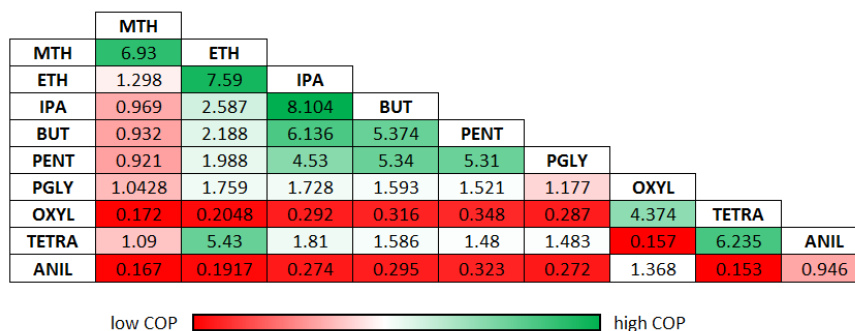


Figure 4.2: Cooling Coefficient of Performance for dual circuit CLHPs operating between 20°C and 35°C.

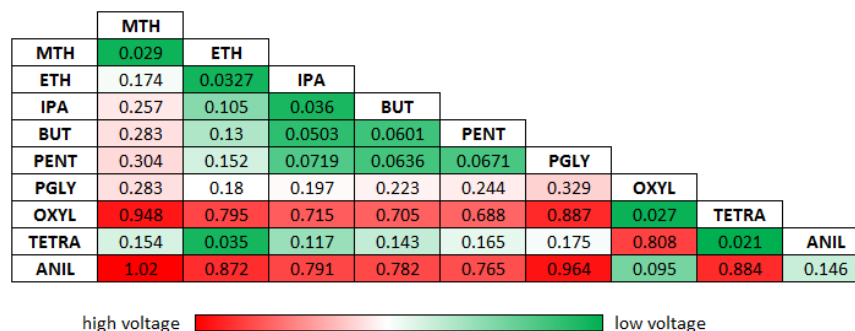


Figure 4.3: Voltage requirements of dual circuit CLHP operating between 20°C and 35°C.

For the operating conditions chosen, the working fluids isopropanol, ethanol, and methanol produced the highest COPs when paired with themselves. As a result, a single circuit CLHP employing these fluids would most likely be the most promising CLHP arrangement system due to reduced complexity in relation to the dual circuit configuration.

4.2.2 CLHP Parametric Study

The PEM cell chemical looping heat pump model was exercised to gain some insights into the performance characteristics of the system. Since the previous results showed that the single circuit arrangement was superior to the dual circuit layout, it was the focus of this stage of the investigation. Several assumptions were made about the performance of various cycle components. A parametric study allowed for the evaluation of the sensitivity of the system performance to various component characteristics. The baseline component properties were the same as for section 4.2.1. For each parametric test, one of the component properties was varied while the rest were held constant.

The performance of heat exchangers can vary depending on their geometry, size, and the type of fluids utilized. The simplified model employed an approach temperature to generalize the performance of the heat exchange between the source and the sink reservoirs. A lower approach temperature would indicate that the heat exchanger is able to more effectively exchange heat between the fluid and its surroundings. The results of an approach temperature parametric study are shown in Figure 4.4. Results for each fluid are plotted over the range of approach temperatures up until their maximum temperature lift is exceeded.

For most of the fluids, the COP_C drops off sharply as approach temperature is increased and then it experiences a more gradual decline. The propylene glycol and aniline systems show consistently poor performance with gradual losses as approach temperature increases. This insensitivity to system changes can be attributed to the fact that these reactions consume much more power than their counterparts. Irrespective of other changes occurring in the system, this high-power consumption dominates their performance results.

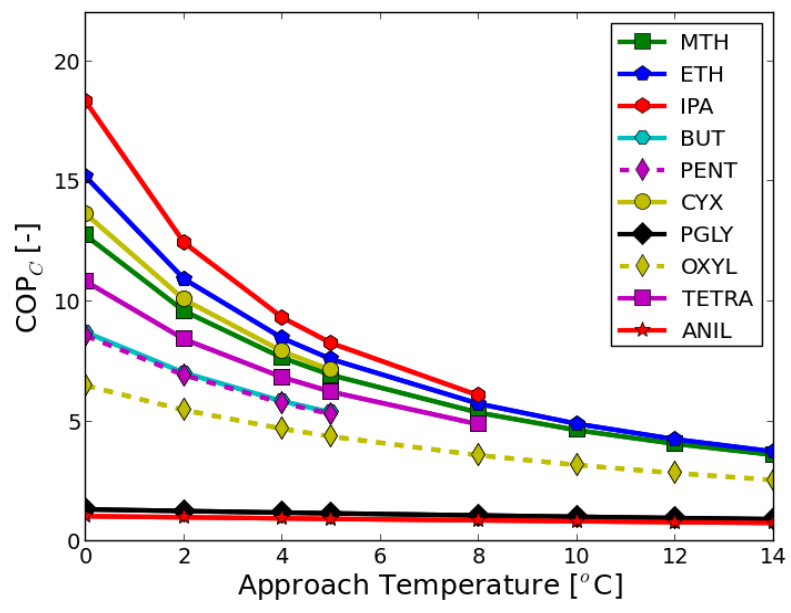


Figure 4.4: Parametric analysis of heat exchanger approach temperature.

The sink temperature was also varied to determine the system’s reaction to increasing ambient temperatures. Like the results shown for increasing the approach temperature, as the sink temperature increased the temperature lift across the heat pump increased and the coefficient of performance dropped, Figure 4.5.

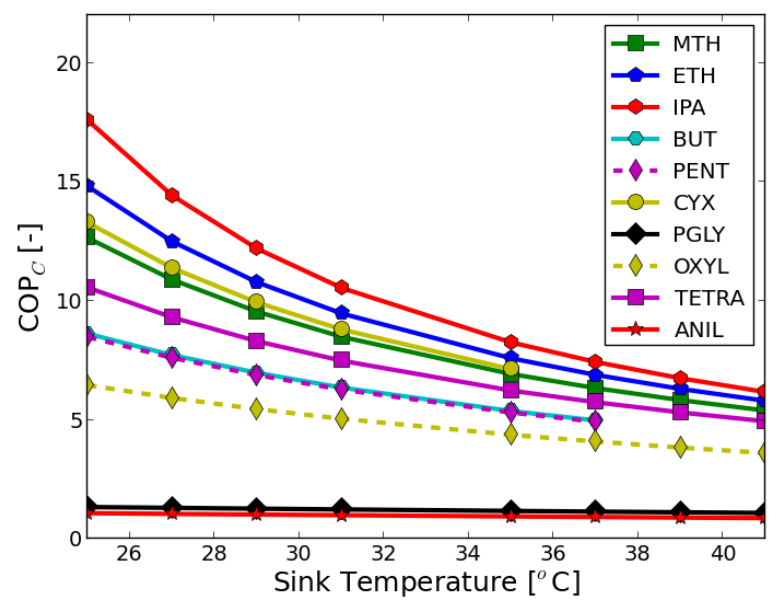


Figure 4.5: Parametric analysis of sink temperature variation.

As previously stated, one of the main features of the chemical looping heat pump is allowing for the compression of the working fluid to take place in the liquid phase. This being the case, an investigation into the effect of the pump's efficiency on the performance of the overall cycle was performed. As shown in Figure 4.6, the efficiency of the pump had little effect on the performance of the overall cycle. A slight impact due to pump efficiency on performance can be seen only at abysmally low pump efficiencies. The reason for the insensitivity to pump performance is that the work input required to drive the pump is orders of magnitude lower than that needed for the electrochemical cell. As such, only when the pump work input is greatly increased due to poor pump efficiency does an influence in the overall work consumption becomes apparent.

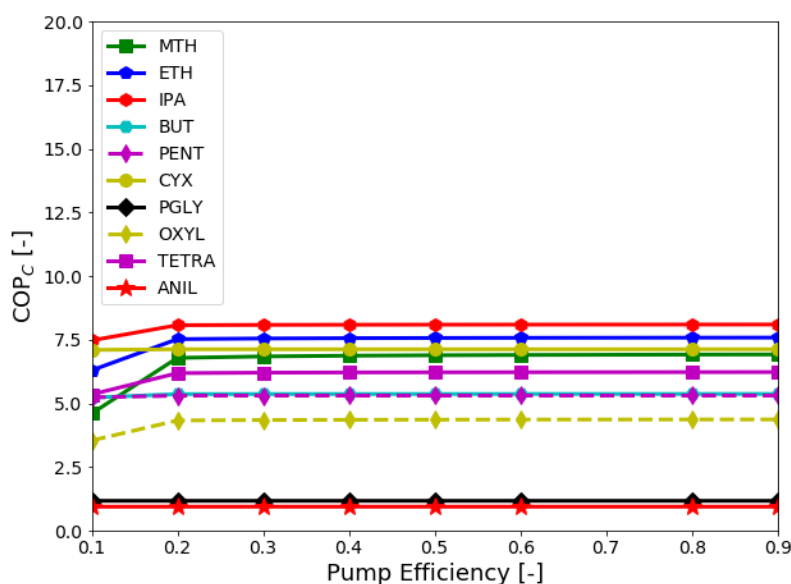


Figure 4.6: Parametric analysis of pump efficiency.

Most of the work input in the CLHP was used to power the electrochemical cell in order to drive the chemical transformations. In the previous analyses using the CLHP model, a typical voltage efficiency was assumed to characterize the cell. In this study, the cell's efficiency was varied over a range to assess the influence of the cell performance on the overall cycle. As shown in Figure 4.7, though the slopes may vary by working fluid, a linear trend can be observed between the cell's efficiency and the system COP.

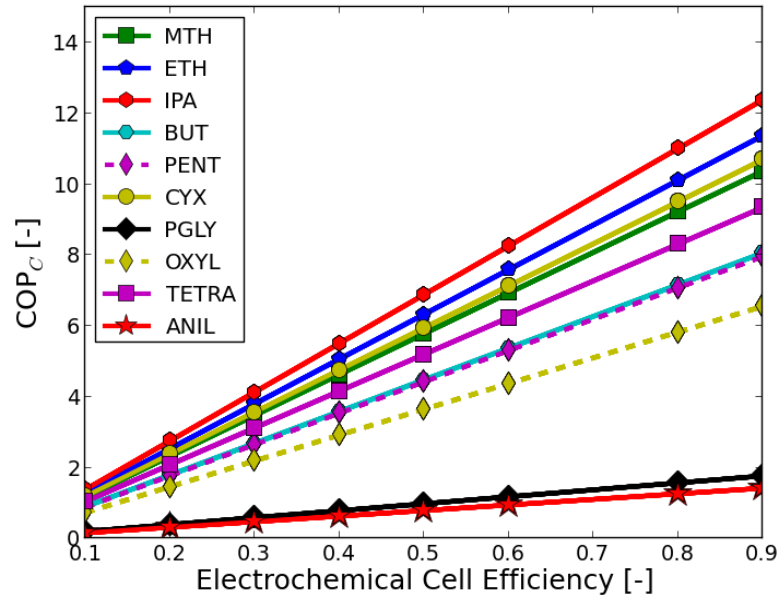


Figure 4.7: Parametric analysis of electrochemical cell efficiency.

This parametric study highlighted the influence of various system parameters on the performance of the overall cycle. The greatest influences on system performance were temperature lift, heat exchanger performance, and cell efficiency. The temperature lift was generally dictated by the environment and set point and cannot be considered a parameter that can be controlled from a system design perspective. The approach temperature of heat exchangers can be improved by allowing more time and providing more surface area for the heat transfer process to take place. The extent of improving this property faces limitations due to the cost for larger heat exchangers, and the need for moderate flow rates for useful cooling capacities. Electrochemical cells come in a variety of forms with varying materials chosen to optimize particular reactions. The characteristics of the electrochemical cell can be influenced during the design stage and can have a significant impact on the performance of the overall system.

4.3 Comparisons to other Heat Pumps

Since the CLHP has been proposed as an alternative to existing heat pumping methods, the thermodynamic model was used in order to compare the performance of the CLHP to other systems. Below are the results of the analysis looking at electrochemical and vapor compression systems.

4.3.1 Electrochemical Systems

As previously mentioned, a number of electrochemically driven heat pump systems have been previously investigated. Being that these systems share some similarities with the CLHP, the performance of the CLHP relative to these systems was assessed. Electrochemical heat pumps are typically highly sensitive to component efficiencies. This is due to the fact that the electrical power cycled between cells in these system is typically orders of magnitude higher than the heat pumped through the system (Gerlach, 2004).

Using the same source, sink, and approach temperatures as section 4.2.1, Figure 4.8 shows the response of COP_C to the efficiency of the electrochemical cells for the direct electrochemical heat pump of Newell (1997), the indirect electrochemical system using the evolution of a condensable gas of Gerlach (2004), and a single circuit CLHP using ethanol/acetaldehyde. Here the cell efficiencies are defined as in Equations 4.16 and 4.17.

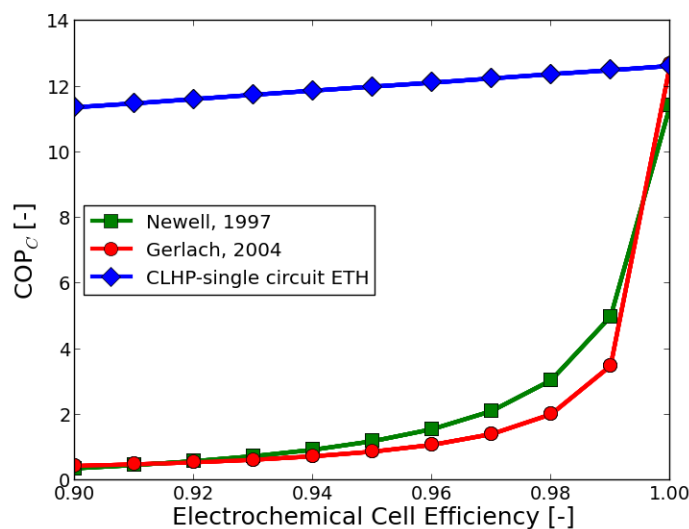


Figure 4.8: Performance of various electrochemical systems in response to electrochemical cell efficiency.

A notable difference between the PEM CLHP and the other electrochemical heat pumps is that the performance of the PEM CLHP is not highly sensitive to component efficiency. This is due to the nature of the bilateral reactions in the CLHP cell. In the CLHP, the product of one side of the electrochemical cell is fed in as the reactant to the other side. While such a flow

configuration would be counterproductive in a fuel cell power generation or electrochemical synthesis application, this greatly reduces the voltage requirements of the cells for the CLHP. By bringing the magnitude of the electrical power requirements closer to that of the heat transferred through the system, the sensitivity to the cell efficiencies decreases.

4.3.2 Conventional Systems

Vapor compression systems account for the majority of heat pumping systems used worldwide. In order to see if the CLHP could serve as a viable alternative, the performance of the CLHP was compared to that of VC systems. Like the previous comparison, the sink and approach temperatures were the same as that of section 4.2.1. For the VC heat pumps, the compressor was modeled using a constant isentropic efficiency of 70% (Hubacher et al. 2002, Xu et al. 2013). The temperatures at the outlets of the evaporator and condenser were determined according to equations 4.26 and 4.27. The superheat out of the evaporator was assumed to be 1.0 °C for both the vapor compression cycle and the CLHP. No sub-cooling was assumed after the condenser for the vapor compression cycle. For the CLHP, the electrochemical cells were assumed to operate at 60% efficiency.

$$T_{evap} = T_{source} - T_{approach} \quad (4.26)$$

$$T_{cond} = T_{sink} + T_{approach} \quad (4.27)$$

The COP_C of the VC and CLHP systems are shown in Figure 4.9 over a range of source temperatures. For the working fluids investigated, the CLHP could provide COP_C improvements in comparison to most common refrigerants including a 20% improvement in comparison to R404A VC heat pumps for the assumed parameters and conditions.

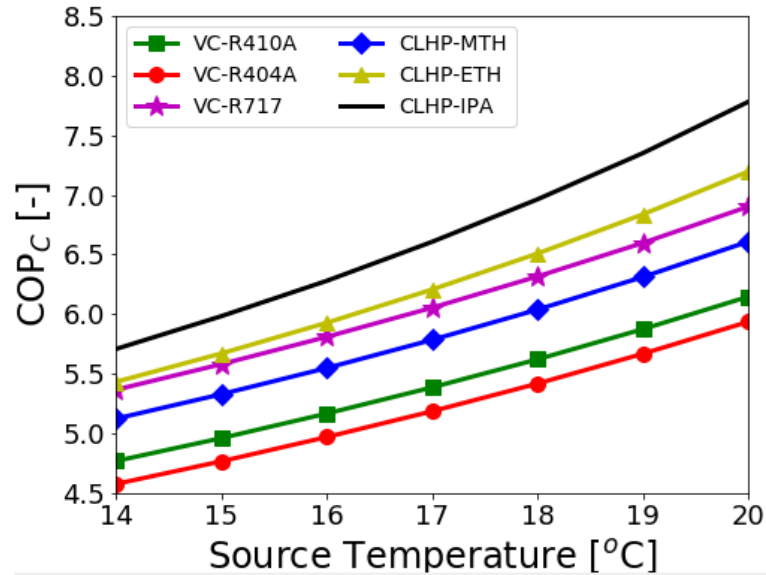


Figure 4.9: COP_C of vapor compression and CLHP systems vs source temperature for sink temperature of 35°C .

4.4 References

Gerlach, D., 2004. An Investigation of Electrochemical Processes for Refrigeration.

Ph.D. Thesis, University of Illinois at Urbana-Champaign.

Gerlach, D., Newell, T., 2007. Basic Modelling of Direct Electrochemical Cooling.

International Journal of Energy Research, vol.31, p.439 – 454

Hubacher, B., Groll, E., 2002. Measurement of Performance of Carbon Dioxide Compressors.

Report: Air-Conditioning and Refrigeration Technology Institute

Newell, T., 2000. Thermodynamic Analysis of an Electrochemical Refrigeration Cycle.

International Journal of Energy Research, vol.24, p.443 - 453

Revankar, S., Majumdar, P., 2014. Fuel Cells: Principles, Design and Analysis, Taylor

and Francis Group Publishing

Wendt, H., Kreysa, G., *Electrochemical Engineering in Chemical and other Industries, Basic Principles and Laws of Electrochemistry*, Springer Berlin Heidelberg, pgs. 8 - 16, 1999

Xu, Xing, Hwang, Y., Radermacher, R. 2013. Performance comparison of R410A and R32 in vapor injection cycles. *International Journal of Refrigeration*, vol. 36, p.892 – 903.

CHAPTER 5. ELECTROCHEMICAL CELL EXPERIMENTAL SETUP

From the simplified thermodynamic model, it could be seen that the performance of the electrochemical cell is of great importance for the chemical looping system to be efficient. To better understand the practical performance of this component, an electrochemical cell test stand was constructed. The overall test stand, individual components, and instrumentation are described in detail below.

5.1 Test Stand Overview

The experimental test stand was constructed to evaluate the performance of an electrochemical cell under conditions typical of a chemical looping heat pump cycle. The system was designed for simplicity with a single pass of reactants to the cell. There were 5 major components, 3 actively powered and 2 passive components. An image of the test stand is shown in Figure 5.1.

Active Components

1. Electrochemical Cell
2. Peristaltic Pump
3. Vortex Tube

Passive Components

1. Evaporator
2. Metering Valve

The system was equipped with thermocouples to measure reactant and cell temperatures. Pressure transducers and liquid flow meters were used to monitor system conditions. Voltage and current measurements were used to monitor cell operation and a photometric reading was used to measure the concentration of the reactants after leaving the cell. A schematic with the system arrangement and measurement locations is shown in Figure 5.2.

Two fluids were fed into the cell. As shown in the schematic, the less volatile fluid 'A' is on the left while the more volatile fluid 'B' is on the right. Fluid A was pumped through a flow meter then to the cell as a liquid. Afterwards, the concentration of the reactants in the stream was

measured to determine the extent of reaction completion. Then the fluid was collected for disposal. Fluid B's flow rate was measured as a liquid and then, it was throttled to low pressure. Heat was absorbed from the ambient to evaporate fluid B. The gaseous fluid B was then sent to the cell. A vortex tube cooled fluid B's collection container. This allowed for the re-condensation of any residual fluid B for disposal.



Figure 5.1: Electrochemical cell experimental setup.

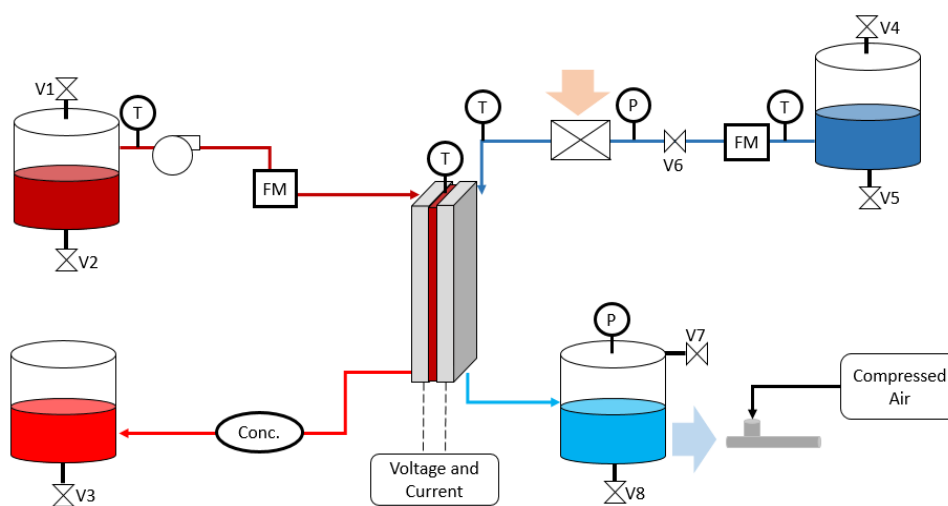


Figure 5.2: Instrumentation and piping diagram of electrochemical cell test stand.

The supplier and model numbers of the major components are shown in Table 5.1.

Table 5.1: List of major components supplier and model numbers.

Component	Supplier	Model Number
Electrochemical Cell	ElectroChem Inc.	FC-100
Pump	Langer Instruments	BT100-2J
Vortex Tube	Exair	3225
Evaporator	Lytron	4105G1SB
Metering Valve	McMaster-Carr	7836K25

5.1.1 Working Fluid Selection

From the previous thermodynamic analysis, isopropanol and acetone were found to be a promising working fluid pair for a high efficiency CLHP. Although the flammability of these fluids could raise issues that would need to be addressed in a commercial system, they are relatively non-toxic and fairly abundant. Therefore, they were determined to be suitable for the preliminary experimental investigation into the performance of electrochemical cells for the CLHP. Acetone serves as the more volatile component while isopropanol is used as the less volatile fluid.

5.1.2 Component Sizing

To determine the appropriate size for the test stand's components, the thermodynamic model was utilized for guidance. The predicted flow rates were determined by the predicted reaction rates at the cell. From the literature, a number of fuel cells using solid polymer electrolytes operate at a current density of ~ 100 mA/cm². Fuel cell assemblies sized at 100 cm² were readily available. Assuming operation at 100 mA/cm² and a 100 cm² cell, this would translate to a total current of 10 A. Since the current is proportional to the conversion rate of reactants, this in turn would lead to a fluid flow rate of 0.0035 g/s of isopropanol. Based on these assumptions, the components and sensors for the test stand were sized. A CAD model was used to assist in the initial placement of the components for the test stand as shown in Figure 5.3.

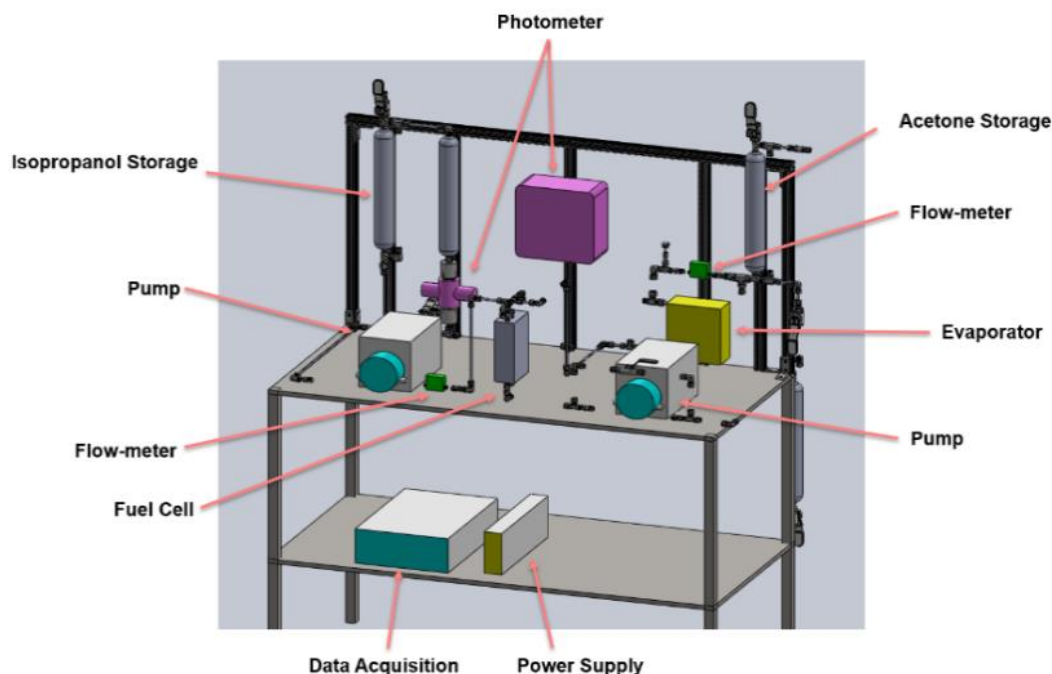


Figure 5.3: CAD model used during construction phase of electrochemical cell test stand.

5.2 Components

The primary components used to construct the electrochemical test stand are described below. Attention was paid to component cost, performance, chemical compatibility, and ease of use.

5.2.1 Electrochemical Cell

The heart of the test stand was a solid electrolyte electrochemical cell. A 100 cm² FC-100 fuel cell was purchased from ElectroChem Inc. to serve as the test stand's electrochemical cell, Figure 5.4. The fuel cell hardware measured approximately 3" x 7" x 11". An exploded view of such an electrochemical cell is shown in Figure 5.5. The endplates provided support to compress the assembly together while the flow fields provided a path for the reactants to flow to the cell. Electrically conductive sheets of carbon served as the electrodes for the anode and cathode. They were impregnated with a catalyst to help promote the reactions. The membrane provided a path for protons to migrate through the cell. The unit consisting of the membrane sandwiched between the electrodes is referred to as the membrane electrode assembly (MEA).



Figure 5.4: FC-100 100 cm² electrochemical cell hardware.

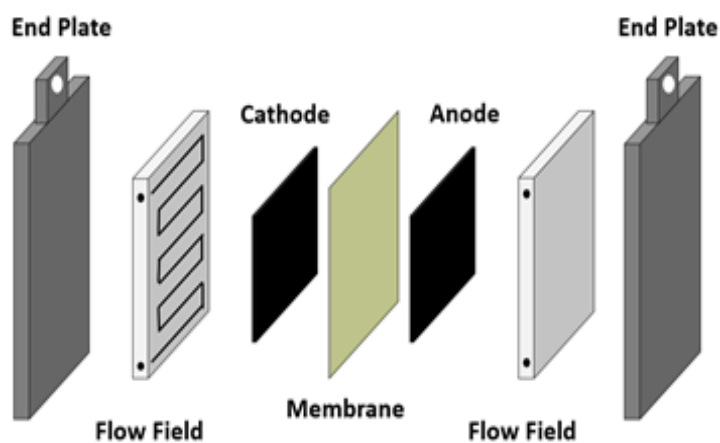


Figure 5.5: Exploded view of electrochemical cell components.

The material chosen for the cell membrane was of great importance. In addition to the ability to conduct protons, materials with good thermal, chemical, and mechanical stability are crucial for long term operation of the cell. One of the most popular membrane materials for PEM fuel cells is the polymer Nafion. Developed by DuPont in the 1960's, Nafion is able to conduct protons and cations due to the presence of sulfonic acid groups and it resists the transport of electrons. As a copolymer of Teflon, it also has excellent chemical resistance. Due to its popularity and performance in PEM fuel cells, Nafion was chosen as the membrane material for the start of this investigation.

The carbon electrodes serve multiple purposes in the MEA of electrochemical cells. Sometimes referred to as the gas diffusion layer (GDL), they generally are part of the interface where

reactants, catalyst, and electrolyte meet. At the reaction site, liberated ions will flow through the electrolyte, electrons will flow through the carbon electrode, and reaction products will diffuse away from the site. The continuity of this interface is important to the overall performance of the electrochemical cell. The GDL also can provide structural support to the MEA.

Catalysts are substances that lower the activation energy of a reaction allowing it to proceed at a faster pace without themselves being consumed in the reaction. Platinum is a common catalyst used in fuel cells. For alcohol-based fuel cells, alloys of platinum and rutherfordium are typically used. This is due to the fact that this alloy is more resistant to poisoning from intermediate chemical species generated during alcohol oxidation.

The flow fields were made of graphite and the electrochemical cell assembly was held together by two aluminum slabs. As can be seen in Figure 5.4, the slabs make up the bulk of the mass of the cell. Because the reactions only occurred at the relatively thin MEA, if the amount of heat released by the reactions was not sufficiently high, the temperature of the cell fixture would remain near room temperature due to the thermal mass of the rest of the cell. To allow for simple testing at elevated temperatures, the FC-100 came equipped with silicone heaters attached on each side. These 120V powered heaters could raise the temperature of the cell as desired. To accurately control the temperature, an AutomationDirect SL4824 digital temperature controller was utilized. The SL4824 was configured to receive a temperature reading from a thermocouple probe in the electrochemical cell and then used on-off control to cycle the heating elements until the desired temperature was reached.

5.2.2 Storage Vessels

Four storage vessels were needed on the test stand: two to store the isopropanol before and after use and two to store the acetone before and after use. Stainless steel 500 cm³ 304L-HDF4-500 sampling cylinders from Swagelock were used for this purpose. The supply cylinders for the isopropanol and acetone were both equipped with liquid level lines to track the amount of fluid in each as shown in Figure 5.6. A pressure equalization line was placed between the supply and collection cylinders for the isopropanol to prevent a vacuum from forming and unwanted pressurization as fluid was transferred from one container to the other. The supply container for

the acetone was equipped with a check valve to allow ambient air to flow into the container as fluid was drawn out to prevent the formation of a vacuum. The collection cylinder for the acetone was cooled in order to condense any gaseous products that may enter.



Figure 5.6: Supply cylinder for isopropanol with liquid level line installed.

5.2.3 Pump

From the component sizing, it was determined that a low fluid flow rate would be needed to properly test the chemical looping concept with the FC-100 electrochemical cell. Gear pumps and peristaltic pumps were considered for the purpose of accurately metering the flow. Ultimately a peristaltic pump was chosen due to the ease of ensuring chemical compatibility with the working fluid. A Langer Instruments BT100-2J peristaltic pump was used to meter the flow of the isopropanol to the electrochemical cell. Peristaltic pumps are positive displacement machines that house the fluid to be pumped within flexible tubing. Using a process called peristalsis, a roller contacts and rolls along the length of the tube. As it rolls, the tube is compressed and the fluid is propagated through the tube. The pump's rotational speed can be set from 0 - 100 RPM in 0.1 RPM increments. A $\frac{1}{4}$ " OD - $\frac{1}{8}$ " ID EPDM rubber tube was used in conjunction with the pump. Together, the pump speed and displacement volume determined by the tubing geometry control the flow rate of the fluid.

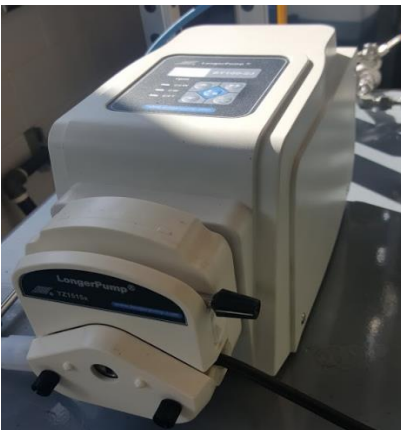


Figure 5.7: BT100-2J peristaltic pump.

5.2.4 Metering Valve

The flow rate of the acetone was controlled by a metering valve. The acetone side of the electrochemical cell was kept at vacuum pressure. With the acetone storage container being at atmospheric pressure, when the metering valve was opened acetone throttled to low pressure and flowed towards the electrochemical cell. The valve was obtained from McMaster-Carr and was made of stainless steel with Teflon packing for chemical compatibility. It had an orifice diameter of 0.031” and a flow coefficient of 0.02.



Figure 5.8: Acetone metering valve.

5.2.5 Evaporator

After throttling to low pressure, the acetone needed to be evaporated in order for gaseous reactant to be fed to the cell as would be in an actual chemical looping heat pump. For this

purpose, a Lytron 4105G1SB stainless steel heat exchanger was used as an evaporator. Designed for up to 1300 btu/hr cooling capacity and 150 psi it came equipped with a Mechatronics UF12A12 fan to increase airflow across the heat exchanger.



Figure 5.9: Lytron 4105G1SB heat exchanger with mounted UF12A12 fan.

5.2.6 Condenser

The accumulation vessel for the acetone after it passed through the cell needed to be cooled in order to condense any gases that may remain. Cold air blowing through a copper tube was used to drive the condensation. The tube was tightly wrapped around the accumulation vessel to ensure good thermal contact as shown in Figure 5.10. Fiberglass insulation was then wrapped around the accumulation vessel to ensure sub-ambient temperatures could be maintained.



Figure 5.10: Copper tubing and insulation used to facilitate condensation of leftover vapor.

5.2.7 Vortex Tube

An Exair 3225 vortex tube was used to generate the cold air used in the condenser. Vortex tubes are devices that use spinning vortices of air to separate a pressurized air stream into a high temperature and a low temperature stream. They are convenient devices since they require no moving parts. However, they are not as efficient as vapor compression cycles for cooling. Due to the availability of compressed air in the laboratory, the vortex tube was deemed suitable for the cooling need. The Exair 3225 can flow 25 cfm of air and provide 1700 Btu/hr of cooling.



Figure 5.11: Exair 3225 vortex tube used to drive condensation.

5.2.8 Power Supply

To drive the reaction, an electrical input was required. A TDK-Lambda ZUP6-33/U DC power supply was used to deliver power to the cell. This device had a voltage range of 0 – 6 V and a current range of 0 – 33 A. Modifications were made to the connections to increase the versatility of the power supply. An Arduino UNO microcontroller was used in conjunction with a Crydom CC1039-ND solid state relay (SSR) to allow for the delivery of pulsed voltage inputs and remote control of the voltage levels. The Arduino controlled the SSR, which could rapidly open and close the circuit leading to the electrochemical cell to generate a pulsed signal at a specified frequency up to 2500 Hz. The TDK-Lambda ZUP6-33/U could be operated manually and was also able to accept a voltage signal generated by the Arduino to set the unit's DC voltage output. A schematic of the interface is shown in Figure 5.12.

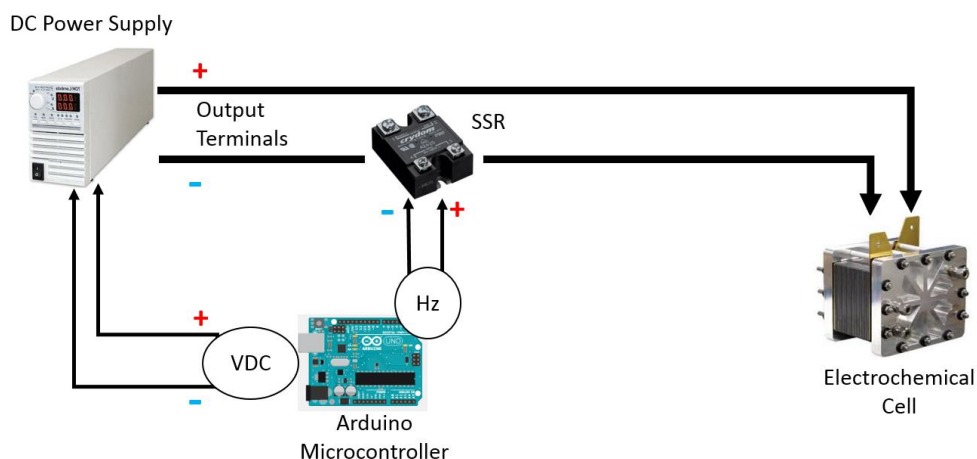


Figure 5.12: Connections and control for TDK-Lambda ZUP6-33/U power supply.

5.3 Instrumentation

The test stand was outfitted with an array of sensors to collect data on the performance of the electrochemical cell. The sensors utilized are described below.

5.3.1 Thermocouples

The performance of electrochemical cells varies with the temperature of the cell and reactants. Therefore, thermocouples were placed at various locations as indicated by Figure 5.2. The thermocouples were T-Type thermocouple probes with stainless steel sleeves and ungrounded junctions. The ungrounded junction refers to the electrical insulation of the thermocouple junction from the stainless-steel sleeve. This was done to prevent any noise that could result from unwanted electrical signals which could conduct through the rest of the structure. Ungrounded junctions do not have a temperature response as fast as that of grounded junctions, however since rapid changes in temperature were not expected, ungrounded junctions were deemed appropriate.

5.3.2 Pressure Transducers

The acetone side of the electrochemical cell operated under vacuum to allow the acetone to evaporate as would be the case in an actual chemical looping heat pump. To ensure that the acetone evaporated and to monitor the conditions of the cell, pressure transducers were installed after the evaporator and after the electrochemical cell. A Setra-205-2 pressure transducer was

placed after the evaporator and an Omega PX176-050A5V pressure transducer was placed after the cell.

5.3.3 Flow Meters

To measure the flow rates through the cell, Sensirion SLI-0430 liquid flow meters were used. This sensor utilizes a calorimetric sensing principle as shown in Figure 5.13. After introducing a negligible amount of heat to the fluid, temperature sensors were used to measure the fluid profile and thus determine the flow rate of the fluid. The isopropanol flow rate was measured after the pump and the acetone flow rate was measured before the expansion valve while the fluid was still in the liquid state.

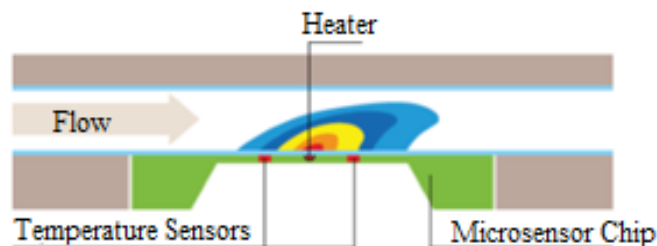


Figure 5.13: Calorimetric sensing of Sensirion SLI-0430 flow meters.

5.3.4 Current Transducer

The electrical current drawn by the cell is an important measurement for calculating the power consumption of the cell and can be used as an indicator of the rate at which the reactions are taking place. To measure the current drawn by the cell, a CR Magnetics CR5210-12 DC Hall effect current transducer was used.



Figure 5.14: CR Magnetics CR5210-12 Current transducer.

5.3.5 Concentration Sensor

After the reactions take place in the cell, it is desirable to measure the extent to which the reactant is converted to the product. A method was needed to determine the concentration of an isopropanol-acetone mixture. If isopropanol is fed into a cell as a reactant, then the concentration of acetone after the cell gives an indication of how much of the IPA reacted. A number of methods exist to determine the concentration of chemical species in a mixture. These methods include gas chromatography, refractive index measurements, boiling point evaluation, and mass spectroscopy. Ultimately a spectroscopic method was employed due to the simplicity of integrating it in line with the overall process. To accomplish this, a Kemtrak DCP007 was acquired. This device emits radiation in the UV range. At these particular wavelengths, acetone has a moderately high absorbance while IPA and water has near zero absorbance. Hence, by measuring the degree of UV absorbance through a test column, as shown in Figure 5.15, the concentration of acetone could be determined.

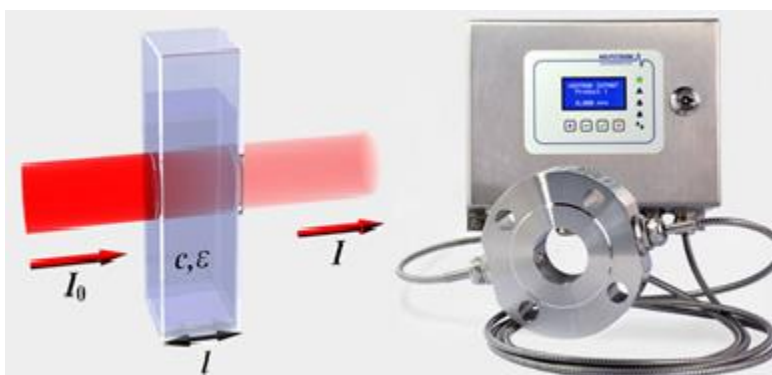


Figure 5.15: Photometric sensor used for acetone concentration detection (http://www.kemtrak.com/products_DCP007.html).

5.3.6 Data Acquisition

The signals from the various sensors were all collected by an Agilent 34970A data acquisition system. It was equipped with an Agilent 34901A 20 channel multiplexer with a built-in thermocouple reference junction. The 34901A multiplexer was capable of reading voltage signals at a rate of 60 channels/second. The 34970A was directly used to measure the voltage across the electrochemical cell. The data acquisition system was connected to a desktop

computer using a serial connection. National Instruments Labview Software was used to create a virtual environment to manage and log the data collected by the 34970A.



Figure 5.16: Agilent 34970A data acquisition system.

5.3.7 Sensor Accuracy

A degree of uncertainty is always included with any sensor measurement. A list of all the sensors and their specifications are shown in Table 5.2.

Table 5.2: Sensor specifications.

Sensor	Range	Accuracy
Flow meter (Sensirion SLI-0430)	0 – 600 $\mu\text{l}/\text{min}$	<5%
T-Type thermocouples (Omega)	-200 $^{\circ}\text{C}$ – 350 $^{\circ}\text{C}$	$\pm 1^{\circ}\text{C}$
Pressure Transducer (Setra -205-2)	0 – 1700 kPa	± 1.25 kPa
Pressure Transducer (OMEGA PX176-050A5V)	0 – 340 kPa	± 3.4 kPa
Concentration sensor (Kemtrak DCP007)	0 – 5 AU	< 0.1%
Current Transducer (CR magnetics CR5210-12)	0 – 12 A	$\pm 1\%$ FS
Voltage (Agilent 34970A)	0 – 300 V	0.004%

5.4 Sensor Calibration

The sensors will each generate a voltage or current output in response to physical stimuli. In order to accurately determine the relationship between each sensor's electrical response and the applied stimuli, the calibration of the instrumentation was performed as follows.

5.4.1 Pressure Transducer Calibration

The pressure transducers were expected to be operating under a vacuum and therefore a Supco VG64 vacuum gauge was used to calibrate the sensors. A vacuum pump was used to reduce the pressure along a common line shared by the pressure transducers and the Supco VG64. The voltage readout of the pressure transducers was recorded and correlated to the pressure reading of the Supco VG64. Pressure values above ambient were included in the calibration through the use of pressurized nitrogen and an Omega PCL-1B pressure calibration tool as a reference for pressure values. Calibration results are provided in Figures 5.17 and 5.18.

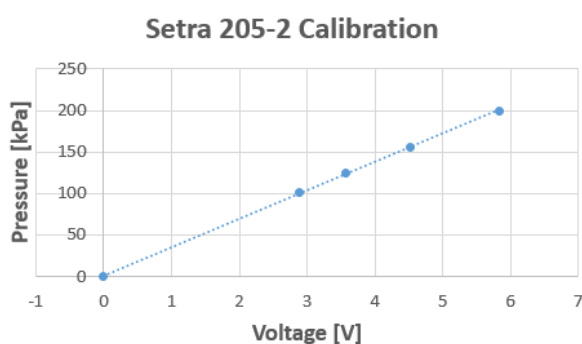


Figure 5.17: Setra 205-2 calibration results.

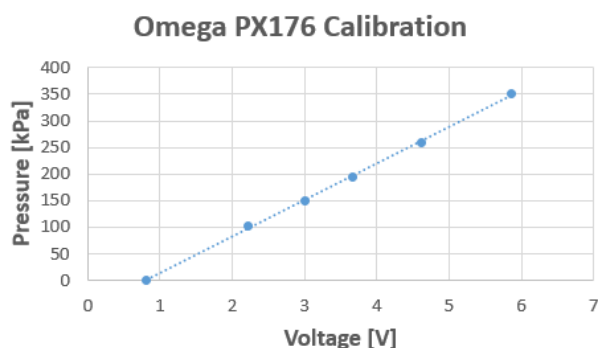


Figure 5.18: Omega PX176 calibration results.

5.4.2 Thermocouple Calibration

The thermocouples were calibrated with the aid of an Omega CL122 Calibration Cool/Heat Source. The thermocouples were placed into the CL122 and the CL122 was set to a desired temperature. The thermocouple readings could be directly converted to a temperature using native functions of the Agilent 34970A data acquisition system. The temperature readings from the thermocouples were compared to that of the CL122 and a corrective correlation was applied to adjust the thermocouple readings to be in line with those of the CL122. Calibration results are shown in Figures 5.19 and 5.20 for different temperature ranges.

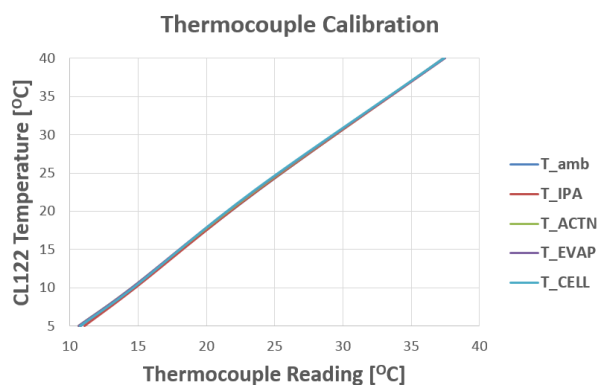


Figure 5.19: Thermocouple calibration results.

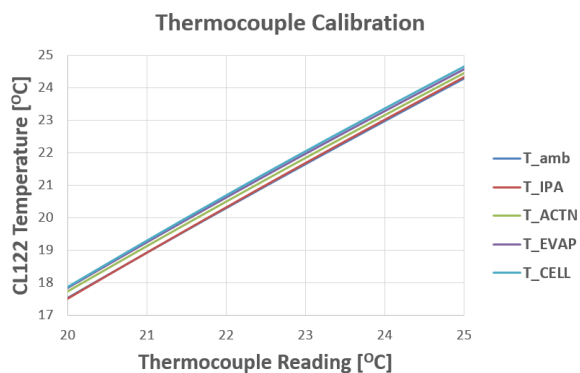


Figure 5.20: Thermocouple calibration results over selected temperature range.

5.4.3 Flow Meter Calibration

Two flow meters were calibrated separately for acetone and isopropanol. The peristaltic pump was used to pump fluid at a fixed RPM through the flow meter. The fluid was then collected in a flask which was weighed to determine the mass of the fluid. The total time that the fluid was being pumped into the flask was recorded. The total mass flow rate was then determined by dividing the final mass of liquid pumped by the time required for the pumping. Since the sensirion SLI-0430 is a volumetric flow meter, the mass flow rate was converted to a volumetric flow rate using the density of the isopropanol and acetone. The calibration setup is shown below in Figure 5.21 with calibration results shown in Figures 5.22 and 5.23.



Figure 5.21: Calibration setup for liquid flow meters.

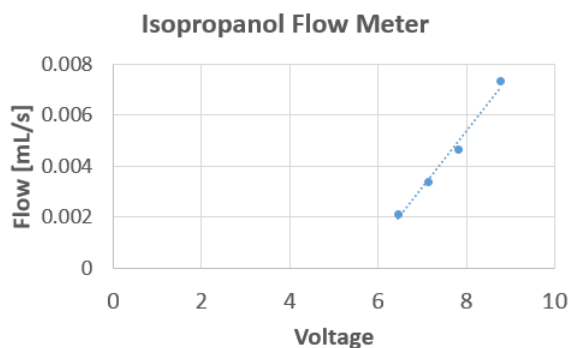


Figure 5.22: Calibration results for isopropanol flow meter.

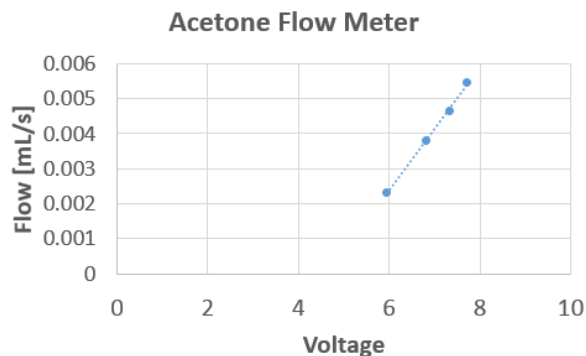


Figure 5.23: Calibration results for acetone flow meter.

5.4.4 Current Transducer Calibration

The CR Magnetics CR5210-12 current transducer was designed to measure DC currents from 0 - 12 amps and correlate current to a 0 - 5 VDC output signal. To calibrate this sensor, the TDK-Lambda ZUP6-33/U power supply was connected in series with a 0.5Ω resistance and a Klein Tools MM1000 multimeter. The TDK-Lambda ZUP6-33/U voltage was increased to impose different currents throughout the series. These currents were measured with the MM1000 then correlated to the CR5210-12 voltage output as shown in Figure 5.24.

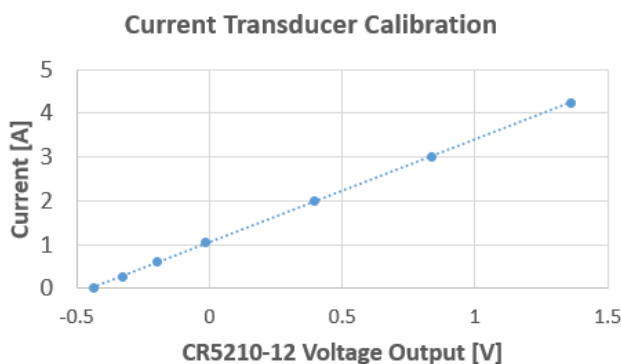


Figure 5.24: Current transducer calibration results.

5.4.5 Photometric Sensor Calibration

The photometric sensor was calibrated by feeding known concentrations of isopropanol-acetone mixtures through the concentration cell and then measuring the absorbance. The concentration

cell was mounted horizontally on the stand during this process. The mixture concentrations were prepared on a mass basis using a scale. The milliamp output of the photometric sensor was set so that 0 AU would correspond to 4 mA and 0.85 AU would correspond to 20 mA. The concentrations were then correlated to the absorbance readings. Two sets of correlations were developed as shown in Figures 5.25 and 5.26: one for low concentrations below 20% acetone by mass and one for high concentrations above 20%. A 324.5Ω resistor was placed across the terminals of the data acquisition port receiving the milliamp signal. Through converting the absorbance to a milliamp signal to a voltage signal, the values of the concentration could be determined.

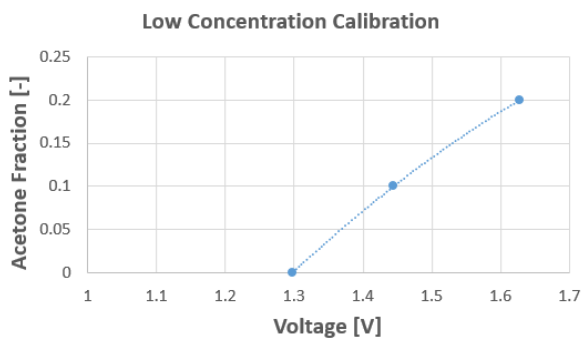


Figure 5.25: Calibration results for concentration sensor at low concentration.

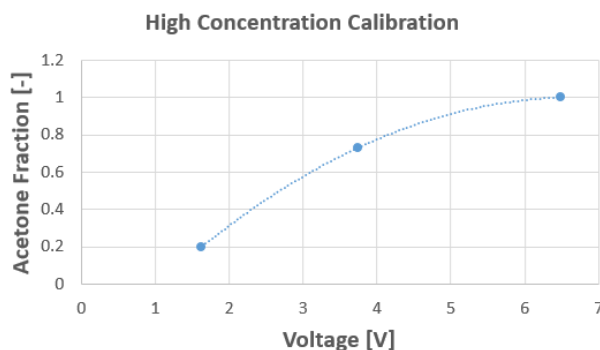


Figure 5.26: Calibration results for concentration sensor at high concentrations.

5.5 Flammability Concerns

The use of flammable fluids, such as isopropanol and acetone, necessitated the implementation of additional safety measures to ensure safe operation of the test stand. These safety measures are outlined in Table 5.3.

Table 5.3: Flammability Precautions.

Safety Measure	Purpose
Limit flammable substance volume	The Occupational Health and Safety Administration has published exposure limits of ~400 ppm for isopropanol and acetone. Given the volume of the room housing the test stand the maximum amount of fluid permissible can be determined assuming that all of the fluid leaks and evaporates.
Blow air over test stand	Like most flammable vapors acetone and isopropanol need to build up a sufficiently high concentration before the vapor-air mixture becomes combustible. By circulating air over the apparatus the likelihood of a flammable mixture accumulating is reduced.
Handheld leak detector	A handheld detector was obtained which can allow for the examination of various component of the test stand to identify any leaks before operation.
Auto shut-off leak detector	A leak detector with an integrated relay was used to shut off the main high voltage devices on the test rig. In the event a leak is detected the devices that have the highest likelihood of creating a spark and igniting the vapors are shut down.

5.6 Operating Procedures

The test stand was designed for simple operation to allow for the rapid evaluation of cell performance. An overview of the typical operating procedure is provided below.

1. Isopropanol and acetone are charged into the supply vessels
2. Vacuum pump is used to pull vacuum on acetone side of electrochemical cell
3. Vortex tube activated to begin cooling acetone collection vessel
4. Temperature controller used to set electrochemical cell temperature
5. Isopropanol flow rate set by adjusting pump speed
6. Acetone flow rate set by adjusting expansion valve opening position
7. Power supply used to apply DC voltage across cell terminals
8. Allow system to run till steady state achieved

5.7 Data Reduction

Certain parameters used for analyzing the system were not directly measured and needed to be derived. They were calculated from the available measurement data, fluid thermophysical and chemical properties, and electrochemistry principles.

Acetone and isopropanol have a stoichiometric molar ratio of one during hydrogenation and dehydrogenation reactions. Therefore, it was desirable to control the molar flow rates of the two fluids to be approximately equal during operation of the test stand. Since only the volume flow rate were directly measured, the molar flow rates needed to be determined according to Equations 5.1 – 5.6.

$$\rho_{IPA} = f(T, P) \quad (5.1)$$

$$\rho_{ACTN} = f(T, P) \quad (5.2)$$

$$\dot{m}_{IPA} = \dot{v}_{IPA} \cdot \rho_{IPA} \quad (5.3)$$

$$\dot{m}_{ACTN} = \dot{v}_{ACTN} \cdot \rho_{ACTN} \quad (5.4)$$

$$\dot{n}_{IPA} = \frac{\dot{m}_{IPA}}{M(IPA)} \quad (5.5)$$

$$\dot{n}_{ACTN} = \frac{\dot{m}_{ACTN}}{M(ACTN)} \quad (5.6)$$

Determining the voltage efficiency with which the electrochemical cell can perform the bilateral hydrogenation/dehydrogenation reactions with isopropanol and acetone was the primary objective of the test stand. To do this, the reversible voltage required to drive the reaction was calculated as in Equation 4.14. Then the ratio of the reversible voltage to the measured voltage was used to define the voltage efficiency as in Equation 5.7.

$$\eta_V = \frac{V^o}{V_{meas}} \quad (5.7)$$

CHAPTER 6. 1ST GENERATION CELL EXPERIMENTATION

After completing construction of the experimental test stand, an experimental campaign was undertaken to evaluate the performance of the electrochemical cell under the isopropanol-acetone chemical looping heat pump conditions. For the first phase of testing, standard off-the-shelf MEAs were obtained from ElectroChem Inc., which were designed for use in conventional hydrogen-oxygen fuel cells. The properties of these MEAs are shown in Table 6.1.

Table 6.1: Membrane electrode assemblies used for first phase of testing.

Designation	Membrane Material	Catalyst	Catalyst Loading
FC100-MEA-A	Nafion 117	30% wt. Pt/Ru on Carbon	1 mg/cm ²
FC100-MEA-B	Nafion 117	30% wt. Pt/Ru on Carbon	2 mg/cm ²
FC100-MEA-C	Nafion 117	30% wt. Pt/Ru on Carbon	4 mg/cm ²

6.1 Initial Testing

Many challenges were faced at the onset of the testing. For the initial test, no appreciable current was detected in the expected voltage range. Upon consulting with the electrochemical cell vendor, it was discovered that the labeling of the anodes and cathodes were mistakenly inverted. Rather than dehydrogenating the IPA and hydrogenating the acetone, the cell was attempting to dehydrogenate the acetone and additionally hydrogenate the IPA. To solve this, the connections between the power supply and the cell were simply inverted. In addition, the isopropanol was also fed as a solution with water. This was because the Nafion membrane required some degree of hydration for proton conductivity. Even though such mixtures with water would be detrimental to the performance of a CLHP cycle, they were utilized here to aid in the initial cell testing. After making these changes, some preliminary results of the current-voltage relationship of the cell were obtained as shown in Figure 6.1 for different isopropanol feed concentrations. These results show that reactions were indeed progressing within the cell.

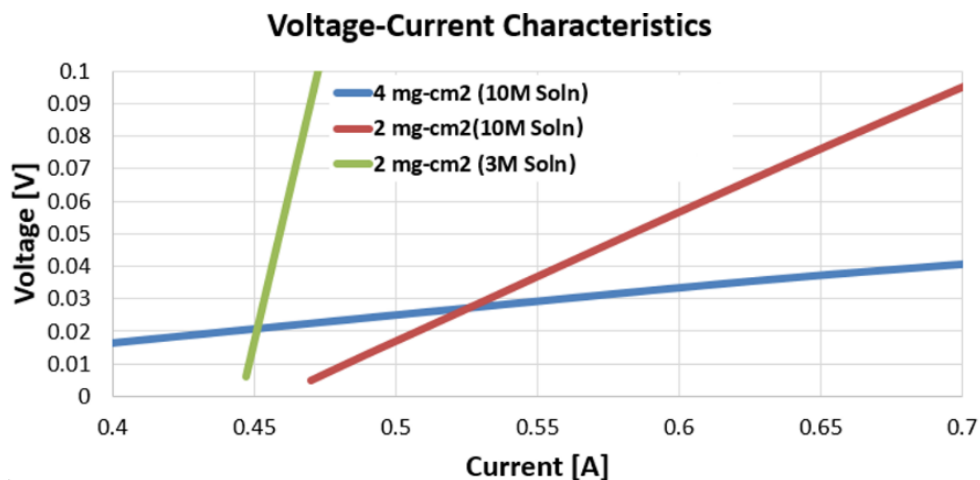


Figure 6.1: Voltage current relationship from standard MEA testing.

Though it was possible to obtain some results, the testing faced another obstacle. While testing, the flow of reactants to the cell started out constant and then eventually reduced to zero. Even as the IPA pump speed was increased, the flow could not be maintained. After examining the cell, it was discovered that the flow channels were being blocked by the membrane and the carbon sheets that comprised the cell electrodes. This blockage is shown in Figure 6.2. This made it impossible to conduct long term tests with a single membrane.



Figure 6.2: Blockage of flow channels by carbon electrodes.

The reason for the blockage was unknown. Ultimately, it was theorized that this was due to either physical or chemical interactions. The membrane was fairly thin at ~100 microns. Since a vacuum needed to be applied to the cell to simulate the conditions of a potential CLHP, the stress applied on the membrane from the vacuum was seen as a possible reason for the channel

blockage. Essentially, application of the vacuum over time may have led to the membrane and in turn the electrodes protruding into the flow channels and inhibiting the flow.

Another cause for the blockage could be due to chemical incompatibility between the MEA and the working fluids. Should the working fluids somehow compromise the membrane it could be possible for the electrodes to become lodged in the flow channels. From looking through the literature, it was found that the conventional Nafion membranes are prone to swelling when used in conjunction with alcohol fuel cells. This phenomenon could become exaggerated as the alcohol concentration increases. This was later confirmed through observations of the tested membranes. As seen in Figure 6.3, after operation for a period of time the membrane became engorged and the electrodes were detached from the surface. Finding methods to prevent this channel blockage would be absolutely necessary for the viability of the CLHP using PEM electrochemical cells.



Figure 6.3: Swollen membrane after operating cell using alcohol.

6.2 Test Stand Modifications

Two approaches were taken to address the issue of the membrane obstructing the flow channels due to swelling. The first was to design flow fields with narrower flow channels. This was done with the hopes that smaller flow channels would provide greater resistance to the membrane flowing into the channels. The second approach involved searching for a proton conductive membrane material that would not swell when in the presence of isopropanol and acetone.

The original flow fields provided from ElectroChem Inc. were constructed out of graphite and utilized flow channels that were 1/8" and 1/32". These flow fields are shown in Figures 6.4 and 6.5. The blockage was primarily observed within the 1/8" channels.



Figure 6.4: ElectroChem Inc. flow field with 1/8" channels.



Figure 6.5: ElectroChem Inc. flow field with 1/32" channels.

A number of options were investigated for the manufacturing of alternative flow fields. ElectroChem Inc. offered to supply new flow fields at ~\$800 per plate. It would be desirable to test multiple flow field configurations, and so a lower cost option was desired. Another avenue investigated was Purdue's Research Machining Services. This facility houses a number of machines and a skilled staff. After consultation with the staff, a quote of ~\$750 for the manufacture of a flow field was obtained. This also seemed rather high if future goals would be to test multiple flow fields.

In addition to the Research Machining Services, Purdue has machining services available for student use on research, class, or personal projects. One of these facilities, Purdue's Artisan Fabrication Lab allowed the use of their machines to manufacture two flow fields. To accomplish this, the flow fields were first modeled in CAD. From here, CAM software was used to generate the machining instruction. Finally, a CNC mill was utilized to machine the flow fields into aluminum plates, Figures 6.6 and 6.7.

Aluminum was chosen due to its low cost and relative ease of machining. Graphite is typically used for fuel cell flow fields due to its chemical inertness. However, due to its high cost and being brittle, it is not amenable to high volume machining as described by Karimi et al. (2012).

Much research has been carried out looking into metallic flow fields as a replacement to graphite. Metals are typically more susceptible to corrosion. In the case of aluminum in standard PEM fuel cells, an oxide layer can form over the metal, which can increase the resistance within the cell. Although the cell resistance may increase through the use of aluminum, the fact that a metal such as this may ultimately be used in a mass production product led us to deem this a suitable choice for a flow field material.

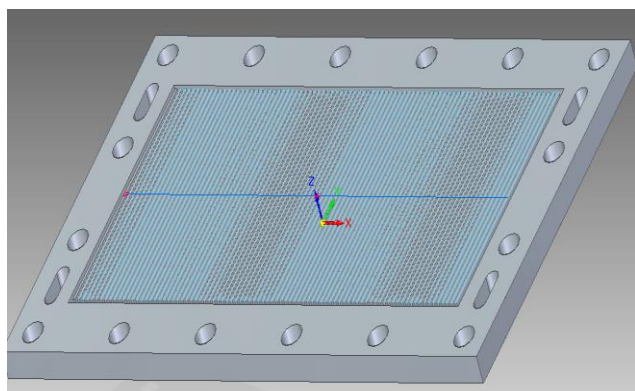


Figure 6.6: CAD file of custom fuel cell flow field.



Figure 6.7: CNC machining of custom flow fields.

Two aluminum flow fields were manufactured. Both fields consisted of $1/32$ " wide channels with 0.04 " depths. One was manufactured with parallel vertical channels and the other was designed with a serpentine flow arrangement. These are shown in Figures 6.8 and 6.9.

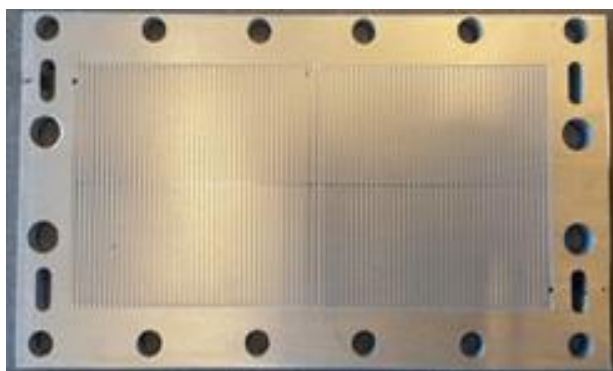


Figure 6.8: Custom flow field with $1/32$ " vertical channels.



Figure 6.9: Custom flow field with $1/32$ " serpentine channel.

The second approach to address the channel blockage was to find a membrane material that would not swell as much in the presence of isopropanol. From searching through the literature, Nafion membranes were found to be the primary choice for use with alcohol based fuel cells. Typically, these types of fuel cells utilize dilute solutions of alcohol and water. This may in turn minimize the effect of swelling on the membrane. A study was found where pure isopropanol was used in a PEM fuel cell Qi et al. (2003). Rather than Nafion, the investigators utilized a sulfonated polyether ether ketone (sPEEK) membrane. They were able to obtain moderate ion conductivity and noted that the membrane swelled much less than Nafion.

Membranes made of sPEEK were obtained from FUMATECH. This material was provided to ElectroChem Inc., which then created membrane electrode assemblies to fit the 100 cm² cell hardware. To maximize the ion conductivity of the membrane, a pre-treatment step consisting of sulfuric acid treatment could be applied to the membrane. However, this was not compatible with ElectroChem Inc.'s manufacturing process. Hence, the pre-treatment was skipped and the sPEEK membranes were used as is.

The electrochemical cell was then re-assembled using the modified flow fields and sPEEK membranes. After a period of operation, the cell was taken apart to inspect the membrane and the channels. Unlike before, the membrane was not deformed due to swelling and the carbon electrodes were not obstructing the flow channels. The sPEEK MEA after operation is shown in Figure 6.10. Contrasting this to the Nafion MEA in Figure 6.3, it was clear that the sPEEK MEA was more compatible with this particular application.



Figure 6.10: SPEEK membrane after operation in alcohol electrochemical cell.

6.3 Additional Testing

Using the modified flow fields and MEAs, another round of testing was commenced. The properties of the custom MEAs obtained from ElectroChem Inc. are shown in Table 6.2. A Nafion membrane was included because ElectroChem Inc. ran out of the provided SPEEK membrane material.

Table 6.2: Membrane electrode assemblies used for testing after equipment modifications.

Designation	Membrane Material	Catalyst	Catalyst Loading
EC-MEA-Custom A	50 μm SPEEK	30% wt. Pt/Ru on Carbon	2 mg/cm^2
EC-MEA-Custom B	50 μm SPEEK	30% wt. Pt/Ru on Carbon	4 mg/cm^2
EC-MEA-Custom C	Nafion 212	80% wt. Cu on Carbon	10 mg/cm^2

For this stage of testing, the operating procedure was modified. Previously, the applied cell voltage was held constant with the goal of observing the conversion rate after the cell achieved steady state operation. However, due to the low currents observed and therefore, slow reaction speeds, performing tests in this manner would be time consuming and would not readily provide the information needed to model cell characteristics and compare different cell parameters. Instead, a voltage sweep approach was utilized. Applied throughout fuel cell research, a voltage sweep involves varying the voltage across the electrodes in a linear manner. This way, the current-voltage relationship can be rapidly determined for a given cell operating condition.

The results of the voltage sweeps are shown in Figures 6.11 – 6.12. Figure 6.11 displays voltage current relationship of EC-MEA-Custom A. To hydrate the membrane, the isopropanol was fed as a 10 molar solution. In general, as the cell temperature increased, the cell current and hence the rate of the reaction increased for a particular applied voltage. Using the reversible voltage from Equation 4.14 as a reference and converting the measured current to a mass flow rate of converted reactant, Equation 4.5, the voltage efficiency vs. the mass flow of useful refrigerant from the cell was derived with results shown in Figure 6.12.

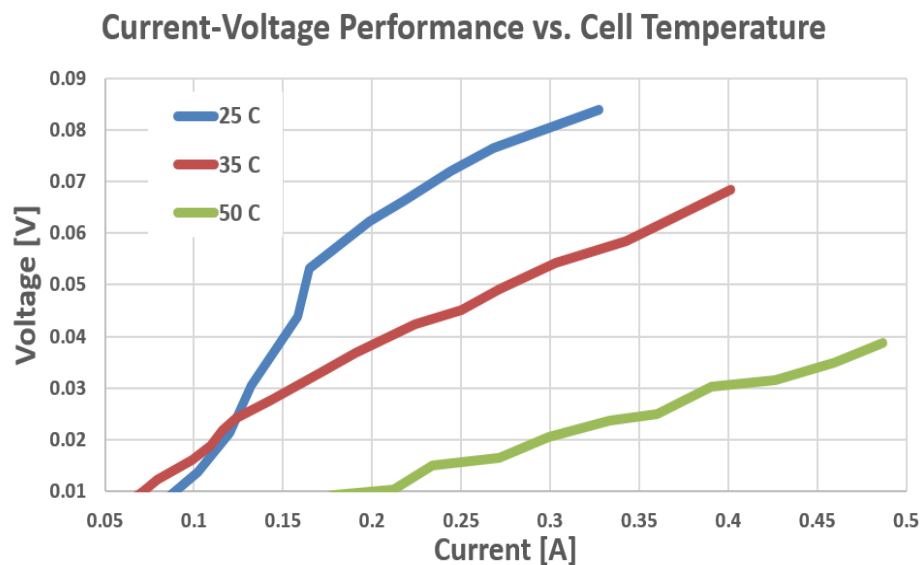


Figure 6.11: Voltage current relationship of EC-MEA-Custom-A.

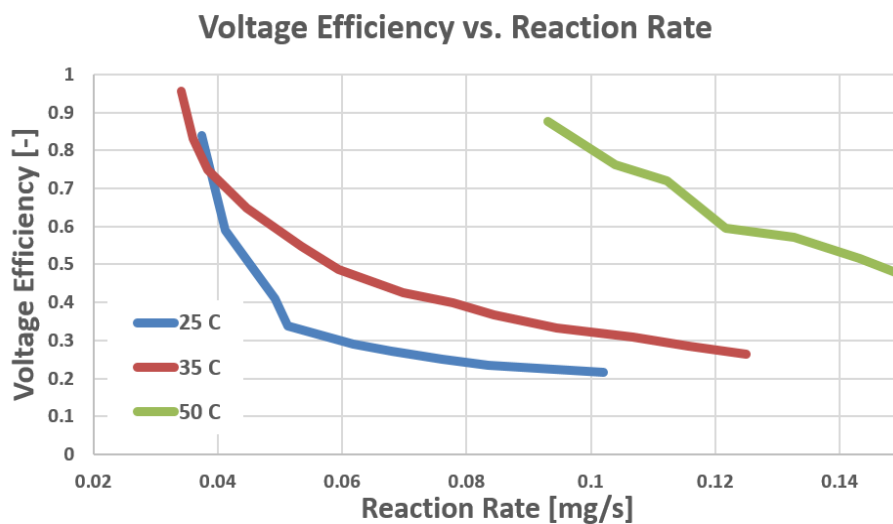


Figure 6.12: Reaction rate vs. voltage efficiency for EC-MEA-Custom-A.

The results of EC-MEA-Custom-B testing are shown in Figure 6.13 and 6.14. Similar to EC-MEA-Custom-A, the reaction rate at a particular applied voltage increased for higher cell temperatures.

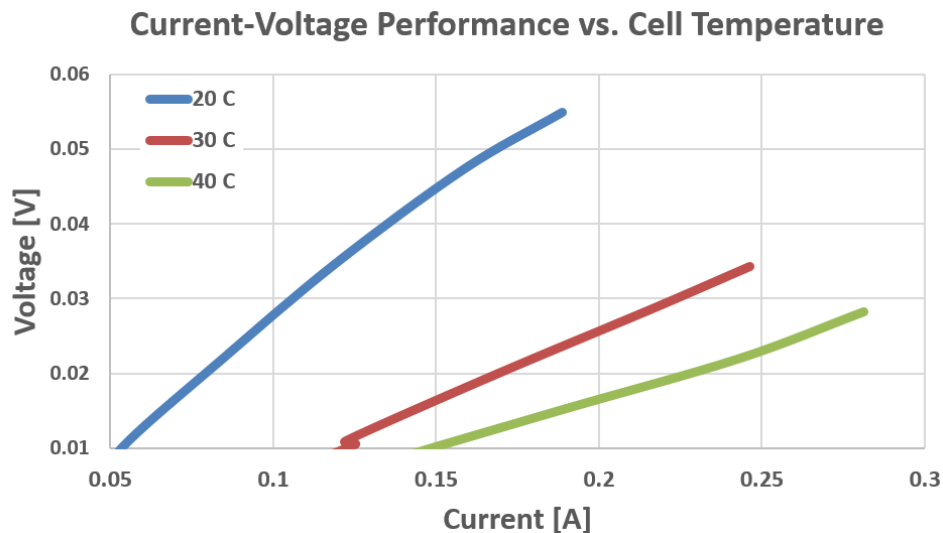


Figure 6.13: Voltage current relationship of EC-MEA-Custom-B.

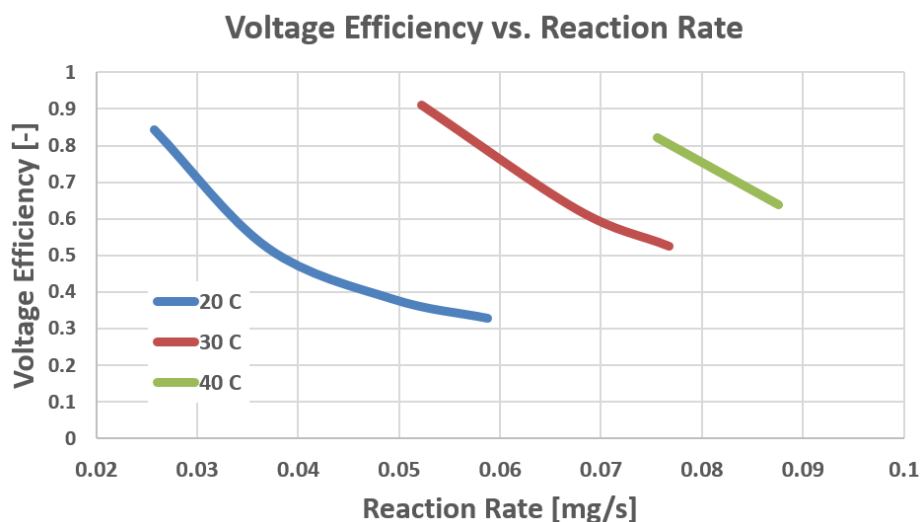


Figure 6.14: Reaction rate vs. voltage efficiency for EC-MEA-Custom-B.

Although platinum is the most popular fuel cell catalyst, thermal isopropanol dehydrogenation has been performed with other catalysts such as nickel and copper (Xin et al. 2014, Setzler et al. 2012). Using less precious metals may ultimately lead to the creation of less expensive electrochemical cells. To this end, a membrane using copper as a catalyst at a loading of 10 mg/cm² and using Nafion 212 as a membrane was tested. Since Nafion was used as the membrane material, the testing could only be performed up until the membrane swelling caused

problems. The result of the current voltage relationship is shown in Figure 6.16. The performance of the copper catalyst was notably lower than that of the platinum-based catalyst.

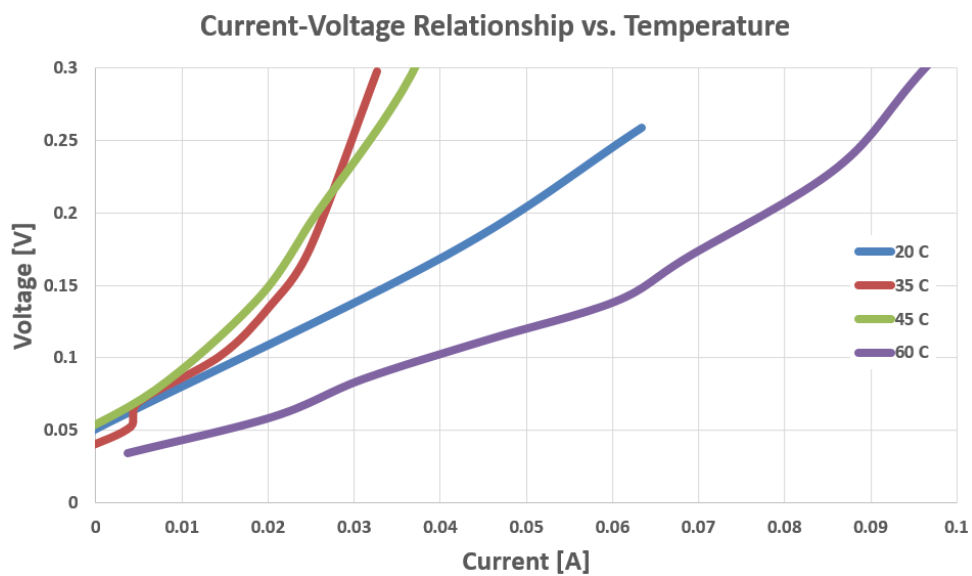


Figure 6.15: Voltage current relationship of EC-MEA-Custom-C.

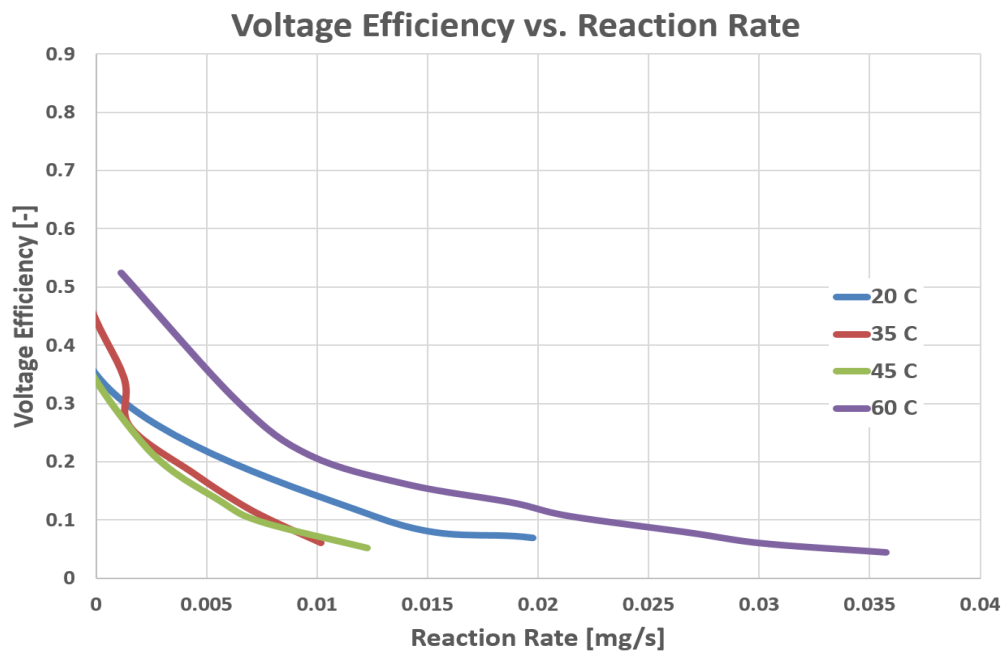


Figure 6.16: Reaction rate vs. voltage efficiency for EC-MEA-Custom-C.

The results of these tests led to two important conclusions. The first was that it was possible to perform the hydrogenation/dehydrogenation reactions needed for an electrochemically driven CLHP using isopropanol and acetone as working fluids. The second was that the reactions proceeded at what appeared to be a slow rate. To increase the rates of the reactions in the cell, an optimization effort would be needed to see just how far the reaction rates of the isopropanol-acetone reactions could be pushed.

6.4 References

Karimi, S., Fraser, N., Roberts, B., Foulkers, F., 2012. A Review of Metallic Bipolar Plates for Proton Exchange Membrane Fuel Cells - Materials and Fabrication Methods, *Advances in Materials Science and Engineering*, vol.2012

Setzler, B., Al-Ansary, H., 2012, Further Development of the Isopropanol-Acetone Chemical Heat Engine. World Renewable Energy Forum, 41st American Solar Energy Society Annual Conference, Denver, CO.

Toyota Motor Sales, U.S.A., Inc, 2016. 2016 Toyota Mirai Fuel Cell Sedan Production Information. <https://pressroom.toyota.com/releases/2016+toyota+mirai+fuel+cell+product.htm>

Qi, Z., Kaufman, A., 2003. Liquid-feed direct oxidation fuel cells using neat 2-propanol as fuel, *Journal of Power Sources*, vol.118, p.54-60

Xin, F., Xu, M., Huai, X., Li, X., 2014. Characteristic and kinetic of liquid-phase isopropanol dehydrogenation over Raney nickel catalysts for chemical heat pump. *Applied thermal Engineering*, vol. 70, p.580-585

CHAPTER 7. CUSTOM CELL FABRICATION

The first-generation electrochemical cell testing primarily utilized off the shelf components prepared by vendors. The results revealed that a great deal of improvement to the reaction rate would be needed if the CLHP were to ever utilize a reactor of a reasonable size. The reactions take place at the membrane electrode assembly within the cell. There are multiple parameters that can be changed in order to influence the performance of the MEA. In order to have tighter control over these factors and to develop MEAs at lower cost, in-house means of manufacturing the MEAs needed to be developed, and the test stand needed to be modified.

7.1 New Cell Hardware

The cell hardware used in the 1st generation testing had an active area of 100 cm². This large area allowed for greater resolution between state points because higher currents were produced and could be measured with greater accuracy. Though good for data acquisition, this large area was undesirable from a material cost perspective. A larger area meant that more materials would need to be input into the manufacturing process. To reduce material cost while still maintaining sufficient active area for reliable measurements, a cell fixture with 20 cm² active area was constructed.

The first attempt at reducing the cell's active area was to solely modify the flow fields such that the reactants would primarily flow over an area of 20 cm². This would allow for the reuse of the other cell components without having to make any modifications to any interconnects between the test stand components. As shown in Figure 7.1, feeder grooves were cut into a plate of the same size as the flow plates used in the 100 cm² cell. The main feeder plates flow over a central area measuring 4 cm x 5 cm. To make sure that reactant only interacted with the MEA in the 20 cm² target region, a fitted gasket was laser cut and placed over the flow plate, Figures 7.2 and 7.3.



Figure 7.1: Flow fields with 20 cm² active area.

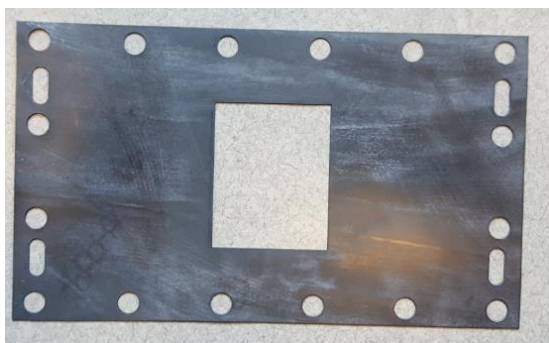


Figure 7.2: Laser cut EPDM gasket.

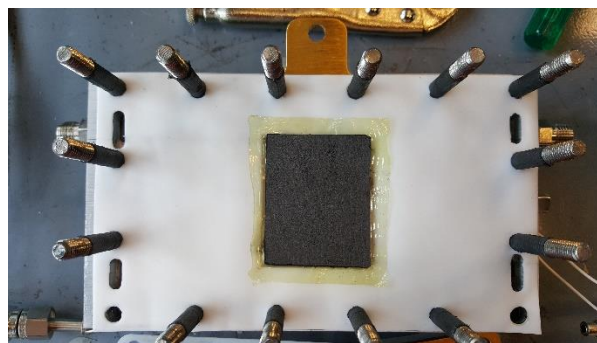


Figure 7.3: Gasket fitted to expose 20 cm² active area.

The use of the new flow fields with the previous cell hardware was appealing, but the sealing provided by the gasket fitted over the active area in the center was inadequate, Figure 7.4. With the installation of the new plates, the system could not maintain a seal between the interior and the ambient. This was particularly troublesome since part of the cell needed to operate under vacuum pressures. Various manufacturing and polishing methods were used to improve the finish of the plates, however the leak persisted. The reuse of the 100 cm² cell hardware was abandoned to create a cell fixture better sized for the 20 cm² active area.

measurements, flow plates were remanufactured out of graphite plates. Laser etching of graphite was found to be a novel means of machining intricate patterns into a graphite plate. To see if this would be amenable to the flow field manufacture for our cell, the laser etching facilities at Purdue's Bechtel Innovation Design Center were used to etch into the plate. Unfortunately, the strengths of the lasers at the center were insufficient to significantly cut into the plates. They were, however, able to make clearly visible patterns which were then machined down with a mill to depths of 0.040", Figure 7.6.

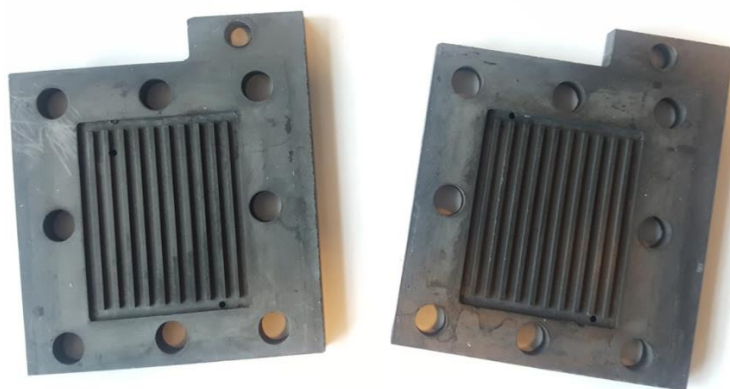


Figure 7.6: Machined graphite flow plates.

7.2 MEA Fabrication

Literature on fuel cell development and testing was explored to determine common practices for creating membrane electrode assemblies. The development of MEAs for electrochemical cells typically follows four main steps (Frey et al. 2004, Lakshmanan et al. 2003).

1. Membrane Treatment
2. Catalyst Ink Preparation
3. Catalyst Ink Dispersion
4. Electrode-Membrane Lamination

The treatment of the membrane is an important step to maximize the ion transfer through the material. When ordering membranes for fuel cell applications, the membranes were typically delivered in a deactivated form. Membrane materials such as Nafion can conduct protons due to the presence of sulfonic ion groups. By boiling the membrane material in a sulfuric acid solution, the membrane becomes protonated and the ion conductivity increases, Lakshmanan et al. (2003).

SPEEK membranes obtained from FUMATECH were given a similar recipe for protonation. We utilized a chemical fume hood at the Herrick Labs and appropriate PPE to ensure the safe handling and boiling of the sulfuric acid.

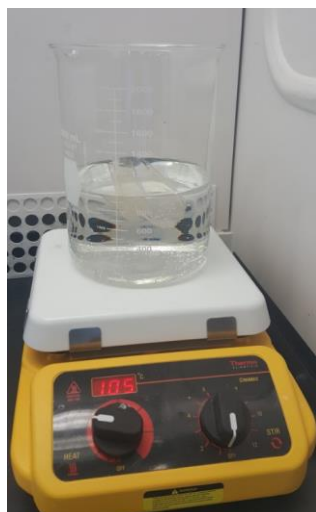


Figure 7.7: Boiling membrane in 1M sulfuric acid.

The next stage in MEA fabrication was the creation of a catalyst ink. The catalyst layer is a complex interface where reactants, ions, and electrons need to simultaneously exist. The creation and then application of the catalyst ink should be done in a manner such as to allow for the seamless linkage of electrode, membrane and catalyst.

The catalyst ink was created by weighing out a designated amount of catalyst powder. The powder was then mixed with 1-part distilled water followed by 2-parts isopropanol in a $\frac{3}{4}$ oz glass jar. An ionomer solution was then added to the mixture. We utilized a 5% by mass Nafion ionomer solution obtained by FuelCellStore.com. The Nafion in the solution would allow for the conduction of protons at the catalyst interface. Then isopropanol was added to serve as a dispersant.

To create a homogenous ink, the slurry needed to be mixed. First, the mixture in the jar was manually stirred using a glass rod and the mixture was ultrasonically mixed. This was done by placing vials of the ink solution in to a Sper Scientific 100004 Ultrasonic Cleaner for 1 hr. Images of the ink before and after mixing are shown in Figure 7.8 and 7.9.

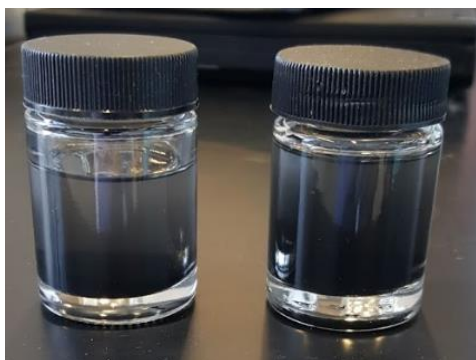


Figure 7.8: Catalyst ink before sonication.



Figure 7.9: Catalyst ink after sonication.

Once the catalyst ink was prepared, it then needed to be applied to a substrate. Many researchers apply the catalyst using either a scalpel to spread the catalyst solution over a region (Park et al. 2010), or by spraying the catalyst mixture with an airbrush over a desired area (Dreyer et al. 2011, Zheng et al. 2012). In this work, the catalyst ink was applied using an airbrush directly to the membrane. A stencil was used to ensure that the catalyst was only deposited in the desired area, Figure 7.10. The spraying took place over a hot plate at low heat to accelerate the drying of the catalyst on the substrate.

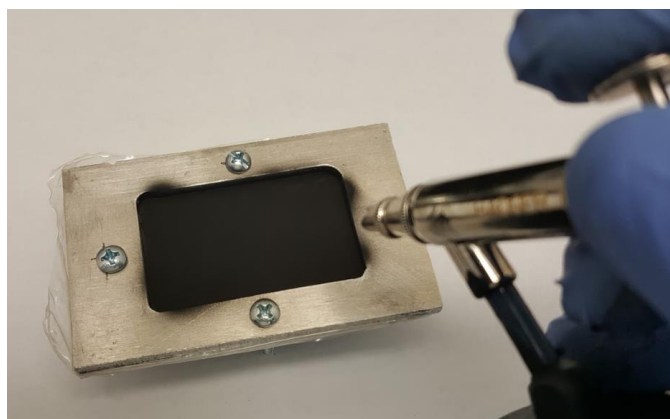


Figure 7.10: Catalyst spray application on membrane in area outlined by metal stencil.

After the catalyst layers were applied to the membrane, the entire assembly needed to be compressed together to ensure good contact between the layers. This was done through a process called hot pressing. Carbon sheets are placed over the catalyst coated electroactive area on each side of the membrane. The sheets serve as diffusion layers for the reactants as well as help

provide mechanical support to the membrane. The temperature and pressure of the hot-pressing process can have a great influence on the conductivity through the cell layers and are parameters that can be optimized for a manufacturing process. For this study, the temperature and pressure of the hot press were set to 130 °C and 1,000 psi, respectively, to correspond to values found in literature (Therdthianwong et al. 2007, Lakshmanan et al. 2003, Xing et al. 2005, Yang et al. 2003). To mount the MEA into the cell fixture, holes needed to be cut into the membrane to aid in alignment and allow the bolts to pass through the whole assembly. Different methods were investigated to perform this step, including laser cutting the patterns, Figure 7.11. With the adoption of sturdier membrane materials, the alignment patterns were ultimately cut out with a blade using a stencil. An example of an in-house fabricated membrane electrode assembly is shown in Figure 7.12.

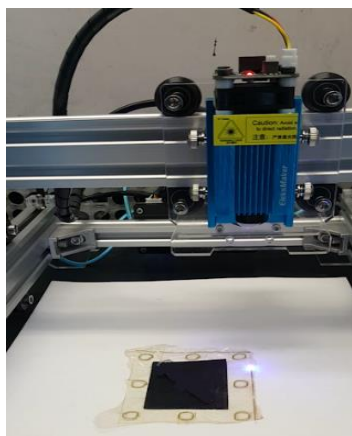


Figure 7.11: Laser cutting mounting pattern into membrane electrode assembly.



Figure 7.12: In-house manufactured membrane electrode assembly after hot-pressing.

The membrane electrode assemblies were typically fabricated in batches of three at a time. With the refinement of in-house fabrication methods, and the custom 20 cm² cell fixture, control over many of the critical aspects of cell manufacturing for PEM reactors could be easily controlled. Using these capabilities, a search for more suitable material input to the cell was commenced.

7.3 References

- Dreyer, H., 2011. A comparison of catalyst application techniques for membrane electrode assemblies in SO₂ depolarized electrolyzers. Ph.D. Thesis, North-West University. Potchefstroom, South Africa.
- Frey, T., Linardi, M., 2004. Effects of membrane electrode assembly preparation on the polymer electrolyte membrane fuel cell performance. *Electrochimica Acta*, vol.50 p.99-105
- Lakshmanan, B., Huang, W., Olmijer, D., 2003. Polyetheretherketone Membranes for Elevated Temperature PEMFCs. *Electrochemical and Solid-State Letters*, vol.6, p. A282-A285
- Park, I., Li, W., Manthiram, A., 2010. Fabrication of catalyst-coated membrane-electrode assemblies by doctor blade method and their performance in fuel cells. *Journal of Power Sources*, vol. 195, p.7078-7082.
- Therdthianwong, A., Manomayidthikar, P., Therdthianwon, S., 2007. Investigation of membrane electrode assembly (MEA) hot-pressing parameters for proton exchange membrane fuel cell. *Energy*, vol. 32, p. 2401-2411
- Xing, D., Yi, B., Fu, Y., Zhang, H., 2005. Characterization of Sulfonated Poly(Ether Ether Ketone) /Polytetrafluoroethylene Composite Membranes for Fuel Cell Applications. *Fuel Cells* vol. 5, p.406-411
- Yang, B., Manthiram, A., 2003. Sulfonated Poly(ether ether ketone) Membranes for Direct Methanol Fuel Cells. *Electrochemical and Solid-State Letters*, vol. 6, p.A229-A231
- Zheng, W., Suominen, A., Tuominen, 2012. Discussion on the Challenges of DMFC Catalyst Loading Process for Mass Production. *Energy Procedia*, vol. 28, p. 78-87.

CHAPTER 8. IONOMER AND MEMBRANE SELECTION

With the development of the capability to manufacture membrane electrode assemblies in-house, a more detailed study into how the components of the cell affect the overall performance could be undertaken. The majority of the irreversibilities that occur within these types of electrochemical cells are typically ohmic losses due to resistance to proton transport and activation losses in the catalyst layer (Benziger et al. 2006). Proton transport begins at the 3-phase interface in the catalyst layer. Here, electrons, protons, and reacting species all need to be transported to and from the reaction sites. Protons migrate through ionomer material similar to that in the membrane. Once they reach the bulk membrane phase they are transferred to the other side of the cell. A representation of the catalyst layer membrane interface is shown in Figure 8.1. The construction of the catalyst layer and the material chosen for the membrane have significant impacts on the resistance to mass and charge transfer throughout the cell.

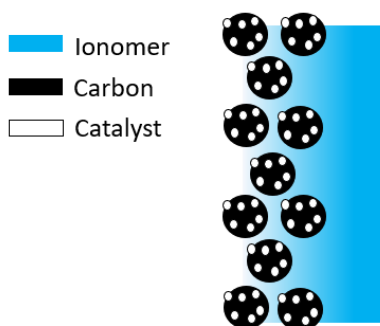


Figure 8.1: Interface of catalyst layer and membrane.

8.1 Ionomer Content

The catalyst layer is a porous region. As stated previously, the catalyst ink is first prepared as a mixture of catalyst powders, proton conducting ionomer, and dispersant for spraying. Nafion was used as the ionomer solution. Even though compatibility issues were found between Nafion and the CLHP working fluids, it was the only ionomer solution readily available at this stage in the testing. Each component in the catalyst ink was measured out and the solution was mixed in a set ratio. Changes to the proportion of any of these constituents could affect the structure and the function of the catalyst layer. The pores provided paths for reactant transfer, the carbon

transmitted electrons, the ionomer transmitted protons, and the catalyst facilitated the reaction. The proportions of each component must be balanced to allow for the optimal operation of the cell. Should one transport medium be blocked by the excessive presence of another phase, then the cell will not be able to function properly. The ratio of ionomer content added to the catalyst ink has been the target of optimization by researchers in the fuel cell industry (Mu et al. 2012, Cho et al. 2017, and Afsahi et al. 2015). If too little ionomer is present, then the proton conductivity decreases. With too much ionomer, the reactant paths can become blocked. Tests were needed to determine appropriate ionomer loadings for the in-house fabricated MEAs.

Membrane electrode assemblies were assembled using 130 μm Nafion membranes. Since the goal was to determine the influence of the ionomer content, low cost carbon supported copper catalysts were used at 2.5 mg/cm^2 loadings. The mass fraction of ionomer to catalyst was varied from 5% to 30%. Simple water electrolysis tests were carried out to gauge cell performance and the normalized results at 2.5 V are shown in Figure 8.2. The ideal Nafion ionomer content seemed to lie in the range of 20% in relation to the catalyst mass, which aligned with the ranges outlined by other researchers (Mu et al. 2012).

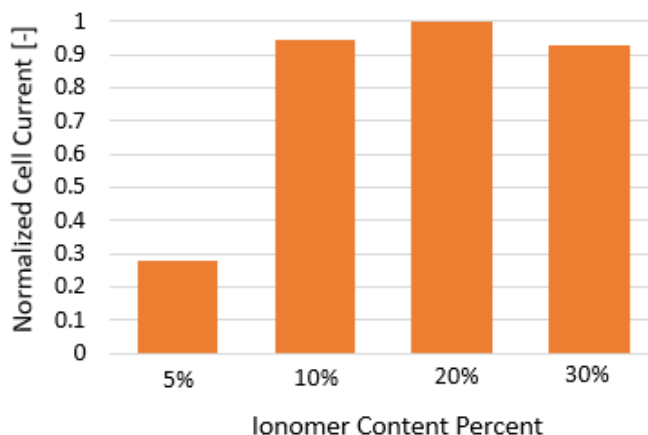


Figure 8.2: Comparison of different ionomer contents in catalyst layer.

8.2 Membrane Selection

The membrane used in electrochemical cells has a significant influence on the overall performance of the device. It is the path through which protons migrate and any changes to the

proton conductivity of this layer can shift the overall resistance within the cell. Most low temperature fuel cells using proton conducting membranes have Nafion membranes. Our initial test with Nafion membranes proved to be disappointing due to the low conductivity of the membranes and the loss of structural integrity. Nafion membranes need to maintain a high water content in order to maintain their proton conductivity. When exposed to high isopropanol concentrations, Nafion membranes tend to swell. This can lead to the delamination of the catalyst layers (Cao et al. 2003). The swelling was a result of the water molecules in the membrane being displaced by the alcohol (Santasalo et al. 2009). Affoune et al. (2005) did a study on the conductivity of Nafion membranes in isopropanol solutions of varying concentrations. They found that as the isopropanol concentration increased, the Nafion's proton conductivity sharply declined. The ideal membrane for the CLHP using isopropanol and acetone would be one capable of operating in a high alcohol environment under anhydrous conditions.

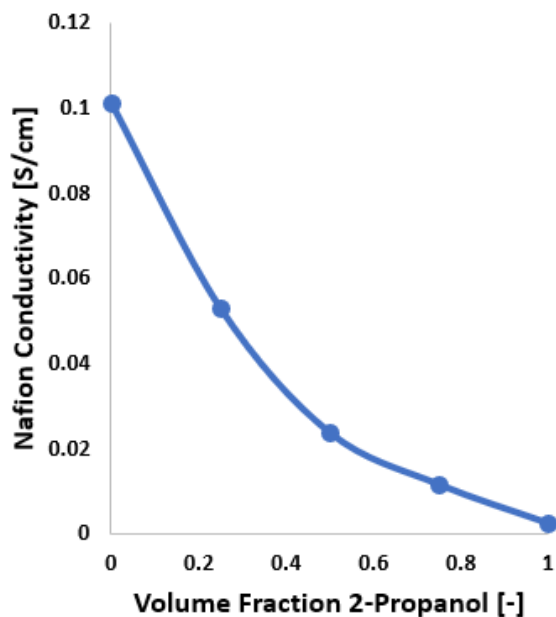


Figure 8.3: Effect of isopropanol concentration on Nafion conductivity (Affoune et al. 2005).

High concentrations of isopropanol and acetone would be necessary for the operation of the proposed CLHP cycle. For efficient operation, membrane materials more amenable to operation under anhydrous conditions were desired. Fortunately, the development of anhydrous fuel cells has been an active area of research. There is a desire to operate fuel cells at temperatures in

excess of 100 °C to achieve efficiency improvements. At these temperatures, liquid water evaporates, and membrane hydration declines. Proposed solutions to help maintain membrane conductivity are the doping of Nafion membranes with additives to retain water, and the use of alternative membrane materials.

8.3 Composite Membranes

Durable membranes were necessary for reliable and consistent testing. One way to increase membrane mechanical strength is to use thicker membranes. Unfortunately, this also increases the proton resistance within the membrane due to an increased length of travel. Another way to increase membrane strength is by using composite membranes (Xing et al. 2004 and Wang et al. 2007). These membranes are made by incorporating ion conducting materials into a porous substrate. The substrate is chosen such that it is mechanically stronger than the pure ion conducting material. Typically, porous Teflon is used for the supporting material. The ion conduction is gained through the impregnation of the Teflon with an ionomer solution such as Nafion.

Three types of porous Teflon sheets were investigated for the development of composite membranes. These were expanded PTFE with 1 µm pores, expanded PTFE with 3 µm pores, and Porex filter paper with 0.5 µm pores. Since tests showed little differences between the Teflon substrates and Porex, the Porex was primarily used due to availability. To facilitate proton conductivity, a Nafion solution was used to impregnate the Teflon structures. Multiple methods were investigated for loading the Nafion. The methods investigated were solution immersion, air brushing, and gravity filling.

Solution immersion consisted of placing the Teflon sheet into a bath containing 5% Nafion solution. After 24 hours of soaking, the sheet was removed, dried, and then weighed to determine the degree of Nafion uptake. Measurements showed that negligible amounts of Nafion were incorporated into the membrane. This may have been due to the concentration of the available Nafion solution being too low. The next method was to spray the Nafion solution onto the Teflon in a similar way to catalyst application. The Nafion solution was loaded into the air brush and sprayed onto the Teflon surface in layers. This application method proved to be infeasible due to

the coagulation of the Nafion solution in the air brush and the blockages developed in the composite membranes. For the gravity filling method, the Teflon sheet was placed in a fixture and Nafion solution was dropped onto the surface, Figure 8.4. The solution soaked through the material while the fixture sat over a heated plate. As the solvent in the ionomer solution evaporated, the Nafion content remained behind. Weight measurements confirmed appreciable uptakes of Nafion into the Teflon substrate.

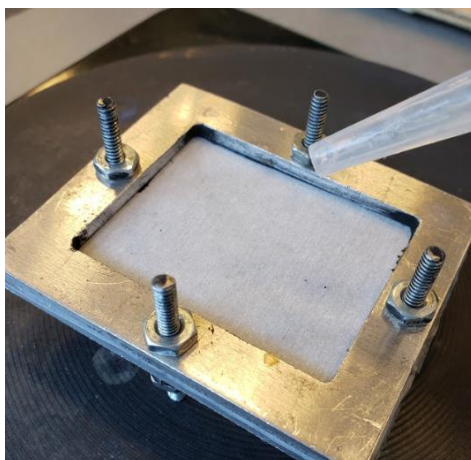


Figure 8.4: Setup for impregnating Teflon sheet with Nafion solution with gravity filling.

8.4 Nafion Doping

The use of composite membranes should increase the mechanical strength of the membranes. To allow for improved operation under anhydrous conditions, modifications were needed for the ionomer phase. To help retain water in the membrane structure, studies have been done introducing hygroscopic inorganic particles such as TiO_2 into a ionomer blend (Barbora et al. 2009, Baglio et al. 2008, and Kalappa et al. 2007). This approach was replicated by creating mixtures of a Nafion solution in alcohol and powdered forms of the inorganic filler materials TiO_2 , SiO_2 , MgSO_4 . After mixing by sonication, the slurry solution was then cast over the Porex film to create a composite membrane with additives in the Nafion.

The optimal mass fraction of filler material in relation to the conductive ionomer has been a subject of debate. Too little filler and the benefits of increased water retention would not be realized. Too much filler and the inorganic component may begin to interfere with the proton

transport properties within the membrane. Some sources placed the optimal filler fraction at ~5% for traditional H₂-O₂ fuel cells (Barbora et al. 2009). To determine the optimal filler fractions to use in our testing, isopropanol dehydrogenation tests were carried out using our experimental setup. In these tests, a solution of 50% by weight isopropanol and water was fed to the anode side of the cell while pure water was sent to the cathode side of the cell. This was done to create a partially anhydrous environment to allow for sufficiently high conductivities to obtain measurable currents from each cell. To create the membrane, TiO₂ nanoparticles were measured out in order to create 5%, 10%, and 20% loadings in relation to the Nafion content. After mixing, the Nafion-TiO₂ mixtures were then used to impregnate the PTFE sheets in order to create composite membranes. The catalyst layers consisted of 1.25 mg/cm² loadings of 30% wt. PtRu catalyst. The Nafion ionomer content in the catalyst was measured out to be 20% by weight in comparison to the catalyst weight.

The results of the testing to determine the desired hygroscopic filler content are shown in Figure 8.5. Here we see that even slight additions of TiO₂ to the Nafion solution improved water retention and allowed for operation in an environment with significant alcohol content. For the range tested, the cell current increased with increasing TiO₂ content. This was indicative of increased conductivity in the ionomer phase. From observing the outlet channels from the cell during testing, it appeared that some of the filler failed to fully integrate into the catalyst layer and was visibly washed away. This would be problematic for an actual CLHP cell and to this end a reduced mass fraction of 10% was used for future testing.

8.5 Alternative Membrane Materials

Although Nafion is by far the most popular membrane material for low temperature fuel cells, other membranes have been investigated for reasons of lower cost or performance benefits. Two membrane materials that have been proposed for anhydrous operation are sulphonated polyether-ether-ketone (sPEEK) and acid doped Polybenzimidazole (PBI). SPEEK membranes were previously investigated during the initial testing. Literature sources had shown that they can be successfully used with high alcohol concentration solutions (Qi et al. 2003). During our previous test with sPEEK membranes, issues occasionally arose with the mechanical strength of the membrane. Cases of ruptures and short-circuiting would occur during the testing. For this next

stage of testing, we acquired more traditional sPEEK membranes as well as reinforced sPEEK membranes from FumaTech Inc. The reinforced membranes were 130 μm composite membranes containing a PET plastic backbone to give extra support to the membrane structure.

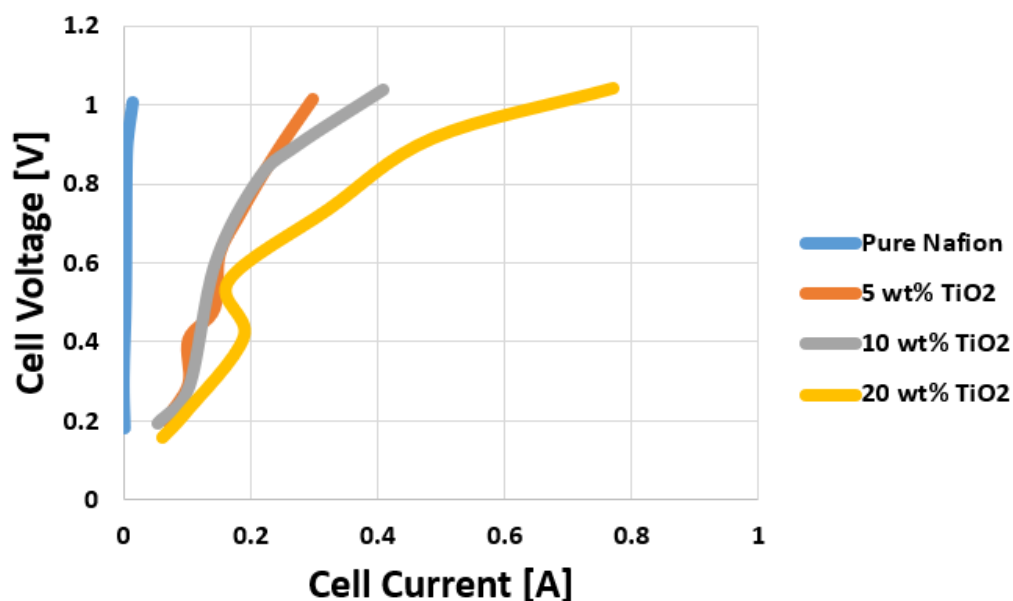


Figure 8.5: Comparison of Inorganic filling content in Nafion for composite membranes.

PBI membranes differ from membranes such as Nafion and SPEEK in that they do not utilize sulphonic acid groups to support proton mobility. Instead, the PBI is used to immobilize an acid such as phosphoric acid which can serve as the proton conductor in the absence of water (Wang et al. 1995, Pu et al. 2002, Li et al. 2010). These membranes typically like to operate at moderately high temperatures in excess of 100 $^{\circ}\text{C}$. To develop PBI membranes, a 6% solution of PBI in DMAc was obtained from FumaTech. The PBI solution was found to be too viscous to impregnate PTFE sheets. Instead, the solution was cast over a polyurethane mesh to create a course composite membrane. The composite PBI membrane was then doped by immersion in either an 80% phosphoric acid solution or 30% sulphuric acid solution for 48 hrs. Catalyst layers were then sprayed onto the membrane as in the traditional membrane fabrication procedure.



Figure 8.6: Composite PBI membrane with catalyst layers.

8.6 Membrane Selection

For membrane comparison, all other aspects of the MEA fabrication and testing conditions were held constant. Catalyst layers were created using 1.25 mg/cm^2 of 40 wt% PtRu catalyst for the anode and 2.5 mg/cm^2 50 wt% Cu catalyst for the cathode. The use of a copper catalyst was a cost saving measure since only the membrane material was currently under investigation. Pure isopropanol was flowed over the anode and pure water was flowed over the cathode while the cell was held at $80 \text{ }^\circ\text{C}$. Water was included in the testing to provide a slight degree of hydration to ensure that measurements could be obtained from all membrane materials. The results of the membrane comparison testing can be seen in Figure 8.7. As expected, pure Nafion membranes displayed low conductivities and negligible current measurements. Both H_2SO_4 and H_3PO_4 doped PBI membranes also showed low conductivities. This may have been due to the temperature not being high enough for the immobilized acid conduction mechanism, or due to acid leaching. Acid leaching occurs when the acid that is normally immobilized by the PBI is washed away by fluid within the cell (Myles et al. 2017). TiO_2 , SiO_2 and MgSO_4 additives all increased the conductivity of the Nafion membrane, with the improvement due to MgSO_4 being the highest. The sPEEK membrane and reinforced sPEEK membranes both fared better than pure Nafion. The reinforced membrane sPEEK membrane performed significantly better than the unreinforced membrane. This may be due to the increased mechanical strength of the membrane allowing it to resist any solvent driven deformations that could impact the contact between the cell layers. Reinforced sPEEK was chosen as the standard membrane for all future testing.

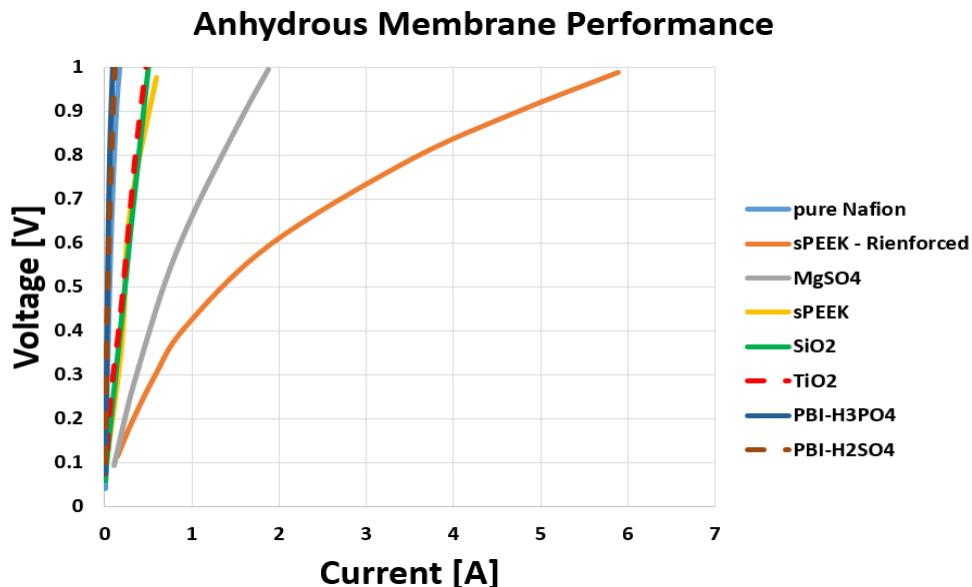


Figure 8.7: Results of membrane comparison testing.

Membrane selection is a crucial aspect of PEM electrochemical cell design. Multiple materials were screened for compatibility with the proposed CLHP working fluids. Using reinforced sPEEK as the new standard membrane material other aspects of the cell were then investigated.

8.7 References

- Affoune, A., Yamada, A., Umeda, M., 2005. Conductivity and surface Morphology of Nafion membrane in water and alcohol environments. *Journal of Power Sources*, vol.148, p. 9-17.
- Afsahi, F., Mathieu-Potvin, F., Kaliaguine, S., 2015. Impact of Ionomer Content on Proton Exchange Membrane Fuel Cell Performance. *Fuel Cells*, vol. 16, p.107-125.
- Baglio V., Ornelas, R., Matteucci, F., Martina, F., Ciccarella, G., Zama, I., Arriaga, L., Antonucci, V., Arica, A., 2008. Solid Polymer Electrolyte Water Electrolyser Based on Nafion-TiO₂ Composite Membrane for High Temperature Operation. *Fuel Cells*, vol. 9, p. 247-252.

- Barbora, K., Acharya, S., Verma, A., 2009. Synthesis and Ex-situ Characterization of Nafion/TiO₂ Composite Membranes for Direct Ethanol Fuel Cell. *Macromolecular Symposia*, vol. 277, p. 177-189.
- Benziger, J., Satterfield, M., Hogarth, W., Nehlsen, J., Kevrekidis, I., 2006. The power performance curve for engineering analysis of fuel cell. *Journal of Power Sources*, vol. 155, p. 272 – 285.
- Cao, D., Bergens, S., 2003. A direct 2-propanol polymer electrolyte fuel cell, *Journal of Power Sources*, vol.124, p.12-17.
- Cho, M., Park, H., Lee, S., Lee, B., Kim, H., Henkensmeier, D., Yoo, S., Kim, J., Han, J., Park, H., Sung, Y., Jang, J., 2017. Effect of Catalyst Layer Ionomer Content on Performance of Intermediate Temperature Proton Exchange Membrane Fuel Cells (IT-PEMFCs) under Reduced Humidity Conditions. *Electrochimica Acta*, vol. 224, p.228-234.
- Kalappa, P., Le, J., 2007. Proton conducting membranes based on sulfonated poly(ether ether ketone)/TiO₂ nanocomposites for a direct methanol fuel cell. *Polymer International*, vol. 56, p. 371-375.
- Li M., Scott, K., 2010. A polymer electrolyte membrane for high temperature fuel cells to fit vehicle applications. *Electrochimica Acta*, vol. 55, p.2123-2128.
- Mu, S., Tian, M., 2012. Optimization of perfluorosulfonic acid ionomer loadings in catalyst layers of proton exchange membrane fuel cells. *Electrochimica Acta*, vol. 60, p.437-442.
- Myles, T., Bonville, L., Maric, R., 2017. Catalyst, Membrane, Free Electrolyte Challenges, and Pathways to Resolutions in High Temperature Polymer Electrolyte Membrane Fuel Cells. *Catalysts*, vol. 7

- Pu, H., Meyer, W., Wegner, G., 2002. Proton Transport in Polybenzimidazole Blended with H₃PO₄ or H₂SO₄. *Journal of Polymer Science: Part B: Polymer Physics*, vol. 40, p. 663-669.
- Santasalo, A., Kallio, T., Kontturi, K., 2009. Performance of Liquid Fuels in a Platinum Ruthenium-Catalysed Polymer Electrolyte Fuel cell. *Platinum Metals Review*, vol.53, p.58-66.
- Qi, Z., Kaufman, A., 2003. Liquid-Feed Direct Oxidation Fuel Cells Using Neat 2 Propanol as Fuel. *Journal of Power Sources*, vol.118, p.54-60
- Wang, L., Yi, B., Zhang, H., Liu, Y., Xing, D., Shao, Z., Cai, Y., 2007. Novel multilayer Nafion/SPI/Nafion composite membrane for PEMFCs. *Journal of Power Sources*, vol.164, p.80-85
- Wang, J., Wasmus, S., Savinell, R., 1995. Evaluation of Ethanol, 1-Propanol, and 2-Propanol in a Direct Oxidation Polymer-Electrolyte Fuel Cell. *Journal of the Electrochemical Society*, vol. 142, p. 4218 -4224.
- Xing, D., Yi, B., Fu, Y., Liu, F., Zhang, H., 2004. Pt-C/SPEEK/PTFE Self Humidifying Composite Membrane for Fuel Cells. *Electrochemical and Solid-State Letters*, vol. 7 p. A315-A317

CHAPTER 9. CATALYST SELECTION

As previously mentioned, the MEA is made up of a proton conducting membrane and a catalyst containing anode and cathode. The proton conductivity of the ionomer phase is of great importance to the overall performance of the cell. However, before protons are even generated a reaction must take place. The site of the reactions is at the catalyst surface. Catalysts help to promote a reaction by reducing the activation energy (E_A) needed to kickstart the reaction as depicted in Figure 9.1 (Zhang et al. 2016).

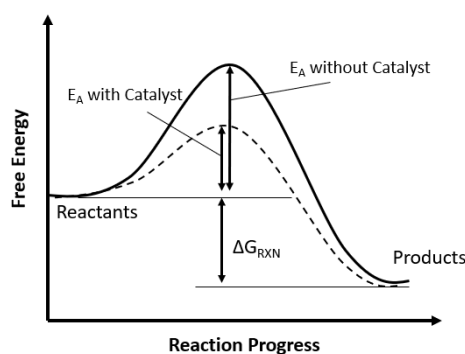


Figure 9.1: Reaction progress diagram with and without catalyst.

Catalyst materials in electrochemical cells are traditionally metals and the properties of these metals can influence the activation energy of the reaction. Most cells in the fuel cell industry utilize platinum-based catalysts. This is to promote the hydrogen dissociation and the oxygen reduction reactions. The optimal catalyst material varies from reaction to reaction. Most alcohol-based fuel cells use either PtRu based catalysts or PtSn based catalysts. This is done with hopes to completely oxidize the compound while avoiding poisoning of the catalyst surface by intermediate products.

For the CLHP, the objective is only partial dehydrogenation, not complete oxidation. Hence, the ideal catalyst may not be traditional PtRu catalyst. Isopropanol dehydrogenation has been achieved by a number of different catalysts in industry, including Raney nickel, cobalt, and copper (Rioux et al. 2003, Kolboe 1969, Mears et al. 1966). A thorough study of catalyst selection for isopropanol in PEM cells has not been done in the literature. Experimentation and

modeling were undertaken to determine if better catalyst combinations could be found for the CLHP dehydrogenation reactions.

9.1 Catalyst Mixtures

Electrochemical cell catalyst can consist of single elemental material or they can be compounds of multiple elements. Studies have been performed on the influence of catalyst mixtures for a number of fuel cells (Xiong et al. 2002 and Lee et al. 2009). One means of creating catalyst mixtures is by alloying the metallic components by chemical means. A simpler approach that has been used is the mixing of catalyst powders containing different elements (Mazurek et al. 2006 and Xi et al. 2006). Commercial catalyst powders contain nanoscale metallic particles. When mixed together, the interaction of these nanoparticles is thought to mimic that of the alloyed metal (Mazurek et al. 2006). To create our own catalyst mixtures, catalyst powders with properties shown in Table. 9.1 were obtained from FuelCellStore.com.

Table 9.1: Properties of catalyst powders.

Catalyst Metal	Metal Loading	Metal Particle Diameter
Platinum	30%	2.5
Platinum-Ruthenium (1:1)	40%	1.5
Gold	20%	25
Silver	20%	25
Cobalt	20%	3
Nickel	20%	2.5
Copper	20%	2.5
Rhodium	20%	3
Palladium	20%	4
Iridium	20%	3
Platinum-Tin (3:1)	20%	2.5

The following experimental plan was proposed to investigate the influence of the catalyst selection on the performance of the isopropanol-acetone reaction in the electrochemical cell, Table 9.2. Binary catalyst combinations were platinum based to keep in line with conventional catalyst materials used for high performance fuel cell systems. The tertiary combinations were based off the pre-alloyed catalyst powders PtRu and PtSn mixed with single element catalyst powders.

Table 9.2: Proposed catalyst combinations to investigate for CLHP usage.

Single Element	Binary Catalyst	Tertiary Catalyst	
Au	PtAu	PtRuAu	PtSnAu
Pt	PtSn	PtRuCo	PtSnCo
Co	PtCo	PtRuNi	PtSnNi
Ni	PtNi	PtRuCu	PtSnCu
Cu	PtCu	PtRuRh	PtSnRh
Rh	PtRu	PtRuPd	PtSnPd
Pd	PtRh	PtRuAg	PtSnAg
Ag	PtPd	PtRuIr	PtSnIr
Ir	PtAg		
	PtIr		

9.2 Catalyst Testing

For the comparative catalyst testing, all MEAs were fabricated with an overall catalyst powder loading of 1.25 mg/cm^2 . The catalyst powders were mixed in a 50-50 mass ratio by powder weight to create a binary catalyst. Nafion ionomer was mixed into the catalyst solution at a concentration of 20% by weight in relation to the catalyst powder. With the goal of determining how the catalyst materials interact with the likely chemical species present in a CLHP, neat liquid isopropanol was fed into the anode chamber of the cell and neat liquid acetone was fed into the cathode chamber. Voltage sweeps were then carried out at multiple cell temperatures to determine the cell's current-voltage relationship. Ideally, the potentials at the electrode would be measured independently as referenced from the ionomer phase. In the absence of a reference electrode, the performance of the catalyst combinations was assumed to be that of the combined anode and cathode performance.

The results of the binary catalyst combinations are shown in Figures 9.2 – 9.4. Here, the resistance of the overall cell was calculated using Ohm's Law. Lower resistances were desired as higher currents and in turn higher reaction rates would be achievable for a given applied voltage. The combinations PtRu, PtAu, and PtCo resulted in the lowest resistances of the binary materials investigated.

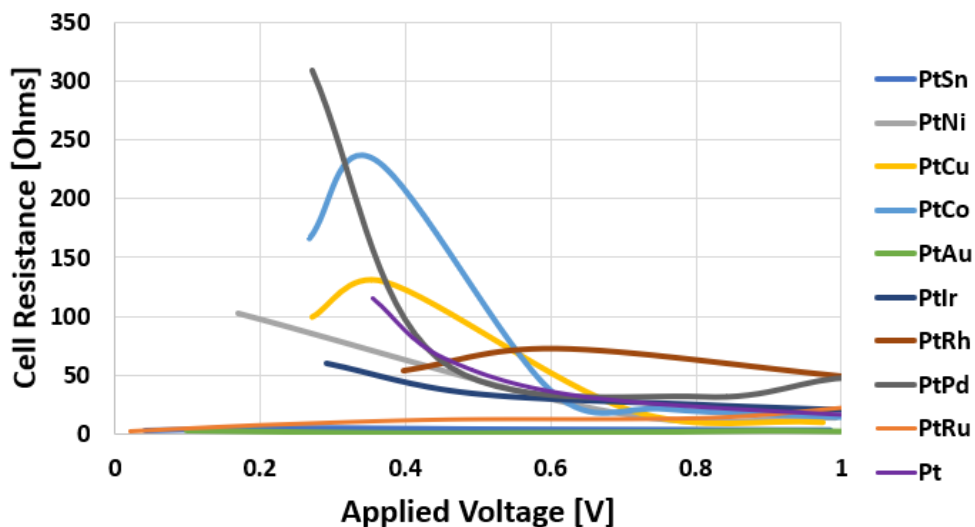


Figure 9.2: Binary catalyst comparisons for cell operated at 30 °C.

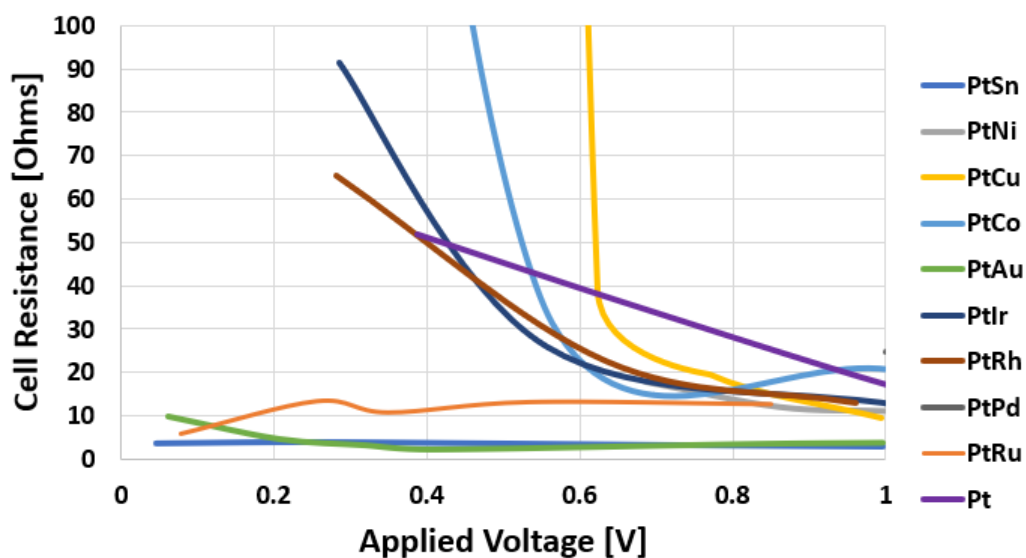


Figure 9.3: Binary catalyst comparisons for cell operated at 40 °C.

The PtRu and PtSn based tertiary catalyst were created in a similar manner to the binary catalyst. The total powder loading was held at 1.25 mg/cm², and the powders were mixed together in 50-50 weight ratios. All of the proposed PtRu and PtSn combinations were not tested due to some membranes getting damaged and the need to begin investigating the trends already established. The results of the tertiary testing are shown in Figures 9.5 - 9.10.

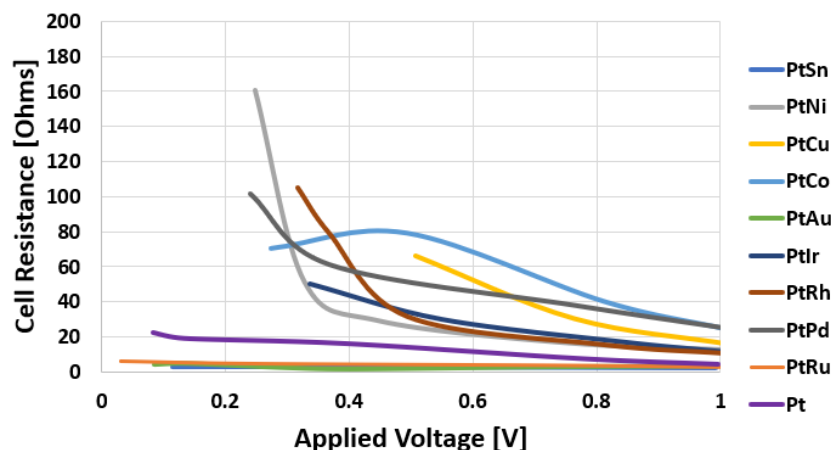


Figure 9.4: Binary catalyst comparisons for cell operated at 50 °C.

9.3 Catalyst Performance Prediction Methods

The discovery of more active catalysts is of great importance to those in chemical processing industries. When multiple material choices are available for use in a single catalyst, the material combinatorial space can become massive. Our previous tests only looked at 50-50 powder mass ratios, however any mass ratio could have been used and different catalyst performances would have been expected. Computational tools were a necessity in order to search a wide design space to find a more suitable catalyst for a particular reaction. Two tools that have seen extensive use in recent years for catalyst performance prediction are Machine Learning Frameworks and Density Functional Theory (DFT).

9.3.1 Machine Learning Approach

Machine learning pertains to a field of artificial intelligence where data is used to train models to make predictions without explicitly defining the relationship a priori (Mohri et al. 2012). Artificial neural networks (ANN) are a subset of machine learning that have been widely applied to catalyst discovery. Here, a set of nodes are arranged such that there is an input layer, an arbitrary number of hidden layers, and an output layer, Figure 9.11. In sequential networks, the outputs of the neurons are governed by a transfer function and the sum of the inputs from previous neurons multiplied by weighting factors. During the model training process, the weighting factors are adjusted to bring the model outputs in line with the training data outputs (Wang 2003).

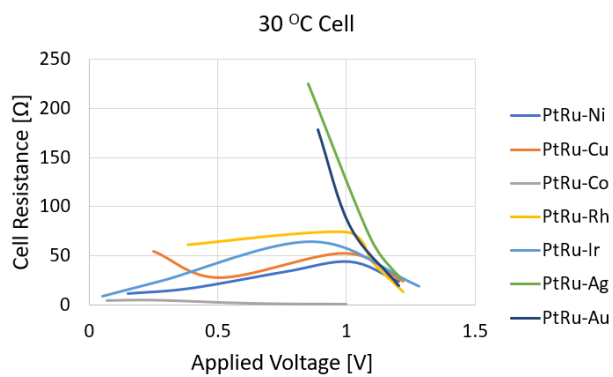


Figure 9.5: PtRu Tertiary Catalyst at 30 °C.

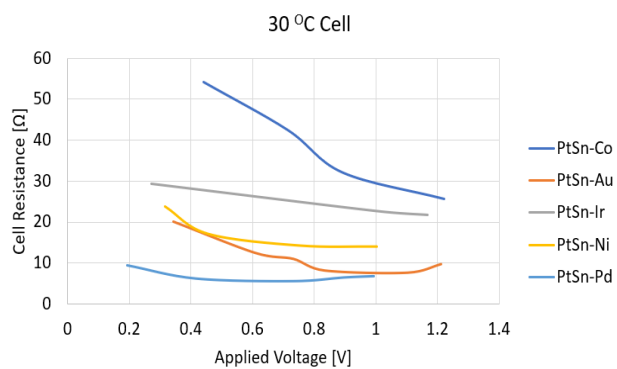


Figure 9.6: PtSn Tertiary Catalyst at 30 °C.

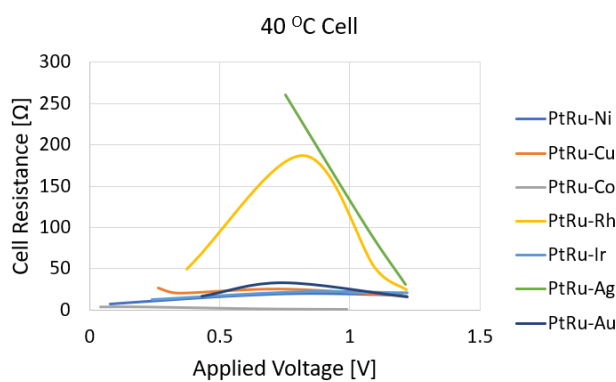


Figure 9.7: PtRu Tertiary Catalyst at 40 °C.

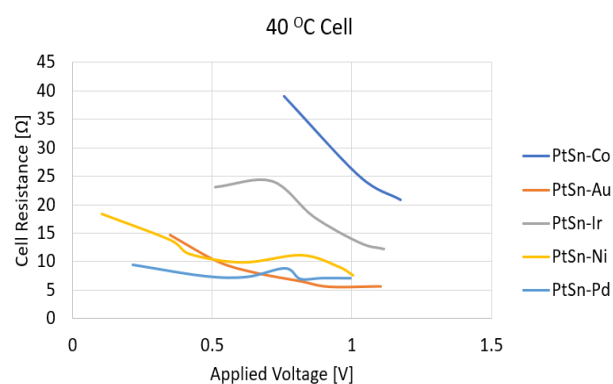


Figure 9.8: PtSn Tertiary Catalyst at 40 °C.

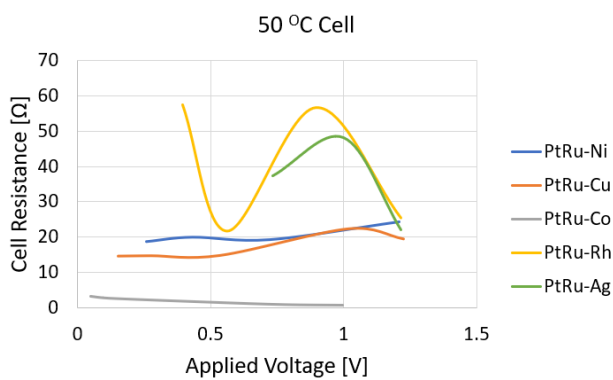


Figure 9.9: PtRu Tertiary Catalyst at 50 °C.

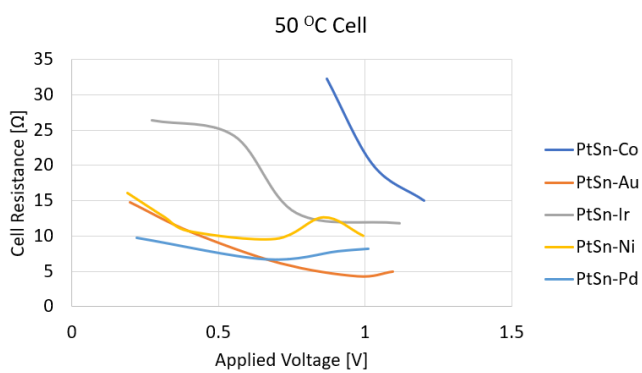


Figure 9.10: PtSn Tertiary Catalyst at 50 °C.

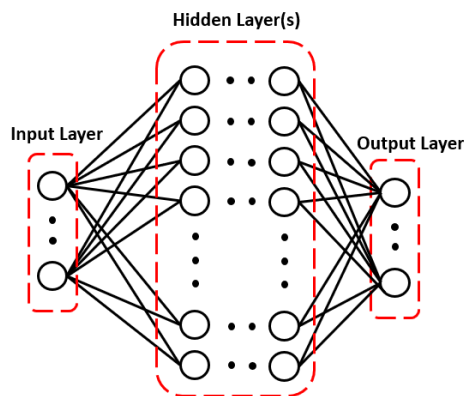


Figure 9.11: Artificial neural network system architecture.

Artificial neural networks have previously been developed to predict catalyst activity using information about the catalyst as inputs to the model. Researchers have used the composition of the catalyst material as inputs into an ANN model (Holena et al. 2003). Additionally, properties such as ionic radius, ionization potential, enthalpy of formation, and more have been used as ANN model inputs to predict catalyst performance (Tayao et al. 2018, Kito et al. 1994).

To determine if this modeling approach would be capable of capturing trends for the CLHP catalyst testing, an ANN framework was developed in Python with the aid of the Keras package (Chollet et al. 2015). Examples of the physiochemical properties investigated are shown in Table 9.3. For each catalyst combination used in the testing, the metallic mole fraction of the catalyst mixture was determined. This mole fraction was then used to determine the effective properties for the mixture by taking the mole weighted averages of the physiochemical properties of the elements in the catalyst mixture. An example of the averaging calculation for a mixture with n components and known mole fractions x , is shown in Equation 9.1.

$$Property_{effective} = \sum_1^n x_i Property_i \quad (9.1)$$

Multi-layer perceptron and radial basis neural networks were created using Keras with various architectures. During the training process, part of the experimental dataset was used for training, while another part of the dataset was reserved for validation. Unfortunately, no combination of physiochemical properties could be found that would generate a network that correlated well to

the experimental data. This was thought to be due in part to the effective physiochemical properties investigated for the mixture not simply being equal to a weighted molar averaging of the individual constituents.

Table 9.3: Example physiochemical properties used in artificial neural network catalyst prediction.

$\Delta H_{f,oxide}$	$\Delta S_{f,oxide}$	1st Ionization Energy
2 nd Ionization Energy	Ionic Radius	H ₂ Binding Energy
H ₂ Tunneling Temperature	H ₂ Metal Binding Distance	Surface Energy
Bond Energy	Electron Bandwidth	Ionic Valency
Electronegativity	D-Band Center	Specific Heat Capacity
Heat of Fusion	Heat of Vaporization	Thermal Conductivity
Melting Point	Lattice Constant	

9.3.2 Density-Functional Theory Approach

Density functional theory is a computational technique from quantum mechanics that allows for the determination of various properties of molecular systems including system energy. The goal of a catalyst is to bring the reaction's activation energy down as much as possible. There are numerous ways that DFT has been applied to determining the activation energy associated with a catalyst. DFT can be used to simulate each step of a reaction. In such a scenario, a molecular dissociation or association is performed on a catalyst surface. The energy of the system over the course of the reaction is plotted and the reaction's activation energy can be extracted from the plot, Figure 9.12. To do this however, detailed knowledge of the reaction path, adsorption sites, and molecular orientations are generally needed (Greeley et al. 2003). Significant computational resources are also necessary to calculate results in a reasonable time.

Before the onset of computationally intensive DFT calculations, the use of scaling relationships proved useful for the comparison of catalyst performance. Scaling relationships essentially correlate a more easily measured quantity to the activation energy of a reaction. The Brønsted-Evans-Polanyi (BEP) relations correlate the changes in the enthalpy of a reaction and the reaction's activation energy (Michaelides et al. 2003). These relations have been expanded by other researchers. The binding of reaction intermediates is thought to influence the overall activation energy of a reaction. Known as the Sabatier principle, it is believed that there is an

optimal bond strength on reactant species that corresponds to the optimal catalyst for a particular reaction (Medford et al. 2015). If the binding energies of reaction intermediates could be calculated, then they could also be correlated to the activation energy. Rather than try to calculate the binding energy of dozens of different possible reaction intermediates, some researchers have utilized descriptor molecules to estimate the binding energies of a wide array of potential intermediates (Wang et al. 2010, Yu et al. 2018). The binding energies of simple atoms and molecules such as OH, CO, C, O to a surface have been shown to correlate to reaction activation energies.

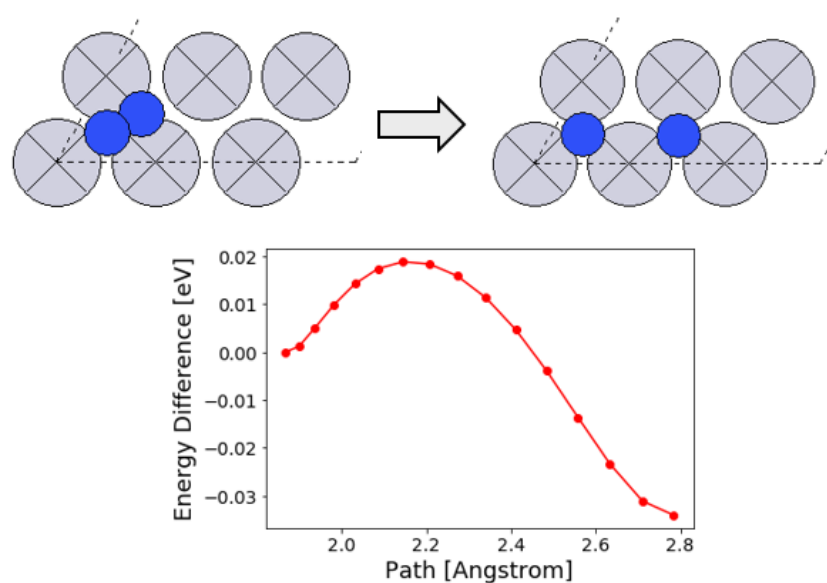


Figure 9.12: Example simulation of molecular dissociation on a metallic surface.

With the goal of calculating the binding energy of descriptor molecules to metallic surfaces, two Python packages were utilized. Atomic Simulation Environment (ASE) allowed for the easy setup and visualization of molecular simulations (Larsen et al. 2017). ASE was integrated with the Grid-Based Projector Augmented Wave (GPAW) method (Mortensen et al. 2005, Enkovaara et al. 2010) which is used as a calculation package to implement DFT and molecular dynamics (MD) calculations. An example of the graphical output of the binding calculations is shown in Figure 9.13.

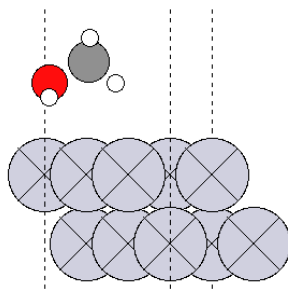


Figure 9.13: Example of alcohol binding to 3x2x2 atom metallic slab.

The binding energy of an atom/molecule to a surface was calculated as the difference between the energies of the combined adsorbate-adsorbent system and the independent energies of the adsorbate atoms and an adsorbent slab, Equation 9.2 (Pang et al. 2006, Fajin et al. 2014). The individual energies of the slab and binding molecule were calculated in isolation. For the combined system, the binding atom or molecule was first placed above the surface of the slab. A molecular dynamics routine was run to relax the system to a resting state until the force on all individual atoms was below a tolerance of 0.05 eV/Angstrom. Once relaxed, a potential energy routine could be called to determine the total energy of the system (Larsen et al. 2017).

$$E_{ads} = E_{slab+atoms} - (E_{atoms} + E_{slab}) \quad (9.2)$$

Initially, differences in electronic potential energies were used to calculate changes in binding energy. In actuality, it is the changes in Gibbs free energy that are needed for binding energy calculations (Viswanathan et al. 2012, Lausche et al. 2012). ASE contains separate routines to estimate Gibbs free energy. In this framework, the internal energy is assumed to be equal to the sum of the electronic potential energy, the translational, rotational, and vibrational energies, and the zero-point energy, Equation 9.3. Assuming the pV term for the molecular system is negligible, then the change in Gibbs free energy is approximated as shown in Equations 9.4 – 9.6 (Larsen et al. 2017).

$$U_{int}(T) = E_{elec} + E_{ZPE} + E_{trans} + E_{rot} + E_{vib} \quad (9.3)$$

$$G \approx U_{int} - TS \quad (9.4)$$

$$G_i = U_{int}(T)_i - TS(T)_i \quad (9.5)$$

$$\Delta G_{ads} = G_{slab+atoms} - (G_{atoms} + G_{slab}) \quad (9.6)$$

The calculations required to determine the changes in Gibbs free energy for the molecular systems took significantly longer to complete than the previous calculations of solely electronic potential energy. To speed up calculations, the programs were run on a 20 x 2.6 GHz core RHEL Linux server. The calculated internal energies varied very little over the desired temperature range and were assumed to be temperature independent for this study. For each molecular system, the values for the entropies at 300 K, 350 K, and 400 K were extracted and a 2nd order polynomial regression was used to fit an expression for the entropy in terms of temperature using Python's numpy package. Similar regression techniques have been used by various researchers utilizing the Shomate equation (Lausche et al. 2012, Grabow et al. 2011).

The change in Gibbs free binding energies of isopropanol, acetone and the descriptor compounds CO, OH, H₂O, O₂, O, C, H, and CH on each of the pure 11 metallic surfaces were calculated. The results of these calculations are available in Appendix A. To estimate the binding energy of catalyst mixtures, the surface area weighted binding energies of the pure metallic substances was used. The binding energy of a metallic mixture has been shown to correlate to the weighted surface of the atoms at the catalyst surface (Ko et al. 2015). This lends increased credence to the use of this averaging method to estimate the binding energy of catalyst mixtures.

After mixture binding energies were calculated, a means of correlating them to catalyst activity was needed. For this purpose, activity maps were chosen. These are graphical representations showing the relationship between some descriptive characteristic such as binding energies and the catalytic activity of a catalyst (Lausche et al. 2012, Li et al. 2017, Norskov et al. 2011). Activity maps have been successfully employed in the prediction of catalytic behavior based on the DFT calculated binding energy of descriptor molecules (Mehmood et al. 2012). Using our experimental results, the following steps were taken to generate an activity map for the isopropanol-acetone reaction, Figure 9.14.

1. Conductivity data for each catalyst combination was extracted at 1-volt operating conditions at 30 °C. As a performance metric, higher conductivity correlates to faster reaction rates within the cell.

2. For each catalyst combination, the effective binding energy for a descriptor molecule was calculated by taking the mole fraction weighted average of the descriptor molecule's binding energy to each of the pure metallic surface as calculated using ASE and GPAW.
3. Python was then used to create a color contour map showing the relationship between the estimated binding energies of two descriptor molecules and the cell conductivity.
4. Descriptor molecule combinations that showed clear trends in the conductivity were considered to be good representations of the overall reaction process. The combination of Oxygen (O) and hydroxide (OH) produced very good results.

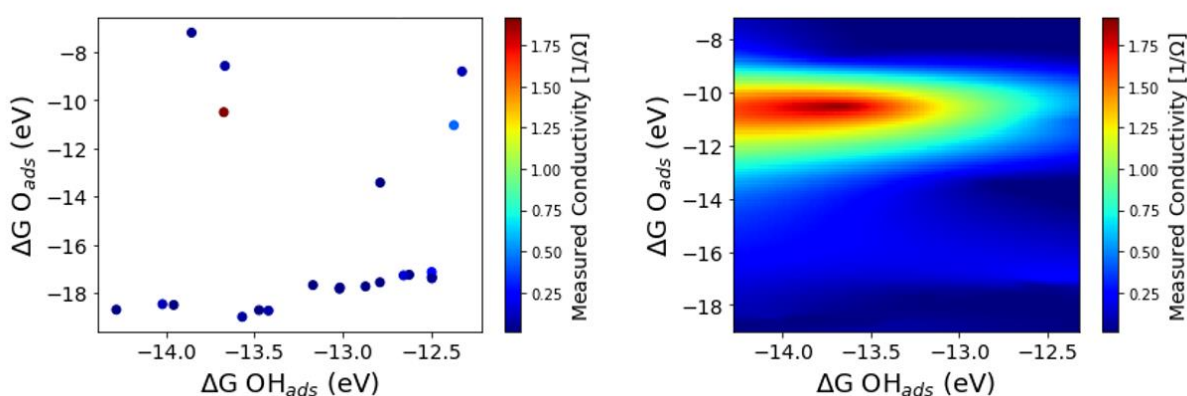


Figure 9.14: Scatter and contour plot for the Isopropanol-Acetone cell conductivity based on DFT calculated binding energies.

If the effective OH and O binding energies of a catalyst powder mixture can be controlled, then it may be possible to intentionally design catalyst materials to exhibit desired binding characteristics. The O and OH binding energies on the pure surfaces of 10 metals investigated as well as the results from being alloyed with PtRu in different ratios are shown in Figure 9.15. In this framework, alloying any metal with another will bring the respective binding energy of the mixture to a mole weighted average between their pure surface binding energy values. In this way, combinations could be created to move nearly anywhere within the region indicated by the dashed lines in Figure 9.15. One of the main benefits to developing computational tools to calculate the binding energies of the descriptor molecules is that we can theoretically screen catalyst combinations consisting of any of the metallic elements in the periodic table.

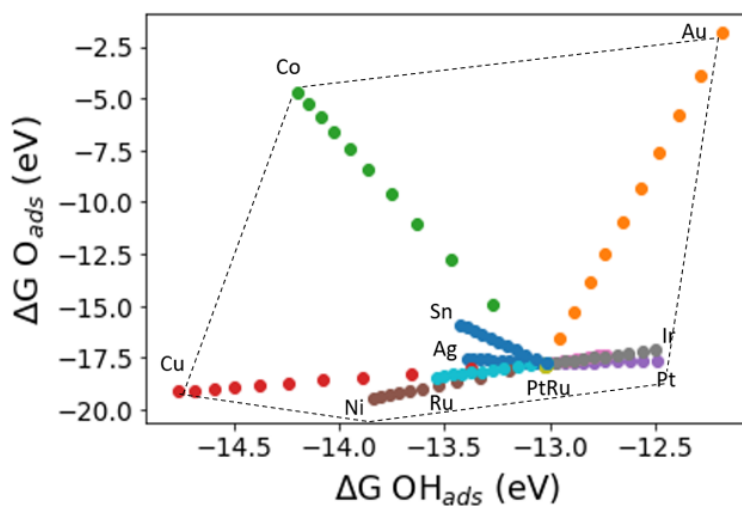


Figure 9.15: Plot showing the binding energies of O and OH the pure metallic surfaces and combinations of these elements in varying ratios to PtRu.

The data collected contained one point which produced a significantly higher cell conductivity than the rest. The catalyst material at this point consisted of $\text{PtRu}_{0.66}\text{Co}_{0.33}$. To determine the viability of using binding energy predictions in catalytic performance estimations, 7 more catalyst combinations were fabricated to fill in missing data points in and around the identified area of high catalytic activity. The additional catalyst combinations are shown in Table 9.4, and the resulting activity plots are shown in Figures 9.16 and 9.17.

Though there was still a sudden peak for the catalyst combination $\text{PtRu}_{0.66}\text{Co}_{0.33}$, the additional test produced notably higher conductivities than most of the other catalyst samples tested. This supports the concept that tailoring catalyst powder mixtures to achieve effective binding energies via mole weighted averaging of mono-elemental binding energies derived via DFT calculations can be used to guide catalyst selection.

Table 9.4: Tailored Catalyst combinations to investigate validity of binding energy approach.

$\text{PtRu}_{0.55}\text{Co}_{0.1}\text{Au}_{0.35}$	$\text{PtRu}_{0.33}\text{Co}_{0.33}\text{Cu}_{0.33}$	$\text{PtRu}_{0.46}\text{Co}_{0.54}$	$\text{PtRu}_{0.57}\text{Co}_{0.43}$
$\text{PtRu}_{0.75}\text{Co}_{0.25}$	$\text{Au}_{0.75}\text{Cu}_{0.25}$	$\text{PtRu}_{0.6}\text{Co}_{0.25}\text{Au}_{0.15}$	

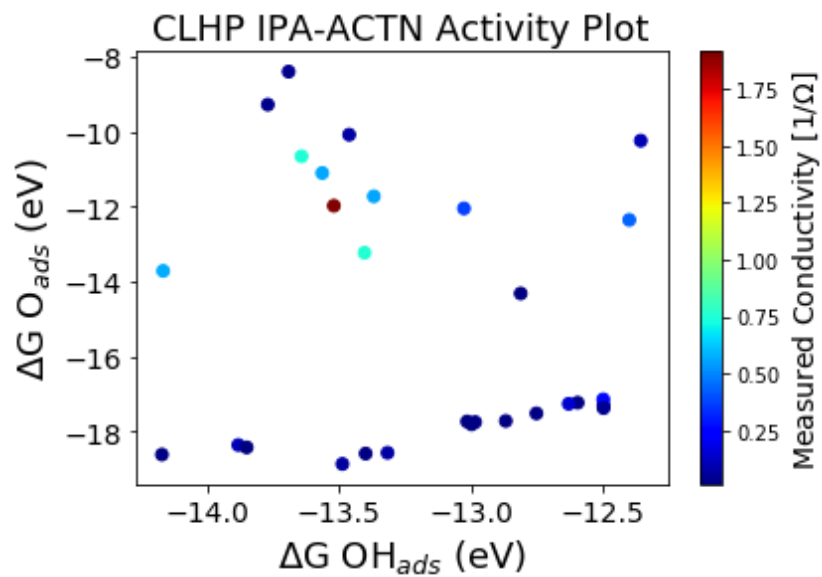


Figure 9.16: Scatterplot of cell conductivity for different catalyst combinations.

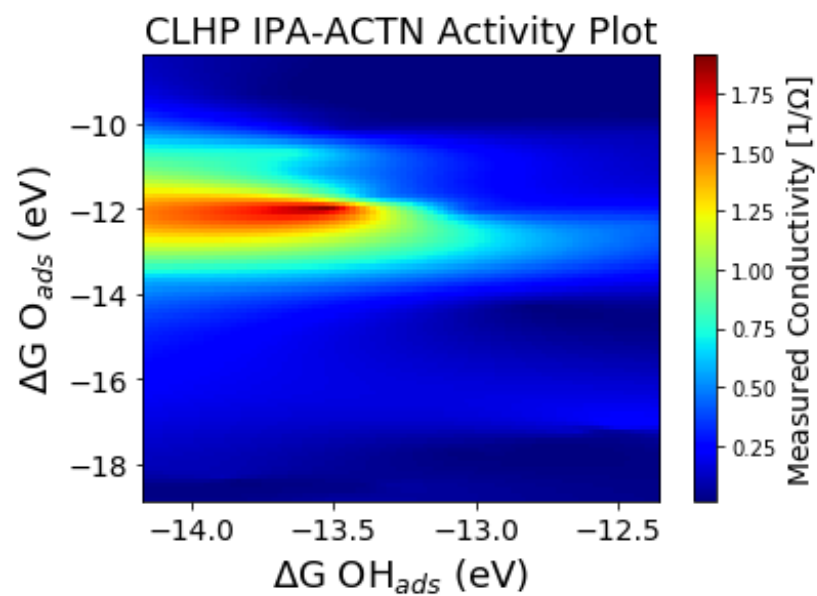


Figure 9.17: Contour plot of cell conductivity for different catalyst combinations.

9.4 References

Chollet, F., et al. 2015. Keras, <https://keras.io>

Enkovaara, J., Rostgaard, C., Mortensen, J., 2010. Electronic structure calculations with GPAW: a real-space implementation of the projector augmented-wave method. *Journal of Physics: Condensed Matter*, vol. 22, p. 253202.

Fajin, J., Natalia, M., Cordeiro, D., Gomes, J., 2014. *Journal of Physical Chemistry*, vol. 118, p. 5832-5840

Grabow, L., Mavrikakis, M., 2011. Mechanism of Methanol Synthesis on Cu through CO₂ and CO Hydrogenation. *ACS Catalysis*, vol. 1, p. 365-384

Greeley J., Mavrikakis, M., 2003. Competitive Paths for Methanol Decomposition on Pt(111). *Journal of the American Chemical Society*, vol. 126, p. 3910-3919.

Holena, M., Baerns, M., 2003. Feedforward neural networks in catalysis A tool for the approximation of the dependency of yield on catalyst composition, and for knowledge extraction. *Catalysis Today*, vol. 81, p. 485-494.

Kito, S., Hattori, T., Murakami, Y., 1994. Estimation of catalytic performance by neural network – product distribution in oxidative dehydrogenation of ethylbenzene. *Applied Catalysis A: General*, vol. 114, p. L173-L178.

Ko, J., Kwon, H., Kang, H., Kim, B., Han, J., 2015. Universality in surface mixing rule of adsorption strength for small adsorbates on binary transition metal alloys. *Physical Chemistry and Chemical Physics*, vol. 17, p. 3123-3130.

Kolboe, S., 1969. Kinetics of dehydrogenation of isopropyl alcohol over a zinc oxide catalyst: Consistency with the adsorption function of isopropyl alcohol on zinc oxide. *Journal of Catalysis*, vol. 13, p. 208-214.

- Larsen et al., 2017. The Atomic Simulation Environment—A Python library for working with atoms. *Journal of Physics: Condensed Matter*, vol. 29, p.273002.
- Lausche, A. Hummelshoj, J., Abild-Pedersen, F., Studt, F., Norskov, J., 2012. Application of a new informatics tool in heterogeneous catalysis: Analysis of methanol dehydrogenation on transition metal catalysts for the production of anhydrous formaldehyde. *Journal of Catalysis*, vol. 291, p. 133-137
- Lee, K., Jeon, M., Woo, S., 2009. Composition optimization of PtRuM/C (M = Fe and Mo) catalysts for methanol electro-oxidation via combinatorial method. *Applied Catalysis B: Environmental*, vol. 91, p. 428-433.
- Li, Z., Wang, S., Chin, W., Achenie, L., Xin, H., 2017. High-throughput screening of bimetallic catalysts enabled by machine learning. *Journal of Materials Chemistry A*, vol. 5, p. 24131
- Mazurek, M., Benker, N., Roth, C., Fuess, H., 2006. Binary Mixtures of Carbon Supported Pt and Ru Catalysts for PEM Fuel Cells. *Fuel Cells*, vol. 6, p. 208-213.
- Mears, D., Boudart, M., 1966. The dehydrogenation of isopropanol on catalysts prepared by sodium borohydride reduction. *AIChE Journal*, vol. 12, p.313-321.
- Medford, A., Vojvodic, A., Hemmelshoj, J., Voss, J., Abild-Pedersen, F., Studt, F., Bligaard, T., Nilsson, A., Norskov, J., 2015. From the Sabatier principle to a predictive theory of transitionmetal heterogeneous catalysis. *Journal of Catalysis*, vol. 328, p. 36-42.
- Mehmood, F., Rankin, R., Greeley, J., Curtiss, L., 2012. Trends in methanol decomposition on transition metal alloy clusters from scaling and Brønsted–Evans–Polanyi relationships. *Physical Chemistry and Chemical Physics*, vol. 14, p. 8644-8652.

- Michaelides, A., Liu, Z., Zhang, J., Alavi, A., King, D., Hu, P., 2003. Identification of General Linear Relationships between Activation Energies and Enthalpy Changes for Dissociation Reactions at Surfaces. *Journal of the American Chemical Society*, vol. 125, p. 3704-3705.
- Mohri, M., Rostamizadeh, A., Talwalkar, A., 2012. *Foundations of Machine Learning*. The MIT Press, Cambridge, Massachusetts.
- Mortensen, J., Hansen, L., Jacobsen, K., 2005. Real-space grid implementation of the projector augmented wave method. *Physical Review B*, vol. 71, p. 035109
- Norskov J., Pedersen, F., Studt, F., Bligaard, T., 2011. Density functional theory in surface chemistry and catalysis. *Proceedings of the National Academy of Sciences*, vol. 108, p. 937-943.
- Pang, X., Xue, L., Wang, G., 2006. Adsorption of Atoms on Cu Surfaces: A Density Functional Theory Study. *Langmuir*, vol. 23, p. 4910-4917.
- Rioux, R., Vannice, M., 2003. Hydrogenation/dehydrogenation reactions: isopropanol dehydrogenation over copper catalysts. *Journal of Catalysis*, vol. 216, p. 362-376.
- Toyao, T., Suzuki, K., Kikuchi, S., Takakusagi, S., Shizuma, K., Takigawa, I., 2018. Toward Effective Utilization of Methane: Machine Learning Prediction of Adsorption Energies on Metal Alloys. *Journal of Physical Chemistry C*, vol. 122, p. 8315-8326.
- Viswanathan, V., Hansen, H., Rossmeisl, J., Norskov, J., 2012. Universality in Oxygen reduction Electrocatalysis on Metal Surfaces. *ACS Catalysis*, vol. 2, p. 1654-1660
- Wang, SC., 2003. Artificial Neural Network. In: *Interdisciplinary Computing in Java Programming*. The Springer International Series in Engineering and Computer Science, vol 743. Springer, Boston, MA

- Wang, S., Petzold, V., Tripkovic, V., Kleis, J., Howalt, J., Skulason, E., Fernandez, E., Hvolbaek, B., Jones, G., Toftelund, A., Falsig, H., Bjorketun, M., Studt, F., Pedersen, F., Rossmeisl, J., Norskow, J., Bligaard, T., 2010. Universal transition state scaling relations for (de)hydrogenation over transition metals. *Physical Chemistry Chemical Physics*, vol. 13, p. 20760-20765.
- Xi J., Wang, J., Yu, L., Qiu, X., Chen, L., 2006. Facile approach to enhance the Pt utilization and CO-tolerance of Pt/C catalysts by physically mixing with transition-metal oxide nanoparticles. *Chemistry Communications*, p.1656-1658
- Xiong, L., Kannan, A., Manthiram, A., 2002. Pt–M (M=Fe, Co, Ni and Cu) electrocatalysts synthesized by an aqueous route for proton exchange membrane fuel cells. *Electrochemistry Communications*, vol. 4, p. 898-903.
- Yu, L., Vilella, L., Pedersen, A., 2018. Generic approach to access barriers in dehydrogenation reactions. *Chemistry Communications*, vol.1, p.1 – 7.
- Zhang, Z., Jiang, Z., Shanguan, W., 2016. Low-temperature catalysis for VOCs removal in technology and application: A state-of-the-art review. *Catalysis Today*. Vol. 264, p. 270-278.

CHAPTER 10. ELECTROCHEMICAL CELL MODELING

The development of models has been an important step in the design of more efficient electrochemical cells. Tools for modeling PEM based cells such as those used in the fuel cell industry have ranged from simple empirical equations, to fully deterministic models guided by first-principles (Weber et al. 2014 and Hao et al. 2016). To get more detailed information about the inner workings of the cell used in the CLHP, a comprehensive model would be needed. Such a model would need to track the relevant charge, mass, and heat transfers, as well as account for the effect of material properties on these transfer processes.

Most comprehensive models used in the literature have been implemented in commercial software packages such as COMSOL and FLUENT, or they were developed in-house. In these cases, the source code is generally unavailable which can limit the ability to tackle new scenarios and make it difficult to extend the model (Weber et al. 2014). Multiple open-source packages have been developed to help aid in the modeling and analysis of fuel cells. Two prominent open source packages for PEM systems are OpenFCST and FAST-FC. Though in theory one can edit any aspect of these programs, they are large packages with steep learning curves (Weber et al, 2014 and Vetter et al. 2018). OpenFCST contains over 120,000 lines of C++ code and FAST-FC has around 12,000 lines of code on top of OpenFOAM.

To make comprehensive models with spatial resolution more accessible, Vetter et al. (2018) developed a 1D MatLab implementation of a 5-layer MEA model. Borrowing from this framework and using open-source tools, a program was developed in Python to model the CLHP electrochemical cell. The framework proposed by Vetter et al. (2018) was expanded into a 2D model, incorporated additional relevant cell layers, accounted for temperature, pressure, and reactant concentration changes along the direction of the fluid flow, and incorporated additional details about the catalyst layer structure. The model was assumed to operate under quasi-steady state conditions.

10.1 One-Dimensional Model

The cell model consists of 11 domains. As shown in Figure 10.1, each domain represents a layer that would be present in a single cell of the CLHP reactor. The entire cell assembly is assumed to be insulated at the edges, and fluid flow occurs in the y-direction. In domains 1 and 11, a coolant such as water or air flows on the edges of the cell removing excess heat. Domains 2 and 10 represent the flow plates. These plates contain grooves to help feed the reactants to the membrane electrode assembly. They also help to conduct heat and charge to and from the cell center. Domains 3 and 9 represent the reactant flows. For the CLHP, the flow in domain 3 would undergo dehydrogenation, while the flow in domain 9 would experience hydrogenation. Domains 4 and 8 represent the diffusion layers. These are porous carbon sheets that provide rigidity to the MEA and help spread the reactants along the catalyst sites. Domain 5 represents the anode catalyst layer, and domain 7 represents the cathode catalyst layer. The proton exchange membrane is contained in the center of the assembly at domain 6.

In such a cell, the bulk fluid flow progresses in the y-direction. For the 1-D model, heat, mass, and charge transfers are only considered in the x-direction. All properties are considered constant and uniform in the y-direction. The coolant channel temperatures in domains 1 and 11, and the reactant concentrations in domains 3 and 9 are uniform for the 1D implementation. The thickness of each layer was an input into the model.

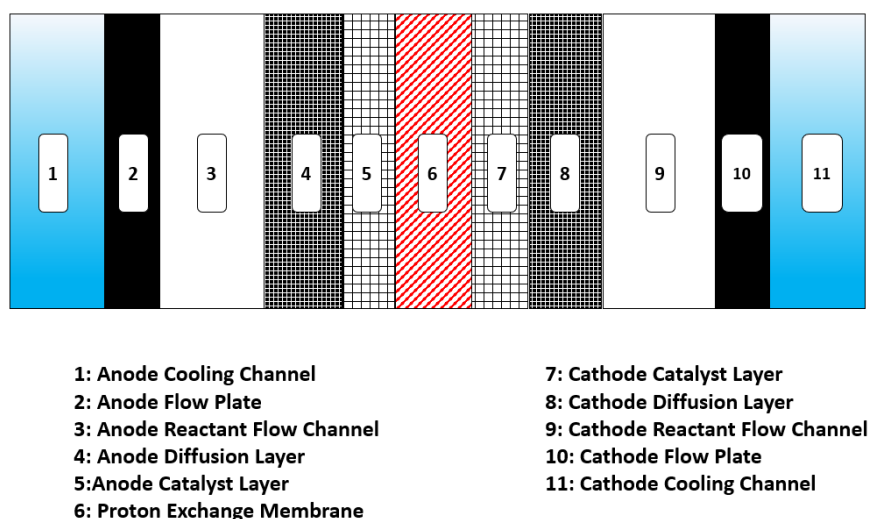


Figure 10.1: Schematic of domains for 1-D cell model.

10.1.1 Anode Coolant Channel

The anode coolant channel removes heat from the anode side of the cell. The coolant is assumed to be at a uniform temperature throughout domain 1 for the 1D model. In this case, the heat transferred to the coolant is approximated knowing the temperature of the boundary interface (1,2) using Newtons Law of Cooling, Equation 10.1. The convective heat transfer coefficient for the anode coolant channel is approximated using the Dittus-Boelter equation (Incropera, et al. 2007).

$$j_{T(1,2)} = h_{(1)}(T_{(1,2)} - T_{(1)}) \quad (10.1)$$

$$Nu_{(1)} = \frac{h_{(1)}D_{H,(1)}}{k_{(1)}} \quad (10.2)$$

$$Nu_{(1)} = 0.023Re_{(1)}^{\frac{4}{5}}Pr_{(1)}^{0.4} \quad (10.3)$$

10.1.2 Anode Flow Plate

The anode flow plate makes up the second domain in the 1D model. It is made of a conductive material and helps direct reactants to the anode catalyst layer and conduct heat and charge. Here, heat transfer occurs via conduction and the heat flux at every point within domain 2 is governed by Fourier's Law (Vetter et al. 2018) and reduced to 1 dimension, Equation 10.4. Electrons generated during the reaction conduct through the layers until they ultimately leave the cell through the anode flow plate. The conduction of electrons is governed by Ohm's Law (Vetter et al. 2018) and reduced to 1 dimension, Equation 10.5.

$$j_{T(2)} = -k_{(2)}\nabla T_{(2)} \approx -k_{(2)}\frac{dT_{(2)}}{dx} \quad (10.4)$$

$$j_{e(2)} = -\sigma_{e(2)}\nabla\varphi_{e(2)} \approx -\sigma_{e(2)}\frac{d\varphi_{e(2)}}{dx} \quad (10.5)$$

The heat flux is not uniform through the entirety of the anode flow plate domain. The anode flow plate has a degree of electrical resistance associated with it. Anytime electrical current flows through a resistance, heat is generated through the process of Joule heating. Equation 10.6 accounts for how the heat flux varied over the extent of domain 2 in 1 dimension, (Vetter et al.

2018). Unlike the heat flux, the flux of electrons is uniform throughout the domain. Charged species like electrons and protons are only generated or consumed in the catalyst layers, the site of the reactions. Hence, the change in electron flux is given by Equation 10.7.

$$\frac{dj_{T(2)}}{dx} = \sigma_{e(2)} \left(\nabla \varphi_{e(2)} \right)^2 = -j_{e(2)} \nabla \varphi_{e(2)} \approx -j_{e(2)} \frac{d\varphi_{e(2)}}{dx} \quad (10.6)$$

$$\frac{dj_{e(2)}}{dx} = 0 \quad (10.7)$$

Domain 2 forms an impermeable layer to reactant mass-flow. The four coupled ODE's in Equations 10.4 – 10.7 fully define the transfers in this cell layer. To solve this system of equations, appropriate boundary conditions are required. The boundary conditions for domain 2 are given in Equations 10.8 – 10.11. As shown in Equation 10.9, the heat flux at the anode side of the cell is not initially known. As this will depend on the extent of heat generated within all the layers, it must have an initial guess. Likewise, the current flowing through the cell is not known a-priori and must be have an initial guess value. It is updated based on the cumulative resistance throughout each layer and the applied voltage.

$$T_{(2)(1,2)} = \frac{j_{T(1,2)}}{h_{(1,2)}} + T_{(1)} \quad (10.8)$$

$$j_{T(2)(1,2)} = j_{T,guess} \quad (10.9)$$

$$\varphi_{e(1,2)} = 0 \quad (10.10)$$

$$j_{e(2)(1,2)} = j_{e,guess} \quad (10.11)$$

10.1.3 Anode Reactant Flow Channel

In addition to conducting charge and heat into and out of the cell, the flow plates also serve to direct the flow of reactants to the catalyst layers, and guide products out of the cell. The interior side of the flow plates contains channels for fluid to flow through. A view looking down at the cell assembly from the y-direction is shown in Figure 10.2. The channels in the flow plates are assumed to be rectangular grooves parallel to the direction of the fluid flow. Along the x-direction, the 1D model treats the reactant flow channels and the flow plates as separate domains.

In actuality, both regions physically overlap along the x-direction. It is also assumed that the fluid does not react with the plates. The reacting fluid moves through the cell slowly. Hence, the thermal and electrical conductivities of the plates are significantly higher than those of the fluid. As such, the heat and charge transfer characteristics in the 1D model's reactant channel layers are assumed to be properties of the flow plate characteristics.

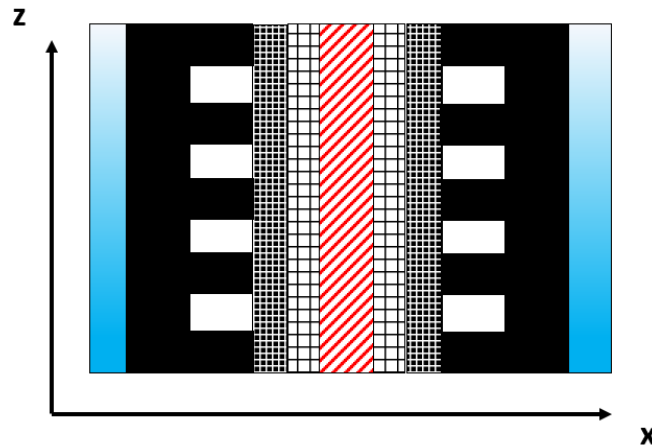


Figure 10.2: Top-view of the electrochemical cell showing flow field grooves.

The governing equations for heat and charge transfer in the reactant channel layer are given in Equations 10.12 – 10.15. The peaks and valleys of the flow plate grooves are assumed to have the same width. As a result, the thermal conductivity and electrical conductivity values for the channel flow region are equal to $\frac{1}{2}$ the values used for the flow plates. These conductivity values are significantly higher than anything that would be present in the flow stream.

$$j_{T(3)} = -k_{(3)} \nabla T_{(3)} \approx -k_{(3)} \frac{dT_{(3)}}{dx} \quad (10.12)$$

$$j_{e(3)} = -\sigma_{e(3)} \nabla \varphi_{e(3)} \approx -\sigma_{e(3)} \frac{d\varphi_{e(3)}}{dx} \quad (10.13)$$

$$\frac{dj_{T(3)}}{dx} = \sigma_{e(3)} \left(\nabla \varphi_{e(3)} \right)^2 = -j_{e(3)} \nabla \varphi_{e(3)} \approx -j_{e(3)} \frac{d\varphi_{e(3)}}{dx} \quad (10.14)$$

$$\frac{dj_{e(3)}}{dx} = 0 \quad (10.15)$$

In the electrochemical cell, as the reaction progresses, the concentration of the reactants is expected to change. Since this change is expected to occur along the direction of the flow in the y-direction, the concentration is assumed to be constant for the 1D cell model. The boundary

conditions for domain 3 are shown in Equations 10.16 -10.19. Here the values of the properties evaluated at the boundary of the previous domain are used as the inputs to the boundary for the current domain.

$$T_{(3)(2,3)} = T_{(2)(2,3)} \quad (10.16)$$

$$j_{T_{(3)(2,3)}} = j_{T_{(2)(2,3)}} \quad (10.17)$$

$$\varphi_{e_{(3)(2,3)}} = \varphi_{e_{(2)(2,3)}} \quad (10.18)$$

$$j_{e_{(3)(2,3)}} = j_{e_{(2)(2,3)}} \quad (10.19)$$

10.1.4 Anode Diffusion Layer

After entering the flow field, the reactants then move to the catalyst layer through the process of diffusion. The diffusion layer is typically a porous carbon sheet that helps provide mechanical support to the membrane and disperse the reactants across the catalyst layer. The heat and charge transfers in this region are given by Equations 10.20 – 10.23.

$$j_{T_{(4)}} = -k_{(4)} \nabla T_{(4)} \approx -k_{(4)} \frac{dT_{(4)}}{dx} \quad (10.20)$$

$$j_{e_{(4)}} = -\sigma_{e_{(4)}} \nabla \varphi_{e_{(4)}} \approx -\sigma_{e_{(4)}} \frac{d\varphi_{e_{(4)}}}{dx} \quad (10.21)$$

$$\frac{dj_{T_{(4)}}}{dx} = \sigma_{e_{(4)}} \left(\nabla \varphi_{e_{(4)}} \right)^2 = -j_{e_{(4)}} \nabla \varphi_{e_{(4)}} \approx -j_{e_{(4)}} \frac{d\varphi_{e_{(4)}}}{dx} \quad (10.22)$$

$$\frac{dj_{e_{(4)}}}{dx} = 0 \quad (10.23)$$

In addition to charge and heat transfer, mass transfer also occurs in this region. In the anode flow channel, the reactant of interest is liquid isopropanol. Fickian diffusion is used to model the concentration of isopropanol in the diffusion layer (Vetter et al. 2018), Equation 10.24. The diffusivity of liquid isopropanol is estimated using the Stokes-Einstein equation (Revankar et al. 2014). The Lennard-Jones collision parameter was taken from Wilhelm et al. (1971). The molar flux of isopropanol is given by Faraday's Law, Equation 10.25.

$$j_{IPA_{(4)}} = -C_{IPA_{(4)}} D_{IPA_{(4)}} \nabla x_{IPA_{(4)}} \quad (10.24)$$

$$j_{IPA(4)} = \frac{j_{e(4)}}{n_e F} \quad (10.25)$$

The boundary conditions for domain 4 are given in Equations 10.26 - 10.31. The concentration in the reactant stream is uniform for the 1D model and serves as one of the boundary conditions to the diffusion layer.

$$T_{(4)(3,4)} = T_{(3)(3,4)} \quad (10.26)$$

$$j_{T(4)(3,4)} = j_{T(3)(3,4)} \quad (10.27)$$

$$\varphi_{e(4)(3,4)} = \varphi_{e(3)(3,4)} \quad (10.28)$$

$$j_{e(4)(3,4)} = j_{e(3)(3,4)} \quad (10.29)$$

$$x_{IPA(4)(3,4)} = x_{IPA(3)} \quad (10.30)$$

$$j_{IPA(4)(4,5)} = 0 \quad (10.31)$$

10.1.5 Anode Catalyst Layer

The catalyst layers houses the sites of the reactions within the electrochemical cell. This is where reactants are converted into products and protons and electrons are generated and consumed. The catalyst materials used in this study are carbon supported catalysts. As shown in Figure 8.1, these nanoparticle carbon centers host even smaller particles of metallic material. The use of nanomaterials allows for the achievement of large surface areas with small volumes. During manufacturing, the catalyst ink was sprayed onto the membrane and allowed to dry. This left behind a layer of carbon catalyst. To estimate the thickness of the catalyst layer, the bulk density of the carbon nanoparticle precursor as obtained from the catalyst vendor was used, Equations 10.32 - 10.33.

$$Vol_{catLayer} = \frac{m_{carbon}}{\rho_{carbon}} \quad (10.32)$$

$$L_{catLayer} = \frac{Vol_{catLayer}}{A_{cell}} \quad (10.33)$$

In the catalyst layer, heat and electron conduction remain and the generation of protons and hence proton conduction must also be considered. The catalyst layer is a mixture of proton conducting ionomer, and electron conducting carbon. The conductivities of these two phases are assumed to be equal to the conductivity of the ionomer and carbon, respectively. In the catalyst layer, heat conduction is no longer solely due to electronic Joule heating. Protonic Joule heating, the activation heat associated with the electrode's overpotential, and Peltier heating associated with the entropy change of the reaction must also be considered (Vetter et al. 2018).

$$j_{T(5)} = -k_{(5)} \nabla T_{(5)} \approx -k_{(5)} \frac{dT_{(5)}}{dx} \quad (10.26)$$

$$j_{e(5)} = -\sigma_{e(5)} \nabla \varphi_{e(5)} \approx -\sigma_{e(5)} \frac{d\varphi_{e(5)}}{dx} \quad (10.27)$$

$$j_{p(5)} = -\sigma_{p(5)} \nabla \varphi_{p(5)} \approx -\sigma_{p(5)} \frac{d\varphi_{p(5)}}{dx} \quad (10.28)$$

$$\frac{dj_{T(5)}}{dx} = \sigma_{e(5)} \left(\nabla \varphi_{e(5)} \right)^2 + \sigma_{e(5)} \left(\nabla \varphi_{e(5)} \right)^2 + \frac{j_{e(5)}}{L_{anode}} \eta_a - \frac{j_{e(5)}}{n_e F} \frac{\Delta S_a}{L_{anode}} \quad (10.29)$$

$$\frac{dj_{e(5)}}{dx} = \frac{j_{e,guess}}{L_{anode}} \quad (10.30)$$

$$\frac{dj_{p(5)}}{dx} = \frac{j_{e,guess}}{L_{anode}} \quad (10.31)$$

During reactions, there are losses associated with all electrodes called overpotentials. The overpotentials can be modeled by the Butler-Volmer equation, Equation 10.32. Unlike Vetter et al. (2018), overpotentials were not used to directly govern the current fluxes within the catalyst layer. Alternatively, the overall current fluxes in the catalyst were used to determine effective electrode overpotentials. These calculated overpotentials were then later used in the global cell solver. This was found to be a more robust solution method for the CLHP cell 1D model.

$$i = i_o \left(e^{\left(\frac{\beta n_e F \eta}{RT} \right)} - e^{\left(\frac{-(1-\beta) n_e F \eta}{RT} \right)} \right) \quad (10.32)$$

The boundary conditions for the anode catalyst layer are given in Equations 10.33 – 10.38. The conditions of the electron and proton fluxes are given such that the flux of the electrons at boundary (5,6) is zero and the flux of protons at boundary (4,5) is zero. This is because electrons

are not conducted in the membrane phase, and protons are not conducted outside of the ionomer in the catalyst layer.

$$T_{(5)(4,5)} = T_{(4)(4,5)} \quad (10.33)$$

$$j_{T(5)(4,5)} = j_{T(4)(4,5)} \quad (10.34)$$

$$\varphi_{e(5)(4,5)} = \varphi_{e(4)(4,5)} \quad (10.35)$$

$$j_{e(5)(5,6)} = 0 \quad (10.36)$$

$$\varphi_{e(5)(4,5)} = 0 \quad (10.37)$$

$$j_{p(5)(4,5)} = 0 \quad (10.38)$$

10.1.6 Proton Conducting Membrane

In the center of the cell lies the proton conducting membrane. In this model, only heat and proton transfer were considered in the membrane. Equations 10.39 – 10.42 represent how the transfers were governed in this domain. The proton flux is assumed to be uniform due to the absence of any reactions. The boundary conditions are given in Equations 10.43- 10.46.

$$j_{T(6)} = -k_{(6)} \nabla T_{(6)} \approx -k_{(6)} \frac{dT_{(6)}}{dx} \quad (10.39)$$

$$j_{p(6)} = -\sigma_{p(6)} \nabla \varphi_{p(6)} \approx -\sigma_{p(6)} \frac{d\varphi_{p(6)}}{dx} \quad (10.40)$$

$$\frac{dj_{T(6)}}{dx} = \sigma_{e(6)} \left(\nabla \varphi_{e(6)} \right)^2 \quad (10.41)$$

$$\frac{dj_{p(6)}}{dx} = 0 \quad (10.42)$$

$$T_{(6)(5,6)} = T_{(5)(5,6)} \quad (10.43)$$

$$j_{T(6)(5,6)} = j_{T(5)(5,6)} \quad (10.44)$$

$$\varphi_{e(6)(5,6)} = \varphi_{e(5)(5,6)} \quad (10.45)$$

$$j_{p(6)(5,6)} = j_{p(5)(5,6)} \quad (10.46)$$

As mentioned earlier, the use of sPEEK membranes for the CLHP is desirable due to the increased compatibility with high alcohol environments. Nafion membranes have seen extensive use in fuel cell modeling. Empirical equations have been derived to estimate the proton conductivity of the Nafion material given its temperature and humidification levels (Weber et al., 2004). For sPEEK membranes, no universally accepted correlations were available. Researchers that have measured the conductivity of sPEEK membranes typically use an Arrhenius equation with experimentally determined parameters to correlate their results to temperature, Equation 10.47.

$$\sigma_p = \sigma_o e^{\left(\frac{-E_A}{k_B T}\right)} \quad (10.47)$$

10.1.7 Cathode Catalyst Layer

The cathode catalyst layer modeling is similar to that of the anode catalyst layer. The layer thickness is again estimated using Equations 10.32 – 10.33. The governing equations for this domain are given in Equations 10.48 – 10.53, whereas boundary conditions are given in Equations 10.54 – 10.59. Since the membrane acts as an electronic insulator, the value of the electronic potential immediately after the membrane is unknown and must be guessed.

$$j_{T(7)} = -k_{(7)} \nabla T_{(7)} \approx -k_{(7)} \frac{dT_{(7)}}{dx} \quad (10.48)$$

$$j_{e(7)} = -\sigma_{e(7)} \nabla \phi_{e(7)} \approx -\sigma_{e(7)} \frac{d\phi_{e(7)}}{dx} \quad (10.49)$$

$$j_{p(7)} = -\sigma_{p(7)} \nabla \phi_{p(7)} \approx -\sigma_{p(7)} \frac{d\phi_{p(7)}}{dx} \quad (10.50)$$

$$\frac{dj_{T(7)}}{dx} = \sigma_{e(7)} \left(\nabla \phi_{e(7)}\right)^2 + \sigma_{e(7)} \left(\nabla \phi_{p(7)}\right)^2 + \frac{j_{e(7)}}{L_{cathode}} \eta_c - \frac{j_{e(7)}}{n_e F} \frac{\Delta S_c}{L_{cathode}} \quad (10.51)$$

$$\frac{dj_{e(7)}}{dx} = -\frac{j_{e,guess}}{L_{cathode}} \quad (10.52)$$

$$\frac{dj_{p(7)}}{dx} = \frac{j_{e,guess}}{L_{cathode}} \quad (10.53)$$

$$T_{(7)(6,7)} = T_{(6)(6,7)} \quad (10.54)$$

$$j_{T(7)(6,7)} = j_{T(6)(6,7)} \quad (10.55)$$

$$\varphi_{e(7)(6,7)} = \varphi_{e_{guess}} \quad (10.56)$$

$$j_{e(7)(6,7)} = 0 \quad (10.57)$$

$$\varphi_{e(7)(6,7)} = \varphi_{e(6)(6,7)} \quad (10.58)$$

$$j_{p(7)(6,7)} = j_{p(6)(6,7)} \quad (10.59)$$

10.1.8 Cathode Diffusion Layer

The cathode diffusion layer model resembles that of the anode diffusion layer. In this model, the diffusing reactant of interest is acetone. The diffusion of acetone gas is modeled using correlations from Bird et al. (2002) and Revankar et al. (2014). The governing equations are given in Equations 10.60 – 10.65. The boundary conditions are given in Equations 10.66 – 10.71.

$$j_{T(8)} = -k_{(8)} \nabla T_{(8)} \approx -k_{(8)} \frac{dT_{(8)}}{dx} \quad (10.60)$$

$$j_{e(8)} = -\sigma_{e(8)} \nabla \varphi_{e(8)} \approx -\sigma_{e(8)} \frac{d\varphi_{e(8)}}{dx} \quad (10.61)$$

$$\frac{dj_{T(8)}}{dx} = \sigma_{e(8)} \left(\nabla \varphi_{e(8)} \right)^2 = -j_{e(8)} \nabla \varphi_{e(8)} \approx -j_{e(8)} \frac{d\varphi_{e(8)}}{dx} \quad (10.62)$$

$$\frac{dj_{e(8)}}{dx} = 0 \quad (10.63)$$

$$j_{CTNA(8)} = -C_{ACTN(8)} D_{ACTN(8)} \nabla x_{ACTN(8)} \quad (10.64)$$

$$j_{ACTN(8)} = \frac{j_{e(8)}}{n_e F} \quad (10.65)$$

$$T_{(8)(7,8)} = T_{(7)(7,8)} \quad (10.66)$$

$$j_{T(8)(7,8)} = j_{T(7)(7,8)} \quad (10.67)$$

$$\varphi_{e(8)(7,8)} = \varphi_{e(7)(7,8)} \quad (10.68)$$

$$j_{e(8)(7,8)} = j_{e(7)(7,8)} \quad (10.69)$$

$$x_{ACTN(8)(8,9)} = x_{ACTN(9)} \quad (10.70)$$

$$j_{ACTN(8)(7,8)} = 0 \quad (10.71)$$

10.1.9 Cathode Flow Channel

The cathode flow channel model is similar to the model of the anode flow channel. The concentration of the reactant is assumed to be uniform for the 1D model. The governing relations are shown in Equations 10.72-10.75 and the boundary conditions are in Equations 10.76 – 10.79.

$$j_{T(9)} = -k_{(9)} \nabla T_{(9)} \approx -k_{(9)} \frac{dT_{(9)}}{dx} \quad (10.72)$$

$$j_{e(9)} = -\sigma_{e(9)} \nabla \varphi_{e(9)} \approx -\sigma_{e(9)} \frac{d\varphi_{e(9)}}{dx} \quad (10.73)$$

$$\frac{dj_{T(9)}}{dx} = \sigma_{e(9)} \left(\nabla \varphi_{e(9)} \right)^2 = -j_{e(9)} \nabla \varphi_{e(9)} \approx -j_{e(9)} \frac{d\varphi_{e(9)}}{dx} \quad (10.74)$$

$$\frac{dj_{e(9)}}{dx} = 0 \quad (10.75)$$

$$T_{(9)(8,9)} = T_{(8)(8,9)} \quad (10.76)$$

$$j_{T(9)(8,9)} = j_{T(8)(8,9)} \quad (10.77)$$

$$\varphi_{e(9)(8,9)} = \varphi_{e(8)(8,9)} \quad (10.78)$$

$$j_{e(9)(8,9)} = j_{e(8)(8,9)} \quad (10.79)$$

10.1.10 Cathode Flow Plate

The cathode flow plate is similar to the anode flow plate. The governing equations are shown in Equations 10.80 – 10.83 and the boundary conditions are shown in Equations 10.84 – 10.87.

$$j_{T(10)} = -k_{(10)} \nabla T_{(10)} \approx -k_{(10)} \frac{dT_{(10)}}{dx} \quad (10.80)$$

$$j_{e(10)} = -\sigma_{e(10)} \nabla \varphi_{e(10)} \approx -\sigma_{e(10)} \frac{d\varphi_{e(10)}}{dx} \quad (10.81)$$

$$\frac{dj_{T(10)}}{dx} = \sigma_{e(10)} \left(\nabla \varphi_{e(10)} \right)^2 = -j_{e(10)} \nabla \varphi_{e(10)} \approx -j_{e(10)} \frac{d\varphi_{e(10)}}{dx} \quad (10.82)$$

$$\frac{dj_{e(10)}}{dx} = 0 \quad (10.83)$$

$$T_{(10)(9,10)} = T_{(9)(9,10)} \quad (10.84)$$

$$j_{T(10)(9,10)} = j_{T(9)(9,10)} \quad (10.85)$$

$$\varphi_{e(10)(9,10)} = \varphi_{e(9)(9,10)} \quad (10.86)$$

$$j_{e(10)(9,10)} = j_{e(9)(9,10)} \quad (10.87)$$

10.1.11 Cathode Cooling Channel

The cathode cooling channel is the final segment in the 1D model. Like the anode cooling channel, Newtons Law of Cooling is used to determine the heat flux into the coolant stream, Equation 10.88. and the Dittus-Boelter relation are used to determine the convective heat transfer coefficient, Equation 10.90. The bulk temperature of the cooling channel is uniform for the 1D model.

$$j_{T(10,11)} = h_{(11)}(T_{(10,11)} - T_{(11)}) \quad (10.88)$$

$$Nu_{(11)} = \frac{h_{(11)}D_{H,(11)}}{k_{(11)}} \quad (10.89)$$

$$Nu_{(11)} = 0.023Re_{(11)}^{\frac{4}{5}}Pr_{(11)}^{0.4} \quad (10.90)$$

10.1.12 Cell Overpotentials

During the operation of the cell, losses dictate that voltages need to be more than the thermodynamically determined reversible potential required to drive the reaction forward. These losses are termed overpotentials, and three types of overpotentials were considered that have significant impact on the operation of the cell: electrode, proton flow, and concentration losses. Overpotentials associated with the electrodes are due to electro-kinetic limitations. These losses for the anode and cathode can be implicitly determined from the Butler-Volmer relationship given a current density value, Equation 10.32. Generally, protonic resistance is much greater than the electronic resistance in PEM cells. The voltage drop associated with the proton flow is assumed to account for all ohmic losses and are determined during the calculations of domains 5 – 7 and represented by $\varphi_{p(7)(7,8)}$.

Concentration losses were the final major overpotential included in the modeling. Changing the chemical composition of the working fluid is the objective of the cells in the CLHP. Hence, the impacts that the concentration of different chemical species have on the reaction will be of great importance. The Nernst equation relates how the concentration ratio of products to reactants influences the potentials within the cell, Equation 10.91 (Revankar et al. 2014). Products and reactants are determined via dehydrogenation of isopropanol to acetone taking place in the anode, and hydrogenation of acetone to isopropanol taking place in the cathode. The concentration at the catalyst interface after the diffusion layer is used.

$$\eta_{con} = \frac{RT}{n_e F} \ln \left(\frac{\prod C_{products}}{\prod C_{reactants}} \right) = \frac{RT}{n_e F} \ln \left(\frac{x_{ACTN(4)(4,5)} x_{IPA(8)(7,8)} P_{(9)}}{x_{IPA(4)(4,5)} x_{ACTN(8)(7,8)} P_0} \right) \quad (10.91)$$

10.1.13 Solution Procedure

Once defined, all domains need to be coupled together to simulate the cell performance in 1D. Each domain represents a 2-point boundary value problem. Within each domain, the solution is determined using the `solve_bvp` function from Python's SciPy package. The domains are solved sequentially, with the output boundary properties from one domain feeding into the input boundary conditions of the next. Figure 10.3.

As stated in the formulation of the boundary conditions, certain parameter values are not known beforehand. At the start of each run of the 1D model, the heat flux entering the anode cooling channel, the electron flux through the anode side of the cell, and the electronic potential at the cathode side of the membrane interface are all guessed. To check the validity of the guesses, three residual values are determined. These are the temperature at the cathode cooling channel interface needed to drive the calculated heat flux at that interface, Equation 10.92, the electronic potential at the end of the cathode flow plate, Equation 10.93, and the applied voltage relative to all the voltage losses across the cell, Equation 10.94.

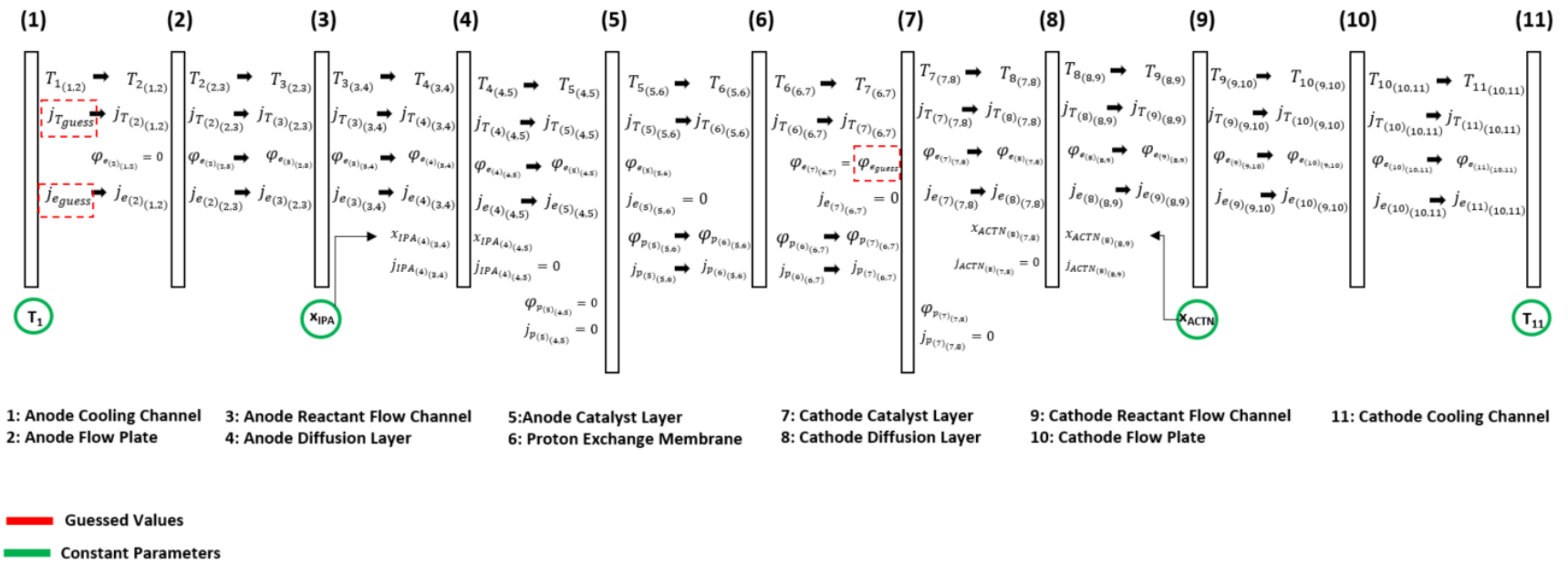


Figure 10.3: Calculation diagram for 1D cell model solution.

$$residual_1 = T_{(10)(10,11)} - \left(\frac{j_{T(10,11)}}{h_{(11)}} + T_{(11)} \right) \quad (10.92)$$

$$residual_2 = V_{applied} - \varphi_{e(10)(10,11)} \quad (10.93)$$

$$residual_3 = (V_o + \eta_a + \eta_c + \eta_m + \eta_{conc}) - V_{applied} \quad (10.94)$$

The solution procedure consists of attempting to minimize the value of the residuals. The Jacobean root solver, broyden1, from Python's SciPy package is used to iterate on the guess values. For the model to converge, each of these residuals are driven to a below a tolerance of 6e-6.

10.2 Parameter Identification

Most of the parameters used to describe the model could be referenced from literature. A list of some of the standard parameters used is given in Table 10.1.

Table 10.1: Constant parameters referenced from literature (Vetter et al. 2018).

Parameter	Value
$k_{FlowPlate}$	11 $\left[\frac{W}{m-K} \right]$
$k_{CatalystLayer}$	0.27 $\left[\frac{W}{m-K} \right]$
$k_{DiffusionLayer}$	1.6 $\left[\frac{W}{m-K} \right]$
k_{PEM}	0.3 $\left[\frac{W}{m-K} \right]$
$\sigma_{FlowPlate}$	1250 $\left[\frac{S}{m} \right]$
$\sigma_{DiffusionLayer}$	1250 $\left[\frac{S}{m} \right]$
$\sigma_{CatalystLayer}$	350 $\left[\frac{S}{m} \right]$

Two important aspects of the cell model that were not readily available in the literature were the electrode characteristics for isopropanol-acetone reactions, and the membrane conductivity. The performance of the electrodes was encapsulated in the exchange current density parameter (i_0) used in the Butler-Volmer relationship, Equation 10.32. Different estimates of i_0 have been made

for hydrogen-oxygen and methanol fuel cell systems using a limited number of catalyst materials. Such details for isopropanol reactions were not found in literature. Even if a list was published, it would be difficult to expand exchange current density data to other catalyst mixtures.

A method was needed for extracting exchange current density information from the experimental data obtained. Tests, such as cyclic voltammetry and electrochemical impedance spectroscopy, can be used to determine properties such as the exchange current density and membrane conductivity (Revankar et al. 2014). The experimental test setup developed for this project obtained voltage sweep data. This data could not easily be translated into exchange current and conductivity values. Other researchers have used methods of parameter fitting to estimate the exchange current densities and membrane conductivities (Hao et al. 2016, Vang et al. 2015, Fraser et al. 2008). In this method, a simple relationship accounting for the various voltage losses within the electrochemical cell is developed. Here, the reversible voltage determined from thermodynamics, the electrode voltage losses, and the membrane ohmic losses can be determined, Equation 10.95. Due to the slow rates of the reactions and relatively high reactant flow rates, mass transfer losses were assumed to be negligible. The electrode losses were determined from the Butler-Volmer relationship, Equation 10.32. The conductivity value was expressed using the Arrhenius relationship, Equation 10.47.

$$V_{cell} = V_0 + \eta_{electrode} + \frac{t_{mem}}{\sigma_p} j \quad (10.95)$$

Three unknown parameters needed to be determined. These were the exchange current density (i_0), the membrane activation energy (E_A), and the membrane reference conductivity (σ_0). The parameter fitting process was applied to 20 of the catalyst combinations previously tested. The procedure for determining the parameters was as follows:

1. Voltage-current relationship for a single catalyst combination extracted at multiple temperatures.
2. Equation 10.95 used to determine the expected voltage for each current value tested.
3. Genetic optimization algorithm (James et al., 2016) used to vary the unknown parameters to minimize the error between the measured voltages and the calculated values, Equation 10.96.

$$error = \sum_N \left(\frac{V_{calc,i} - V_{meas,i}}{V_{meas,i}} \right)^2 \quad (10.96)$$

The estimated parameters determined by the fitting procedure for the 20 catalyst combinations, are shown in Table 10.2.

Table 10.2: Results of parameter fitting to determine membrane and electrode properties.

Catalyst Combination	Reference Membrane Conductivity (σ_0) [S-m]	Membrane Activation Energy (E_A) [eV]	Exchange Current Density (j_0) [A/m^2_t]	Model Error
Pt	0.000136457	0.019235595	0.008713652	0.5404
PtSn	0.015675706	0.107153778	4.974999792	0.6028
PtNi	9.22E-06	-0.065935169	0.01029617	0.2147
PtCu	0.016945722	0.115893885	0.000134837	0.5627
PtCo	0.001233059	0.070834518	0.002630635	0.5792
PtAg	0.097011049	0.209422435	0.000432226	0.2719
PtIr	0.007448315	0.124279977	0.014266161	0.2845
PtRh	0.007188239	0.117798638	0.00923535	0.2066
PtPd	0.0126146	0.155213021	0.011806577	0.2361
PtRuCu	0.004747724	0.127991546	0.816615906	0.2221
PtRuCo	0.000714715	-0.020342123	2.850105526	1.3019
PtRuAg	0.000146147	0.043036923	0.001188638	0.3890
PtRuAu	0.001763244	0.080965548	0.00023252	0.3383
PtSnCo	0.00287055	0.10705918	0.002126019	0.2169
PtSnAu	0.080018763	0.168503742	0.19270998	0.2257
PtSnIr	0.00801931	0.129217884	0.083679306	0.1904
PtRu _{0.60} Co _{0.40}	0.001162764	0.016369078	5.321685545	1.3585
PtRu _{0.40} Co _{0.60}	0.006147897	0.062004913	5.500147569	0.6692
PtRu _{0.33} Co _{0.33} Cu _{0.33}	1.98E-05	-0.085063674	0.964681536	1.3368
PtRu _{0.55} Co _{0.10} Au _{0.35}	0.008872954	0.094740103	1.981677915	1.2062
Au _{0.75} Cu _{0.25}	0.001031115	0.023782812	2.923181875	1.6861
PtRu _{0.60} Co _{0.25} Au _{0.15}	0.015968695	0.094558367	10.80689432	0.5861

Variations in the predicted conductivity values of the sPEEK membranes were believed to be attributed to differences in the membrane fabrication process. Many steps where the membrane was exposed to drying were performed manually and as such for varying durations of time. This was believed to lead to variations in the final properties of the prepared membranes, even though similar fabrication procedures were followed. The literature on anhydrous sPEEK membranes

with similar characteristics has also shown order of magnitude differences between reported conductivities (Li et al. 2010, Jothi et al. 2014, He et al. 2014, Wang et al. 2015).

10.3 Predicting Exchange Current Density

The exchange current density is a property of the catalyst composition and structure. As previously mentioned, the catalyst materials exist as nanoparticles. The calculated exchange current density from the parameter fitting method was determined relative to the projected area of the cell electrode. A more useful design parameter would be the exchange current density relative to the actual surface area of the catalyst material present (Woodroof, et al. 2015). Using the diameter of the catalyst nanoparticles in nm and the density of the catalyst metal in g/cm^3 , the expression in Equation 10.97 (Tamizhmani et al. 1996 and Krishnamurthy et al. 2009) can be used to estimate the specific surface area of the catalyst material. When mixtures were present, mass weighted properties were used for the density and particle diameter.

$$SA_{cat} = \frac{6000}{\rho_{cat}d_{cat}} \quad (10.97)$$

Previously DFT calculated binding energies were used to predict catalyst performance as determined by overall cell conductivities. A similar approach was applied to the prediction of surface area specific exchange current densities given the effective binding energies of a catalyst mixture. An activity plot showing the relationship between the binding energies of OH and O descriptors is shown in Figure 10.4. Similar to the previous activity plots, a region of high activity emerged.

10.4 2D Model

With the identification of conductivity and exchange current density parameters, the 1D model could be utilized to determine the heat, mass, and charge transfers across the cell domains. The final step in the model development was the extension of the 1D model to a 2D model. In the CLHP, cell properties such as reactant concentration and coolant temperature will vary along the direction of the flow. To help capture these effects, a 2D model was needed. To do this a 2-dimensional domain is discretized into segments along the y-direction, Figure 10.5. The

properties in each segment are approximated using calculations from the 1D model. The output coolant temperature and reactant concentrations from the previous domain are fed in as inputs to the next domain.

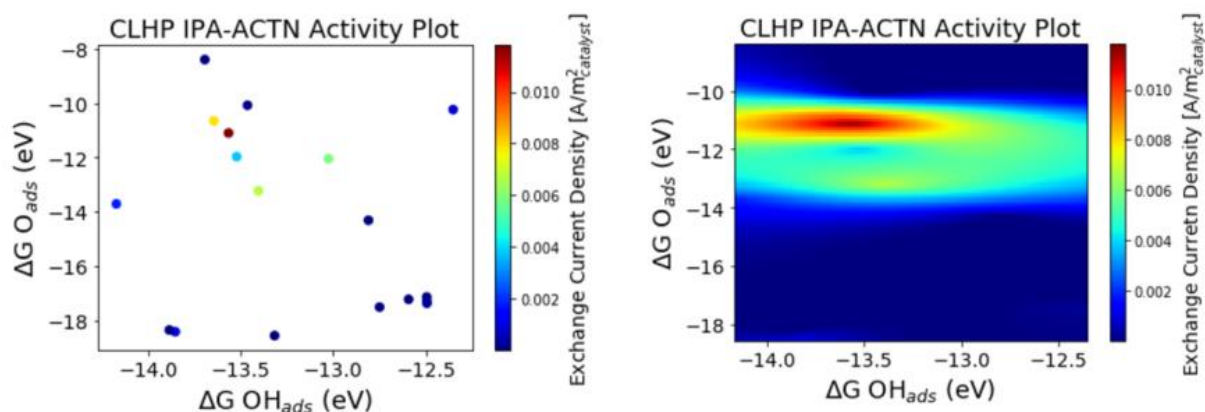


Figure 10.4: Activity plots based on DFT calculated binding energies and catalyst area specific exchange current densities determined through parameter fitting.

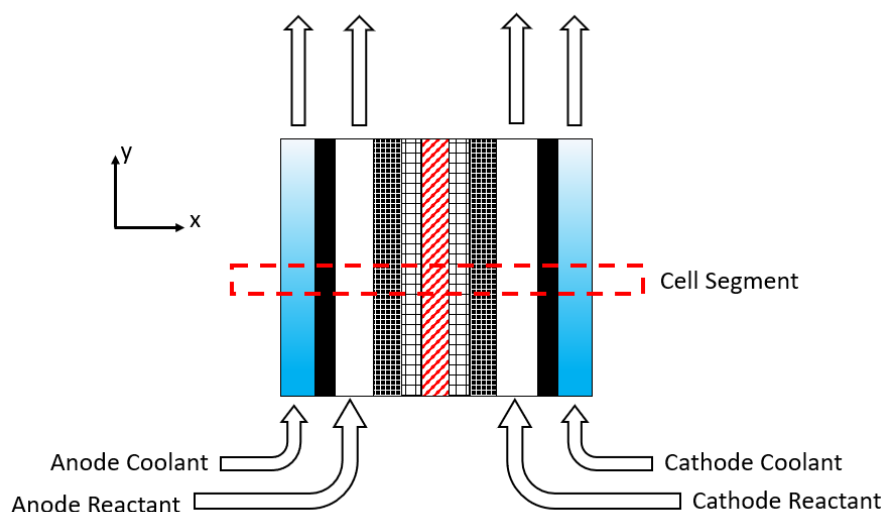


Figure 10.5: Flow through 2D cell model showing a discretization region.

The temperature values in the 1D model are ultimately based on the boundary temperatures of the cell assembly imposed by the coolant temperatures. In each segment, the coolant temperature is uniform. The heat flux to the coolant is also determined by the 1D model. Knowing the heat flux to the coolant, the cross-sectional area of the cell segment, and coolant flow rate, the coolant

temperature change from one 1D segment to the next along the y-direction could be calculated using Equations 10.98 – 10.99.

$$T_{(1)i+1} = \frac{j_{T(1,2)_i} A_{segment}}{\dot{m}_{(1)} \cdot c_{p(1)}} + T_{1(i)} \quad (10.98)$$

$$T_{(11)i+1} = \frac{j_{T(10,11)_i} A_{segment}}{\dot{m}_{(11)} \cdot c_{p(11)}} + T_{11(i)} \quad (10.99)$$

The pressure drops in the coolant channels and the anode reactant channel are calculated using head loss equations for 1-phase laminar fluid flow, Equation 10.100 (Fox et al. 2009). Here the distance travelled for the pressure drop ($L_{\Delta P}$) is the length of the cell segment in the y-direction.

$$\Delta P_{(1ph)} = f \frac{L_{\Delta P}}{D_h} \frac{\bar{v}^2}{2} \quad (10.100)$$

For the CLHP reactor, the flow in the cathode channel consists of a 2-phase mixture. The pressure drop of the two-phase mixture is calculated using correlations from Shannak (2008) in Equations 10.101- 10.102.

$$Re_{(2ph)} = \frac{m_{(2ph)} d \left[x_q^2 + (1-x_q)^2 \left(\frac{\rho_g}{\rho_f} \right) \right]}{\mu_g x_q + \mu_f (1-x_q) \left(\frac{\rho_g}{\rho_f} \right)} \quad (10.101)$$

$$\Delta P = L_{\Delta P} f \frac{1}{D_h} \frac{m_{(2ph)}^2}{2\rho_{(2ph)}} \quad (10.102)$$

One of the main property changes of interest along the y-direction of the cell is the concentration of the reactants in the anode and cathode channels. The molar conversion flux is calculated from Faraday's Law using Equation 10.25 for the anode chamber and a similar expression for the cathode chamber. Using the molar flux and the specified molar flow rates of the reactants, the concentration change along the y-direction of isopropanol in the anode and acetone in the cathode chamber are given using equations 10.103 and 10.104, respectively.

$$x_{IPA(3)i+1} = \frac{x_{IPA(3)_i} \dot{n}_{(3)} - j_{IPA(3)} A_{segment}}{\dot{n}_{(3)}} \quad (10.103)$$

$$x_{ACTN(9)_{i+1}} = \frac{x_{ACTN(9)_i} \dot{n}_{(9)} - j_{ACTN(9)} A_{segment}}{\dot{n}_{(9)}} \quad (10.104)$$

10.5 Validation Studies

Once expanded into 2 dimensions, the cell model was ready to be validated against experimental data. The model's active area was set to 20 cm² and the thicknesses of the domains were set as follows in order to resemble the dimensions of the experimental setup. The flow plates were 6350 μm, the reactant channels were 1000 μm, the diffusion layers were 160 μm, and the membrane was 130 μm. The catalyst layer thicknesses were functions of the catalyst loading. During the validation process, the coolant inlet temperature was set to reflect the operation temperature of the cell.

The 2D cell model was discretized into 25 evenly sized segments along the y-direction. MEA combinations from the catalyst selection testing were run through the 2D model using the electrode and membrane parameters determined from the previous parameter fitting operation. Only low voltage tests of interest to CLHP operation were considered (<0.5 V). The results of the validation are shown in Figure 10.6. Over 75% of the tested points landed within 10 mA of the predicted current value.

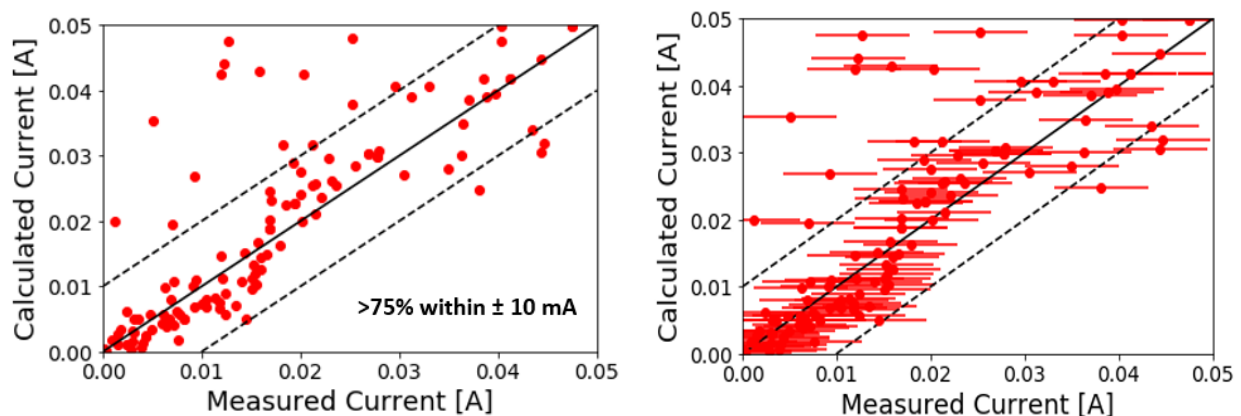


Figure 10.6: Parity plots with and without error bars showing the calculated cell currents from the 2D model and the measured currents from the experimental setup.

Unfortunately, the cell currents were too low, and the flow rates were too high for any appreciable conversion rates to be measured with the equipment present. Having only overall current values for comparisons was insufficient for a rigorous subcomponent validation of the model. Two steps were taken to further assess the model's viability. First, a separate electrochemical device was modeled based on parameters described in the literature and then compared to published results. Secondly, the influence of varying cell parameters was compared to trends observed in the literature for similar electrochemical cells.

PEM electrolyzers have been continually studied as a means of generating clean hydrogen. Since both electrolyzers and the CLHP reactor are PEM based power consuming devices, the 2D model could easily be adapted to simulate both devices. A PEM electrolyzer described and tested by Abdin et al. (2015) was simulated using the developed 2D cell model. To modify the model to represent a PEM water electrolyzer, the membrane conductivity was updated to represent Nafion, and the exchange current densities of the electrodes were changed to match those of typical electrolyzer systems. These devices are typically operated with an excess of reactants and as such no concentration changes were assumed along the direction of the flow. The reversible voltage was changed to match that of the water splitting process. For a given applied voltage, a resulting current through the electrolyzer could be determined. Figure 10.7 shows a parity plot of the measured and calculated current densities flowing through the electrolyzer for multiple operation temperatures. From these results, it can be seen that the 2D model can capture the performance trends of the electrolyzer device.

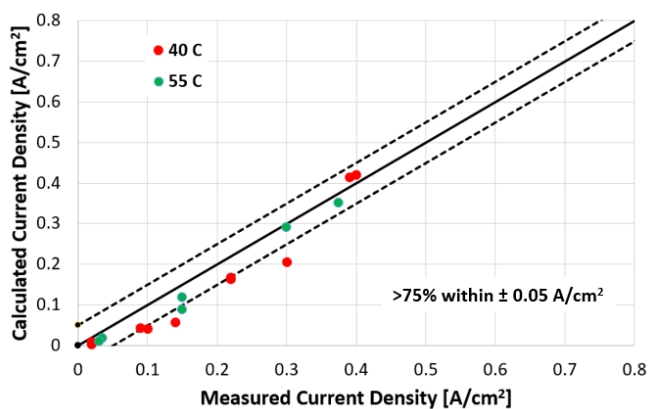


Figure 10.7: Accuracy of 2D cell model in simulating PEM electrolyzer.

The next step in understanding whether the model performed as expected, was to compare experimental trends observed in the literature for PEM electrochemical cells to the simulated trends produced by the model. The CLHP device operates at much lower voltages and currents than many typical electrochemical systems. Therefore, what was of interest in the following comparisons were not the absolute values of the properties, but rather the nature and shape of the property relationships.

The first trend investigated was the effect of the applied voltage on the current density within the cell. The voltage efficiency as defined earlier, relates the thermodynamic minimum required voltage needed to drive a reaction to the actual voltage application. A PEM water electrolyzer study (Laoun et al. 2008) was used to compare trends with the CLHP cell model. Figure 10.8a depicts the relationship between voltage efficiency and current density for the CLHP cell model and Figure 10.8b shows the trend for the Laoun et al. (2008) electrolyzer. The PEM water electrolyzer operated at over 10 times higher voltages than the CLHP cell, employed a perfectly hydrated Nafion membrane with high conductivity, and did not experience concentration losses. All of these factors aided in producing the much higher current densities than the CLHP cell, which were validated by experimental results. Both cells experience negative slopes in their voltage current relationships with a notable inflection point.

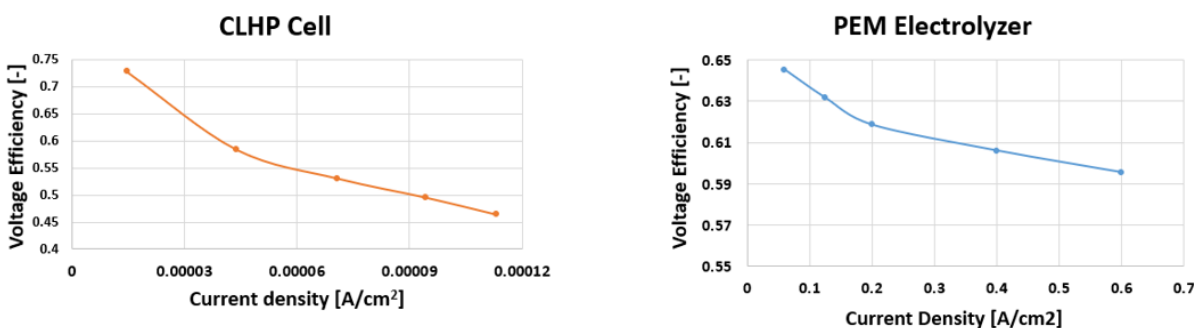


Figure 10.8: Voltage trends between modeled CLHP cell (a) and PEM electrolyzer values (b) from Laoun et al. (2008).

Another cell trend investigated was the relationship between the membrane thickness and the current density. The membrane needs to be thick enough to have the mechanical strength to not

get damaged during operation, but also thin enough to reduce the resistance to proton conduction. For a constant applied voltage, it should be expected that the resistance through a cell should decrease as the membrane thickness decreases. This should lead to higher currents for thinner membranes. PEM electrolyzer data from Laoun et al. 2008 was used to see if the CLHP model would follow the expected trend. Figure 10.9a and 10.9b show that as membrane thickness increases, cell resistance increases and cell current decreases.

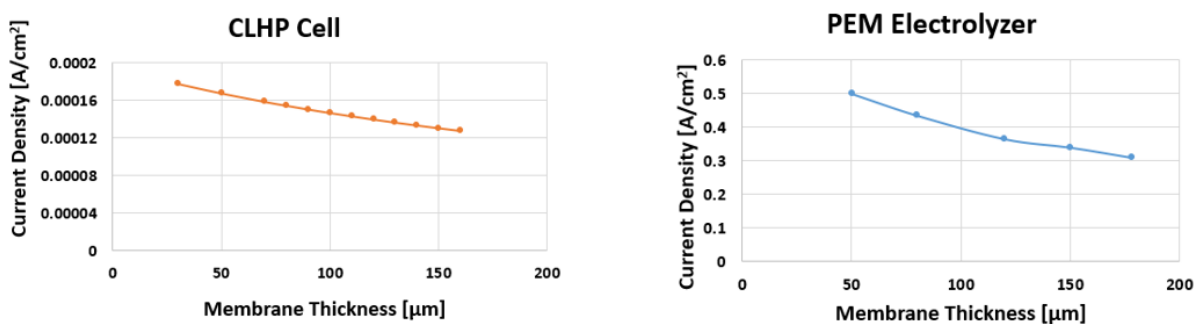


Figure 10.9: Membrane thickness trends between modeled CLHP cell (a) and PEM electrolyzer values (b) from Laoun et al. (2008).

Another aspect of the cell model that was investigated was how the catalyst loading affected the cell performance. As more and more catalyst materials are deposited on the membrane surface to form the electrode, more area becomes available for reactions to take place which can reduce electrode losses. At the same time, the catalyst layer will become thicker. This will introduce more ohmic resistance to protons generated in the catalyst layer. As shown by results obtained from PEM water electrolysis (Nguyen, 2018), and methanol fuel cells (Zhu et al., 2002) in Figures 10.10a and 10.10b, a peak current occurs at an intermediate catalyst loading. The shape and location of this peak will be dependent on the cell operating conditions and reactants used in the cell. The response of the CLHP model to various catalyst loadings is shown in Figure 10.11. Though the decline is initially small, there is similarly a peak that occurs in the current density.

The next comparison used to determine whether the CLHP cell model followed expected trends was looking into the influence of the catalyst carbon fraction. As previously mentioned, the catalyst powder consisted of metallic nanoparticles suspended on larger carbon clusters. The

mass ratio between the carbon and the metallic particles is a design parameter that can be controlled by catalyst manufacturers. Figure 10.12b shows the effect of the catalyst carbon fraction on a methanol fuel cell (Zhu et al. 2002) and Figure 10.12a shows the influence of carbon fraction on the CLHP model. Though the CLHP cell model's current density does not stay truly constant for lower current densities, both the CLHP model's results and the methanol fuel cell results experience sudden drop offs in current at higher carbon fraction values.

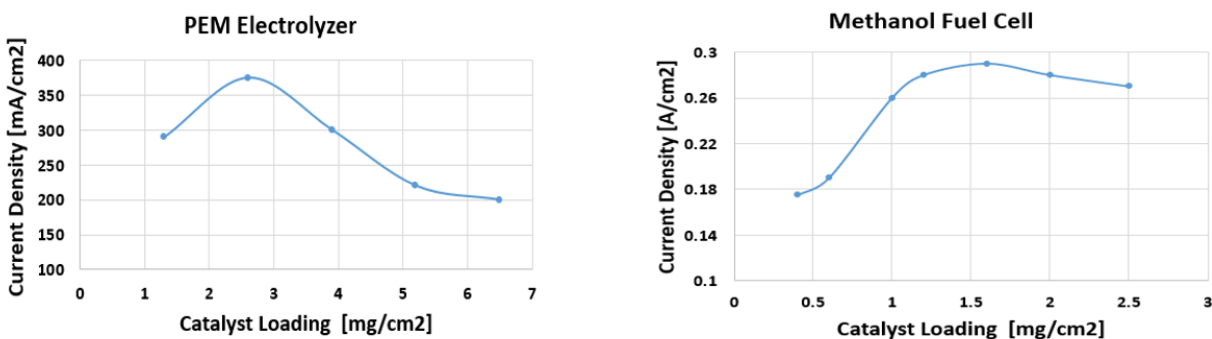


Figure 10.10: Catalyst loading influence on PEM electrolyzer (Nguyen, 2018) (a) and methanol fuel cell (Zhu et al. 2002) (b).

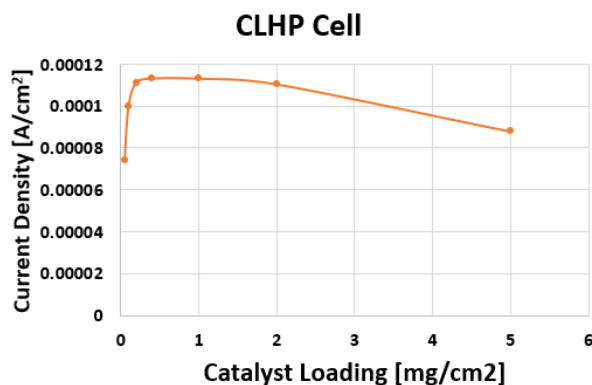


Figure 10.11: Results from CLHP model on the influence of the catalyst layer.

The final trend observed was that of the influence of the reactant flow rate on the voltage efficiency of the cell. Here, the performance of a fuel cell using 1M isopropanol (Qi et al. 2002) was used for comparison. The results of the influence of mass flow rate on the voltage efficiency of the CLHP cell and the isopropanol fuel cell both show increasing trends with increasing reactant flow rates, Figure 10.13. The voltage efficiency of the CLHP cell begins to level off

over the range modeled while the data from Qi et al. (2002) continues to rise. This is most likely due to the fact that Qi et al. (2002) did not measure their flow rates to sufficiently high levels to reach a level region.

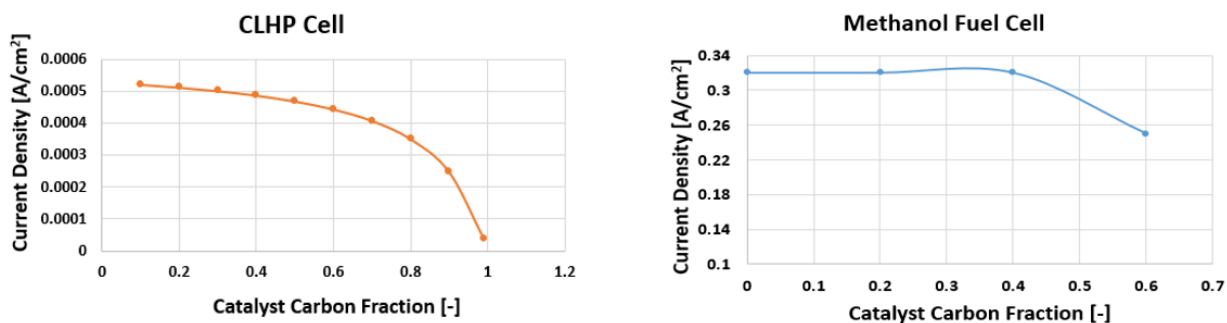


Figure 10.12: Results from CLHP model prediction of influence of carbon fraction (a) and influence of carbon fraction on methanol fuel cell (b) (Zhu et al. 2002).

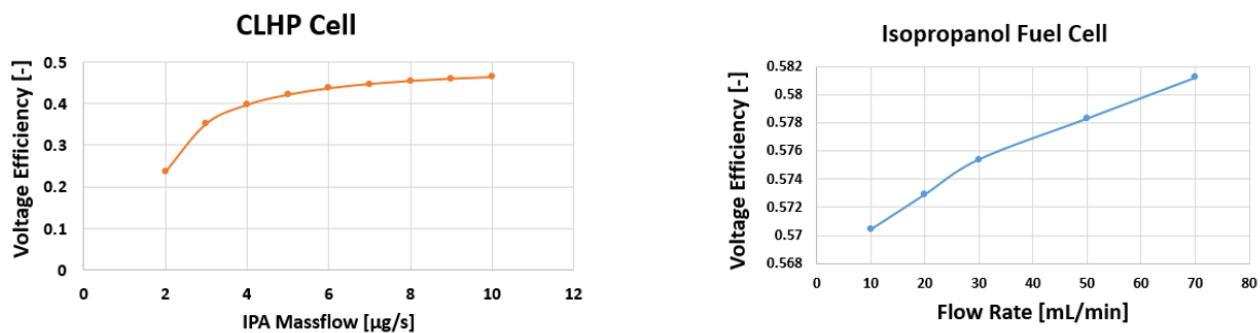


Figure 10.13: Influence of reactant mass flow rate on voltage efficiency for CLHP cell model and isopropanol fuel cell (Qi et al. 2002).

The validation against experimentally determined cell currents for the CLHP and PEM water electrolyzer applications, as well as the general agreement between the sub-model's predicted trends and those found in literature increased confidence in the developed cell model's ability to predict the performance of an actual cell used in the CLHP system.

10.6 Cell Sensitivity Analysis

One of the most beneficial aspects of the model is that it allows for the investigation of the impact of design parameters on the operation of the cell. Baseline parameters were established as shown in Table 10. 3, and various cell parameters were individually varied to assess their impact on the electrochemical cell. As previously described, the thickness of the catalyst layer is a derived property of the catalyst content. Water was used as the cell coolant.

Three parameters were used to evaluate the performance of the cell. These were the conversion efficiency, the voltage efficiency, and the total efficiency. The conversion efficiency denotes the extent to which the reactant stream is fully consumed and converted into products, Equation 10.105. The voltage efficiency is defined by summing the contributions to the overall power consumption in each cell segment. Rather than just using the reversible voltage value, the minimum voltage value was taken as the reversible voltage plus the concentration overpotential, Equation 10.106. This is used because the concentration voltage is a thermodynamically imposed quantity that is not influenced by design parameters. The total efficiency is taken as the product of the conversion and voltage efficiencies, Equation 10.107.

Table 10.3: Baseline Parameters for Sensitivity Study.

Parameter	Value	Units	Layer Thickness	Value	Units
$T_{coolant}$	30	°C	anode cooling channel	100	μm
$P_{coolant}$	200	kPa	anode flow plate	6350	μm
$P_{cathode}$	20	kPa	anode reactant channel	1016	μm
P_{anode}	50	kPa	anode diffusion layer	160	μm
$\dot{m}_{coolant}$	0.5	g/s	anode catalyst layer	-	μm
\dot{m}_{anode}	10	μg/s	PEM	130	μm
cell area	100	cm ²	cathode catalyst layer	-	μm
catalyst loading	0.4	mg/cm ²	cathode diffusion layer	160	μm
particle size	2.1	nm	cathode reactant channel	1016	μm
i_0 catalyst	0.006716	A/m ² -catalyst	cathode flow plate	6350	μm
carbon fraction	0.68	-	cathode cooling channel	100	
voltage	0.05	V			
$\sigma_{o_{SPEEK}}$	1.03e-3	S-m			
$E_{A_{SPEEK}}$	0.02378	eV			

$$\eta_{conv} = \frac{x_{IPAin_{anode}} - x_{IPAout_{anode}}}{x_{IPAin_{anode}}} \quad (10.105)$$

$$\eta_v = \frac{V \sum_i i_{segment_i}}{\sum_i V_{0_i} i_{segment_i} + \sum_i \eta_{conc_i} i_{segment_i}} \quad (10.106)$$

$$\eta_{tot} = \eta_{conv} \eta_v \quad (10.107)$$

The influence of the active area on the cell performance is shown in Figure 10.14. For fixed cell conditions, the efficiencies of the cell appeared to increase with higher surface areas up to a point until it plateaued. The coolant temperature's effect on the cell efficiencies is shown in Figure 10.15. As the temperature increased, the conversion efficiency dropped. This was caused by the concentration loss term increasing with temperature which limited the maximum concentration that could be achieved for the given applied voltage. The voltage efficiency increased with increased coolant temperature. This was due to proton conductivity and electrode kinetics improving at higher temperatures.

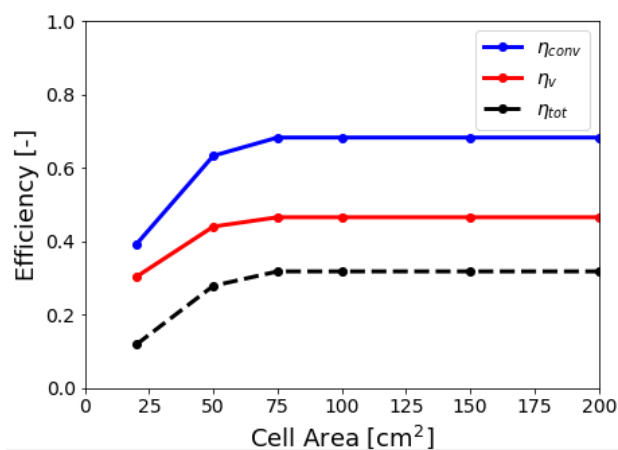


Figure 10.14: Sensitivity study on cell area.

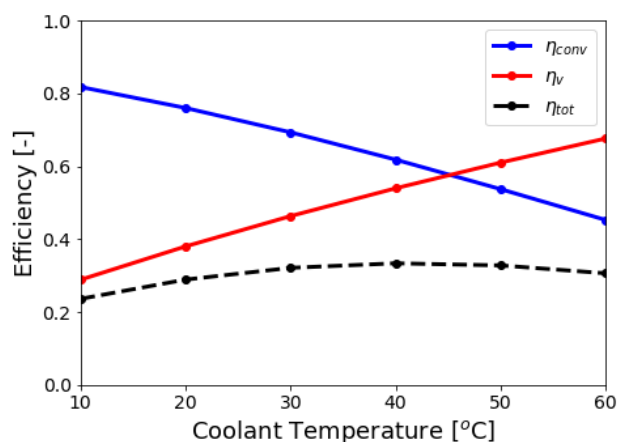


Figure 10.15: Sensitivity study on coolant temperature.

The change in cell performance with cathode pressure is shown in Figure 10.16. Here, the conversion efficiency increased at higher pressures while the voltage efficiency decreased at high pressures. This was again due the changes in the concentration overpotential, with higher pressures leading to lower concentration gradients. The influence of the reactant flow rate entering the anode is shown in Figure 10.17. At lower flow rates, the reactant resides longer in the cell allowing for higher conversion efficiencies. There was an initial rise in the voltage efficiency then as the conversion efficiency decreased at higher flow rates, the concentration

term in the denominator of Equation 10.106 decreased. This reduced the minimum voltage requirements which decreased the voltage efficiency for the same ohmic and electro kinetic losses.

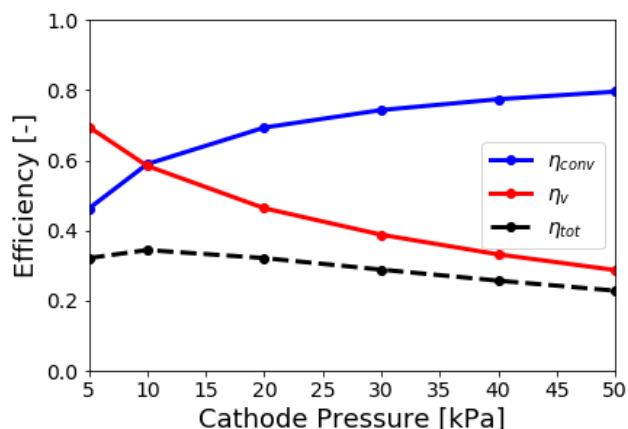


Figure 10.16: Sensitivity analysis for cathode pressure.

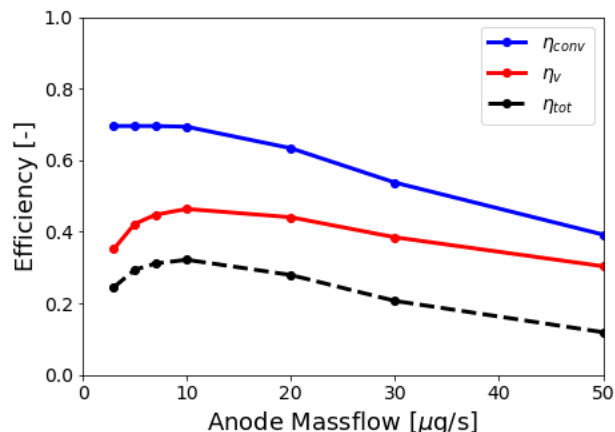


Figure 10.17: Sensitivity analysis for anode flow rate.

For most of the range investigated, the coolant mass flow had minimal effect on the cell performance metrics, Figure 10.18. At very low coolant flow rates, the cell temperature would rise leading to a slight uptick in voltage efficiency and decrease in conversion efficiency. In Figure 10.19, the impact of the catalyst loading is illustrated. At higher catalyst loadings, the electro-kinetic losses decrease leading to the initial rise in performance. As the loading increases, the thickness of the catalyst layer also rises. This eventually leads to drops in performance through increased ohmic losses.

Catalyst properties, such as particle diameter, exchange current density, and the mass fraction of carbon can also influence the cell performance, as shown in Figures 10.20 – 10.22. The particle diameter in the range of interest had minimal impact on performance. Increases in the exchange current density improved cell performance to a point until a plateau was reached. The catalyst carbon fraction only began to strongly influence the cell performance once the carbon content exceeded ~90%.

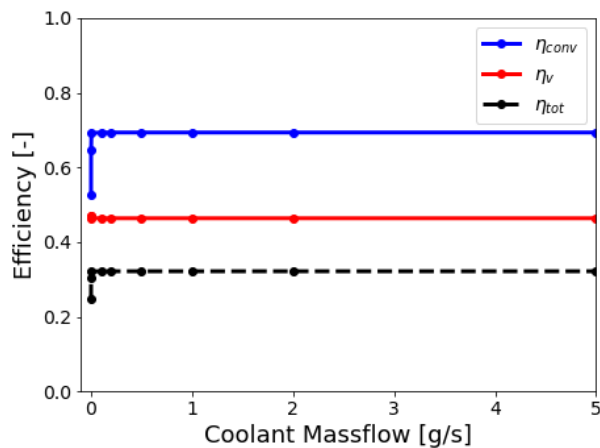


Figure 10.18: Sensitivity analysis for coolant mass flow.

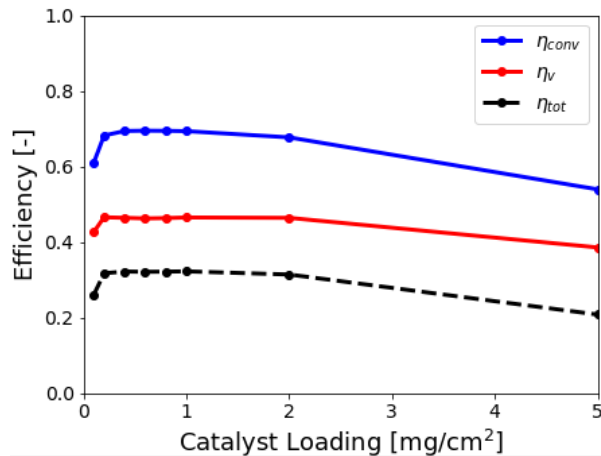


Figure 10.19: Sensitivity analysis for catalyst loading.

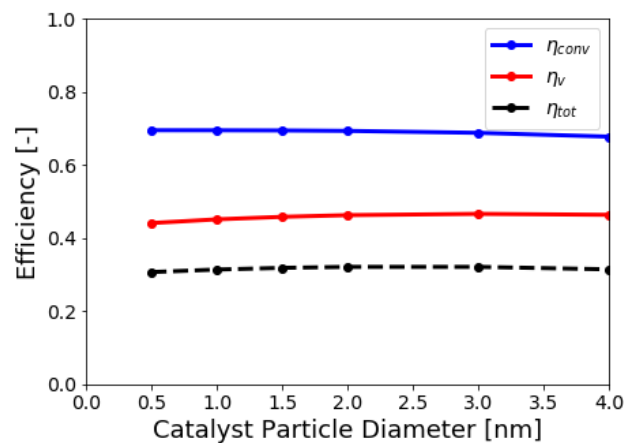


Figure 10.20: Sensitivity analysis for particle diameter.

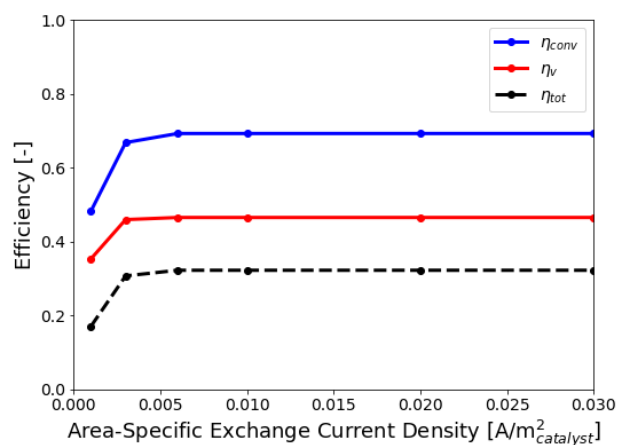


Figure 10.21: Sensitivity analysis for exchange current density.

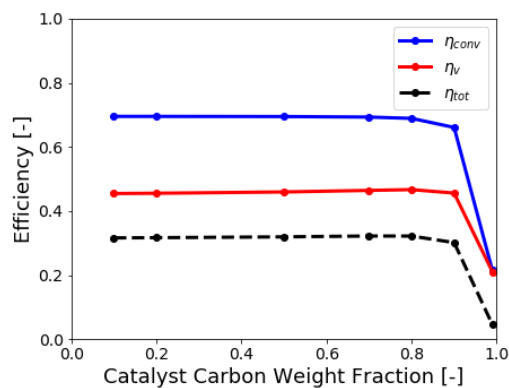


Figure 10.22: Sensitivity analysis for catalyst carbon fraction.

The effects of the cooling channel thickness are shown in Figures 10.23 and 10.24. In addition to the cell efficiency metrics, the influence of the coolant channel size on the pressure drop across the channel is also shown. The channel size had a negligible impact on the cell efficiency over the range investigated, but the pressure drop did increase for thinner channels.

The anode flow plate thickness and diffusion layer thickness have minimal impact on the cell performance over the range investigated, Figures 10.25 and 10.26. The flow plate is highly conductive, so the voltage drop across the plate is negligible compared to other cell losses regardless of minor changes in the plate thickness. The diffusion layer thickness has minimal effect on the cell performance since the cell operates at low currents. At these reaction rates, the reactants have sufficient time to diffuse to the reaction site so there were no appreciable mass transfer losses related to diffusion.

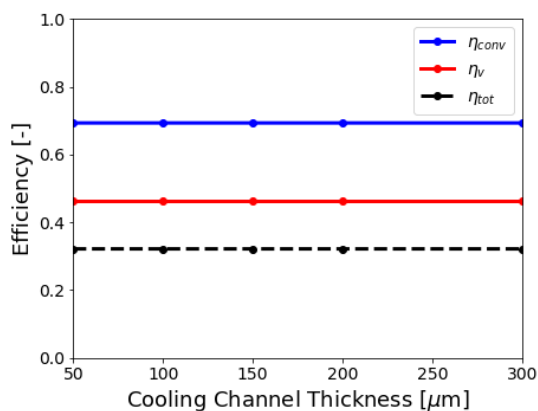


Figure 10.23: Sensitivity analysis for cooling channel thickness.

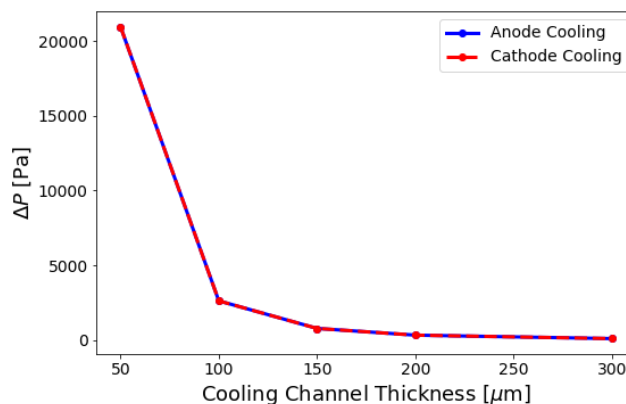


Figure 10.24: Impact of cooling channel thickness on coolant pressure drop.

The impacts of the anode and cathode reactant flow channel thicknesses are shown in Figures 10.27 – 10.29. The flow channel thickness had little impact on the cell efficiencies. The channel thickness did, however, have a notable impact on the pressure drop of the reactants. The anode channel contains liquid throughout its operation. The cathode channel contained a 2-phase mixture and as such had higher pressure drops than the anode channel.

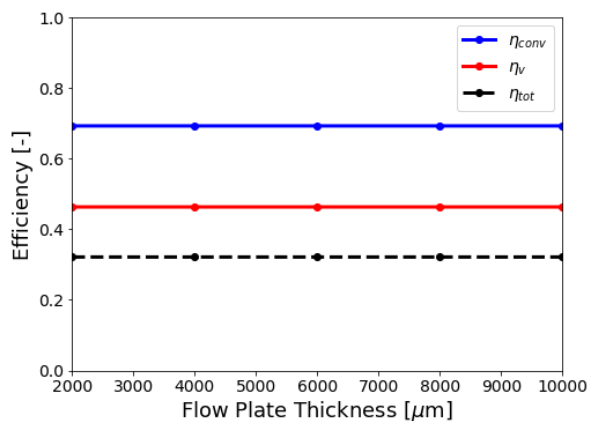


Figure 10.25: Sensitivity analysis for flow plate thickness.

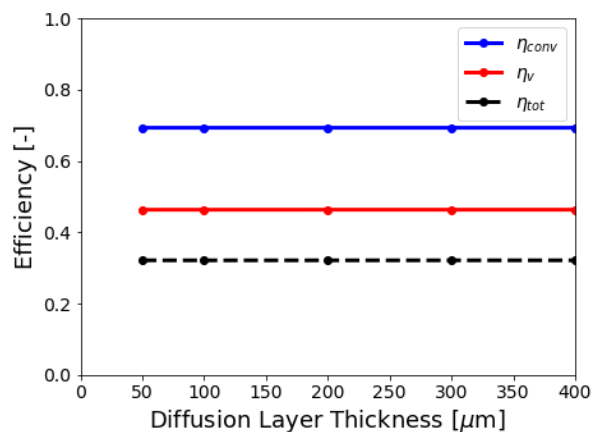


Figure 10.26: Sensitivity analysis for diffusion layer thickness.

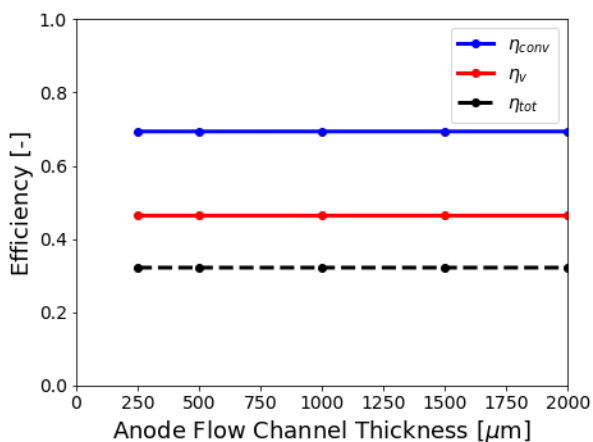


Figure 10.27: Sensitivity analysis for anode channel.

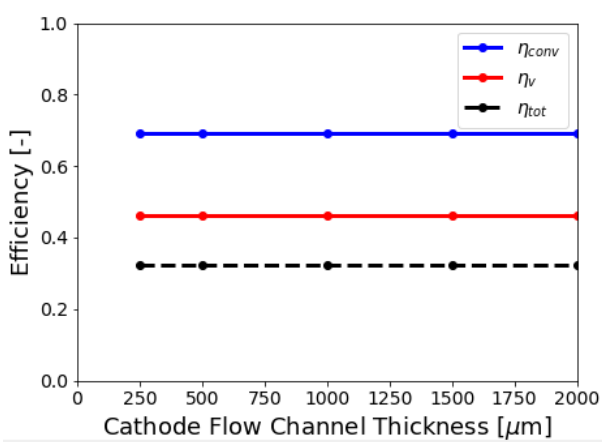


Figure 10.28: Sensitivity analysis for cathode channel.

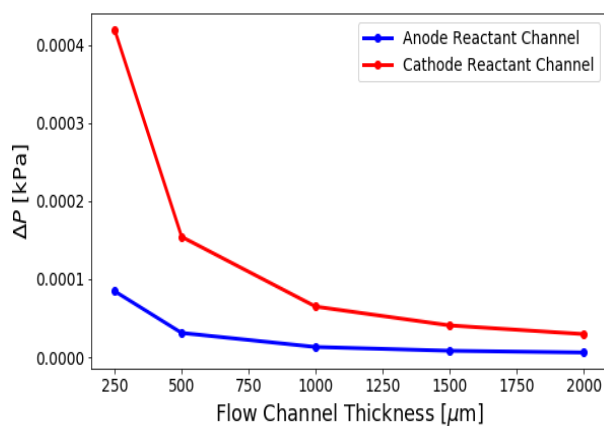


Figure 10.29: Pressure drops in anode and cathode channels.

The cell model has been exercised to assess the impact of varying various cell parameters on the efficiency of the device. To determine the ideal parameter combinations for a particular application, an optimization routine can be used in conjunction with the cell model to reduce losses and maximize performance.

10.7 References

- Adbin, Z., Webb, C., Gray, E., 2015. Modelling and simulation of a proton exchange membrane (PEM) electrolyser cell. *International Journal of Hydrogen Energy*, vol. 40, p. 13243-13257.
- Bird, R., Stewart, W., Lightfoot, E., 2002. *Transport Phenomena*, 2nd Edition, John Wiley & Sons, New York
- Fox, R., Pritchard, P., McDonald, A., 2009. *Introduction to Fluid Mechanics*. John Wiley and Sons, Inc.
- Fraser, S., Hacker, V., 2008. An empirical fuel cell polarization curve fitting equation for small current densities and no-load operation. *Journal of Applied Electrochemistry*, vol. 38, p. 451-456.
- Hao, D., Shen, J., Hou, Y., Zhou, Y., Wang, H., 2016. An Improved Empirical Fuel Cell Polarization Curve Model Based on Review Analysis. *International Journal of Chemical Engineering*, vol. 2016
- He, Y., Wang, J., Zhang, H., Zhang, T., Zhang, B., Cao, S., Liu, J., 2014. Polydopamine-modified graphene oxide nanocomposite membrane for proton exchange membrane fuel cell under anhydrous conditions. *Journal of Materials Chemistry A*, vol. 2, p. 9548
- Incropera, F., Dewitt, D., Bergman, T., Lavine, A., 2007. *Introduction to Heat Transfer*, John Wiley and Sons, 5th Edition.

- James, N., Braun, J., Groll, E., Horton, W., 2016. Semi-empirical modeling and analysis of oil flooded R410A scroll compressors with liquid injection for use in vapor compression systems. *International Journal of Refrigeration*, vol. 66, p. 50-63
- Jothi, P., Dharmalingam, S., 2014. An efficient proton conducting electrolyte membrane for high temperature fuel cell in aqueous-free medium. *Journal of Membrane Science*, vol. 450, p. 389-396.
- Krishnamurthy, B., Deepalochani, S., 2009. Performance of Platinum Black and Supported Platinum Catalysts in a Direct Methanol Fuel Cell. *International Journal of Electrochemical Science*. Vol. 4, p. 386-395.
- Laoun, B., Belhamel, M., Naceur, W., Serir, L., 2008. Electrochemical Aided Model to Study Solid Polymer Electrolyte Water Electrolysis. *Revue des Energies Renouvelables*, vol. 11, p. 267-276.
- Li, W., Manthiram, A., Guiver, M., 2010. Acid–base blend membranes consisting of sulfonated poly(ether ether ketone) and 5-amino-benzotriazole tethered polysulfone for DMFC. *Journal of Membrane Science*, vol. 362, p. 289-297
- Nguyen, T., 2018. The Effect of Anode Catalyst Loading on the Performance of Polymer Electrolyte Membrane Water Electrolyzers. *Proceedings of Academicsera 14th International Conference, Osaka, Japan, March 9-10*
- Qi, Z., Kaufman, A., 2002. Performance of 2-propanol in direct-oxidation fuel cells. *Journal of Power Sources*, vol. 112, p. 121-129.
- Revankar, S., Majumdar, P., 2014. *Fuel Cells: Principles, Design and Analysis*, Taylor and Francis Group Publishing

- Shannak, B., 2008. Frictional pressure drop of gas liquid two-phase flow in pipes. *Nuclear Engineering and Design*. Vol. 238, p. 3277 – 3284.
- Tamizhmani, G., Dodelet, J., Guay, D., 1996. Crystallite Size Effects of Carbon-Supported Platinum on Oxygen Reduction in Liquid Acids, *Journal of the Electrochemical Society*, vol. 143, p. 18 – 23.
- Vang, J., Zhou, F., Andreasen, S., Kaer, S., 2015. Estimating Important Electrode Parameters of High Temperature PEM Fuel Cells by Fitting a Model to Polarisation Curves and Impedance Spectra. *ECS Transactions*, vol. 68, p.13 – 34.
- Vetter, R., Schumacher, J., 2018. Free open reference implementation of a two-phase PEM fuel cell model. *Computer Physics Communications*, vol. 234, p. 223-234
- Wang, J., Bai, H., Zhang, H., Zhao, L., Chen, H., Li., 2015. Anhydrous proton exchange membrane of sulfonated poly(ether ether ketone) enabled by polydopamine-modified silica nanoparticles. *Electrochimica Acta*, vol. 152, p. 443-455.
- Weber, A., Newman, J., 2004. Transport in Polymer-Electrolyte Membranes II. Mathematical Model. *Journal of the Electrochemical Society*, vol. 151, p. A311-A325.
- Weber, A., Borup, R., Darling, R., Das, P., Dursch, T., Gu, W., Hervey, D., Kusogulu, A., Litster, S., Mench, M., Mukundan, R., Owerjan, J., Pharoah, J., Secanell, M., Zenyuk, I., 2014. A Critical review of Modeling Transport Phenomena in Polymer-Electrolyte Fuel Cells. *Journal of the Electrochemical Society*, vol. 161, p. F1254-F1299.
- Wilhelm, E., Barrino, R., 1971. Estimation of Lennard-Jones (6,12) Pair Potential Parameters from Gas Solubility Data. *The Journal of Chemical Physics*, vol. 55. P. 4012-4017.

Woodroof, M., Wittkopf, J., Gu, S., Yan, Y., 2015. Exchange current density of the hydrogen oxidation reaction on Pt/C in polymer solid base electrolyte. *Electrochemistry Communications*, vol. 61, p. 57-60.

Zhu, Y., Brosha, E., Zelenay, P., 2002. Optimization of Carbon-Supported Platinum Cathode Catalyst for DMFC Operation. 202nd Meeting of the Electrochemical Society, Salt Lake City, UT, October 20-25

CHAPTER 11. DETAILED SYSTEM MODELING

With the development of the comprehensive cell model more detailed predictions of the CLHP system performance could be performed. The initial design stage thermodynamic model assumed that the reactions went to completion. A more comprehensive system model was designed to track concentration changes in the working fluid and incorporate the detailed cell model. A diagram of the CLHP cycle for the model is shown in Figure 11.1 including the state points.

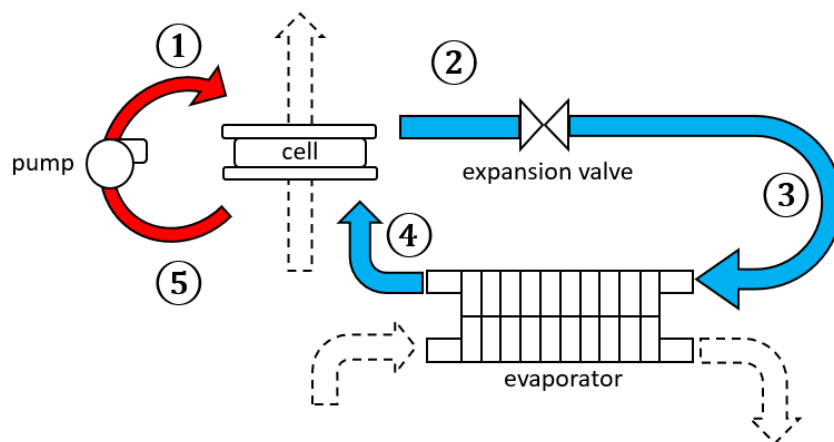


Figure 11.1: System schematic for CLHP cycle modeling.

11.1 Isopropanol-Acetone Mixture Modeling

Mixtures of isopropanol and acetone will appear throughout the CLHP cycle due to incomplete conversions in the cell. To model the 2-component mixture, the Van-Laar equation is used, Equation 11.1 - 11.3 (Mir et al. 1963). The constants A and B were determined as 0.2883 and 0.2770, respectively, by Freshwater et al. (1967).

$$P = x_{IPA}\gamma_{IPA}P_{sat_{IPA}} + x_{ACTN}\gamma_{ACTN}P_{sat_{ACTN}} \quad (11.1)$$

$$\ln(\gamma_{IPA}) = \frac{A}{\left[1 + \left(\frac{x_{IPA}}{x_{ACTN}}\right)\left(\frac{A}{B}\right)\right]^2} \quad (11.2)$$

$$\ln(\gamma_{ACTN}) = \frac{B}{\left[1 + \left(\frac{x_{ACTN}}{x_{IPA}}\right)\left(\frac{B}{A}\right)\right]^2} \quad (11.3)$$

Isopropanol and acetone form a zeotropic mixture. Because of this, a temperature glide will accompany the evaporation process. Examples of the CLHP cycle operation are shown in Figures 11.2 and 11.3, where the bubble and dew lines are drawn for low and high pressures operation regions. State (1) is at high pressure and exists as a subcooled liquid. After entering the cell, the fluid undergoes a concentration change increasing its acetone content, state (2). From here, the fluid is throttled to low pressure, forms a 2-phase mixture, and enters the evaporator, state (3). The fluid then heats up in the evaporator until a given approach temperature is reached, state (4). The outlet of the evaporator can be either a 2-phase mixture or a superheated vapor. The fluid then returns to the cell. From states (4) to (5), the fluid is heated and undergoes another concentration change.

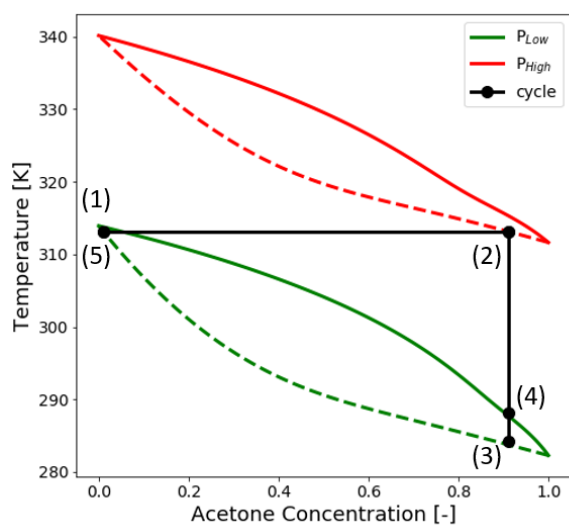


Figure 11.2: T-x diagram of CLHP cycle.

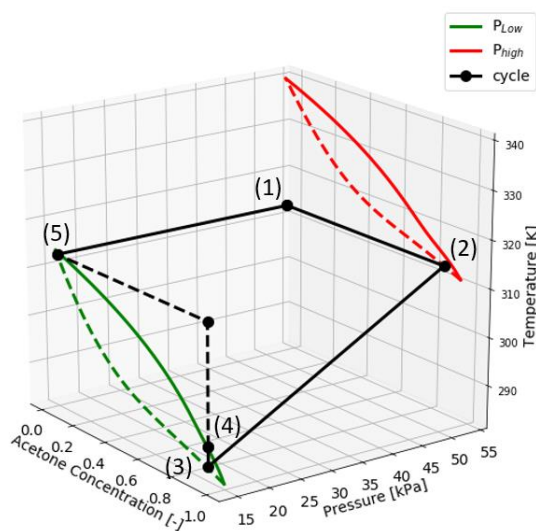


Figure 11.3: T-P-x diagram of CLHP cycle.

The fluid enthalpies are calculated based on mole weighted averages of the isopropanol and acetone content. If the mixture is single phase, then Equations 11.4 or 11.5 are used to find the enthalpy of the liquid or gas phase, respectively. The enthalpy of the pure component is calculated as previously done using Equations 4.10 and 4.11. If two phases are present, first the quality is determined using Equation 11.6. Then, the concentration of each phase is determined using the relationships in Equations 11.1 to 11.3, 11.7 and 11.8. Finally, the enthalpy of the two-phase mixture is determined using Equation 11.9.

$$h_{liq,mix} = x_{IPA}h_{L_{IPA}} + x_{ACTN}h_{L_{ACTN}} \quad (11.4)$$

$$h_{gas,mix} = y_{IPA}h_{G_{IPA}} + y_{ACTN}h_{G_{ACTN}} \quad (11.5)$$

$$quality = \frac{(T - T_{bubble})}{(T_{dew} - T_{bubble})} \quad (11.6)$$

$$y_{IPA} = \frac{x_{IPA}y_{IPA}P_{sat_{IPA}}}{P} \quad (11.7)$$

$$y_{ACTN} = \frac{x_{ACTN}y_{ACTN}P_{sat_{ACTN}}}{P} \quad (11.8)$$

$$h_{2ph,mix} = (1 - quality) \cdot h_{liq,mix} + quality \cdot h_{gas,mix} \quad (11.9)$$

11.2 Calculation Procedures

The final model shares many similarities with the design-stage model described in Chapter 4. Like the design-stage model, the desired source and sink temperatures need to be specified beforehand. An approach temperature is used to determine the temperature of the cell coolant inlet, Equation 11.10. Since much of the cycle performance seems to be contingent on the performance of the cell, it is believed that simple heat exchanger models would again suffice for the system model. A constant isentropic efficiency is again used to model the pump performance, Equation, 4.7.

$$T_{coolant_{in}} = T_{sink} + T_{approach} \quad (11.10)$$

In the design-stage model, saturation pressures of pure acetone are used to determine the system pressures. The influence of fluid mixtures on the system pressures is now incorporated into the model. Since the CLHP seeks to perform compression in the liquid phase, it is necessary for the fluid entering the pump to be a liquid. For a given mixture composition, the temperature and pressure required to form a saturated liquid will vary. With the source and sink temperatures specified, knowledge of the working fluid composition is also needed to determine the high and low system pressures. The low side pressure is chosen such that for the given concentration and cell temperature, state ⑤ would be a saturated liquid. The high side pressure is chosen such that for the given cell temperature and composition at state ② the fluid would also be a saturated liquid.

The valve is assumed to be isenthalpic to determine the conditions at state ③. Since the selection of the system operating pressures is based on the fluid compositions and cell temperature, there is no guarantee that the temperature at the inlet to the evaporator would be low enough to accept heat from the source temperature level for all possible compositions. Hence, the model has to check if the temperature at state ③ is below a certain threshold before continuing with the calculations. The working fluid then absorbs heat in the evaporator from states ③ to ④. The temperature at state 4 is determined by Equation 11.11. The temperature at state ④ is used to determine the phase of the fluid.

$$T_4 = T_{source} - T_{approach} \quad (11.11)$$

With the specified mass flow rates and state point enthalpies determined from the calculated temperature values, the cooling capacity of the cycle are determined using Equation 11.12. To calculate the system coefficient of performance, the cell's power consumption is required. To determine the energy needed to drive the reaction, the comprehensive cell model is used. Given the compositions of the reactants entering the cell, the voltage applied to the cell is varied until the desired outlet composition is achieved. Then the power consumption is determined according to Equation 11.13 by summing the currents from each of segment in the discretized cell and multiplying it by the applied voltage. The COP_C is determined as previously done by Equation 4.24. A summary of the overall calculation procedure is given in Figure 11.4.

$$\dot{Q}_c = \dot{n}_{cathode}(h_4 - h_3) \quad (11.12)$$

$$\dot{W}_{cell} = V \sum i_{segments} \quad (11.13)$$

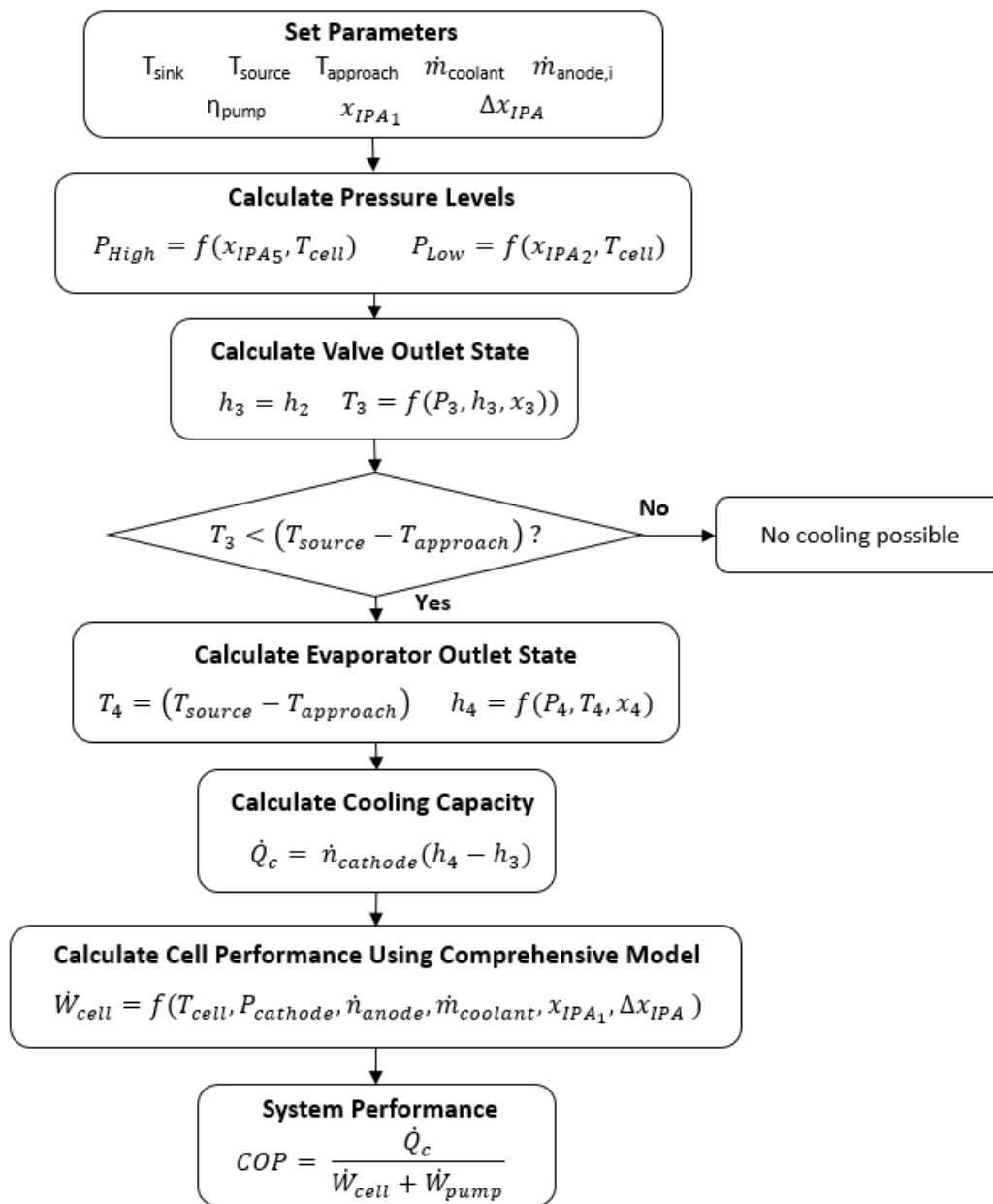


Figure 11.4: Flow chart of calculation process for system model incorporating working fluid composition and comprehensive cell model.

11.3 System Sensitivity Analysis

The CLHP system model was run under different operating conditions to help determine the most suitable parameters for the system. The material properties of the electrochemical cell used in this study are given in Table 11.1. The selection of these properties was guided by results of the sensitivity study on the cell as well as previous experimental results.

Table 11.1: Properties of electrochemical cell for comprehensive model.

Parameter	Value	Units	Layer Thickness	Value	Units
cell area	200	cm ²	anode cooling channel	100	μm
catalyst loading	2.0	mg/cm ²	anode flow plate	1000	μm
particle size	1.6	nm	anode reactant channel	500	μm
i₀ catalyst	0.01	A/m ² - catalyst	anode diffusion layer	100	μm
carbon fraction	0.1	-	anode catalyst layer	-	μm
σ_{0,SPEEK}	1.03e-3	S-m	PEM	50	μm
E_{A,SPEEK}	0.02378	eV	cathode catalyst layer	-	μm
			cathode diffusion layer	100	μm
T_{source}	20	°C	cathode reactant channel	500	μm
T_{sink}	35	°C	cathode flow plate	1000	μm
T_{approach}	5	K	cathode cooling channel	100	
m_{anode}	100	μg/s			
m_{coolant}	0.5	g/s			

The initial concentration of the isopropanol-acetone mixture entering the anode at state ① and the extent to which the isopropanol is converted into acetone was of great importance to the overall performance of the CLHP. Since states ⑤ and ② need to emerge as saturated liquid at the cell temperature, the composition of the working fluids will ultimately determine the pressure levels achieved over the cycle. Figure 11.5 depicts the variation in system COP for various initial isopropanol concentrations at state ①, and the change of concentration that occurs within the cell. For each starting concentration, a maximum emerges at a particular conversion degree. The combination of $x_{IPA,1} = 0.96$ and $\Delta x_{IPA} = 0.91$ produced one of the most favorable COPs of the system states investigated.

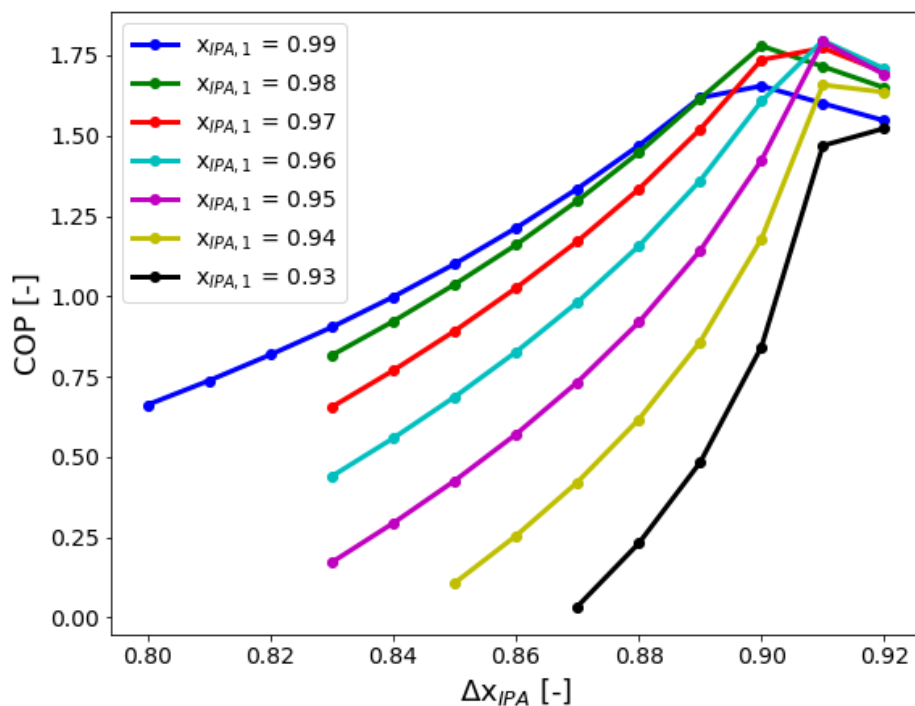


Figure 11.5: Sensitivity analysis for system concentration changes.

Using the values $x_{IPA,1} = 0.96$ and $\Delta x_{IPA} = 0.91$, the influence of the source and sink temperatures were investigated, Figures 11.6 and 11.7. Both plots show a region of near constant COP and then a sharp drop off. This can be explained by the fact that the pressure levels are defined independently of the system temperature lift. At low source temperatures, state ④ moves closer to state ③ in Figure 11.2, lowering the system cooling capacity. As the source temperature rises, state ④ eventually reaches the dew line and becomes a saturated vapor. From this point, any additional increases in the source temperature will only result in the sensible heating of the working fluid, leading to only marginal increases in COP. A similar process holds true for increases in the sink temperature. In this case, the fluid emerging after the expansion valve at state ③ will move close to state ④ for higher sink temperatures.

The influence of the anode reactant flow rate and the coolant flow rates are shown in Figures 11.8 and 11.9. At low anode reactant flow rates, the system COP increased. This was due to longer residence times for the reactants in the cell. The longer the reactants are in the cell, the lower the applied voltage needs to be to convert the reactant during the time it is in the cell. As

expected, at high reactant flow rates, higher voltages are needed to convert the reactants in the residence time and as such lower COPs result. The coolant flow helps maintain the cell temperature at a desired value. The lower the flow rate, the higher the cell temperature will rise. At very low flow rates, this temperature rise becomes detrimental and the system COP decreases.

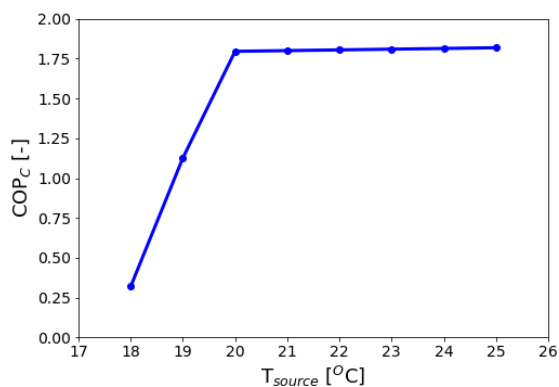


Figure 11.6: Sensitivity analysis for source temperature.

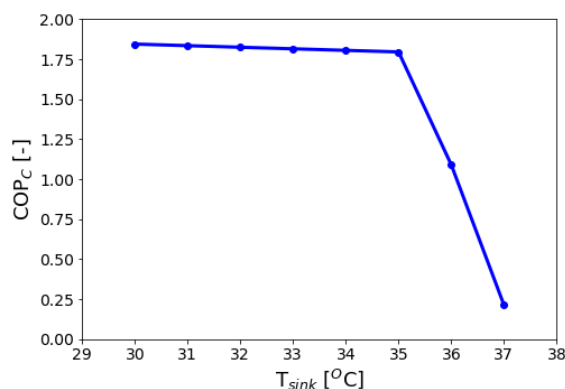


Figure 11.7: Sensitivity analysis for sink temperature.

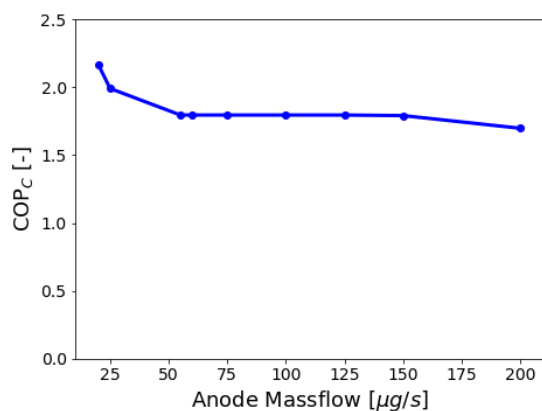


Figure 11.8: Sensitivity analysis of anode reactant flow rate.

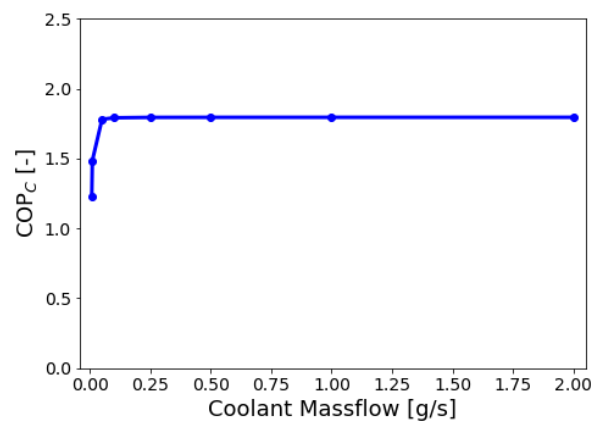


Figure 11.9: Sensitivity analysis of coolant mass flow.

11.4 Cell Modifications

The projected COPs for the system model incorporating concentration changes and the detailed cell model were much lower than those predicted by the design-stage thermodynamic model. One of the most notable differences between the model results was the applied voltage in the cell. The design-stage model assumed a voltage of 0.036 V would be required to drive the isopropanol-acetone CLHP. The comprehensive cell model predicted that voltages on the order

of 0.1 V would be required. This represented a nearly 3 times increase in the applied voltage which would greatly increase power consumption for a given current flow in a cell.

The cause for this steep increase was due to the concentration overpotential within the cell. Shown in Equation 10.91, as the conversion reaction moves closer to completion, a concentration gradient develops that encourages the reaction to proceed in the reverse direction. This requires that a sufficiently high voltage be applied to the entire cell so that the reactants near the end of the reaction can still be converted. An issue with this approach is illustrated by looking at how the cell power is defined in Equation, 11.13. The current in each segment of the cell along the flow path is multiplied by the same applied voltage. The reactant stream near the inlet to the cell has not undergone significant conversion yet. As such, the driving voltage needed to move the reaction forward near the inlet of the cell is significantly lower than that needed near the cell outlet where an adverse concentration gradient has developed.

In an ideal situation, the applied voltage would continuously vary along the reactant flow path in order to compensate for the varying concentration overpotential. One way to approximate this would be to divide the cell into different voltage regions. To accomplish this, multiple cells could be stacked in series, Figure 11.10. In such a configuration, the applied voltage in each segment would need to be optimized. Figure 11.11 shows the results of dividing cells of equal total area into multiple voltage regions. For each cell with multiple segments, the applied voltages of all but the last segment were manually optimized, Appendix B. The voltage of the final segment was determined such that the system model specified conversion degree could be achieved. The power consumption for the segmented cell was determined by Equation 11.14.

$$\dot{W}_{cell} = \sum_i V_i i_{segment} \quad (11.14)$$

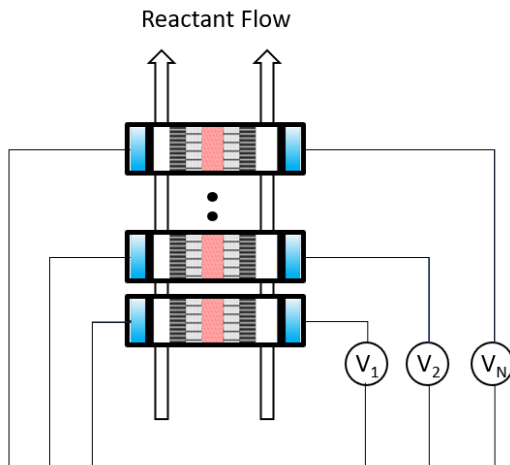


Figure 11.10: Cell divided into multiple voltage regions.

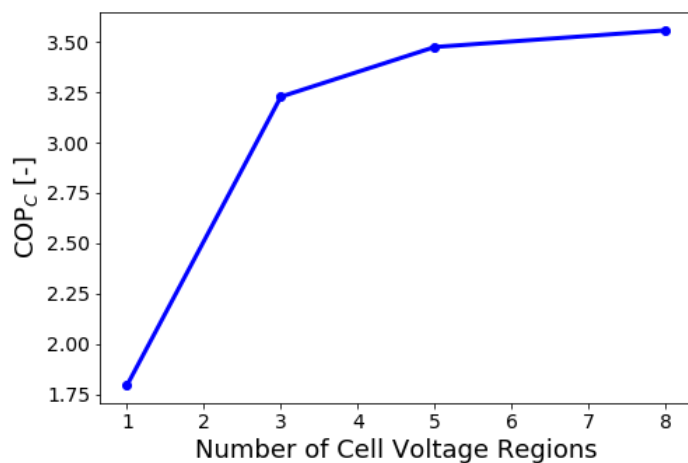


Figure 11.11: Effects of dividing the cell into multiple voltage regions.

The operation point $x_{\text{IPA},1} = 0.96$ and $\Delta x_{\text{IPA}} = 0.91$ was identified as a near optimum concentration for the CLHP for a solid cell with a single applied voltage. An 8-segment cell was used in conjunction with the CLHP system model and the operating conditions in Table 11.1. Figure 11.12 shows that the point $x_{\text{IPA},1} = 0.99$ and $\Delta x_{\text{IPA}} = 0.89$ provided one of the highest system performances with this cell configuration.

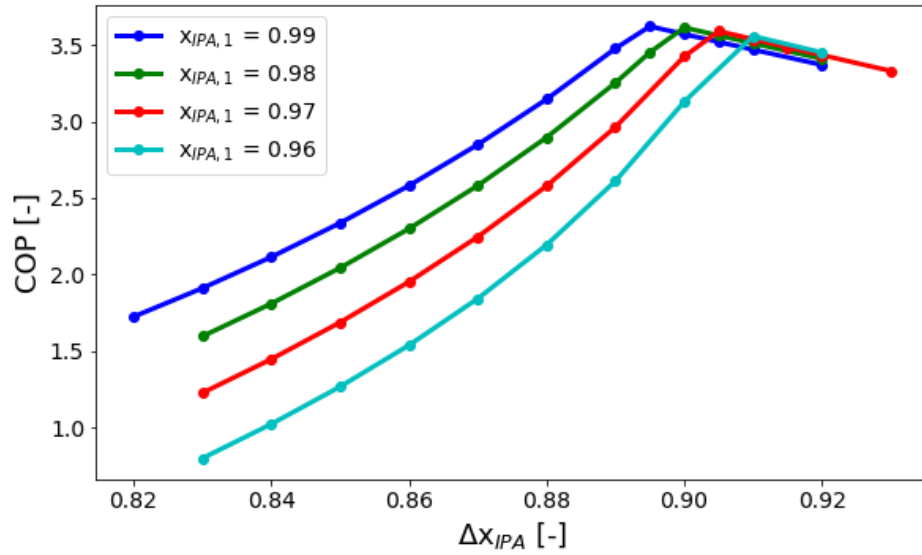


Figure 11.12: Concentration impact on performance for 8-segment cell with multiple applied voltages.

11.5 System Modifications

A possible improvement that could be made to the CLHP system in addition to modifying the cell architecture was to include a regeneration stage between the cell and the evaporator, Figure 11.13. The fluid leaving the evaporator should always be at a lower temperature than the cell. By using a regenerator, the fluid entering the expansion valve can be subcooled to increase the overall cooling capacity. The regenerator was modeled using an effectiveness of 95% and Equations 11.15 - 11.17.

$$\dot{Q}_{regen} = \varepsilon_{regen} \text{MIN}[\dot{n}_{anode}(h_2 - h(T_4, P_2)) , \dot{n}_{cathode}(h(T_2, P_4) - h_4)] \quad (11.15)$$

$$h_{2b} = h_2 - \frac{\dot{Q}_{regen}}{\dot{n}_{anode}} \quad (11.16)$$

$$h_{4b} = h_4 + \frac{\dot{Q}_{regen}}{\dot{n}_{cathode}} \quad (11.17)$$

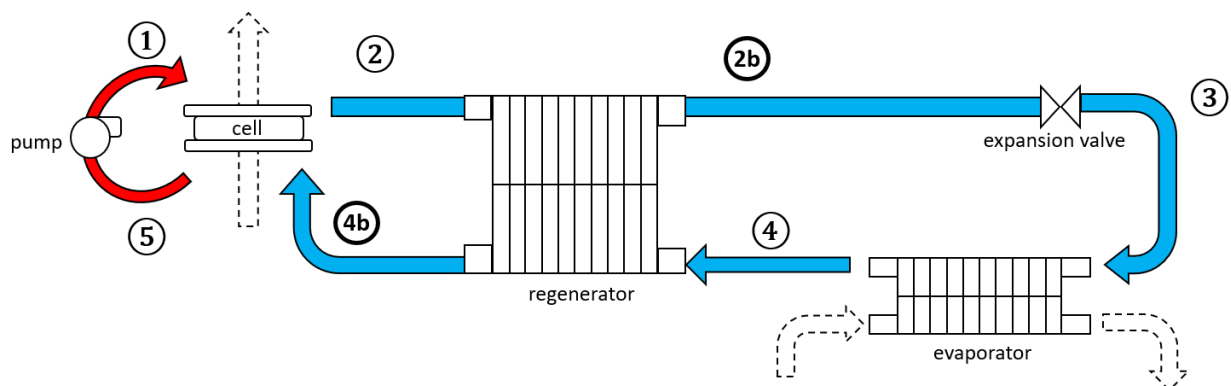


Figure 11.13: Schematic for CLHP system incorporating a regenerator.

Using the parameters from Table 11.1 and a cell divided into 8 voltage regions, the performance of a CLHP using regeneration was modeled. With the introduction of regeneration, the optimal concentration operation changed to $x_{IPA,1} = 0.99$ and $\Delta x_{IPA} = 0.84$, as seen in Figure 11.14.

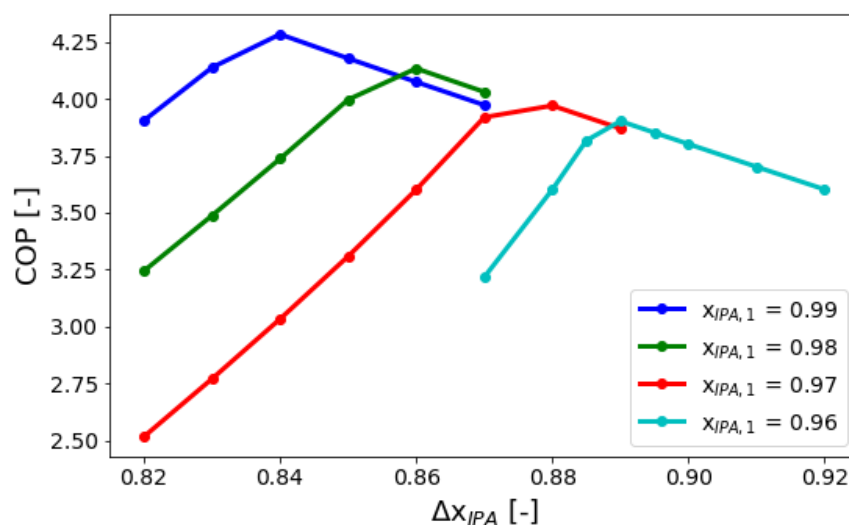


Figure 11.14: Concentration effects on CLHP performance with segmented cell and regeneration.

Besides the operation temperatures, the flow rate of the reactants has one of the greatest influences on the performance of the CLHP system. The comparisons of three CLHP systems, one using a single voltage application cell, another using a segmented cell with multiple voltages, and another using a segmented cell coupled with regeneration are shown in Figures 11.15 and

11.16. At lower flow rates, the COP of all 3 systems increase. As previously mentioned, this was because lower input voltages were required due to increased residence time of the reactants in the cell. The lower flow rates also come with the penalty of lower system capacities. A balance between efficiency and capacity must be made for any CLHP application.

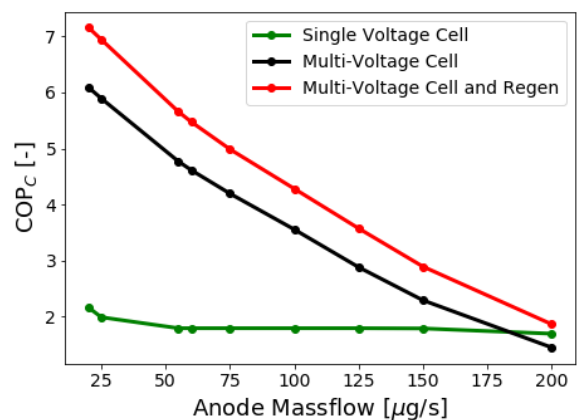


Figure 11.15: Effect of reactant mass flow on system COP for different CLHP architectures using a 200 cm² cell.

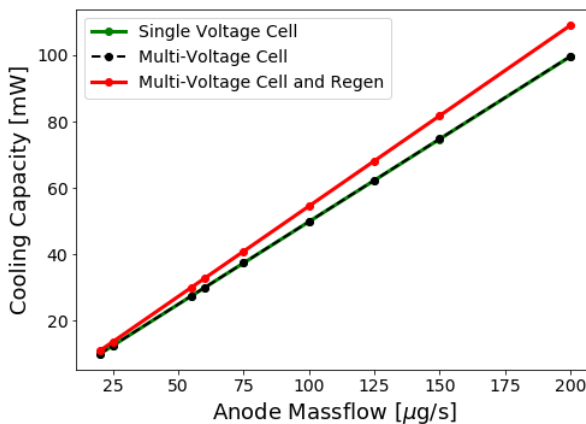


Figure 11.16: Effect of reactant mass flow on system capacity for different CLHP architectures using a 200 cm² cell.

11.6 Energy Savings and System Scale

The developed system model has provided valuable insight into the performance characteristics of the CLHP cycle under realistic operating conditions. An important goal of this investigation was to better understand the techno-economic feasibility of the CLHP as a heating and cooling alternative to traditional technologies. To do this, the generated modeling results were used to determine the energy performance and system scale.

As mentioned earlier, the development of higher efficiency air conditioning and heat pumping devices will be of great importance in the decades to come. The CLHP system model demonstrated the ability to produce high efficiencies over a range of capacities. Figure 11.17 shows how the projected CLHP performance compares to SEER targets set by the International Energy Agency for residential central air conditioning equipment (Goetzler et al. 2016 and Hendron et al. 2010). The CLHP system modeled incorporated a segmented cell and a regenerator. Minor optimization led to an operation condition consisting of an initial isopropanol

concentration of 0.99 and a cell concentration change of 0.5. The SEER calculations were performed using the conditions outlined by ANSI/AHRI Standard 210/240 for single speed compressor units (AHRI, 2012). A heat exchanger effectiveness of 80% was used to determine the approach temperature in the evaporator assuming that the capacity of the airflow stream was equal to or greater than that of the refrigerant, Equations 11.18 and 11.19. Humid air properties were calculated using CoolProp (Bell et al. 2014). Assuming a 10 K temperature change in the air temperature across the evaporator, the air mass-flow and volumetric flow rates necessary to heat the refrigerant were determined and then used by relations from ANSI/AHRI Standard 210/240 to estimate a fan power, Equation 11.20. This fan power was then used to modify the COP relation, Equation 11.21, and the calculated COP was then converted into a SEER rating, Equations 11.22 and 11.23. By controlling the flow rate through the cell, the CLHP has the potential to meet and exceed prospective air conditioning efficiency targets.

$$\dot{Q}_{evap} = \varepsilon_{evap}(\dot{n}_{cathode}(h_4(T_{source}, P_4, x_4) - h_3)) \quad (11.18)$$

$$h_4 = h_3 + \frac{\dot{Q}_{evap}}{\dot{n}_{cathode}} \quad (11.19)$$

$$\dot{W}_{fan} = \frac{365 W}{1000 scfm} \dot{V}_{air} \quad (11.20)$$

$$COP = \frac{\dot{Q}_{evap} - \dot{W}_{fan}}{\dot{W}_{cell} + \dot{W}_{pump} + \dot{W}_{fan}} \quad (11.21)$$

$$EER = 3.41214 \cdot COP \quad (11.22)$$

$$SEER = PLF(0.5) \cdot EER_{test,B} \quad (11.23)$$

The comprehensive cell model developed incorporated data about the electrochemical reactor's various dimensions. This allowed for the determination of the reactor size needed to achieve a given cooling capacity. Using the cell geometries and conditions given in Table 11.1, and derived catalyst layer thicknesses of 23 μm , the volumetric cooling capacity of the cell was defined using Equation 11.24. The cell volume was determined as the product of the cell area and the sum of all the layer thicknesses. Figure 11.18 illustrates how many Watts of cooling could be achieved per cubic meter of cell volume for a given system COP.

$$\dot{Q}_V = \frac{\dot{Q}_c}{A_{cell} \sum_i LayerThickness_i} \quad (11.24)$$

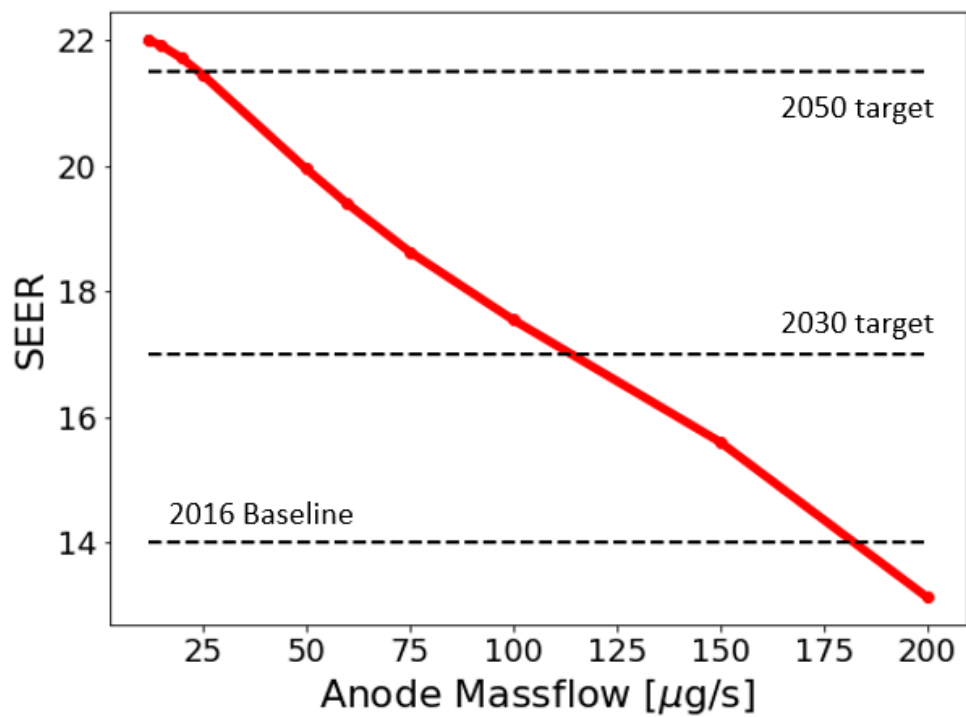


Figure 11.17: Comparison of CLHP efficiency to IEA performance targets.

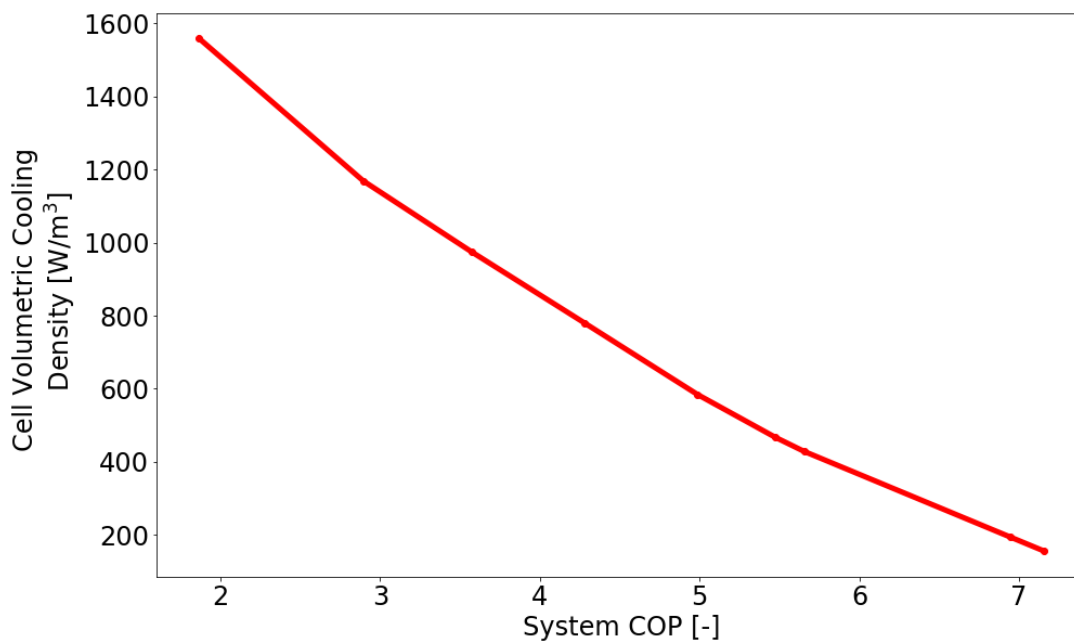


Figure 11.18: Variation in volumetric cooling density as a function of COP.

Using the current rate of reactions taking place in the cell modeled, large cell volumes would be required to achieve cooling capacities on par with traditional vapor compression systems. Operating with a COP of 7, the volumetric cooling density of the cell would be near 200 W/m^3 . To achieve a 1 ton of cooling capacity a reactor of 17.55 m^3 would be required. The reaction density of the cell must be significantly increased in order to achieve large cooling capacities within reasonable packages.

11.7 References

- Air-Conditioning, Heating, and Refrigeration Institute (AHRI), 2012. 2008 Standard for Performance Rating of Unitary Air-Conditioning & Air-Source Heat Pump Equipment. Report
- Bell, I., Wronski, J., Quoilin, S., Lermort, V., 2014. Pure and Pseudo-pure Fluid Thermophysical Property Evaluation and the Open-Source Thermophysical Property Library CoolProp. *Industrial and Engineering Chemistry Research*, vol. 53, p. 2498 – 2508.
- Freshwater, D., Pike, K., 1967. Vapor-liquid equilibrium data for systems of acetone-methanol isopropanol. *Journal of Chemical & engineering Data*, vol. 12, p. 179-183.
- Goetzler, W., Guernsey, M., Young, J., Fuhrman, J., Abdelaziz, O., 2016. The Future of Air Conditioning for Buildings. U.S. Department of Energy, Building Technologies Office, Report
- Hendron, B., Engebrecht, C., 2010. Building America House Simulation Protocols. U.S. Department of Energy, Building Technologies Office, Report
- Mir, L., Stiedler, F., 1963. A Least Squares Solution for the Van Laar Constants of a Binary Mixture. *Journal of Physical Chemistry*, vol. 67, p. 2503 -2504.

CHAPTER 12. CONCLUSIONS AND RECOMMENDATIONS

The chemical looping heat pump is a novel heat pumping cycle employing liquid phase compression of the working fluid and a chemical reaction to alter the fluid's volatility. Solid polymer electrolyte electrochemical cells similar to those used in the fuel cell industry were proposed as possible reaction drivers for the cycle. A thermodynamic system model was developed and used to identify a variety of potential working fluids for an electrochemically driven CLHP. Of the fluids investigated, isopropanol-acetone was deemed to be one of the most suitable pairs. This was due not only to its superior performance but also due to its ease of availability and low toxicity.

An experimental campaign was undertaken to investigate the nature of the isopropanol-acetone reaction under conditions similar to those of a potential CLHP. A test rig was designed and constructed to feed reactants to a cell and measure the rates of reactions. A number of challenges were encountered during the initial testing stemming from compatibility issues between the working fluids and traditional Nafion membranes.

From the experiments, it was found that the rate of the isopropanol-acetone hydrogenation-dehydrogenation reactions were slower than expected for the cell configurations that were tested. This would have led to a low power density for any potential CLHP system using these reactants. To address this, an optimization effort was undertaken to find materials that would better facilitate the reactions in the CLHP. A procedure for developing membrane electrode assemblies was developed in house to provide control over all the manufacturing steps of the cell. In this manner, multiple combinations of membrane materials and catalyst materials were investigated for use in the isopropanol-acetone reactions.

The search for new membrane materials of anhydrous membranes. Since the CLHP would ideally need to operate only with isopropanol and acetone, a membrane capable of operating in the absence of alcohol was a necessity. Multiple membranes were fabricated into electrochemical cells and tested in high alcohol concentration environments. Of the membrane materials

investigated, reinforced sPEEK membranes were found to be the most suitable to use with the desired working fluids.

The influence of multiple catalyst metals on the performance of an isopropanol-acetone cell was also evaluated. Mixtures of several different catalyst materials together were also evaluated. In order to gain further insight into how the properties of various catalyst impact the reaction rate, computational methods to predict catalyst performance were investigated. Ultimately, the use of density-functional theory proved to be a useful means for modeling the catalyst activity. A library was generated of the binding energies of various descriptor molecules to the surface of the pure metal surfaces of the catalyst materials used in the study. A mole weighted average of these calculated values for pure surfaces were used to approximate the properties of catalyst mixtures. By using an activity map, regions of interest were identified to help guide further catalyst selection. Mixtures of Pt, Co, Au, and Cu were found to produce superior catalytic activities compared to most other materials investigated.

Using the experimental data gained, a comprehensive model of the electrochemical cell was developed. With this, more accurate predictions of the performance of a possible CLHP system could be performed. The model was developed using open source tools incorporating aspects of pressure drop and reactant concentration changes. The model was validated against current-voltage data gained from the experimental campaign. Additionally, the accuracy of the model's sub-models was evaluated against trends of similar systems in the literature.

A detailed system model of the CLHP was developed through utilization of the comprehensive cell model and incorporating reactant concentration changes throughout the system. The initial COP predictions of the model were lower than previously expected based on initial thermodynamic studies. This was found to be due to concentration overpotentials developing in the cell as the reactions progressed. A method of dividing the cell into multiple voltage regions was proposed and found to be beneficial to the overall system performance. The benefit of a regeneration stage in the cycle was also evaluated.

The results obtained from the final system modeling showed that the CLHP driven by solid polymer electrochemical cells has the potential to produce COPs higher than current and future energy efficiency standards for vapor compression systems. In its present embodiment, the energy density of the system would be a serious hindrance to immediate commercialization of such a concept. Cells with large volumes would be required as reactors to convert the working fluid at an appreciable rate to produce a reasonable cooling capacity in comparison to traditional equipment. The currently proposed CLHP concept may still find use in niche applications where high efficiency, a low profile and low cooling loads are required.

It is important to note that the work done here is not inconclusive of all that could be done with the chemical looping heat pump concept. The restriction to polymer membrane based electrochemical cells was based on the desire to separate the pressure regions of the cycle and use off the shelf components. Other reactive vessels and devices could be explored for greater volumetric capacity from the cycle. Alternative working fluids may also play a role in improving the viability of the CLHP for traditional heat pumping applications. Fluids with more favorable electro-kinetics and higher enthalpies of vaporizations may be more suitable for the system. The need to completely convert the reactants in the system leads to severe concentration overpotentials which hinder performance. A working fluid combination where products and reactants could naturally be separated would be of great benefit to the overall cycle performance. Heat engines are the thermodynamic inverse of heat pumps. Adapting the CLHP concept to a power generation device could also be an interesting avenue of future investigation.

The work done here represents a significant addition to the investigation of heat pumping systems using chemically reactive working fluids. The use of the reaction to intentionally alter the volatility of a fluid to allow for liquid compression has not seen extensive development. The identification of membrane materials and the development of catalyst selection aids for the anhydrous bilateral reactions between isopropanol and acetone may prove useful to future CLHP investigation as well as other fields such as energy storage. The comprehensive cell model expanded on previous methods described in the literature and was developed using an easily accessible open source platform which can be further advanced by other researchers. No single technology holds the solution to meeting the increasing heating and cooling demands of the

future, but with further development, the chemical looping heat pump may make an important contribution towards this end.

APPENDIX A. DFT CALCULATIONS

Table A.1: DFT energies of clean surfaces.

	Clean surface			
	U	dS (300 K)	dS (350 K)	dS (400 K)
Au	-38.7341	0.006662	0.007136	0.007547
Pt	-76.0877	0.005973	0.00644	0.00685
Fe	-100.5507	0.004544	0.0050064	0.0054101
Co	-94.56074	0.005295	0.00576151	0.0061677
Ni	-85.000778	0.005281289	0.00574	0.006149
Cu	-43.6233	0.00455947	0.005018	0.0054199
Mo	-139.40673	0.004426	0.004878	0.005276
Ru	-109.9458	0.00574	0.0062099	0.00661735
Rh	-85.36135	0.005876	0.006344	0.00675
Pd	-47.2033	0.0058584	0.00632696	0.0067348
Ag	-35.377	0.006224	0.006696	0.007107
Sn	-67.20474	0.005570464	0.006048948	0.006454184
Ir	-106.8984	0.00636	0.006833	0.00724

Table A.2: DFT energies of free gasses.

	dU	dS (300 K)	dS (350 K)	dS (400 K)
CO	-13.8688	0.000424	0.000495	0.000558
H₂	-5.87908	0.000246	0.000296	0.000342
H₂O	-13.8688	0.000424	0.000495	0.000558
O₂	-10.2772	0.000381	0.000441	0.000495

Table A.3: DFT energies of CO adsorbed system.

	dU	dS (300 K)	dS (350 K)	dS (400 K)
Au	-56.4561	0.048423	0.048957	0.049421
Pt	-94.1475	0.048079	0.04861	0.049076
Fe	-119.736	0.0478	0.048328	0.048788
Co	-113.683	0.048733	0.049266	0.049729
Ni	-104.053	0.048312	0.048845	0.049307
Cu	-62.0501	0.047845	0.048381	0.048848
Mo	-157.416	0.04809	0.048625	0.04909
Ru	-128.398	0.04808	0.048614	0.049078
Rh	-104.053	0.048436	0.048971	0.049436
Pd	-66.4396	0.04825	0.04878	0.04925
Ag	-53.1446	0.048386	0.04891	0.04938
Sn	-102.88	-0.12112	-0.12059	-0.12015
Ir	-125.149	0.047907	0.048436	0.048898

Table A.4: DFT energies of OH adsorbed system.

	dU	dS (300 K)	dS (350 K)	dS (400 K)
Au	-49.7855	0.046734	0.047262	0.04772
Pt	-87.285	0.046607	0.047132	0.047589
Fe	-113.399	0.046175	0.046694	0.047147
Co	-107.384	0.046182	0.046701	0.047154
Ni	-97.2896	0.046742	0.04726	0.047715
Cu	-56.6533	0.04664	0.047166	0.047625
Mo	-152.184	0.046143	0.046667	0.047124
Ru	-122.193	0.046343	0.04687	0.047329
Rh	-97.233	0.046018	0.04654	0.046996
Pd	-58.6707	0.046365	0.046892	0.047351
Ag	-47.5958	0.046443	0.046967	0.047425
Sn	-102.989	-0.11722	-0.11676	-0.11635
Ir	-118.329	0.046218	0.046746	0.047206

Table A.5: DFT energies of O adsorbed system.

	dU	dS (300 K)	dS (350 K)	dS (400 K)
Au	-45.7119	0.006847	0.007352	0.007792
Pt	-83.8156	0.054151	0.054657	0.055098
Fe	-116.131	0.054043	0.054549	0.054989
Co	-104.479	0.005273	0.005759	0.006186
Ni	-94.9973	0.053648	0.054151	0.054589
Cu	-52.8872	0.054229	0.054734	0.055174
Mo	-149.083	0.053869	0.054377	0.054818
Ru	-118.902	0.054122	0.054631	0.055073
Rh	-93.8741	0.054005	0.05451	0.05495
Pd	-55.0549	0.054311	0.054817	0.055257
Ag	-43.4174	0.054674	0.055182	0.055624
Sn	-73.2175	0.055372	0.05589	0.056337
Ir	-115.259	0.054033	0.054538	0.054978

APPENDIX B. CELL OPTIMIZATIONS

Table B.1: Optimization of voltages for 3 segment cell.

V1	V2		
0	0.05	COP	3.185342
		V _{final}	0.09871
0.005	0.05	COP	3.213586
		V _{final}	0.098465
0.01	0.05	COP	3.22728
		V_{final}	0.09821
0.015	0.05	COP	3.225103
		V _{final}	0.097978
0.01	0.04	COP	3.17635
		V _{final}	0.09987
0.01	0.06	COP	3.181629
		V _{final}	0.096939
0.01	0.045	COP	3.2139
		V _{final}	0.099
0.01	0.055	COP	3.21612
		V _{final}	0.09753

Table B.2: Optimization of voltages for 5 segment cell.

V1	V2	V3	V4		
0.01	0.03	0.05	0.07	COP	3.452818
				V _{final}	0.102427
0.01	0.03	0.05	0.06	COP	3.416158
				V _{final}	0.105411
0.01	0.03	0.05	0.08	COP	3.40893
				V _{final}	0.0998
0.01	0.03	0.04	0.07	COP	3.42446
				V _{final}	0.103951
0.01	0.03	0.06	0.07	COP	3.411203
				V _{final}	0.10103
0.01	0.04	0.05	0.07	COP	3.418934
				V _{final}	0.101665
0.01	0.02	0.05	0.07	COP	3.422958
				V _{final}	0.10324
0.005	0.03	0.05	0.07	COP	3.474043
				V_{final}	0.102611
0	0.03	0.05	0.07	COP	3.48305
				V _{final}	0.102791

Table B.3: Optimization of voltages for 8 segment cell.

V1	V2	V3	V4	V5	V6	V7		
0	0.005	0.015	0.025	0.035	0.045	0.065	COP	3.1221
							V _{final}	0.132852
0.001	0.005	0.015	0.025	0.035	0.045	0.065	COP	3.117967
							V _{final}	0.1328
0	0.005	0.015	0.025	0.035	0.045	0.08	COP	3.257
							V _{final}	0.1247
0	0.005	0.015	0.025	0.035	0.045	0.09	COP	3.275177
							V _{final}	0.11955
0	0.005	0.015	0.025	0.035	0.05	0.08	COP	3.30788
							V _{final}	0.12294
0	0.005	0.015	0.025	0.035	0.06	0.08	COP	3.373094
							V _{final}	0.119551
0	0.005	0.015	0.025	0.035	0.07	0.08	COP	3.386235
							V _{final}	0.116328
0	0.005	0.015	0.025	0.035	0.065	0.08	COP	3.386326
							V _{final}	0.11791
0	0.005	0.015	0.025	0.045	0.065	0.08	COP	3.445886
							V _{final}	0.115741
0	0.005	0.015	0.025	0.05	0.065	0.08	COP	3.457687
							V _{final}	0.114693
0	0.005	0.015	0.025	0.06	0.065	0.08	COP	3.44417
							V _{final}	0.112681
0	0.005	0.015	0.025	0.055	0.065	0.08	COP	3.457111
							V _{final}	0.113672
0	0.005	0.015	0.035	0.05	0.065	0.08	COP	3.501805
							V _{final}	0.11329
0	0.005	0.015	0.04	0.05	0.065	0.08	COP	3.506449
							V _{final}	0.112612
0	0.005	0.015	0.05	0.05	0.065	0.08	COP	3.480282
							V _{final}	0.111293
0	0.005	0.03	0.04	0.05	0.065	0.08	COP	3.540142
							V _{final}	0.111273
0	0.005	0.02	0.04	0.05	0.065	0.08	COP	3.528821
							V _{final}	0.11216
0	0.01	0.025	0.04	0.05	0.065	0.08	COP	3.55368
							V _{final}	0.111433
0	0.015	0.025	0.04	0.05	0.065	0.08	COP	3.556727
							V_{final}	0.111151
0	0.02	0.025	0.04	0.05	0.065	0.08	COP	3.549074
							V _{final}	0.110869

VITA

Nelson James is one of four children born to parents Neil and Bridget. Prior to his studies at Purdue, he received his B.S. degree in mechanical engineering from Stanford University. Afterwards he attended Purdue University and received a M.S. degree in mechanical engineering studying novel cycles for solar thermal power generation. Through the GEM fellowship program, he interned multiple times at Oak Ridge National Laboratory studying advanced energy saving appliances under the direction of Omar Abdelaziz and Kyle Glusenkamp.

While at Purdue he worked as a research assistant at the Ray W. Herrick Laboratories. He was a teaching assistant for two courses, sustainable energy options and analysis, and Solar Energy Technology. Through the Lambert Fellowship he served as an instructor for undergraduate Thermodynamics I. He received a Bilsland Dissertation Fellowship to complete his doctoral work.

Nelson has accepted a position as a postdoctoral fellow with the United States Department of Energy's Building Technology Office.